EIGENFUNCTION EXPANSION METHOD FOR ANALYSIS OF MITIGATING WAVE LOAD ON AN ELASTIC PLATE AND A SEA WALL IN THE PRESENCE OF THICK POROUS STRUCTURE(S)

A Thesis Submitted

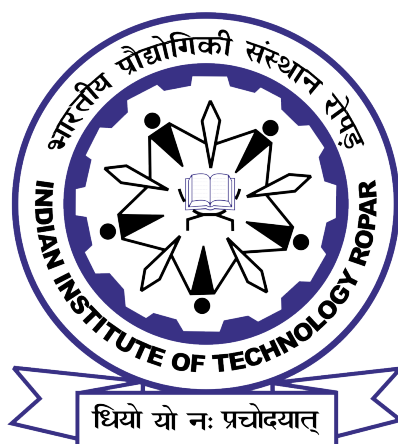*in Partial Fulfilment of the Requirements*

for the Degree of

DOCTOR OF PHILOSOPHY

by

GAGAN SAHOO

(Entry number: 2019MAZ0002)

DEPARTMENT OF MATHEMATICS

INDIAN INSTITUTE OF TECHNOLOGY ROPAR

AUGUST, 2024

Dedicated to

My Father Mr. Gouranga Charan Sahoo
and
My Mother Mrs. Laxmi Sahoo

Declaration of Originality

I hereby declare that the work which is being presented in the thesis entitled **"Eigenfunction Expansion Method for Analysis of Mitigating Wave Load on an Elastic Plate and a Sea Wall in the Presence of Thick Porous Structure(s)"** has been solely authored by me. It presents the results of my own independent investigation/research conducted during the time period from July 2019 of joining the Ph.D. program to June 2024 of Ph.D. thesis submission under the supervision of Dr. S. C. Martha, Associate Professor, Department of Mathematics, IIT Ropar. To the best of my knowledge, it is an original work, both in terms of research content and narrative, and has not been submitted or accepted elsewhere, in part or in full, for the award of any degree, diploma, fellowship, associateship, or similar title of any university or institution. Further, due credit has been attributed to the relevant state-of-the-art and collaborations (if any) with appropriate citations and acknowledgments in line with established ethical norms and practices. I also declare that any idea/data/fact/source stated in my thesis has not been fabricated/ falsified/ misrepresented. All the principles of academic honesty and integrity have been followed. I fully understand that if the thesis is found to be unoriginal, fabricated, or plagiarized, the Institute reserves the right to withdraw the thesis from its archive and revoke the associated Degree conferred. Additionally, the Institute also reserves the right to appraise all concerned sections of society of the matter for their information and necessary action (if any). If accepted, I hereby consent for my thesis to be available online in the Institute's Open Access repository, inter-library loan, and the title & abstract to be made available to outside organizations.

Name: Gagan Sahoo

Entry Number: 2019MAZ0002

Program: PhD

Department: Mathematics

Indian Institute of Technology Ropar

Rupnagar, Punjab 140001

Date: August 09, 2024

Acknowledgement

the CSE Department, with whom I have spent some of my best moments at IIT Ropar.

My acknowledgment would be incomplete without mentioning my family members, especially my father Mr. Gouranga Charan Sahoo, my mother Mrs. Laxmi Sahoo, and my sister Mrs. Minati Sahoo, for their boundless love, moral support, and constant encouragement. Their inspiration and encouragement have been the cornerstone of my perseverance and success.

Last but not least, I sincerely thank the Council of Scientific and Industrial Research (CSIR), Government of India, for providing me with a fellowship during my doctoral study. I am also thankful to IIT Ropar for offering all the necessary facilities for my research and the financial support that enabled me to present my work at various conferences in India and abroad.

Finally, I am profoundly grateful to the Almighty for blessing me with everything I have. Without divine blessings, I would not have been able to complete my research.

Date: August 09, 2024
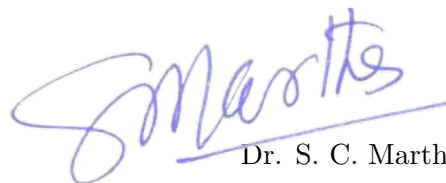
Gagan Sahoo
Department of Mathematics
Indian Institute of Technology Ropar

Certificate

This is to certify that the thesis entitled "**Eigenfunction Expansion Method for Analysis of Mitigating Wave Load on an Elastic Plate and a Sea Wall in the Presence of Thick Porous Structure(s)**", submitted by **Mr. Gagan Sahoo (2019MAZ0002)** for the award of the degree of **Doctor of Philosophy** of Indian Institute of Technology Ropar, is a record of bonafide research work carried out under my guidance and supervision. To the best of my knowledge and belief, the work presented in this thesis is original and has not been submitted, either in part or full, for the award of any other degree, diploma, fellowship, associateship or similar title of any university or institution.

In my opinion, the thesis has reached the standard fulfilling the requirements of the regulations relating to the Degree.

Date: August 09, 2024

Dr. S. C. Martha
Associate Professor
Department of Mathematics
Indian Institute of Technology Ropar
Rupnagar, Punjab 140001

Lay Summary

This thesis presents a comprehensive analysis for finding approximate solutions to boundary value problems associated with the interaction of water waves and various configurations of thick porous structures, namely (i) porous structure extending from the bottom to the free surface, (ii) bottom-standing porous structure, (iii) surface-piercing porous structure, and (iv) submerged porous structure, designed to protect coastal infrastructure, such as very large floating structure (VLFS) and sea wall. Under suitable assumptions, the physical problems of water wave interaction are modeled mathematically. The resulting boundary conditions are linearized using small amplitude wave theory. The boundary value problems are solved using eigenfunction expansions in conjunction with the orthogonality of eigenfunctions, giving rise to a system of equations that are solved numerically. The numerical values of physical quantities of reflection, transmission, and dissipation coefficients, force on the porous structure and force on the sea wall, free surface elevation, plate deflection, shear force, and strain are obtained and plotted for different parameters. These physical quantities play a significant role in Ocean and Marine Engineering for constructing coastal structures such as VLFS, sea walls, and breakwaters. These porous structures mentioned above are essential for protecting ports, harbors, floating bridges, floating storage bases, floating buildings, sea walls, and more from natural calamities such as tsunamis, cyclones, red tides, harmful algal blooms, and rising sea levels. These structures can be built at offshore, parallel to the coastline, to mitigate the impact of incoming wave loads, thereby reducing coastal erosion and ensuring the safety of coastal infrastructures and facilities near the shoreline. Clearly, studying wave-structure interaction problems is of immense importance in ocean engineering for various applications.

Abstract

This thesis presents a comprehensive analysis of a class of water wave problems pertinent to Ocean and Marine Engineering, particularly focusing on the interaction of water waves with thick porous structures designed to protect coastal infrastructure, such as VLFS and sea walls. The physical phenomena related to water wave propagation are mathematically modeled, assuming that the fluid is homogeneous, inviscid, incompressible, and exhibits irrotational and harmonic motion over time. Additionally, the wave motion is considered to be influenced by gravity, with the free surface deviations from its horizontal position assumed to be small enough to justify the application of linearized water wave theory. The objective of this thesis is to focus on a specific class of wave-structure interaction problems, emphasizing the following key areas: (i) reducing the wave impact on an elastic plate by employing thick porous structure(s), (ii) minimizing wave impact on sea wall when an elastic plate and thick porous structure are present, and (iii) investigating the role of submerged porous structure in reducing wave load on sea wall in a step type bottom topography. In Case (i) and Case (ii), the porous structure is a vertical porous structure extended from top to bottom or bottom-standing or surface-piercing. When formulating the physical problems, the governing partial differential equation is the Laplace equation for the case of normal incidence of surface waves, while it is the Helmholtz equation for the oblique incidence of surface water waves. The combined dynamic and kinematic boundary condition at the free surface is of the Robin type, and the impermeable boundary condition at the bottom is of the Neumann type. The elastic plate is modeled by using the thin plate theory, while the flow past the thick porous structure is modeled by using the Sollit and Cross model. Furthermore, far-field conditions are imposed at infinite fluid boundaries to ensure the uniqueness of the solution. The resulting boundary value problems are linearized using small amplitude water wave theory. The boundary value problem is transformed into a system of algebraic equations by employing eigenfunction expansions and leveraging the orthogonality of eigenfunctions. These equations are then solved numerically using the Gauss-Elimination method with the help of MATLAB. For each physical problem, the energy identity is derived using Green's integral theorem, and verifying this identity ensures the accuracy of the numerical results obtained for the physical quantities. Also, the present numerical results are compared with those available in the literature to validate each model. Additionally, in some problems, the convergence on the number of evanescent modes in the eigenfunction series expansions is evaluated numerically. To study the effectiveness of the above thick porous structure(s) in reducing the wave load on the elastic plate/sea wall, the quantities such as reflection, transmission and dissipation coefficients, force on the porous structure, force on the sea wall, and free surface elevation, plate deflection, shear force and strain are calculated numerically. The variations of these quantities with various system and wave parameters are analyzed and illustrated through different graphs. These problems provide information to safeguard essential coastal structures such as VLFS and sea walls. Hence, the study in this thesis play an essential role in the field of ocean and marine engineering, particularly towards

the protection of coastal infrastructure.

List of Publications

I. Papers Published/Under Review:

1. **Gagan Sahoo**, Sofia Singla, and S. C. Martha. "Scattering of oblique water waves by thick porous structure and thin elastic plate." *Ocean Engineering - Elsevier*, 248:110526 (2022), doi: 10.1016/j.oceaneng.2022.110526.

2. **Gagan Sahoo**, Sofia Singla, and S. C. Martha. "Mitigation of wave impact on sea wall by a floating elastic plate and a porous structure." *Journal of Offshore Mechanics and Arctic Engineering - ASME*, 145(5):051202 (2023), doi: 10.1115/1.4056787.

3. **Gagan Sahoo**, Sofia Singla, and S. C. Martha. "Interaction of surface water waves with partial porous structure and floating elastic plate in the presence of sea wall." *Ships and Offshore Structures - Taylor & Francis*, pages 1-18 (2024), doi: 10.1080/17445302.2024.2340920.

4. **Gagan Sahoo**, and S. C. Martha. "Semi-analytical study of reduction of wave impact on an elastic plate in the presence of a vertical porous structure", *Acta Mechanica - Springer*, pages 1-16 (2024), doi: 10.1007/s00707-024-03992-1.

5. **Gagan Sahoo**, and S. C. Martha. "Wave attenuation on a sea wall by submerged thick porous structure over a step-type seabed" (Under review).

6. **Gagan Sahoo**, V. Venkateswarlu and S. C. Martha. "Mitigation of structural response on a floating elastic plate in the presence of multiple porous structures" (Under review).

II. Conference Abstracts/ Presentations:

1. **Gagan Sahoo**, Sofia Singla, and S. C. Martha, "Interaction of oblique water waves with a bottom-standing porous structure and an elastic plate", poster presentation in *"CYNOSURE-2024: National Symposium on Advances in Mathematics"*, held at Department of Mathematics, Indian Institute of Technology Ropar on February 24, 2024.

2. **Gagan Sahoo**, "Wave interactions with submerged porous structure", oral presentation in 68th *Conference of the Indian Society of Theoretical and Applied Mechanics (ISTAM 2023)*, held at NIT Warangal, Warangal during December 7-9, 2023.

3. **Gagan Sahoo**, Sofia Singla, and S. C. Martha, "Mitigation of hydrodynamics response of water wave on elastic plate in the presence of a bottom-standing porous structure", oral presentation in *"Mathematics of Sea Ice and Ice Sheets (MOSSI)"*, organized by Harbin Engineering University, Harbin, China and University of Newcastle, Newcastle, Australia during November 29-30, 2023 (online mode).

4. **Gagan Sahoo**, and S. C. Martha, "The role of vertical porous structure in attenuating the wave impact on an elastic plate", oral presentation in *"International Energy Workshop & the 45th Ocean Engineering Conference (IEWOE)"*, held at National Taiwan Ocean University, Keelung, Taiwan during October 5-6, 2023.

5. **Gagan Sahoo**, Sofia Singla and S. C. Martha, "Reduction of high wave load on a sea wall by an elastic plate and a porous structure", oral presentation in *"10th International Congress on Industrial and Applied Mathematics"*, held at Waseda University, Tokyo, Japan during August 20-25, 2023.

6. **Gagan Sahoo**, Sofia Singla and S. C. Martha, "Interaction of oblique water waves with a surface-piercing porous structure and an elastic plate", oral presentation in *"88th Annual Conference of the Indian Mathematical Society: An International Meet"*, held at Birla Institute of Technology, Mesra, Ranchi, India during December 27-30, 2022.

Contents

List of Figures

List of Tables

Chapter 1

Introduction

1.1 Preamble

In the modern era characterized by rapid population growth, the scarcity of land has become an urgent issue. Very Large Floating Structures (VLFS), which are artificial structures constructed on the sea's surface, have emerged as a promising solution for nations having extensive coastal areas, which can provide an alternative solution for the shortage of land. Also, VLFS offers a cost-effective and environment-friendly alternative, driving infrastructure development such as bridges, docks, and floating airports. This advancement has also facilitated exploring and utilizing offshore resources like oil fields and minerals, leading to increased marine transportation activities. It is important to note that wave impacts can cause damage to this VLFS. Hence, not only the construction of VLFS but also its safety and stability are important.

Like VLFS, rigid vertical sea walls also play an important role in coastal environments. It has been seen that the rigid vertical sea wall is constructed near the shoreline to protect the backland. In some locations, potential hazard happens due to shore erosion; for example, the road or buildings near the shoreline are about to fall into the water due to shore erosion. Hence, constructing a sea wall provides an alternative approach to coastal protection. Further, it may be noted that the sea wall may collapse due to wave impact. These waves not only affect the sea wall but also move the sand away from the base of the sea wall. Hence, the structural safety and stability of the sea wall should be considered when designing offshore structures.

Breakwaters play a crucial role in protecting coastal infrastructure by reducing wave impacts. Traditional rigid barriers, commonly used as breakwaters, face challenges when exposed to extreme climatic conditions, as they reflect a large amount of incident wave energy, leading to increased loads and potential collapse, thus reducing the serviceability of VLFS, sea wall, ports, and harbors. Porous structures have been introduced to dissipate wave energy to mitigate the impact of wave loads and prolong the service life of existing rigid vertical structures. Additionally, vertical flexible porous structures have been proposed as wave barriers due to their lightweight nature and quick deployment compared to fixed rigid barriers. Their structural flexibility and porosity significantly reduce wave forces. Horizontal breakwaters are also effective in protecting harbors, marinas, and shorelines, as they cause minimal interference with water circulation, sediment flow, and aquatic life movement. However, to use and understand the performance of thick porous structures requires a comprehensive analysis of various physical parameters, including

wave reflection, transmission, and energy dissipation. These parameters are influenced by factors such as height, porosity of the porous structure, water depth, incident wave height, crest width, breakwater slope, and wave period.

In the past, analyses of wave-structure interaction were primarily focused on rigid structures, considering physical phenomena such as refraction, diffraction, reflection, shoaling, breaking, and large-scale vortex formation and shedding, which are associated with wave parameters like wave height, direction, period, and phase lag. However, including structural permeability and flexibility has made these physical problems more complex, rendering theoretical analyses of wave-structure interaction challenging. Nevertheless, advancements in high-speed computers in recent decades have led to significant progress in the numerical modeling of wave-structure interaction problems.

In this thesis, to study the sustainability and resilience of VLFS and the sea wall, six problems are taken and each problem is formulated as a mixed boundary value problem (BVP), where the governing partial differential equation is Laplace's equation for normal incidence or the Helmholtz equation for oblique incidence in wave. This governing equation is coupled with a mixed boundary condition at the free surface, condition at the porous structure, conditions within the gap, conditions on the thin elastic plate representing VLFS, condition at the sea wall, and condition at the bottom. Since the fluid region extends infinitely, the far-field condition is used for problem uniqueness. To solve each problem, the eigenfunction expansion method is used to leverage the orthogonality of free surface eigenfunctions. This coins to a system of algebraic equations, which are solved using the Gauss-elimination method by using MATLAB. Once the system of equations is solved numerically, the physical quantities like reflection, transmission, and dissipation coefficients are obtained. We examine how these coefficients vary with different physical parameters, presenting graphical analyses. Additionally, the forces on the thick porous structure and the sea wall, free surface elevation, plate deflection, shear force, and strain on the elastic plate are investigated for various wave and structural parameters. Some problems involve deriving the energy identity using Green's integral theorem, an important relation involving reflection, transmission, and dissipation coefficients in water wave scattering problems. This identity verifies the accuracy of numerical results. In each problem, the results are compared with existing literature, aiming to progress towards practical applications in Mathematical Sciences and Engineering.

1.2   Brief History and Motivation

Wave-structure interaction problems require understanding fluid dynamics in contact with the atmosphere and the structure's behavior in contact with the fluid. Additionally, it is essential to comprehend the phenomena of wave propagation. In Book II, Prop. XLV of Principia, 1687, Sir Isaac Newton first attempted the development of the theory of water waves (see Craik [1]). This work inspired scientists such as Euler and French mathematicians Laplace, Lagrange, Poisson, and Cauchy, who made significant theoretical

advances in the linear theory of water waves. Later, between 1830 and 1850, Russel, Green, Kelland, Airy, and Earnshaw further contributed to the development of linear water wave theory. The books by Lamb [2], Rahman [3] and Dean and Dalrymple [4], along with the literature cited within, provide comprehensive details on the various phenomena associated with water wave propagation. Further, research on wave interaction with various structures has been progressing, which are briefed in the following subsections.

1.2.1 Water Wave Scattering by Thick Porous Structure

The scattering of water waves by thick porous structures is a vital area of research in coastal engineering. Thick vertical porous structures, which have been increasingly proposed over the past few decades, play a crucial role in managing wave dynamics in ports and harbors. These structures are designed to dissipate wave energy through their porous nature, effectively reducing wave height and energy before reaching the shore. By scattering and absorbing the energy of incoming waves, thick porous structures help to protect coastal infrastructure and mitigate erosion. To analyze the usefulness of thick porous structures, it is essential to conduct a detailed study of physical parameters such as wave reflection, wave transmission, and wave energy dissipation. The key factors influencing the hydrodynamic performance of thick porous breakwaters include their height, porosity, water depth, incident wave height, crest width, slope of the structures, and wave period. Many researchers have examined water waves interaction with thick porous structures of finite width, such as rubble-mound breakwaters, through the fulfillment of Lorentz's equivalent work condition, as detailed in Sollitt and Cross [5]. This model introduces a complex dispersion relation to analyze wave motion within the porous medium. Using this model, several researchers studied the water wave interaction with thick porous structures (see McIver [6], Zhu [7], Behera and Sahoo [8], Venkateswarlu and Karmakar [9] and literature cited therein). Madsen [10] provided a solution for the reflection and transmission for normally incident water waves interacting with a complete rectangular porous structure which is extended from top to bottom. To extend this work, Dalrymple et al. [11] examined the oblique wave characteristics past a complete rectangular porous structure of finite width and investigated the plane wave as well as the long wave solutions. Using the Boundary Element Method (BEM), Sulisz [12] investigated the wave scattering performance of rubble mound breakwaters. These results were validated with experimental data, and the comparative study concluded that the numerical and experimental results showed a reasonably acceptable correlation for the wave transmission coefficient. Lee [13] utilized the boundary element model to study wave interactions with a porous structure and validated the model's accuracy by comparing the results with analytic solutions. Further, Liu and Li [14] developed a new analytical solution for water wave motion through a porous structure using velocity potential decompositions in the porous structure and matched eigenfunction expansions. Das and Bora [15, 16] analyzed the impact of water waves on a complete porous structure placed on an elevated horizontal bottom in the presence of a rigid vertical wall. Due to the high costs associated with

this complete porous structure, truncated porous structures such as bottom-standing and surface-piercing porous structures are preferred for material efficiency. Dattatri et al. [17] conducted laboratory measurements to test impermeable and permeable structures of various shapes. Their study reported and analyzed wave transmission by trapezoidal, rectangular, semi-trapezoidal, and vertical barrier-type breakwaters. Losada et al. [18] examined the scattering properties of bottom-standing submerged porous structures, while Koley et al. [19], Behera et al. [20], Tabssum et al. [21], Kaligatla et al. [22], Athul Krishna et al. [23] investigated the usefulness of bottom-standing and surface-piercing porous structures to dissipated the incident wave energy.

1.2.2 Water Wave Scattering by Multiple Porous Structures

Recently, coastal engineers have concentrated on multiple permeable barriers to enhance wave energy trapping, taking advantage of the multiple confined regions they create. Researchers have explored the wave damping and trapping performance of multiple porous breakwaters using analytical, numerical, and experimental methods (see Losada et al. [24], Hsu et al. [25], Twu and Liu [26], Liu et al. [27], Behera and Ng [28], Liu et al. [29], Guo et al. [30], Vijay et al. [31], Tran et al. [32], Tsai et al. [33]). These studies have shown that multiple porous structures significantly improve energy dissipation and reduce wave reflection compared to a single barrier. The confined regions between the barriers facilitate better wave energy absorption. Khan and Behera [34] studied the interactions of water waves with double rectangular porous structures installed at the bottom. Working in a similar direction, Cao et al. [35] examined the scattering of water waves by double trapezoidal submerged porous structures. However, Twu and Lin [36] observed that a wave absorber with more than two porous plates is more effective than one plate or two plates, and arranging these plates with decreasing material constants from front to back results in a significantly lower reflection coefficient. Hsu et al. [37] conducted wave flume experiments to investigate Bragg reflection using three different shapes of artificial bars: rectangular, triangular, and rectified sinusoidal geometries. The results indicated that rectangular bars produced a higher reflection coefficient compared to the other two shapes. Moreover, Tsai et al. [38] employed experimental as well as theoretical methods to investigate the behavior of water waves interacting with multiple composite artificial bars of different shapes. Zhao et al. [39] investigated the scattering of water waves generated by multiple submerged porous bars placed in front of a vertical wall, employing the EEM for their analysis. Rambabu and Mani [40] presented results from a numerical model study on the transmission characteristics of submerged breakwaters, aiming to determine the effects of submergence depth, crest width, initial wave conditions, and material properties on its performance. Liu et al. [41] examined water waves interacting with multiple submerged semi-circular breakwaters and observed that the peak reflection coefficient significantly increases with the number of bars while the corresponding bandwidth decreases. Venkateswarlu and Karmakar [42] studied wave transformation in the presence of stratified porous block with a sea wall, considering flat, elevated,

and stepped seabed scenarios. Their research revealed that the stepped seabed reduced wave force on the leeward wall more effectively than the uniform and elevated seabeds when a stratified porous block is present. Further, Venkateswarlu and Karmakar [43] investigated the wave dissipation performance of multiple fully extended porous blocks, focusing on both the leeward unbounded region and the confined region or leeward wall. The most common finding from the various studies is that emerged structures of finite thickness can achieve nearly zero transmission due to enhanced wave damping. However, bottom-mounted structures effectively distribute incident wave energy among reflection, transmission, and energy-damping coefficients.

1.2.3 Water Wave Scattering by VLFS

The concept of VLFS was first introduced by the renowned French novelist and one of the pioneers of science fiction, Jules Verne [44], in his book "L'île à hélice", where he described a floating island. Later, Armstrong [45] proposed the idea of constructing multiple floating islands at regular intervals to facilitate the landing and refueling of airplanes during transatlantic flights. As the population grows and urban development intensifies, land-scarce island nations such as the Netherlands, Singapore, and Japan, as well as countries with extensive coastlines, turn to land reclamation from the ocean to alleviate pressure on their heavily utilized land. So, engineers and researchers proposed that VLFS can be an alternative solution to these problems. These VLFS have been built to use ocean space for various humanitarian purposes, such as floating airports, bridges, wind farms, storage facilities, etc. (see Wang et al. [46]), and at the same time, these VLFS have a minimal effect on aquatic habitats, tidal current flows. In some situations, VLFS is assumed to behave elastically as the localized deflection/vibration of the long structure becomes significant due to the continuous excitation of small amplitude waves, although the motion of the whole body is small compared to its length (see Ohkusu and Namba [47] and Sahoo [48]). Moreover, there are analogies between models of VLFS and ice floes in the polar regions, as the wave-induced responses of ice floes exhibit elastic behavior similar to that of VLFS under ocean waves. Although the research objectives in these two fields differ, the mathematical modeling and solution methodologies used to analyze these systems are quite similar. One of the earliest studies in this direction was reported by Greenhill [49], who proposed characterizing ice as a thin elastic beam, deriving a dispersion equation, and incidentally mentioned that the first-ever experimental determination of Young's modulus was performed on ice. Fox and Squire [50] modeled sea ice as a thin elastic plate and studied the interaction of water waves with an ice-covered surface by utilizing the eigenfunction expansion method (EEM). Meylan [51] employed a solution methodology by combining the coupled boundary element method and finite element method to investigate the scattering and wave-induced forces on ice floes with arbitrary geometries. Since then, several researchers have utilized the thin elastic plate model to study how ocean waves interact with sea ice (Kerr [52], Fox and Squire [53], Meylan and Squire [54], Manam et al. [55], Mohapatra and Bora [56], Maiti et al. [57], Meylan et al. [58], Stepanyants and

Sturova [59], and the works cited therein).

On the other hand, a considerable amount of research has been conducted on the interaction between water waves and VLFS. Significant contributions in this area include works by Kashiwagi [60], Namba and Ohkusu [61], Watanabe et al. [62], Taylor [63], Evans and Porter [64], Xu and Lu [65], Naskar et al. [66] and literature cited there in. In these studies, VLFS is modeled using thin plate theory to investigate their interactions with water waves. Due to the substantial size of the structure poses a significant computational challenge, making the analysis difficult. To address this issue, Kagemoto et al. [67] as well as Sahoo et al. [68] assumed that the structure is semi-infinitely long relative to the wavelength of the incident wave. Takagi [69] utilized the parabolic approximation to determine the elastic deformation of a thin semi-infinite quarter plate. Further, to reduce the computational burden, Hermans [70] considers a finite floating elastic plate instead of the infinitely or semi-infinitely long floating elastic plate. Gerostathis et al. [71] employed the modal expansion method to investigate how changing bathymetry affects the hydroelastic analysis of three-dimensional floating VLFS. Recently, Koley [72] employed the multi-domain boundary element method (MBEM) to investigate how variable bottom topography influences the structural response of a floating flexible porous plate. Meanwhile, Tsubogo [73] utilized the boundary element method to examine the responses of floating elastic plates under the shallow water wave approximation. Using the modal expansion method, Gerostathis et al. [71] studied the effect of variable bathymetry on hydroelastic analysis of three-dimensional floating VLFS. The challenges within contemporary hydroelasticity, along with their evolution, mathematical methodologies, and analytical aspects, are outlined in the review article authored by Korobkin et al. [74].

1.2.4   Water Wave Scattering by VLFS in the Presence of Breakwater

The primary goal in the hydroelastic analysis of VLFS is to minimize the hydroelastic response on VLFS, which is crucial for optimal system performance. Reducing this response enhances safety and elevates the serviceability standards of VLFS. Researchers have suggested several methodologies to achieve this reduction in hydroelastic response for floating structures. The most conventional approach involves enhancing the structural stiffness of VLFS, as demonstrated by Andrianov and Hermans [75]. However, higher structural stiffness necessitates increased material usage and incurs higher costs, making it less cost-effective for VLFS. An intriguing alternative is to construct breakwaters around VLFS. Takagi et al. [76] proposed anti-motion devices placed on the edge or bottom surface of the floating structure. Ohta et al. [77] investigated the effect of attaching a horizontal or vertical plate on the wave response of VLFS. Watanabe et al. [78] performed hydroelastic analyses on VLFS featuring a submerged horizontal plate attached to the fore-end of the structure. Cheng et al. [79] experimentally analyzed VLFS with submerged horizontal plates at the edges. Cheng et al. [80] studied the fluid-structure interaction of irregular waves with VLFS equipped with dual inclined perforated plates, using time-domain

theory and employing a hybrid finite element-boundary element method along with the eigenfunction matching method. Ohmatsu [81] studied the hydroelastic behavior of VLFS in the presence of a thin vertical breakwater. Yang [82] developed a hybrid active and passive control method to reduce structural vibrations, enhancing the serviceability of the controlled VLFS. Singla et al. [83] investigated the effectiveness of vertical porous barriers in mitigating the hydroelastic response of VLFS. Pu and Lu [84] extended this work by using a vertical porous flexible barrier connected to a VLFS instead of a porous barrier. Recently, Singla et al. [85, 86] analyzed the effectiveness of a thin horizontal permeable plate or box-type porous structure in dissipating wave energy impacting the elastic plate.

To the best of our knowledge, mitigating the wave response of the elastic plate by the thick porous structure has not been investigated so far. Hence, this research aims to reduce the structural response of an elastic plate in the presence of various configurations of single or multiple thick porous structure(s).

1.2.5   Water Wave Scattering by Sea Wall in the Presence of Breakwater

The interaction between waves and sea walls is a critical aspect of coastal engineering, influencing coastal protection, wave energy dissipation, and shoreline stability. Sea walls are designed to withstand wave forces and protect coastal areas from erosion and flooding. However, it is important to note that wave impacts can cause the sea walls to collapse. These powerful waves threaten the sea wall and erode sand from its base. Therefore, the sea walls' structural safety and stability must be carefully considered when designing offshore structures. In this direction, Hsu and Wu [87] developed the boundary element method and utilized it to analyze the heave and sway behavior of a floating rectangular structure in water with finite depth, considering the presence of a vertical sea wall. Zheng et al. [88] studied the radiation and diffraction of water waves using a rectangular floating structure positioned near a sidewall. Evans and Porter [89] conducted a hydrodynamic analysis on an oscillating water column containing a vertical surface-piercing barrier adjacent to a vertical wall. Wu et al. [90] addressed wave reflection from a vertical wall using a horizontal submerged porous plate through eigenfunction expansion methodology. Liu et al. [91] investigated wave interaction with a perforated breakwater to reduce wave reflection and wave force on seawalls. Schay et al. [92] examined the hydrodynamic performance of a heaving point absorber positioned close to a stationary vertical wall. Sahoo et al. [93] studied the trapping of waves by partial thin porous barriers near the wall and this was further extended by Yip et al. [94], who used the flexible porous structure to examine the trapping phenomena of waves. Moreover, Koley and Sahoo [95] investigated the trapping of water waves by a vertical permeable membrane barrier located near a sea wall. However, natural sea bottoms are irregular. Bhattacharjee and Soares [96] studied the wave loads exerted on a floating rectangular box located near a wall in a step-type bottom undulations. Behera et al. [97] examined the problem of wave trapping by a porous barrier over an arbitrary bottom topography using a modified mild-slope equation and the eigenfunction expansion method. By using the same method, Kaligatla et al. [98] analyzed the usefulness

of a dual porous barrier to protect a sea wall over an arbitrary bottom topography.

To the best of our knowledge, mitigating the wave load on a sea wall by a thick porous structure in the presence of an elastic plate has not been investigated so far. Hence, this research aims to minimize the wave load on a sea wall using a thick porous structure in combination with an elastic plate, contributing to advancements in coastal infrastructure applications. Furthermore, the effectiveness of a submerged thick porous structure, which is neither bottom-standing nor surface-piercing, in protecting sea walls represents a valuable addition to the application of effective breakwaters, which has been examined in this study.

The following section presents a concise overview of the thesis's aims and objectives.

1.3   Aims and Objectives

This thesis primarily focuses on tackling a specific set of challenges concerning the interaction between gravity waves with the elastic plate and the thick porous structures of different configurations, such as complete porous structure (extended from top to bottom), truncated porous structure such as bottom-standing and surface-piercing porous structure, whether in the presence of a sea wall or without it. Also, the interaction of gravity waves with a submerged porous structure in the presence of a sea wall over two steps is examined. The analysis employs the matched eigenfunction expansion method as a key analytical tool to find the solution to each problem. The emphasis is given to:

- To reduce the wave impact on the elastic plate by employing the thick porous structures.

- Minimizing wave impact on the sea wall in the presence of the elastic plate and thick porous structure.

- Analyzing reflection, transmission, and dissipation coefficients for different values of structural and wave parameters.

- Analyzing the elastic plate's shear force, strain, and deflection in the presence of a thick porous structure.

- Analyzing the force exerted on the sea wall.

1.4   Basic Mathematical Equations in Water Wave Theory

Modeling real-life physical problems is inherently challenging. However, certain physical assumptions can be made to develop acceptable mathematical models for these problems. Many physical problems in Ocean Engineering/Coastal Engineering are analyzed using the linear theory of water waves, which applies when the motion under the action of gravity is small (that means the velocity components together with their derivatives are quantities of first order of smallness so that their squares, products and higher

powers can be neglected) and the wave elevation is also small compared to some physical length. Various models involving wave-structure interaction have been developed based on the geometric configurations of the structures. This section briefly discusses the basic equations associated with wave propagation without structure (see Chapter 3 of Dean and Dalrymple [4]) and associated with wave interactions by thick porous structure/elastic plate, as found in various textbooks and research articles. These details are included to make the thesis self-explanatory.

1.4.1 Governing Equation

A rectangular Cartesian coordinate system is chosen where the xz-plane lies along the undisturbed free surface, and the y-axis points vertically upward. The fluid occupies the region $-\infty < x < \infty$, $-\infty < z < \infty$, $-h \leq y \leq 0$, with the bottom surface represented by $y = -h$ as shown in Figure 1.1. The fluid is assumed to be inviscid, incompressible, and its motion is considered to be irrotational and simple harmonic in time and propagates with an angle θ with respect to the x-axis. Given the irrotational nature of the motion, there exists a velocity potential $\Phi(x, y, z, t)$ such that the fluid velocity ($\vec{V}$) can be expressed as

$$\vec{V} = (u, v, w) = \nabla\Phi, \tag{1.1}$$

where u, v, w are the components of $\vec{V}$ along x, y, z-direction, respectively and Φ represents the velocity potential.

The continuity equation for an inviscid and incompressible fluid is

$$\nabla \cdot \vec{V} = 0. \tag{1.2}$$
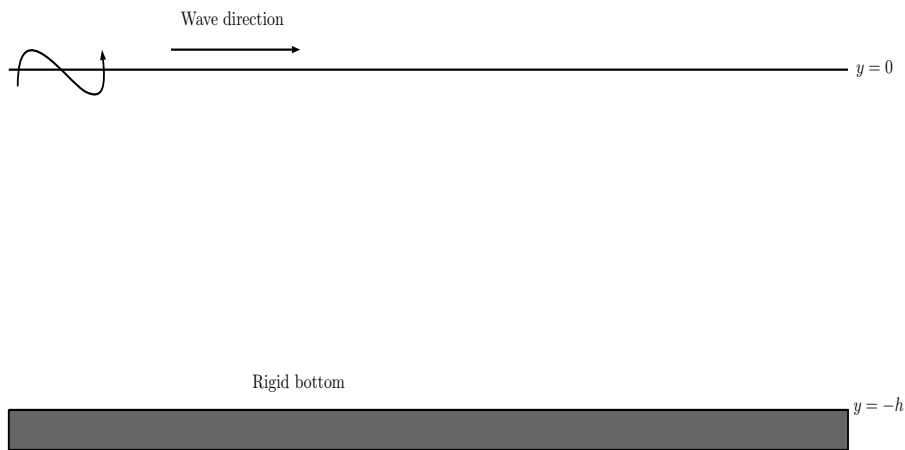
Figure 1.1: Schematic diagram for wave propagation.

Hence, Equations (1.1) and (1.2) give rise to the Laplace's equation

$$\frac{\partial^2 \Phi}{\partial x^2} + \frac{\partial \Phi^2}{\partial y^2} + \frac{\partial^2 \Phi}{\partial z^2} = 0, \quad \text{in the fluid region.} \tag{1.3}$$

1.4.2   Free Surface Boundary Condition

In this subsection, we briefly outline the combined free surface boundary condition.

Dynamic free surface boundary condition:

The Euler's equation of motion is

$$\frac{\partial \vec{V}}{\partial t} + (\vec{V} \cdot \nabla)\vec{V} = g - \frac{1}{\rho}\nabla p \tag{1.4}$$

where p is the fluid pressure, ρ is the fluid density, and g is the acceleration due to gravity.

After integration and simplification, Euler's equation of motion (1.4) becomes (see Dean and Dalrymple [4])

$$\frac{\partial \Phi}{\partial t} + \frac{1}{2}\left[\left(\frac{\partial \Phi}{\partial x}\right)^2 + \left(\frac{\partial \Phi}{\partial y}\right)^2 + \left(\frac{\partial \Phi}{\partial z}\right)^2\right] + \frac{p}{\rho} + gy = 0 \tag{1.5}$$

which is known as Bernoulli's equation. The pressure at the free surface $y = \eta(x, z, t)$ must equal the atmospheric pressure, which is assumed to be constant (taken as zero here). Therefore, Equation (1.5) becomes

$$\frac{\partial \Phi}{\partial t} + \frac{1}{2}\left[\left(\frac{\partial \Phi}{\partial x}\right)^2 + \left(\frac{\partial \Phi}{\partial y}\right)^2 + \left(\frac{\partial \Phi}{\partial z}\right)^2\right] + g\eta = 0, \quad \text{on} \quad y = \eta(x, z, t) \tag{1.6}$$

which is known as the dynamic free surface boundary condition.

Kinematic free surface boundary condition:

The vertical velocity component is equal to the rate of rise of the water surface at any point, resulting in the condition (see Dean and Dalrymple [4])

$$\frac{\partial \Phi}{\partial y} = \frac{\partial \eta}{\partial t} + \frac{\partial \eta}{\partial x}\frac{\partial \Phi}{\partial x} + \frac{\partial \eta}{\partial z}\frac{\partial \Phi}{\partial z}, \quad \text{on} \quad y = \eta(x, z, t) \tag{1.7}$$

which is known as the kinematic free surface boundary condition.

Linearized free surface condition:

Under the assumption of linear water wave theory, the velocity components and the free surface displacement, along with their partial derivatives, are small quantities. Therefore, their squares, higher powers, and products can be neglected. As a result, Equations (1.6) and (1.7) simplify to

$$\frac{\partial \Phi}{\partial t} + g\eta = 0 \quad \text{on} \quad y = \eta(x, z, t) \tag{1.8}$$

and

$$\frac{\partial \Phi}{\partial y} = \frac{\partial \eta}{\partial t} \quad \text{on} \quad y = \eta(x, z, t). \tag{1.9}$$

Further, by employing Taylor's series expansion and neglecting terms of the second order and higher order, the relations (1.8) and (1.9) simplify the linearized boundary conditions:

$$\frac{\partial \Phi}{\partial t} + g\eta = 0 \quad \text{on} \quad y = 0 \tag{1.10}$$

and

$$\frac{\partial \Phi}{\partial y} = \frac{\partial \eta}{\partial t} \quad \text{on} \quad y = 0. \tag{1.11}$$

By eliminating η between Equations (1.10) and (1.11) yields the linearized combined free surface boundary condition as

$$\frac{\partial^2 \Phi}{\partial t^2} + g\frac{\partial \Phi}{\partial y} = 0, \quad \text{on} \quad y = 0. \tag{1.12}$$

1.4.3 Bottom Boundary Condition

In the entire thesis, the seabed is considered to be flat and impermeable. As a result, there is no fluid flow across the rigid bottom, leading to the following condition on the bottom surface:

$$\frac{\partial \Phi}{\partial y} = 0, \quad \text{on} \quad y = -h. \tag{1.13}$$

The governing equation (1.3), in conjunction with the boundary conditions Equations (1.12) and (1.13), constitutes the fundamental equations of linearized water wave theory.

1.4.4 Boundary Value Problem for Water Wave Propagation

Since the motion is assumed to be simple harmonic in time with an angular frequency ω, the velocity potential $\Phi(x, y, z, t)$ is expressed as

$$\Phi(x, y, z, t) = \text{Re}\{\phi(x, y)e^{i(\mu z - \omega t)}\}, \tag{1.14}$$

where $\mu = k_0 \sin\theta$, k_0 is the wavenumber of the propagating wave, Re{.} denotes the real part of a complex-valued function and $\phi(x, y)$ represents the spatial expression of the velocity potential. Therefore, by substituting Equation (1.14) into Equations (1.3), (1.12) and (1.13), we obtain the following equations

$$\left(\frac{\partial^2}{\partial x^2} + \frac{\partial^2}{\partial y^2} - \mu^2\right)\phi = 0, \quad \text{in the fluid region,} \tag{1.15}$$

$$\frac{\partial \phi}{\partial y} - K\phi = 0, \quad \text{on} \quad y = 0, \tag{1.16}$$

$$\frac{\partial \phi}{\partial y} = 0, \quad \text{on} \quad y = -h, \tag{1.17}$$

where $K = \omega^2/g$. For the normal incidence ($\theta = 0°$) case, the mathematical formulation of the problem can be expressed as

$$\frac{\partial^2 \phi}{\partial x^2} + \frac{\partial \phi^2}{\partial y^2} = 0, \text{ in the fluid region,} \tag{1.18}$$

$$\frac{\partial \phi}{\partial y} - K\phi = 0, \quad \text{on} \quad y = 0, \tag{1.19}$$

$$\frac{\partial \phi}{\partial y} = 0, \quad \text{on} \quad y = -h. \tag{1.20}$$

In this context, Laplace's equation (1.18), coupled with boundary conditions (1.19) and (1.20), yields two types of solutions: wave-like solutions and non-wave-like solutions.

Solution for the velocity potential:

Using the separation of variables, we can obtain the solution to the BVP Equations (1.18)-(1.20) as

$$\phi(x,y) = \begin{cases} A_0 e^{-ik_0 x}\psi_0 + \sum_{m=1}^{\infty} A_m e^{-ik_m x}\psi_m(y) & \text{for} \quad x < 0 \\ B_0 e^{ik_0 x}\psi_0 + \sum_{m=1}^{\infty} B_m e^{ik_m x}\psi_m(y) & \text{for} \quad x > 0 \end{cases} \tag{1.21}$$

where $\psi_m(y) = \frac{\cosh k_m(h+y)}{\cosh k_m h}$ ($m = 0, 1, 2, \dots$), are the eigenfunctions of the above BVP and k_0 is known as wavenumber and is the real and positive root of the dispersion relation expressed in terms of k, given by

$$K - k \tanh kh = 0, \tag{1.22}$$

$k_m(m = 1, 2, 3, \dots)$ are the purely imaginary roots (known as the evanescent modes) of the dispersion relation (1.22), A_0, B_0 are the unknown constants associated with the amplitudes of the plane progressive waves and $A_m, B_m, m = 1, 2, 3, \dots$ are the unknown constants associated with the evanescent modes. The expansion formulae for $\phi(x,y)$ as in Equation (1.21) is known as Havelock's expansion formula in finite water depth and was initially derived by Havelock [99]. It can be easily derived that the eigenfunctions $\psi_m(y)$ satisfy the orthogonal inner product

$$\langle \psi_m(y), \psi_n(y) \rangle = \int_{-h}^{0} \psi_m(y)\psi_n(y)dy = \delta_{mn}\mathcal{N}(k_m) \tag{1.23}$$

where

$$\mathcal{N}(k_m) = \frac{\sinh 2k_m h + 2k_m h}{4k_m \cosh^2 k_m h} \tag{1.24}$$

and

$$\delta_{mn} = 1 \text{ for } m = n,$$

$$\delta_{mn} = 0 \text{ for } m \neq n.$$

The eigenfunction expansion method has been applied to many different problems of water wave mechanics (see Losada et al. [100], Yu [101], Lee and Chwang [102] and literature cited therein). Here it may be noted that the eigenfunction expansion method is possible due to the nature of the bottom which is flat type. If the bottom is not flat, then instead of eigenfunction expansion method, some other technique such as Boundary element method (see Lee [13], Kashiwagi et al. [103], Zheng et al. [104] and literature cited therein) and Green function approach (see Renzi et al. [105], Choudhary and Martha [106], Hao et al. [107] and literature cited therein) can be used.
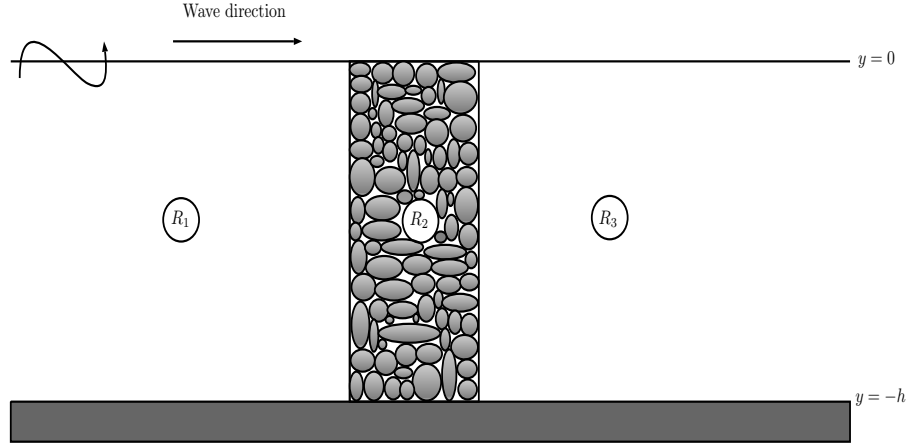
Figure 1.2: Schematic diagram of wave past by thick porous medium.

1.4.5 Basic Equation for Flow Past a Porous Medium (Sollitt and Cross Model)

The wave motion past the thick porous breakwater is modeled using the well-known Sollitt and Cross [5] model in this study. This model characterizes wave motion within a homogeneous isotropic porous medium under the continuum hypothesis. The equation of continuity for incompressible fluid and irrotational flow in the porous medium is represented by (see Sollitt and Cross [5])

$$\nabla.\vec{V} = 0 \Rightarrow \nabla^2\Phi = 0, \tag{1.25}$$

where $\vec{V}$ is of the seepage fluid velocity.

Further, the equation of motion includes resistance forces described by Forchheimer's model and an additional term that evaluates the added resistance caused by the added mass of discrete grains within the porous medium (Sollitt and Cross [5], Dalrymple et al. [11]) and this equation may be written as

$$m_p\frac{\partial\vec{V}}{\partial t} = -\frac{1}{\rho}\nabla\left(P + \rho g y\right) - \left(\frac{\nu_p}{R_p}\epsilon_p\vec{V} + C_f\frac{\epsilon_p^2}{R_p}\vec{V}\left|\vec{V}\right|\right), \tag{1.26}$$

where P is the dynamic pore pressure, ρ is the fluid density, g is the acceleration due

to gravity, R_p is the intrinsic permeability, ν_p is the kinematic viscosity, C_f is the dimensionless turbulent resistance coefficient, ϵ_p is the porosity and m_p is the inertia coefficient of the structure. The parameter m_p is often assumed to be unity in practice, although Sulisz [12] reports a better correlations with laboratory data with values approaching 2.

Assuming time-harmonic motion, with the same angular frequency as the waves ω, Equation (1.26) may be linearized on the basis of Lorentz's principle of equivalent work, the dissipative stress term is replaced by a linear stress term as follows:

$$\frac{\nu_p}{R_p}\epsilon_p\vec{V} + C_f\frac{\epsilon_p^2}{R_p}\vec{V}\left|\vec{V}\right| \simeq f_p\omega\vec{V}, \tag{1.27}$$

where f_p is the dimensionless friction coefficient. Now, by using Equation (1.27), the Equation (1.26) reduces to

$$m_p\frac{\partial\vec{V}}{\partial t} = -\frac{1}{\rho}\nabla\left(P + \rho gy\right) - f_p\omega\vec{V}. \tag{1.28}$$

By using $\vec{V} = \nabla\Phi$ and integrating Equation (1.28), the linearized Bernoulli equation for flow within the porous medium becomes

$$m_p\frac{\partial\Phi}{\partial t} + \frac{P}{\rho} + gy + f_p\omega\Phi = 0. \tag{1.29}$$

Condition at the free-surface $y = \eta(x,t))$ in the porous medium:
According to the Sollitt and Cross model, the derivation of linearized free-surface conditions for waves in a homogeneous isotropic porous medium is similar to those derived for the open water region. By applying same assumptions as taken for the derivation of dynamic free surface boundary condition on the open water region, the linearised form of Equation (1.29) from $y = \eta$ to $y = 0$ can be written as

$$m_p\frac{\partial\Phi}{\partial t} + g\eta + f_p\omega\Phi = 0 \quad \text{on} \quad y = 0. \tag{1.30}$$

The linearized kinematic free surface boundary condition will be the same as mentioned in Equation (1.11).

So, by substituting Equation (1.11) into Equation (1.30), the linearized combined free surface condition in the porous medium is obtained as

$$m_p\frac{\partial^2\Phi}{\partial t^2} + g\frac{\partial\Phi}{\partial y} + f_p\omega\frac{\partial\Phi}{\partial t} = 0 \quad \text{on} \quad y = 0. \tag{1.31}$$

Further, by using Equation (1.14), the linearized combined free surface condition (1.31)

for porous medium reduces to

$$\frac{\partial \phi}{\partial y} - K(m_p + if_p)\phi = 0 \quad \text{on} \quad y = 0. \tag{1.32}$$

Matching boundary conditions:

Let us consider $\vec{V_1}$ and $\vec{V_2}$ to be the velocities of a fluid at any point within the water region R_1 and porous region R_2 (see Figure 1.2), respectively. Then the following relation holds

$$\vec{V_i} = \nabla \Phi_i, \quad i = 1, 2. \tag{1.33}$$

The potential Φ_i is assumed to be harmonic in time. So the dynamic pressure and velocity potential can be written as

$$P_i = Re\{p_i e^{-i\omega t}\}, \tag{1.34}$$

$$\Phi_i = Re\{\phi_i e^{-i\omega t}\}. \tag{1.35}$$

By using Equations (1.34) and (1.35), in Equations (1.5) and (1.29), the linearized equations for the dynamic pressures p_1 in the region R_1 and the pressure p_2 in the porous region R_2, are given by

$$p_1 = i\rho\omega\phi_1 - gy \tag{1.36}$$

and

$$p_2 = -\rho\omega(f_p - im_p)\phi_2 - gy. \tag{1.37}$$

Now, along the vertical boundary between the water region R_1 and porous region R_2, the continuity of pressure ($p_1 = p_2$) from Equations (1.36) and (1.37) results in the following matching condition

$$\phi_1 = (m_p + if_p)\phi_2. \tag{1.38}$$

The mass flux per unit volume and unit time inside the porous region is $\rho\epsilon_p\vec{V_2}$, and the same inside the water region is $\rho\vec{V_1}$. So, along the vertical boundary, the continuity of mass flux implies

$$\phi_{1x} = \epsilon_p\phi_{2x}. \tag{1.39}$$

Similarly, the matching conditions along the vertical boundary between regions R_2 and R_3 can be derived.

1.4.6 Basic Equations and Edge Conditions for Thin Elastic Plate

In this subsection, we briefly outline the boundary condition on the elastic plate. The finite elastic plate is floating at $y = 0$. Assuming no cavitation occurs between the elastic plate and the ocean, the linearized kinematic and dynamic conditions, in the absence of surface

tension, on the elastic plate at $y = 0$ are given by (see Timoshenko et al. [108], Sahoo [48])

$$\frac{\partial \Phi}{\partial y} = \frac{\partial \eta}{\partial t} \quad \text{on} \quad y = 0 \tag{1.40}$$

and

$$\frac{\partial \Phi}{\partial t} + \frac{P}{\rho} + g\eta = 0 \quad \text{on} \quad y = 0, \tag{1.41}$$

where η represents the lateral displacement of the elastic plate, ρ denotes the density of the fluid, and P stands for the surface pressure due to the atmosphere, the static pressure of the elastic plate, and the dynamic pressure due to the inertia and stiffness, etc. of the elastic plate.
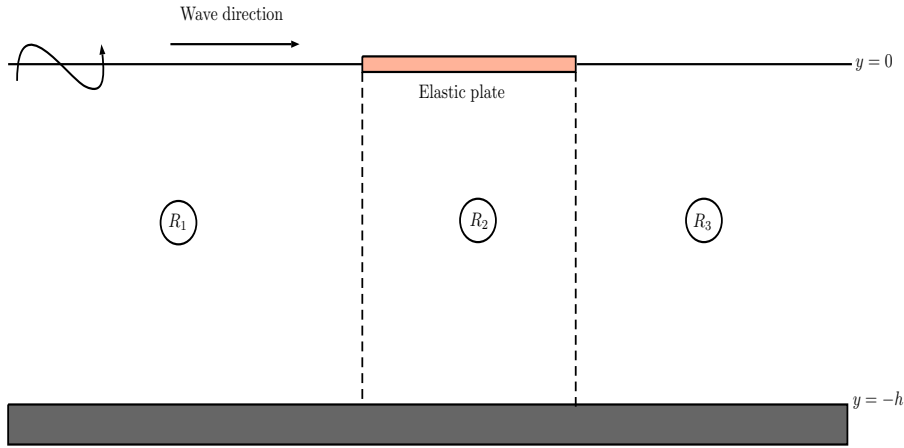
Figure 1.3: Schematic diagram of wave past by elastic plate.

Under the assumption that the plate is a thin, uniform elastic material with consistent mass density ρ_s and thickness h_0 assumed to be small, the displacement η is connected to the differential pressure P_s of the elastic plate through the condition (see Fox and Squire [109])

$$P_s = EI\nabla_{xz}^4 \eta + m_s \left(\frac{\partial^2 \eta}{\partial t^2} + g \right) \quad \text{on} \quad y = 0, \tag{1.42}$$

where EI is the flexural rigidity of the plate, E is the effective Young's modulus of the elastic plate, $I = \frac{h_0^3}{12(1-\nu^2)}$, ν is Poisson's ratio, $m_s = \rho_s h_0$ is the density of the elastic plate. When the surface pressure P in the linearized dynamic condition (1.41) equals to P_s, we find that the velocity potential must satisfy the relation

$$\left(EI\nabla_{xz}^4 + m_s \frac{\partial^2}{\partial t^2} + \rho g \right) \frac{\partial \Phi}{\partial y} + \rho \frac{\partial^2 \Phi}{\partial t^2} = 0 \quad \text{on} \quad y = 0, \tag{1.43}$$

Further, by using Equation (1.14), the boundary condition (1.43) on the elastic plate reduces to

$$\left[D \left(\frac{\partial^2}{\partial x^2} - \mu^2 \right)^2 + 1 - \epsilon_e K \right] \phi_y - K\phi = 0 \quad \text{on} \quad y = 0, \tag{1.44}$$

where $D = EI/\rho g$ is the flexural rigidity of the plate with $\epsilon_e = \rho_s h_0/\rho$.

Further, assuming the elastic plate moves freely, the conditions for the vanishing of bending

moment and shear force at the ends of the plate are described as (see Fox and Squire [109])

$$\left(\frac{\partial^2}{\partial x^2} - \nu\mu^2\right)\frac{\partial\phi}{\partial y} = 0 \quad \text{and} \quad \frac{\partial}{\partial x}\left(\frac{\partial^2}{\partial x^2} - (2-\nu)\mu^2\right)\frac{\partial\phi}{\partial y} = 0. \tag{1.45}$$

To achieve the objectives outlined in Section 1.3, six problems are considered, which are outlined in the following section.

1.4.7 Outline of the Thesis

This thesis consists of eight chapters, with Chapters 2 to 7 as primary chapters focusing on investigating six problems, Chapter 1 as an introductory chapter, and Chapter 8 as the summary and future scope.

Chapter 1 provides a discussion on previous research followed by an overview of essential principles and key equations in the linearized theory of water waves. It also outlines the aims and objectives of this study.

Chapter 2 deals with the usefulness of the vertical porous structure, which is extended from the rigid bottom to the free surface of finite width placed at a finite distance from the elastic plate to mitigate the hydrodynamic response of the elastic plate. The elastic plate is modeled using the thin plate theory, and the wave past the thick porous structure is based on Sollitt and Cross model. Based on the small-amplitude water wave theory and with the aid of the eigenfunction expansion method, the associated boundary value problem is reduced to a system of linear algebraic equations and the system of equations is solved to obtain the numerical values of the hydrodynamic coefficients. The accuracy of the computational results is checked in two ways: (i) by verifying energy identity relation and (ii) by comparing with results from the literature. The effectiveness of the vertical porous structure in minimizing the structural impact on the elastic plate is analyzed by examining plate deflection, free surface elevation, as well as reflection, transmission, and dissipation coefficients. These analyses are presented graphically across various values of structural and wave parameters.

In Chapter 3, the problem involving the reduction of wave load on a sea wall by a vertical porous structure (extended from top to bottom) in the presence of an elastic plate is examined for its solution. The resulting mixed BVP is solved using the eigenfunction expansion method to obtain the reflection and dissipation coefficients. Using Green's identity, the energy balance relation is derived and used to check the accuracy of the computational results. The present study reveals that the force on the wall shifted to the left as the width and frictional factor of the vertical porous structure increased. It is also found that in the presence of a higher value of length and flexural rigidity of the elastic plate, the force acting on the wall is low. Furthermore, it is observed that the vertical porous structure effectively minimizes the free surface elevation in the region between the elastic plate and the wall.

In a few situations, the vertical porous structure, which is extended from top to bottom, is not useful due to high costs, material requirements, and environmental

considerations associated with vertical porous structure. Hence, truncated porous structures are often preferred. In Chapter 4, we have made an effort to study the usefulness of the truncated porous structure of finite width placed at a finite distance from the elastic plate to mitigate the hydrodynamic response of the elastic plate. Two different configurations of the porous structure, namely bottom-standing porous structure and surface-piercing porous structure, are analyzed. With the aid of the eigenfunction expansion method, the associated boundary value problem is reduced to a system of linear algebraic equations, which is solved to identify the hydrodynamic coefficients such as reflection, transmission and dissipation coefficients. For both cases, the energy identity is derived and verified to check the accuracy of the computational results. In this study, it is observed that as the structural length, porosity, and friction factor of the porous structure increase, both plate deflection and free surface elevation decrease. Also, it is found that the wave energy dissipation and amplitude in wave reflection by the surface-piercing porous structure is higher than that of the bottom-standing porous structure case.

Chapter 5 proposes a model composed of either a bottom-standing porous structure or a surface-piercing porous structure in combination with an elastic plate placed at a distance from one another to protect a sea wall. The study uses the eigenfunction expansion and orthogonality of eigenfunction to coin a system of equations, and the system of equations is solved to identify the hydrodynamic coefficients, such as reflection and dissipation coefficients. The impact of the truncated porous structure in reducing the wave load on the sea wall in the presence of the elastic plate is analyzed by examining the force experienced on the wall, free surface elevation, reflection, and dissipation coefficients through graphs for different values of structural and wave parameters. The results of this study demonstrate that the surface-piercing porous structure is more effective in reducing harsh wave impact on the sea walls compared to the bottom-standing porous structure.

Chapter 6 investigates the role of a submerged thick porous structure, which is neither bottom-standing nor surface-piercing porous structure, to safeguard a sea wall in the presence of two steps. Leveraging the governing equation and boundary conditions, a system of equations is derived and subsequently solved to determine force, reflection, and dissipation coefficients. Compared to the scenario without steps, the present study results in a 57% reduction of force experienced by the wall. Observations suggest that varying the submergence depth (ranging from 0.1 to 0.3) and length (ranging from 0.1 to 0.6) of the submerged thick porous structure leads to wave reflection and force on the wall approximately less than 54% and 59%, respectively.

Chapter 7 deals with the interaction of normal incident water waves by multiple bottom-standing porous structures and the elastic plate. The study develops the Laplace equation as the governing equation and mixed boundary conditions under the framework of potential flow theory. The study uses the eigenfunction expansion and orthogonality of eigenfunction coin to a system of equations. These equations are then solved to analyze various factors, including plate deflection, shear force and strain on the elastic plate, and reflection, transmission, and dissipation coefficients. The accuracy of the computational

results is verified by comparing them with the results from the literature. In this study, the primary peak of wave reflection occurs when the wavenumber is 0.25, and its magnitude enhances as the number of bottom-standing porous structures increases, often interpreted as Bragg reflection with a corresponding bandwidth. Afterward, the wave reflection experiences a peak in its oscillatory behavior and reduces to low values, attributed to changes in wave damping. When the number of bottom-standing porous structures $n = 1$ and $n = 2$, no subharmonic peaks are situated between the two harmonic peaks in wave reflection. However, for other n values, the number of subharmonic peaks between two harmonic peaks is $n - 2$. A configuration with four bottom-standing porous structures is highlighted for its exceptional wave-damping capacity, achieving nearly 65%.

At the end, the concluding Chapter 8 contains the summary of the results discussed in the aforementioned main chapters of the thesis. It also highlights the scope of future investigations.

Chapter 2

Mitigation of Structural Response on an Elastic Plate by a Vertical Porous Structure

2.1 Introduction

This chapter analyzes the effect of a porous structure (PS), which is extended from bottom to free surface (see Figure 2.1), on mitigating hydroelastic response on an elastic plate (EP). The focus is on using PS to reduce the wave-induced structural response of EP when PS is positioned at a finite distance from EP. The fluid flow inside PS is modeled using the Sollitt and Cross model, while EP is modeled by using the thin plate theory. An eigenfunction expansion method is applied to solve the boundary value problem associated with the physical problem. The study aims to determine the optimal distance between PS and EP to achieve maximum wave dissipation by PS, thereby reducing the wave loads on EP. Scattering coefficients such as reflection coefficient, transmission coefficient, dissipation coefficient and various hydrodynamic factors such as wave forces on the porous structure, free surface elevation, plate deflection, shear force, and strain, are analyzed for various wave and structural parameters of PS and EP. The energy identity for the given problem is derived and used to verify the accuracy of the computational results and to obtain quantitative information about wave energy dissipation. A major part of the work presented in this chapter has been published in Sahoo and Martha [110].

2.2 Mathematical Formulation

Scattering of oblique ocean waves by a floating EP in the presence of homogeneous and isotropic PS as shown in Figure 2.1 is solved, where y-axis is directed vertically upward, and xz-plane represents the free surface of the fluid. PS with width b is placed at L_1 distance from EP and is infinitely long along the $z-$ axis. The PS is extended from bottom to free surface, and it is situated at $0 \leq x \leq b, \ -h \leq y \leq 0$. EP position is $y = 0$, $c \leq x \leq d$, (i.e., $L_2 = c - d$ is the length of EP). The entire fluid domain is divided into five regions as mentioned in Figure 2.1. It is assumed that the fluid is inviscid, incompressible and the motion is irrotational. The wave motion is considered to be simple harmonic in time with angular frequency ω and the wave propagates with an angle θ with respect to

the x-axis. So there exists a velocity potential $\Phi_j(x, y, z, t) = \text{Re}\{\phi_j(x, y)e^{i(\mu z - \omega t)}\}$ in each region j=1,2,3,4,5. Hence, the equation of continuity becomes the Laplace's equation in Φ_j, which further gives rise to the modified Helmholtz equation in the spatial potential ϕ_j as given by (see Dalrymple et al. [11])

$$\left(\frac{\partial^2}{\partial x^2} + \frac{\partial^2}{\partial y^2} - \mu^2\right)\phi_j = 0, \quad \text{in the region } j = 1, 2, 3, 4, 5, \tag{2.1}$$

where $\mu = k_0 \sin\theta$, k_0 is the wavenumber of the incident wave.
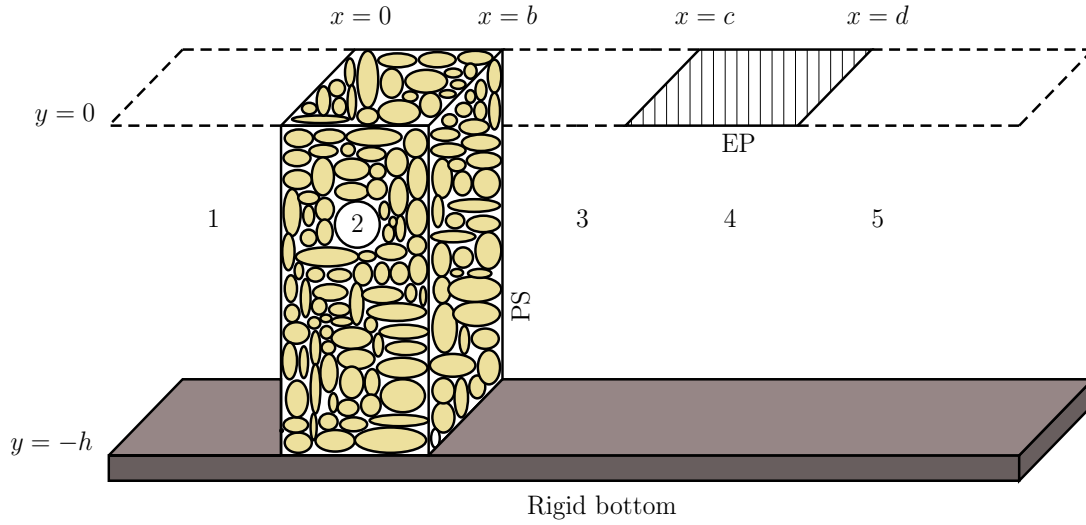
Figure 2.1: PS is located at a finite distance from EP.

It may be noted that, in the z-direction, the variations of solution in each region are considered the same to satisfy the matching conditions at vertical interfaces (by Snell's law, see Dalrymple et al. [11]).

The linearized free surface boundary condition, which is the combination of linearized kinematic free surface condition and Bernoulli's equation, is given by

$$\phi_{jy} - K\phi_j = 0, \quad \text{on} \quad y = 0, \quad \text{for} \quad j = 1, 3, 5, \tag{2.2}$$

with $K = \omega^2/g$, g is the acceleration due to gravity. In PS region 2, the condition at the top surface is expressed by

$$\phi_{2y} - K(m_p + if_p)\phi_2 = 0 \quad \text{on} \quad y = 0, \tag{2.3}$$

with m_p and f_p are the non-dimensionalized inertial coefficient and frictional coefficient, respectively.

The flat rigid bottom condition is given by

$$\phi_{jy} = 0, \quad \text{on} \quad y = -h, \quad \text{for} \quad j = 1, 2, 3, 4, 5. \tag{2.4}$$

In EP region 4 ($y = 0, c \leq x \leq d$), EP condition is given by

$$\left[D \left(\frac{\partial^2}{\partial x^2} - \mu^2 \right)^2 + 1 - \epsilon_e K \right] \phi_{4y} - K\phi_4 = 0 \quad \text{on} \quad y = 0, \tag{2.5}$$

where $D = EI/\rho g$ is the flexural rigidity of the plate, with E being Young's modulus, $I = h_0^3/12(1-\nu^2)$, ν is the Poisson's ratio, ρ is the density of the fluid, h_0 is the thickness of EP assumed to be small, $\epsilon_e = \rho_s h_0 / \rho$ and ρ_s is the density of EP. Further, by assuming that EP is floating freely on the water's surface, the edges of EP give rise to the conditions

$$\left(\frac{\partial^2}{\partial x^2} - \nu\mu^2 \right) \frac{\partial \phi_4}{\partial y} = 0 \quad \text{and} \quad \frac{\partial}{\partial x} \left(\frac{\partial^2}{\partial x^2} - (2-\nu)\mu^2 \right) \frac{\partial \phi_4}{\partial y} = 0 \quad \text{at } (c,0), (d,0). \tag{2.6}$$

The continuity of pressure and velocity at PS interfaces ($x = 0$ and $x = b$) yield

$$\phi_1 = (m_p + if_p)\phi_2, \quad \phi_{1x} = \epsilon_p \phi_{2x} \quad \text{on} \quad x = 0, \quad -h \leq y \leq 0, \tag{2.7}$$

$$\phi_3 = (m_p + if_p)\phi_2, \quad \phi_{3x} = \epsilon_p \phi_{2x} \quad \text{on} \quad x = b, \quad -h \leq y \leq 0, \tag{2.8}$$

where ϵ_p denotes the porosity of PS.

The continuity conditions for pressure and velocity at EP interfaces ($x = c$ and $x = d$) are given as

$$\phi_3 = \phi_4, \quad \phi_{3x} = \phi_{4x} \quad \text{on} \quad x = c, \quad -h \leq y \leq 0, \tag{2.9}$$

$$\phi_4 = \phi_5, \quad \phi_{4x} = \phi_{5x} \quad \text{on} \quad x = d, \quad -h \leq y \leq 0. \tag{2.10}$$

The far-field condition is expressed as follows:

$$\phi_1(x,y) \simeq \left(\frac{ig}{\omega} \right) \frac{\cosh k_0(y+h)}{\cosh k_0 h} \{ e^{ik_{0x}x} + R_0 e^{-ik_{0x}x} \} \quad \text{as} \quad x \to -\infty, \tag{2.11}$$

$$\phi_5(x,y) \simeq \left(\frac{ig}{\omega} \right) T_0 \frac{\cosh k_0(y+h)}{\cosh k_0 h} e^{ik_{0x}(x-d)} \quad \text{as} \quad x \to \infty, \tag{2.12}$$

where R_0 and T_0 denote the unknown complex constants associated with the reflected and transmitted wave, respectively, to be determined here, $k_{0x} = \sqrt{k_0^2 - \mu^2}$, and k_0 is the wavenumber of the incident wave, which is the positive real root for $m = 0$ of the transcendental equation in k_m as given by

$$K - k_m \tanh k_m h = 0. \tag{2.13}$$

2.3   Method of Solution

By using the method of separation of variables in each region, the spatial velocity potential functions are expressed as series solutions in terms of eigenfunctions. The spatial velocity potentials in the open water regions 1, 3, and 5 satisfying Equations (2.1), (2.2), (2.4),

(2.11) and (2.12) are expressed in the forms

$$\phi_1 = \left(\frac{ig}{\omega}\right)\left[e^{ik_{0x}x}\psi_0 + \sum_{m=0}^{\infty} R_m e^{-ik_{mx}x}\psi_m\right] \quad \text{for} \quad -\infty < x \le 0, \ -h \le y \le 0, \quad (2.14)$$

$$\phi_3 = \left(\frac{ig}{\omega}\right)\sum_{m=0}^{\infty}\left[A_m e^{ik_{mx}(x-b)} + B_m e^{-ik_{mx}(x-c)}\right]\psi_m \quad \text{for} \quad b \le x \le c, \ -h \le y \le 0,$$

$$(2.15)$$

$$\phi_5 = \left(\frac{ig}{\omega}\right)\sum_{m=0}^{\infty} T_m e^{ik_{mx}(x-d)}\psi_m \quad \text{for} \quad d \le x < \infty, \ -h \le y \le 0, \quad (2.16)$$

where

$$\psi_m = \frac{\cosh k_m(y+h)}{\cosh k_m h}, \quad m = 0, 1, 2\ldots, \quad (2.17)$$

R_m, A_m, B_m and T_m are unknown constants, $k_{mx} = \sqrt{k_m^2 - \mu^2}$ and k_0 is the positive real root and k_m, $m = 1, 2, 3\ldots$ are the purely imaginary roots of the dispersion relation (2.13).

Here, the eigenfunction $\psi_m(y)$, $m = 0, 1, 2, \ldots$, in $-h \le y \le 0$ satisfies the orthogonality relation given by

$$\int_{-h}^{0} \psi_m(y)\psi_n(y)dy = \delta_{mn}\mathcal{N}(k_m) \quad (2.18)$$

where

$$\mathcal{N}(k_m) = \frac{\sinh 2k_m h + 2k_m h}{4k_m \cosh^2 k_m h} \quad (2.19)$$

and

$$\delta_{mn} = 1 \text{ for } m = n,$$
$$\delta_{mn} = 0 \text{ for } m \ne n.$$

The spatial velocity potential in the porous region 2 satisfying Equations (2.1), (2.3) and (2.4) is expressed in the form

$$\phi_2 = \left(\frac{ig}{\omega}\right)\sum_{m=0}^{\infty}\left[C_m e^{iq_{mx}x} + D_m e^{-iq_{mx}(x-b)}\right]P_m \quad \text{for} \quad 0 \le x \le b, \ -h \le y \le 0, \quad (2.20)$$

where

$$P_m = \frac{\cosh q_m(y+h)}{\cosh q_m h}, \quad m = 0, 1, 2\ldots \quad (2.21)$$

C_m and D_m are unknown constants, $q_{mx} = \sqrt{q_m^2 - \mu^2}$ and q_m, $m = 0, 1, 2\ldots$ are the complex roots of the dispersion relation

$$K(m_p + if_p) - q_m \tanh q_m h = 0. \quad (2.22)$$

Finally, in EP region 4, the spatial velocity potential satisfies Equations (2.1), (2.4) and

(2.5) is expressed in the form

$$\phi_4 = \left(\frac{ig}{\omega}\right) \sum_{m=-2}^{\infty} \left[E_m e^{i\alpha_{mx}(x-c)} + H_m e^{-i\alpha_{mx}(x-d)}\right]\mathcal{G}_m \quad \text{for} \quad c \leq x \leq d, \ -h \leq y \leq 0$$

(2.23)

where

$$\mathcal{G}_m = \frac{\cosh\alpha_m(y+h)}{\cosh\alpha_m h}, \quad m = -2, -1, 0, 1, 2\ldots,$$

(2.24)

E_m and H_m are unknown constants, $\alpha_{mx} = \sqrt{\alpha_m^2 - \mu^2}$ and α_m are the complex roots of the form $\pm a + ib$ for $m = -2, -1$, positive real root for $m = 0$ and purely imaginary roots for $m = 1, 2, 3, \ldots$ (see Fox and Squire [50], Sahoo et al. [68]) of the equation

$$(D\alpha_m^4 + 1 - \epsilon_e K)\alpha_m \tanh\alpha_m h = K.$$

(2.25)

Utilizing Equations (2.14)-(2.16), (2.20) and (2.23) along with orthogonality of ψ_m in matching conditions (2.7)-(2.10), we have

$$U_{0n} + \sum_{m=0}^{\infty} R_m U_{mn} - \sum_{m=0}^{\infty} (m_p + if_p)V_{mn}(C_m + D_m e^{iq_{mx}b}) = 0,$$

(2.26)

$$ik_{0x}U_{0n} - \sum_{m=0}^{\infty} ik_{mx}R_m U_{mn} - \sum_{m=0}^{\infty} i\epsilon_p q_{mx}V_{mn}(C_m - D_m e^{iq_{mx}b}) = 0,$$

(2.27)

$$\sum_{m=0}^{\infty}(A_m + B_m e^{-ik_{mx}(b-c)})U_{mn} - \sum_{m=0}^{\infty}[(m_p + if_p)V_{mn}(C_m e^{iq_{mx}b} + D_m) = 0,$$

(2.28)

$$\sum_{m=0}^{\infty} ik_{mx}(A_m - B_m e^{-ik_{mx}(b-c)})U_{mn} - \sum_{m=0}^{\infty} i\epsilon_p p_{mx}V_{mn}(C_m e^{iq_{mx}b} - D_m) = 0,$$

(2.29)

$$\sum_{m=0}^{\infty}(A_m e^{ik_{mx}(c-b)} + B_m)U_{mn} - \sum_{m=-2}^{\infty}(E_m + H_m e^{-i\alpha_{mx}(c-d)})W_{mn} = 0,$$

(2.30)

$$\sum_{m=0}^{\infty} ik_{mx}(A_m e^{ik_{mx}(c-b)} - B_m)U_{mn} - \sum_{m=-2}^{\infty} i\alpha_{mx}(E_m - H_m e^{-i\alpha_{mx}(c-d)})W_{mn} = 0,$$

(2.31)

$$\sum_{m=-2}^{\infty}(E_m e^{i\alpha_{mx}(d-c)} + H_m)W_{mn} - \sum_{m=0}^{\infty} T_m U_{mn} = 0,$$

(2.32)

$$\sum_{m=-2}^{\infty} i\alpha_{mx}(E_m e^{i\alpha_{mx}(d-c)} - H_m)W_{mn} - \sum_{m=0}^{\infty} ik_{mx}T_m U_{mn} = 0.$$

(2.33)

where

$$U_{mn} = \int_{-h}^{0} \psi_m\psi_n dy, \quad V_{mn} = \int_{-h}^{0} P_m\psi_n dy, \quad W_{mn} = \int_{-h}^{0} \mathcal{G}_m\psi_n dy.$$

(2.34)

Further, free-edge conditions in Equation (2.6) give rise to

$$\sum_{m=-2}^{\infty} \alpha_m(\alpha_{mx}^2 + \nu\mu^2)(E_m + H_m e^{-i\alpha_{mx}(b-c)})\tanh\alpha_m h = 0, \tag{2.35}$$

$$\sum_{m=-2}^{\infty} i\alpha_{mx}\alpha_m(\alpha_{mx}^2 + (2-\nu)\mu^2)(E_m - H_m e^{-i\alpha_{mx}(b-c)})\tanh\alpha_m h = 0, \tag{2.36}$$

$$\sum_{m=-2}^{\infty} \alpha_m(\alpha_{mx}^2 + \nu\mu^2)(E_m e^{i\alpha_{mx}(c-b)} + H_m)\tanh\alpha_m h = 0, \tag{2.37}$$

$$\sum_{m=-2}^{\infty} i\alpha_{mx}\alpha_m(\alpha_{mx}^2 + (2-\nu)\mu^2)(E_m e^{i\alpha_{mx}(c-b)} - H_m)\tanh\alpha_m h = 0. \tag{2.38}$$

For the determination of the unknowns R_m, T_m, A_m, B_m, C_m, D_m, E_m and H_m, a system of linear equations of size $(8N+12) \times (8N+12)$ is obtained after truncating the infinite sum in each of the Equations (2.26)-(2.33) and (2.35)-(2.38) and solved numerically by using the Gauss-Elimination method with the help of MATLAB. The effectiveness of PS to mitigate the structural response on EP can be studied through reflection coefficient $|R_0|$, transmission coefficient $|T_0|$ and dissipation coefficient k_d, where k_d is given by the relation (2.55).

Force on PS: The horizontal force induced by the wave train impinging with PS is evaluated by integrating the pressure distribution along the front face and the rear face of PS. So, the non-dimensionalised force (k_{f1}) on the front face of the structure at $x = 0$ and the force (k_{f2}) on the rear face of the structure at $x = b$ can be respectively written as (see Koley [111])

$$k_{f1} = \left| \frac{i\omega}{gh^2} \int_{-h}^{0} \phi_1(0^-, y)dy \right|, \tag{2.39}$$

$$k_{f2} = \left| \frac{i\omega}{gh^2} \int_{-h}^{0} \phi_3(b^+, y)dy \right|. \tag{2.40}$$

Plate deflection: Using the linearised kinematic condition, the plate deflection of the floating EP is calculated by using the formula

$$\eta_4 = \frac{i}{\omega} \frac{\partial\phi_4}{\partial y} \bigg|_{y=0}. \tag{2.41}$$

Free surface elevation: Using the linearised kinematic condition, the free surface elevation in the respective open water regions is computed by using the formula

$$\eta_j = \frac{i}{\omega} \frac{\partial\phi_j}{\partial y} \bigg|_{y=0}, \quad j = 1, 3, 5. \tag{2.42}$$

Shear force and strain: The shear force S_f and strain S_t on EP are calculated for the normal incident ($\theta = 0°$) of surface waves by using the formulas (see Bhattacharjee and

Soares [112])

$$S_f = \frac{D}{\omega h} \left| \frac{\partial^4 \phi_4}{\partial x^3 \partial y} \right|_{y=0}, \tag{2.43}$$

$$S_t = \frac{h_0}{2\omega} \left| \frac{\partial^3 \phi_4}{\partial x^2 \partial y} \right|_{y=0}. \tag{2.44}$$

2.4 Energy Balance Relation

In the present problem, apart from the reflection and transmission of waves, a major part of wave energy is dissipated by PS. Thus, for a better understanding of the quantitative behavior of wave reflection, transmission, and dissipation, an energy identity is derived. The energy identity relation can be derived using the Green's identity, which is given by

$$\int_{\mathcal{C}} \left(\phi \frac{\partial \phi^*}{\partial n} - \phi^* \frac{\partial \phi}{\partial n} \right) ds = 0,$$

where ϕ^* corresponds to complex conjugate of ϕ and $\frac{\partial}{\partial n}$ corresponds to the outward normal derivative to the boundary $\mathcal{C}$. Consider $\mathcal{C} = \mathcal{C}_1 \cup \mathcal{C}_2 \cup \mathcal{C}_3$, where $\mathcal{C}_1 = \{x = -X, \ -h \leq y \leq 0;$ $y = -h, \ -X \leq x \leq 0; x = 0, \ -h \leq y \leq 0; y = 0, \ -X \leq x \leq 0\}$, $\mathcal{C}_2 = \{x = 0, \ -h \leq y \leq 0;$ $y = -h, \ 0 \leq x \leq b; x = b, \ -h \leq y \leq 0; y = 0, \ 0 \leq x \leq b\}$ and $\mathcal{C}_3 = \{x = b, \ -h \leq y \leq 0;$ $y = -h, \ b \leq x \leq X; x = X, \ -h \leq y \leq 0; y = 0, \ d \leq x \leq X \ ; y = 0, \ c \leq x \leq d \ ;$ $y = 0, \ b \leq x \leq c \ \}$. Due to no flow condition on the bottom bed, the contribution from the boundaries $y = -h, \ -X \leq x \leq 0; y = -h, \ 0 \leq x \leq b$ and $y = -h, \ b \leq x \leq X$ is zero. The contribution from the lines $y = 0, \ -X \leq x \leq 0; y = 0, \ b \leq x \leq c$ and $y = 0, \ d \leq x \leq X$ is zero because of free surface condition.

Due to EP condition, the contribution from the boundary $y = 0, \ c \leq x \leq d$ yields

$$I = \int_{\mathcal{C}} \left(\phi \frac{\partial \phi^*}{\partial n} - \phi^* \frac{\partial \phi}{\partial n} \right) ds = \int_c^d \left(\phi_4 \frac{\partial \phi_4^*}{\partial y} - \phi_4^* \frac{\partial \phi_4}{\partial y} \right) dx$$

$$= \frac{1}{K} \int_c^d \left(\frac{\partial \phi_4^*}{\partial y} \left[D \left(\frac{\partial^2}{\partial x^2} - \mu^2 \right)^2 + 1 - \epsilon_e K \right] \frac{\partial \phi_4}{\partial y} - \frac{\partial \phi_4}{\partial y} \left[D \left(\frac{\partial^2}{\partial x^2} - \mu^2 \right)^2 + 1 - \epsilon_e K \right] \frac{\partial \phi_4^*}{\partial y} \right) dx$$

(by using EP condition (2.5))

$$= \frac{D}{K} \int_c^d \left(\frac{\partial \phi_4^*}{\partial y} \left[\left(\frac{\partial^4}{\partial x^4} - 2\mu^2 \frac{\partial^2}{\partial x^2} \right) \right] \frac{\partial \phi_4}{\partial y} - \frac{\partial \phi_4}{\partial y} \left[\left(\frac{\partial^4}{\partial x^4} - 2\mu^2 \frac{\partial^2}{\partial x^2} \right) \right] \frac{\partial \phi_4^*}{\partial y} \right) dx$$

$$= \frac{D}{K} (I_1 - I_2), \tag{2.45}$$

where

$$I_1 = \int_c^d \left(\frac{\partial \phi_4^*}{\partial y} \left[\left(\frac{\partial^4}{\partial x^4} - 2\mu^2 \frac{\partial^2}{\partial x^2} \right) \right] \frac{\partial \phi_4}{\partial y} \right) dx$$

$$= \frac{\partial \phi_4^*}{\partial y} \frac{\partial^4 \phi_4}{\partial x^3 \partial z} \bigg|_{x=c}^{x=d} - 2\mu^2 \frac{\partial \phi_4^*}{\partial y} \frac{\partial^2 \phi_4}{\partial x \partial z} \bigg|_{x=c}^{x=d} - \nu \mu^2 \frac{\partial^2 \phi_4^*}{\partial x \partial z} \frac{\partial \phi_4}{\partial y} \bigg|_{x=c}^{x=d}$$

$$
+ \int_c^d \left(\frac{\partial^3 \phi_4^*}{\partial x^2 \partial z} \frac{\partial^3 \phi_4}{\partial x^2 \partial z} \right) dx + 2\mu^2 \int_c^d \left(\frac{\partial^2 \phi_4^*}{\partial x \partial z} \frac{\partial^2 \phi_4}{\partial x \partial z} \right) dx \tag{2.46}
$$

(by integration by parts and using edge condion (2.6)).

and

$$
\begin{aligned}
I_2 &= \int_c^d \left(\frac{\partial \phi_4}{\partial y} \left[\left(\frac{\partial^4}{\partial x^4} - 2\mu^2 \frac{\partial^2}{\partial x^2} \right) \right] \frac{\partial \phi_4^*}{\partial y} \right) dx \\
&= \frac{\partial \phi_4}{\partial y} \frac{\partial^4 \phi_4^*}{\partial x^3 \partial z} \Big|_{x=c}^{x=d} - 2\mu^2 \frac{\partial \phi_4}{\partial y} \frac{\partial^2 \phi_4^*}{\partial x \partial z} \Big|_{x=c}^{x=d} - \nu\mu^2 \frac{\partial^2 \phi_4}{\partial x \partial z} \frac{\partial \phi_4^*}{\partial y} \Big|_{x=c}^{x=d} \\
&\quad + \int_c^d \left(\frac{\partial^3 \phi_4^*}{\partial x^2 \partial z} \frac{\partial^3 \phi_4}{\partial x^2 \partial z} \right) dx + 2\mu^2 \int_c^d \left(\frac{\partial^2 \phi_4}{\partial x \partial z} \frac{\partial^2 \phi_4^*}{\partial x \partial z} \right) dx.
\end{aligned} \tag{2.47}
$$

(by integration by parts and using edge condion (2.6)).

Now, by substituting Equations (2.46) and (2.47) in Equation (2.45) , we get

$$
\begin{aligned}
I =& \frac{D}{K} \left\{ \left[\frac{\partial \phi_4^*}{\partial y} \frac{\partial^4 \phi_4}{\partial x^3 \partial z} - 2\mu^2 \frac{\partial^2 \phi_4}{\partial x \partial z} \frac{\partial \phi_4^*}{\partial y} + \nu\mu^2 \frac{\partial^2 \phi_4}{\partial x \partial z} \frac{\partial \phi_4^*}{\partial y} \right] \Big|_{x=c}^{x=d} \right. \\
&\left. - \left[\frac{\partial \phi_4}{\partial y} \frac{\partial^4 \phi_4^*}{\partial x^3 \partial z} - 2\mu^2 \frac{\partial^2 \phi_4^*}{\partial x \partial z} \frac{\partial \phi_4}{\partial y} + \nu\mu^2 \frac{\partial^2 \phi_4^*}{\partial x \partial z} \frac{\partial \phi_4}{\partial y} \right] \Big|_{x=c}^{x=d} \right\} \\
=& \frac{D}{K} \left\{ \frac{\partial \phi_4^*}{\partial y} \left[\frac{\partial^4 \phi_4}{\partial x^3 \partial z} - (2-\nu)\mu^2 \frac{\partial^2 \phi_4}{\partial x \partial z} \right] \Big|_{x=c}^{x=d} - \frac{\partial \phi_4}{\partial y} \left[\frac{\partial^4 \phi_4^*}{\partial x^3 \partial z} - (2-\nu)\mu^2 \frac{\partial^2 \phi_4^*}{\partial x \partial z} \right] \Big|_{x=c}^{x=d} \right\} \\
=& 0 \text{ (by using edge condion Eq. (2.6)).}
\end{aligned} \tag{2.48}
$$

The line $x = 0$, $-h \le y \le 0$ contributes

$$
\int_{\mathcal{C}} \left(\phi \frac{\partial \phi^*}{\partial n} - \phi^* \frac{\partial \phi}{\partial n} \right) ds = \int_{-h}^{0} \left([\epsilon_p(m_p + if_P) - 1] \phi_2 \phi_{2x}^* - [\epsilon_p(m_p - if_p) - 1] \phi_2^* \phi_{2x} \right)_{x=0} dy. \tag{2.49}
$$

The line $x = b$, $-h \le y \le 0$ contributes

$$
\int_{\mathcal{C}} \left(\phi \frac{\partial \phi^*}{\partial n} - \phi^* \frac{\partial \phi}{\partial n} \right) ds = \int_{-h}^{0} \left([\epsilon_p(m_p - if_p) - 1] \phi_2^* \phi_{2x} - [\epsilon_p(m_p + if_p) - 1] \phi_2 \phi_{2x}^* \right)_{x=b} dy. \tag{2.50}
$$

The line $y = 0$, $0 \le x \le a$ contributes

$$
\int_{\mathcal{C}} \left(\phi \frac{\partial \phi^*}{\partial n} - \phi^* \frac{\partial \phi}{\partial n} \right) ds = \int_0^b -2iK f_p |\phi_2|^2 dx. \tag{2.51}
$$

The contribution from the line $x = -X$, $-h \le y \le 0$ is

$$
\int_{\mathcal{C}} \left(\phi \frac{\partial \phi^*}{\partial n} - \phi^* \frac{\partial \phi}{\partial n} \right) ds = (1 - |R_0|^2) \frac{ik_{0x}}{\cosh^2 k_0 h} \left(\frac{\sinh(2k_0 h) + 2k_0 h}{2k_0} \right). \tag{2.52}
$$

The contribution from the line $x = X$, $-h \le y \le 0$ is

$$
\int_{\mathcal{C}} \left(\phi \frac{\partial \phi^*}{\partial n} - \phi^* \frac{\partial \phi}{\partial n} \right) ds = -(|T_0|^2) \frac{ik_{0x}}{\cosh^2 k_0 h} \left(\frac{\sinh(2k_0 h) + 2k_0 h}{2k_0} \right). \tag{2.53}
$$

Adding all the contributions from $\mathcal{C}_1$, $\mathcal{C}_2$ and $\mathcal{C}_3$, the energy balance relation is derived as

$$
|R_0|^2 + |T_0|^2 + k_d = 1 \tag{2.54}
$$

where

$$k_d = \frac{2k_0 \cosh^2 k_0 h}{ik_{0x}(\sinh 2k_0 h + 2k_0 h)} \left[\int_{-h}^{0} \left([\epsilon_p(m_p + if_p) - 1] \phi_2 \phi_{2x}^* - [\epsilon_p(m_p - if_p) - 1] \phi_2^* \phi_{2x} \right)_{x=0} dy \right.$$

$$+ \int_{-h}^{0} \left([\epsilon_p(m_p - if_p) - 1] \phi_2^* \phi_{2x} - [\epsilon_p(m_p + if_p) - 1] \phi_2 \phi_{2x}^* \right)_{x=b} dy$$

$$\left. - \int_{0}^{b} \left(2iK f_p |\phi_2|^2 \right)_{y=0} dx \right].$$

$$(2.55)$$

2.5   Results and Discussion

In this section, for different values of structural parameters, the hydrodynamic quantities, namely reflection coefficient ($|R_0|$), transmission coefficient ($|T_0|$), dissipation coefficient (k_d), hydrodynamic forces on PS (k_{f1} and k_{f2}), EP deflection (η_4), Free surface elevation (η_1, η_3 and η_5), shear force (S_f) and strain (S_t) are calculated. The values of the non-dimensional parameters $k_0 h = 1$, $m_p = 1$, $f_p = 0.5$, $\epsilon_p = 0.55$, $b/h = 0.6$, $L_1/h = 4$, $D/h^4 = 10^2$, $\epsilon_e/h = 0.01$, $L_2/h = 5$, and $\theta = 20°$ are kept fixed in this investigation unless otherwise mentioned. Several computations are performed to investigate the effect of various structural parameters, but few results are shown in this section to avoid repetition.

2.5.1   Convergence Study for N

The convergence on the number of evanescent modes N is studied in Table 2.1. The values of $|R_0|$ and $|T_0|$ are tabulated against various values of $k_0 h$ for various $N = 2, 4, 6$ and 8. Here, it is noticed that the accuracy of $|R_0|$ and $|T_0|$ is achieved up to the fourth decimal point for $N = 6$ for all values of $k_0 h$. Hence, $N = 6$ is considered throughout this study.

$k_0 h$	$N = 2$		$N = 4$		$N = 6$		$N = 8$	
	$|R_0|$	$|T_0|$	$|R_0|$	$|T_0|$	$|R_0|$	$|T_0|$	$|R_0|$	$|T_0|$
0.25	0.1147	0.9324	0.1145	0.9326	0.1144	0.9328	0.1144	0.9328
0.5	0.1328	0.8831	0.1324	0.8831	0.1324	0.8831	0.1324	0.8831
0.75	0.2788	0.7591	0.2785	0.7593	0.2784	0.7595	0.2784	0.7595
1	0.2045	0.7451	0.2048	0.7453	0.2049	0.7453	0.2049	0.7453
1.25	0.4774	0.3425	0.4767	0.3429	0.4766	0.3430	0.4766	0.3430
1.5	0.6572	0.1363	0.6570	0.1362	0.6569	0.1361	0.6569	0.1361

Table 2.1: Convergence on N through $|R_0|$ and $|T_0|$.

2.5.2 Order of Convergence

Let x_k be an approximation to R_0. Then, from the definition of order of convergence (Refer Section 2.5, Chapter 2 of Jain et al. [113]), we can write

$$|E_{k+1}| \approx \mathcal{A}|E_k|^C, \tag{2.56}$$

where C is the positive real number called the order of convergence, for which there exists a finite constant $\mathcal{A} \neq 0$, and $|E_{k+1}| = |x_{k+1} - x_k|$. Similarly, we can write

$$|E_{k+2}| \approx \mathcal{A}|E_{k+1}|^C. \tag{2.57}$$

Now, dividing Equation (2.57) by Equation (2.56), we will get

$$\frac{|E_{k+2}|}{|E_{k+1}|} \approx \frac{|E_{k+1}|^C}{|E_k|^C} \tag{2.58}$$

Applying logarithmic on both sides, we will get

$$C \approx \frac{log\frac{|E_{k+2}|}{|E_{k+1}|}}{log\frac{|E_{k+1}|}{|E_k|}}. \tag{2.59}$$

$$\Rightarrow C \approx \frac{log\frac{|x_{k+2}-x_{k+1}|}{|x_{k+1}-x_k|}}{log\frac{|x_{k+1}-x_k|}{|x_k-x_{k-1}|}} \quad (\text{ using definition } |E_{k+1}| = |x_{k+1} - x_k|). \tag{2.60}$$

To find the order of convergence, we first find the numerical values of $|R_0|$ for various values of N=2,4,6,8,10 and 12, denoted as $|R_0|_N$, N=2,4,6, 8,10,12 and for various values of k_0h which are tabulated in Table 2.2. Hence, following the Equation (2.60), we define the order of convergence 'C' for the number of evanescent modes N through the reflection coefficient $|R_0|$, by the formula

$$C = \frac{\log\left|\frac{|R_0|_{N+4}-|R_0|_{N+2}}{|R_0|_{N+2}-|R_0|_N}\right|}{\log\left|\frac{|R_0|_{N+2}-|R_0|_N}{|R_0|_N-|R_0|_{N-2}}\right|}, N = 4, 6, 8. \tag{2.61}$$

From Table 2.2, it is concluded that the order convergence lies between 0.5 and 1.

k_0h	$N=2$		$N=4$		$N=6$		$N=8$		$N=10$		$N=12$	
	$|R_0|$	C	$|R_0|$	C	$|R_0|$	C	$|R_0|$	C	$|R_0|$	C	$|R_0|$	C
0.25	0.1143687434	-	0.1143664624	0.6689	0.1143659158	0.7536	0.1143657056	0.8048	0.1143656033	-	0.1143655460	-
0.5	0.1323497521	-	0.1323534729	0.6808	0.1323544386	0.7625	0.1323548241	0.8094	0.1323550155	-	0.1323551241	-
0.75	0.2783717262	-	0.2783561425	0.6626	0.2783526462	0.7476	0.2783513475	0.7999	0.2783507281	-	0.2783503855	-
1	0.2045156244	-	0.2048334305	0.6691	0.2049107688	0.7559	0.2049408108	0.8052	0.2049555103	-	0.2049637770	-
1.25	0.4773742207	-	0.4767347252	0.6673	0.4765816966	0.7543	0.4765227703	0.8042	0.4764940832	-	0..4764780037	-
1.5	0.6572077968	-	0.6569386337	0.6702	0.6568766009	0.7534	0.6568534018	0.8025	0.6568423439	-	0.6568362426	-

Table 2.2: Order of convergence for various value of N.
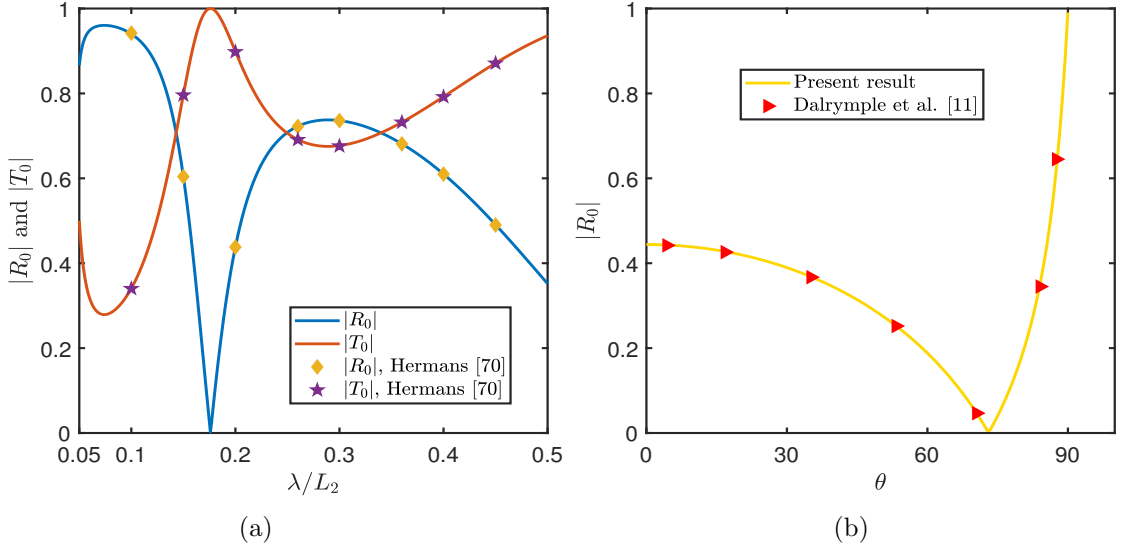
Figure 2.2: Validation of present results with results of (a) Hermans [70] and Dalrymple et al. [11].

2.5.3 Validation

To validate the present methodology and results, it may be noticed that this problem is reduced to the work by Hermans [70] in the absence of PS (i.e., $m_p = 1$, $f_p = 0$, $\epsilon_p = 1$). Figure 2.2a illustrates the numerical values of $|R_0|$ and $|T_0|$ by the present method for $D/h^4 = 10^{-3}$, $\theta = 0°$, $L_2/h = 30$ which are well-matched with the results of Hermans [70]. As a second validation, in the absence of EP (i.e., $D/h^4 = 0$, $\epsilon_e = 0$), the present study reduces to scattering of water waves by PS (Dalrymple et al. [11]). Figure 2.2b illustrates the present results of $|R_0|$ for $Kh = 0.2012$, $\epsilon_p = 0.4$, $f_p = 1$ and $b/h = 1$ in the absence of EP which are well-matched with the results of Dalrymple et al. [11]. Further, to verify the energy identity derived in Section 2.4 and given in relation (2.54), $|R_0|$, $|T_0|$, and k_d values are determined numerically and tabulated in Table 2.3 for different values of k_0h. The last two columns of Table 2.3 reveal that the energy identity is satisfied, showing the accuracy of the present numerical computations.

$k_0 h$	$|R_0|$	$|T_0|$	$1 - |R_0|^2 - |T_0|^2$	k_d
0.25	0.1144	0.9328	0.1168	0.1168
0.5	0.1323	0.8828	0.2031	0.2032
0.75	0.2785	0.7607	0.3438	0.3445
0.1	0.1971	0.7410	0.4141	0.4147
1.25	0.4908	0.3316	0.6497	0.6501
1.5	0.6622	0.1373	0.5497	0.5503

Table 2.3: Verification of energy identity.

2.5.4 Effect of Various Parameter on Reflection Coefficient ($|R_0|$), Transmission Coefficient ($|T_0|$) and Dissipation Coefficient (k_d)

Figure 2.3 illustrates the behavior of $|R_0|$, $|T_0|$ and k_d versus the wavenumber $k_0 h$ for different values of width b/h of PS extended from top to bottom. It is illustrated that as the width b/h increases, $|R_0|$ decreases, $|T_0|$ decreases, and k_d increases because more incident wave energy is dissipated and less incident wave energy is reflected and transmitted by a wider PS. It is also observed that with the increase in $k_0 h$, the dissipation coefficient k_d increases, and the transmission coefficient $|T_0|$ decreases.
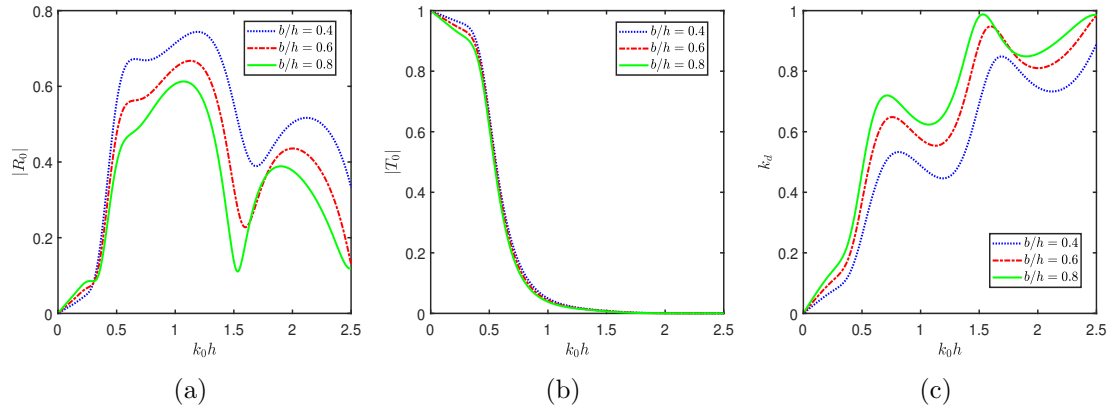
Figure 2.3: $|R_0|$, $|T_0|$ and k_d vs $k_0 h$ for $b/h = 0.4, 0.6, 0.8$ with $\theta = 45°$.
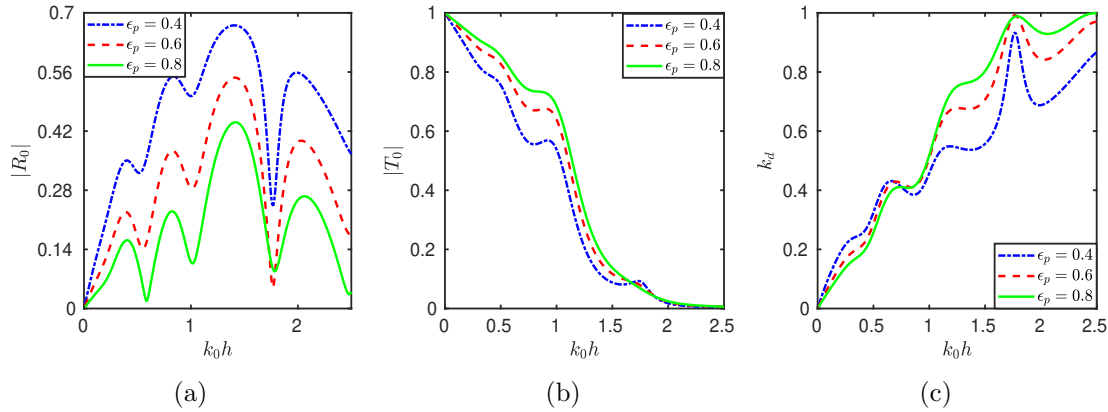
Figure 2.4: $|R_0|$, $|T_0|$ and k_d vs $k_0 h$ for $\epsilon_p = 0.4, 0.6, 0.8$ with $b/h = 1$.

Figure 2.4 reveals the behavior of $|R_0|$, $|T_0|$ and k_d versus the wavenumber $k_0 h$ for different values of porosity ϵ_p of PS. $|R_0|$, $|T_0|$ and k_d show the same behavior with an increase in $k_0 h$ as in Figure 2.3. As the porosity ϵ_p increases, more waves are transmitted and dissipated by PS, due to which there is a decrease in wave reflection, as observed in Koley and Panduranga [114].

Figures 2.5, 2.6 and 2.7 illustrate the behavior of $|R_0|$, $|T_0|$ and k_d versus L_1/h for different values of width b/h, frictional coefficient f_p and porosity ϵ_p, respectively. In these figures, $|R_0|$, $|T_0|$ and k_d show a periodic and oscillatory pattern with L_1/h. The occurrence of optima in wave reflection due to the resonating interaction of waves in a

confined zone is referred to as the trapping of waves, which has significant importance in creating calm zones in the coastal environment, as discussed by Koley et al. [115]. It is also noted from Figures 2.5 and 2.6 that with an increase in b/h and f_p, more water waves are dissipated by PS, and consequently, fewer waves are reflected and transmitted by PS. Because with increases in b/h and f_p, more incident waves are dissipated by PS, and as a consequence, fewer waves are transmitted and reflected by PS. As observed in Figure 2.4, Figure 2.7 shows that the energy dissipation coefficient k_d and transmission coefficient $|T_0|$ increase but reflection coefficient $|R_0|$ decreases with an increase in ϵ_p, however moderate porosity (not producing high transmission) will be helpful for the requirement of creating a calm zone towards the lee side of EP.
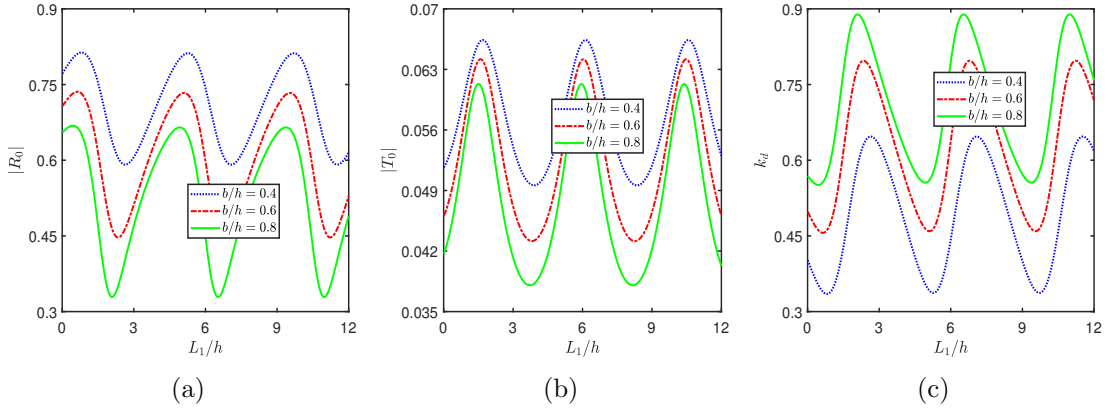
Figure 2.5: $|R_0|$, $|T_0|$ and k_d vs L_1/h for $b/h = 0.4, 0.6, 0.8$ with $\theta = 45°$.
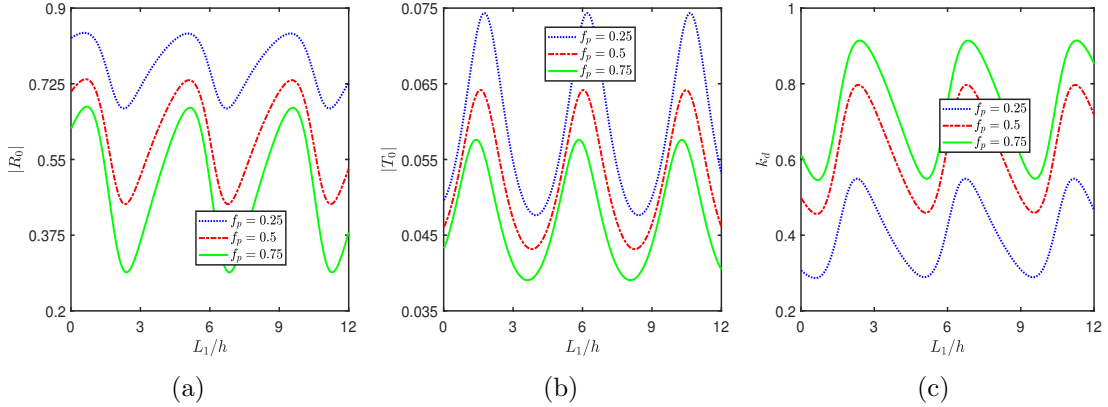
Figure 2.6: $|R_0|$, $|T_0|$ and k_d vs L_1/h for $f_p = 0.25, 0.5, 0.75$ with $\theta = 45°$.

Figure 2.8 demonstrates the behavior of $|R_0|$, $|T_0|$ and k_d versus L_2/h (length of EP) for different values of width b/h. The figure shows that the reflection coefficient $|R_0|$, transmission coefficient $|T_0|$, and dissipation coefficient k_d follow a periodic and oscillatory pattern with EP length. With an increase in b/h, the wave reflection and transmission decrease, but the energy dissipation increases as in Figures 2.3 and 2.5.

Figure 2.9 depicts the behavior of $|R_0|$, $|T_0|$ and k_d versus L_2/h for different values of flexural rigidity D/h^4. With the increase in flexural rigidity D/h^4 of EP, the formation

of the number of maxima and minima for $0 < L_2/h < 32$, in $|R_0|$, $|T_0|$ and k_d curves are decreased. This may be due to the formation of the standing wave. From Figures 2.9a and 2.9b, it is noted that as D/h^4 increases, wave reflection increases and wave transmission decreases. This is due to the reduced flexure of EP, making EP more rigid, which makes more incident waves reflected by EP and fewer waves transmitted. Figure 2.9c shows that as D/h^4 increases, the energy dissipation increases. Here, it is also noted that with an increase in L_2/h, the local maximum value in wave reflection and energy dissipation increase. However, after a certain length, the local maximum values of the $|R_0|$ and k_d become constant. The opposite behavior is noted in transmission coefficient $|T_0|$.
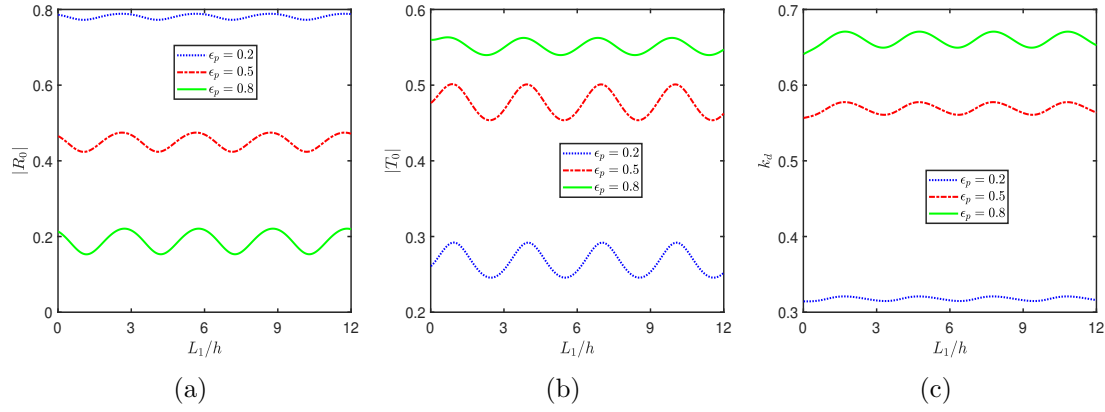
Figure 2.7: $|R_0|$, $|T_0|$ and k_d vs L_1/h for $\epsilon_p = 0.2, 0.5, 0.8$ with $b/h = 1.5$, $L_2/h = 8$, $k_0 h = 1.1$.
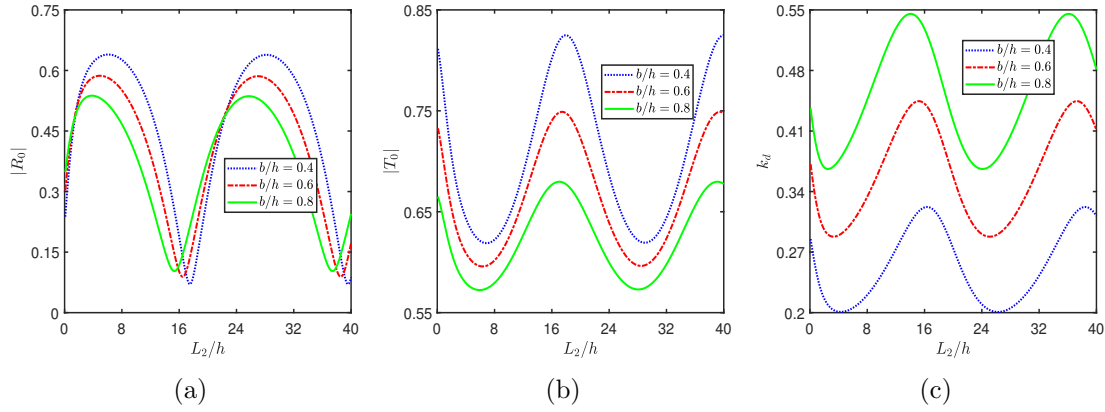
Figure 2.8: $|R_0|$, $|T_0|$ and k_d vs L_2/h for $b/h = 0.4, 0.6, 0.8$ with $D/h^4 = 10$, $\theta = 36°$, $\epsilon_p = 0.5$.

Figure 2.10 depicts the behavior $|R_0|$, $|T_0|$ and k_d versus θ for different values of width b/h. Figures 2.10a and 2.10c show that with an increase in θ, the reflection coefficient decreases and the dissipation coefficient increases except for specific local optima for $0° < \theta < 82°$. However, there is a sudden rise in wave reflection and a sudden fall in energy dissipation for various values of b/h when the wave's angle of incidence is close to $82°$. Furthermore, from Figure 2.10b, it is clear that wave transmission is decreasing in an oscillatory pattern for $0° < \theta < 27°$ and at close to $\theta = 27°$, there is a sharp fall in $|T_0|$

and it became zero when $\theta > 65°$. This local optima in these hydrodynamic quantities may be due to the change of phase of the incident wave and reflected wave in the presence of PS and EP.

(a)   (b)   (c)
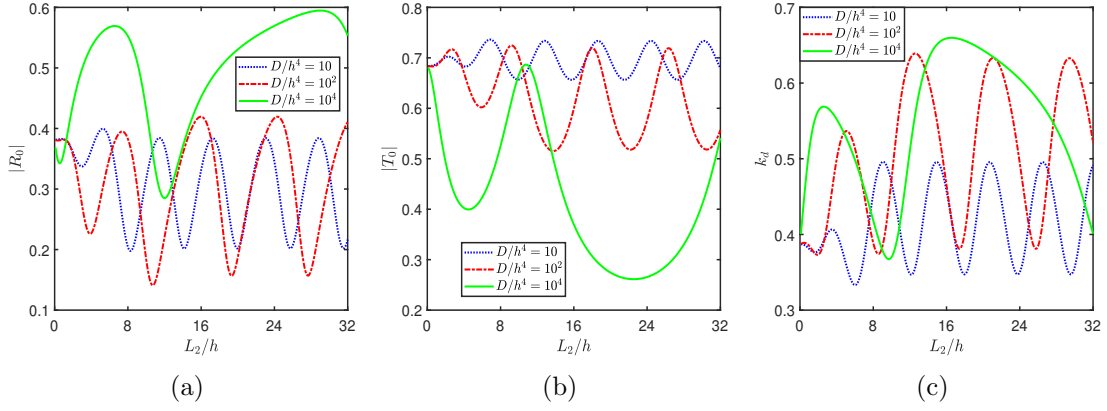
Figure 2.9: $|R_0|$, $|T_0|$ and k_d vs L_2/h for $D/h^4 = 10, 10^2, 10^4$ with $b/h = 1$, $L_1/h = 6$, $k_0 h = 0.83$, $\theta = 10°$.

(a)   (b)   (c)
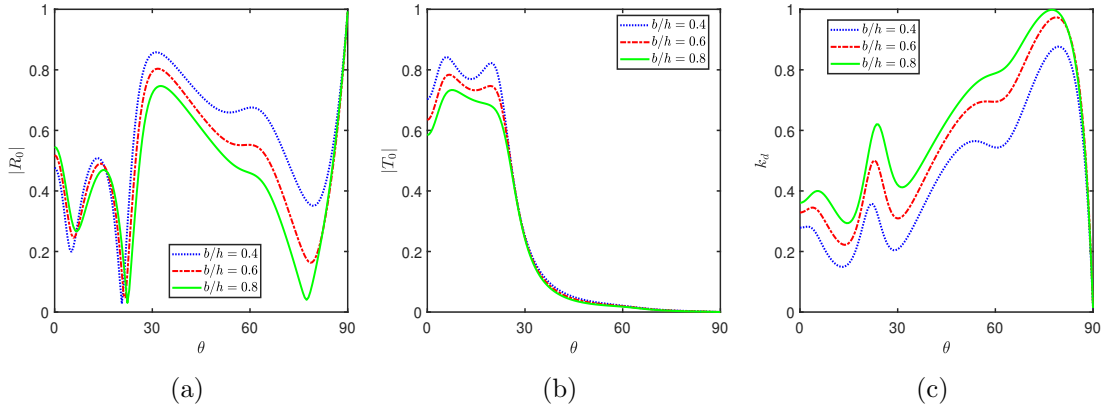
Figure 2.10: $|R_0|$, $|T_0|$ and k_d vs θ for $b/h = 0.4, 0.6, 0.8$.

2.5.5 Effect of Various Parameters on Force (k_{f1} and k_{f2}) Experienced on PS, Plate Deflection ($Re(\eta_4)$), Free Surface Elevation ($Re(\eta_j), j = 1, 3, 5$), Shear Force (S_f) and Strain (S_t)

Figure 2.11 shows the behavior of force k_{f1} (on the front face) and k_{f2} (on the rear face) of PS versus $k_0 h$ for different values of f_p. From the figure, it is found that the wave force k_{f1} and k_{f2} decrease in an oscillatory pattern with an increase in $k_0 h$. Further, Figure 2.11a shows that the wave forces k_{f1} increase with an increase in f_p, but from Figure 2.11b, it is found that the wave force k_{f2} decreases with an increase in f_p.

In Figure 2.12, the behavior of forces k_{f1} (on the front face) and k_{f2} (on the rear face) of PS versus L_1/h for different values of b/h are investigated. Here, both the wave forces show a periodic and oscillatory pattern with the increase in L_1/h as shown in Figure 2.5 for the scattering coefficients with L_1/h. Further, Figure 2.12a shows that with an increase

in b/h, the wave force k_{f1} increases, but the wave force k_{f2} in Figure 2.12b, decreases, which may be due to PS with a larger width leads to more wave damping as discussed by Singla et al. [86].

(a)　　　　　　　　　　　　　　(b)
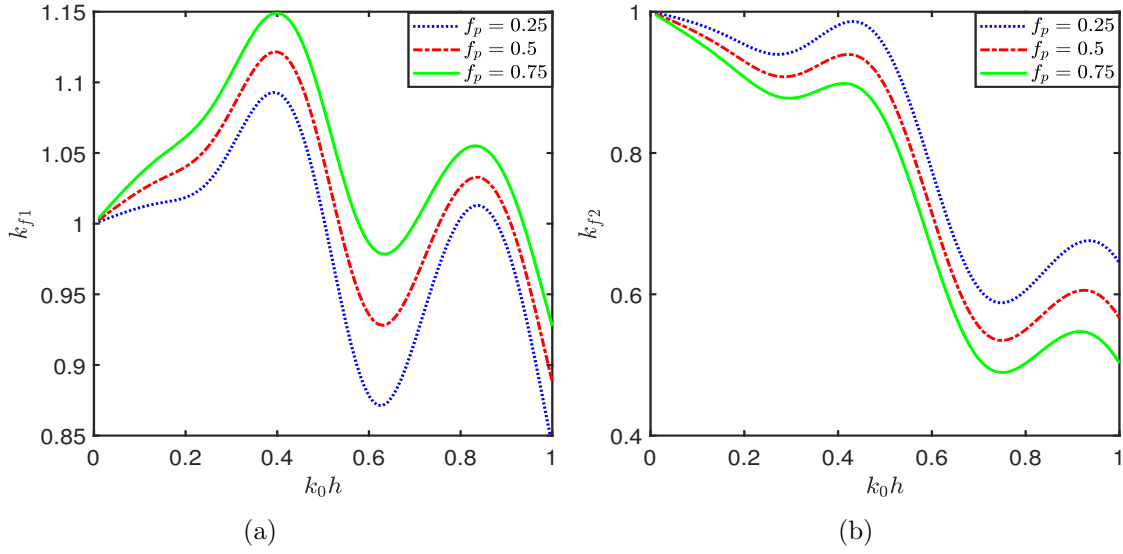
Figure 2.11: k_{f1} and k_{f2} vs k_0h for $f_p = 0.25, 0.5, 0.75$.

(a)　　　　　　　　　　　　　　(b)
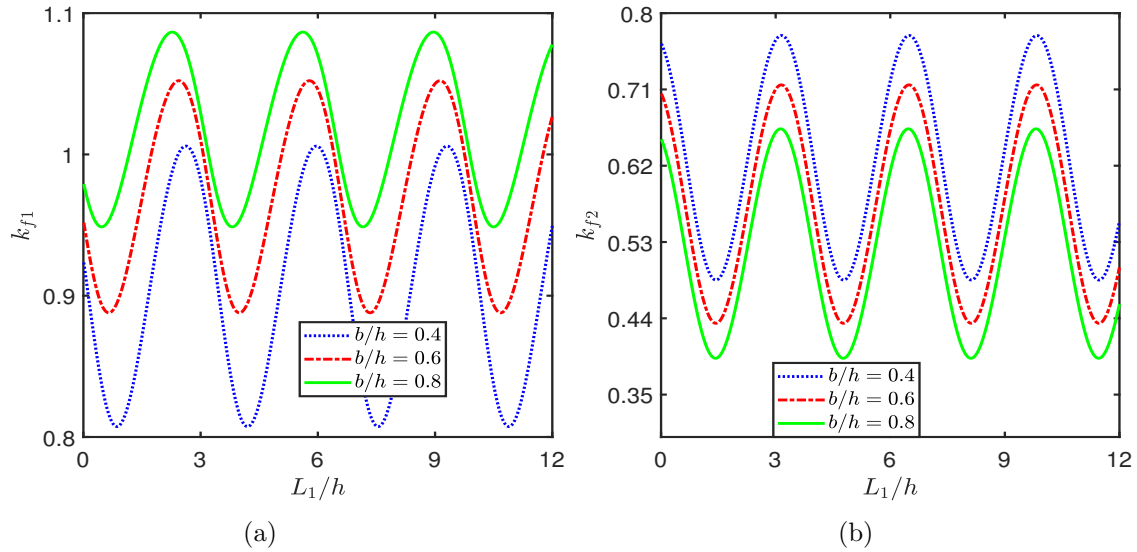
Figure 2.12: k_{f1} and k_{f2} vs L_1/h for $b/h = 0.4, 0.6, 0.8$.

From Figure 2.13 it is observed that the elevation η_5 is significantly less (creating calm zone) as compared to η_1 for fixed values of f_p and ϵ_p, due to the fact that PS dissipates a major part of the wave energy. Furthermore, Figure 2.13a depicts that EP deflection decreases as f_p increases. This is due to, as f_p increases, more wave energy is dissipated by PS, and less wave energy is transmitted towards the lee side of EP as observed in Figure 2.6. Figure 2.13b depicts that with an increase in ϵ_p, plate deflection increases. From these graphs, the higher value of friction coefficient and moderated value of porosity of PS can effectively mitigate the structural response of EP by reducing plate deflection.
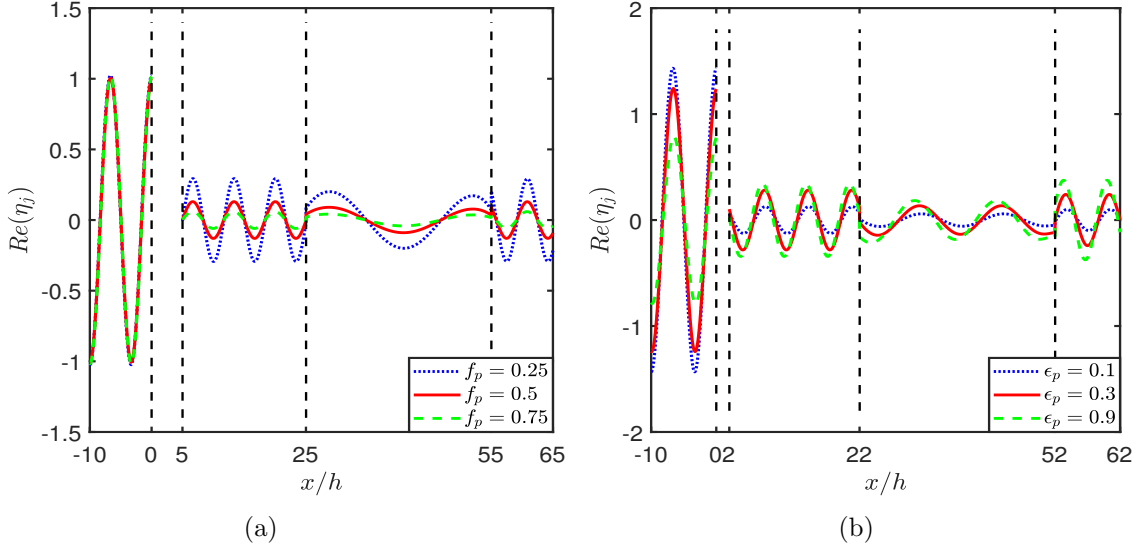
Figure 2.13: Plate deflection and free surface elevation $Re(\eta_j)$ for **(a)** $f_p = 0.25, 0.5, 0.75$ with $L_2/h = 30$, $b/h = 5$, $L_1/h = 20$, **(b)** $\epsilon_p = 0.1, 0.3, 0.9$ with $D/h^4 = 10$, $L_2/h = 30$, $L_1/h = 20$, $b/h = 2$.
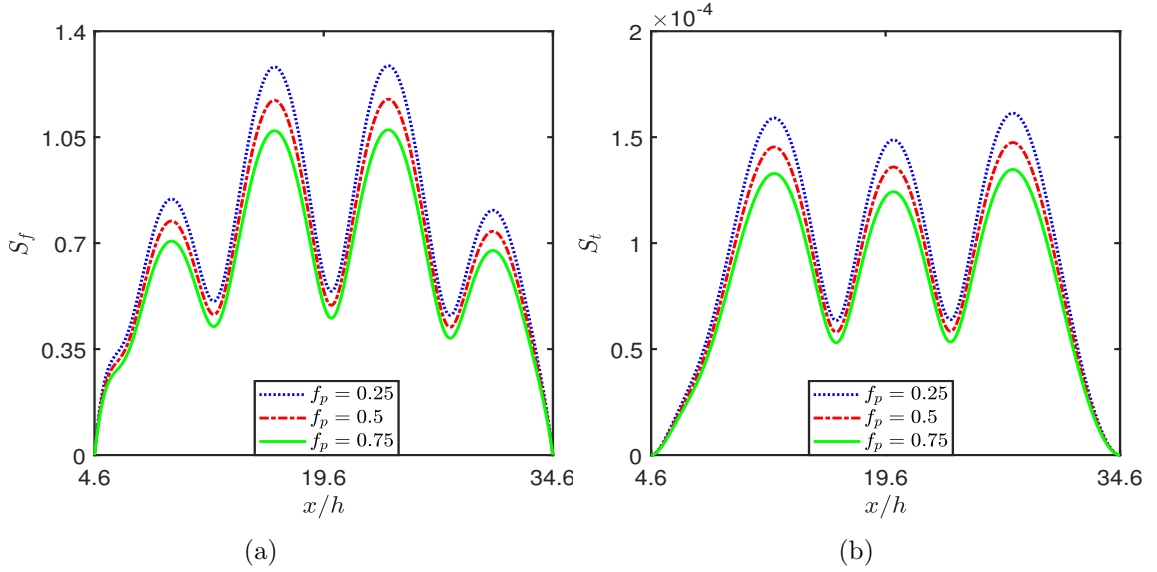
Figure 2.14: S_f and S_t for $f_p = 0.25, 0.5, 0.75$ with $\theta = 0°$ and $L_2/h = 30$.

Figure 2.14 depicts the graphs of the shear force S_f and strain S_t for different values of f_p. Due to the assumption of free edge behavior, S_f and S_t are zero at both ends of EP. Further, the variation of S_f and S_t follows an oscillatory pattern, and their values decrease as the value of f_p increases. This is because with an increase in f_p, more wave energy is dissipated by PS, implying less impact of wave load in EP.

In Figure 2.15, S_f and S_t are plotted for absence of PS (i.e. $m_p = 1$, $f_p = 0$ and $\epsilon_p = 1$) and the present work ($m_p = 1$, $f_p = 0.5$ and $\epsilon_p = 0.55$). The figure shows that shear force and strain in the presence of PS extended from top to bottom are less compared to the absence of PS, implying a reduction in structural response on EP. Hence, it reflects

that PS extended from top to bottom is useful to mitigate the structural response of EP from wave load.

(a)

(b)
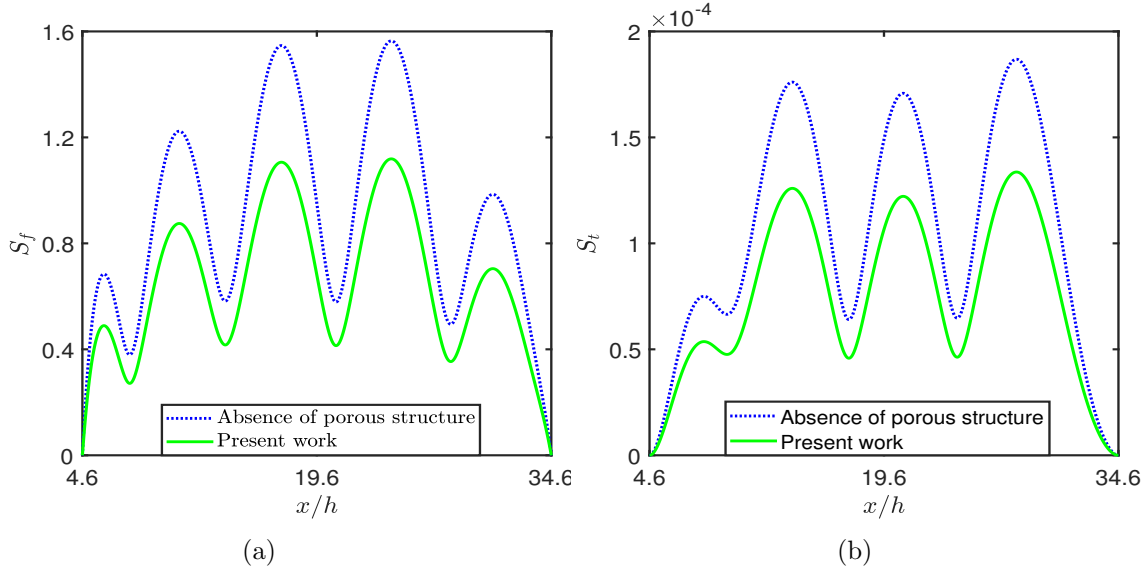
Figure 2.15: S_f and S_t for in the absence of PS, and Present work with $Kh = 1$, $L_1/h = 4$, $b/h = 0.6$ with $\theta = 0°$ and $L_2/h = 30$.

2.6   Conclusion

This chapter analyzes the hydroelastic response of an oblique incident water wave on EP in the presence of PS extending from top to bottom. The matching conditions on interfaces and orthogonality of eigenfunctions are used. A system of linear algebraic equations is solved to determine the value of the reflection and transmission coefficients. The dissipation coefficient is derived through energy identity. These coefficients are plotted through different graphs. The study found that with an increase in the width and frictional coefficient of PS, the wave reflection and transmission decrease as PS dissipates a major part of the incident wave. Further, with an increase in the frictional coefficient, plate deflection, free surface elevation, shear force, and strain decrease, causing a reduction in wave load on EP. In addition, a moderate porosity value of PS is preferable for this problem. The wave forces on PS follow a periodic and oscillatory pattern with the distance between PS and EP. However, it is reduced in an oscillatory pattern with the variation of the angle of incident. Thus, a suitable arrangement of EP and PS of specific configurations can provide a long-term and cost-effective solution to diminish the hydroelastic response of EP, which will be helpful for coastal engineering applications.

Chapter 3

Mitigation of Wave Load on a Sea Wall by a Vertical Porous Structure in the Presence of an Elastic Plate

3.1 Introduction

In Chapter 2, the effectiveness of PS (extended from bottom to top) on mitigating structural response on EP was analyzed. Since the sea wall plays a crucial role in coastal engineering, so in this chapter, we focus on examining the effectiveness of PS in reducing wave loads on the sea wall in the presence of EP. The PS is placed at a finite distance from EP, and EP is positioned at a finite distance from the sea wall to reduce wave loads on the sea wall. The problem is examined for obliquely incident waves, assuming small amplitude and linear water wave theory. Thin plate theory is used to model the flow past EP, while Sollitt and Cross theory is used to model the flow past PS. The eigenfunction expansion method is employed to solve the boundary value problem, which coins to a system of equations that has been solved to determine the reflection and transmission coefficients. The study aims to determine the optimal distances between the PS and EP and between EP and the sea wall to achieve maximum wave dissipation by the PS, thereby reducing wave loads on the sea wall. Scattering coefficients and various hydrodynamic parameters related to wave scattering, such as wave force experienced on the sea wall, free surface elevation, plate deflection, shear force, and strain, are analyzed for various wave and structural parameters of PS and EP. The energy balance relation is derived and verified for the accuracy of the computational results and to provide quantitative information about wave energy dissipation. A major part of the work presented in this chapter has been published in Sahoo et al. [116].

3.2 Mathematical Formulation

In a three-dimensional Cartesian coordinate system, the wave interaction with a rigid wall in the presence of EP and PS is investigated by selecting the y-axis as vertically upward and the undisturbed water surface is denoted as the xz-plane. The whole fluid domain is divided into 5 regions, and $y = -h$ represents the flatbed, as shown in Figure 3.1. EP with length L_2 is retained at a distance L_3 from the stiff wall, while PS with width b is

positioned at L_1 distance from it. Along the z-axis, PS is indefinitely long. To satisfy the matching constraints at vertical interfaces, the solution variations in each region are taken into consideration to be the same (by Snell's law). The fluid is inviscid, incompressible and the flow is irrotational. Let the propagation of time harmonic wave with angular frequency ω move at an angel θ with respect to x-axis. In each region $j = 1, 2, 3, 4$ and 5, the velocity potential $\Phi_j(x, y, z, t) = Re\{\phi_j(x, y)e^{i(\mu z - \omega t)}\}$, where ϕ_j satisfying the partial differential equation

$$\left(\frac{\partial^2}{\partial x^2} + \frac{\partial^2}{\partial y^2} - \mu^2\right)\phi_j = 0, \quad \text{in each region } j, \tag{3.1}$$

where $\mu = k_0 \sin\theta$, k_0 is the wavenumber of the incident wave.
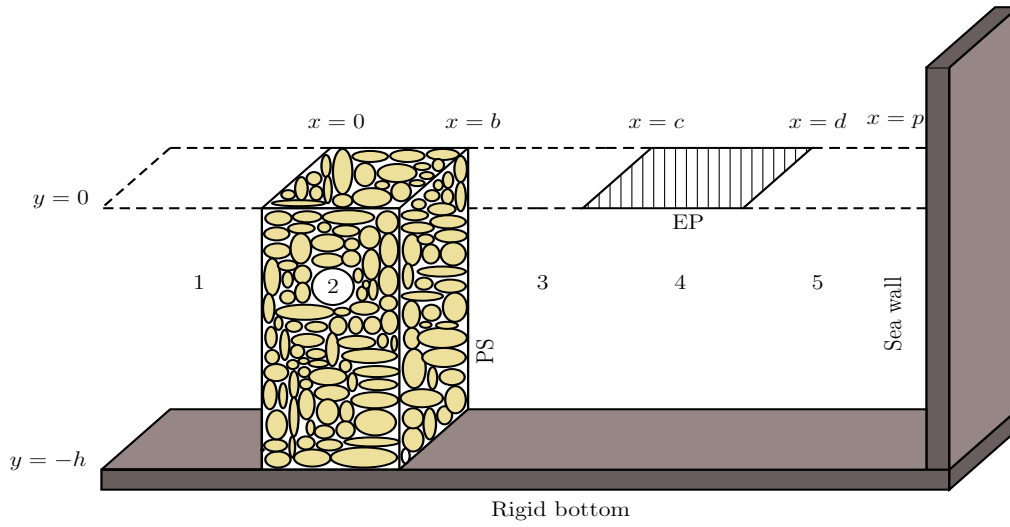
Figure 3.1: Schematic representation of the physical problem.

The no-flow condition on the bottom is given by

$$\phi_{jy} = 0, \quad \text{on} \quad y = -h \quad \text{for } j = 1, 2, 3, 4, 5. \tag{3.2}$$

In the open water regions, the free surface boundary condition is expressed by

$$\phi_{jy} - K\phi_j = 0 \quad \text{on} \quad y = 0, \quad \text{for } j = 1, 3, 5. \tag{3.3}$$

In PS region 2, the free surface boundary condition in porous medium is given by

$$\phi_{2y} - K(m_p + if_p)\phi_2 = 0 \quad \text{on} \quad y = 0, \tag{3.4}$$

with $K = \omega^2/g$, g is the acceleration due to gravity, m_p and f_p are the non-dimensionalized inertial coefficient and friction factor respectively.

At EP the condition is

$$\left[D\left(\frac{\partial^2}{\partial x^2} - \mu^2\right)^2 + 1 - \epsilon_e K\right]\phi_{4y} - K\phi_4 = 0 \quad \text{on} \quad y = 0. \tag{3.5}$$

where $D = EI/\rho g$ is the flexural rigidity of the plate with E being Young's modulus, $I = h_1^3/12(1 - \nu^2)$, h_1 is the thickness of EP, ν is the Poisson's ratio, $\epsilon_e = \rho_e h_1/\rho$, ρ_e is the density of EP and ρ is the density of the fluid.

The shear force and bending moment at the plate's edges vanish when EP is assumed to be floating freely on the water's surface, which gives rise to

$$\left(\frac{\partial^2}{\partial x^2} - \nu\mu^2\right)\phi_{4y} = 0 \quad \text{and} \quad \frac{\partial}{\partial x}\left(\frac{\partial^2}{\partial x^2} - (2 - \nu)\mu^2\right)\phi_{4y} = 0 \quad \text{at } (c, 0), (d, 0). \quad (3.6)$$

Since the solution must be continuous at each interface, the continuity of pressure and velocity at PS interfaces and EP interfaces yield

$$\phi_1 = (m_p + if_p)\phi_2, \quad \phi_{1x} = \epsilon_p\phi_{2x} \quad \text{on} \quad x = 0, -h \leq y \leq 0, \quad (3.7)$$

$$\phi_3 = (m_p + if_p)\phi_2, \quad \phi_{3x} = \epsilon_p\phi_{2x} \quad \text{on} \quad x = b, -h \leq y \leq 0, \quad (3.8)$$

$$\phi_3 = \phi_4, \quad \phi_{3x} = \phi_{4x} \quad \text{on} \quad x = c, -h \leq y \leq 0, \quad (3.9)$$

$$\phi_4 = \phi_5, \quad \phi_{4x} = \phi_{5x} \quad \text{on} \quad x = d, -h \leq y \leq 0, \quad (3.10)$$

where ϵ_p denotes the porosity of PS. The condition at rigid wall located at $x = p$ condition is given by

$$\phi_{5x} = 0 \quad \text{on} \quad x = p, -h \leq y \leq 0. \quad (3.11)$$

Finally, the far-field condition is provided by

$$\phi_1(x, y) \simeq \left(\frac{ig}{\omega}\right)\frac{\cosh k_0(y + h)}{\cosh k_0 h}\{e^{ik_{0x}x} + R_0 e^{-ik_{0x}x}\} \quad \text{as} \quad x \to -\infty. \quad (3.12)$$

where R_0 denotes the unknown constant associated with the reflected wave to be determined here, $k_{0x} = \sqrt{k_0^2 - \mu^2}$, and k_0 is the wavenumber of the incident wave, which is the positive real root for $m = 0$ of the transcendental equation in k_m as given by

$$K - k_m \tanh k_m h = 0. \quad (3.13)$$

3.3 Method of Solution

By using the method of separation of variables in each region, the spatial velocity potential functions are expressed as series solutions in terms of eigenfunctions. The spatial velocity potentials in the open water regions 1, 3 and 5 satisfying Equations (3.1), (3.2), (3.3), (3.11) and (3.12) can be written as

$$\phi_1 = \left(\frac{ig}{\omega}\right)\left[e^{ik_{0x}x}\Psi_0 + \sum_{m=0}^{\infty} R_m e^{-ik_{mx}x}\Psi_m\right] \quad \text{for} \quad -\infty < x \leq 0, -h \leq y \leq 0, \quad (3.14)$$

$$\phi_3 = \left(\frac{ig}{\omega}\right) \sum_{m=0}^{\infty} \left[A_m e^{ik_{mx}(x-b)} + B_m e^{-ik_{mx}(x-c)}\right] \Psi_m \quad \text{for} \quad b \leq x \leq c, -h \leq y \leq 0,$$

(3.15)

$$\phi_5 = \left(\frac{ig}{\omega}\right) \sum_{m=0}^{\infty} T_m \cos k_{mx}(x-p) \Psi_m \quad \text{for} \quad d \leq x \leq p, -h \leq y \leq 0, \quad (3.16)$$

where

$$\Psi_m = \frac{\cosh k_m(z+h)}{\cosh k_m h}, \; m = 0, 1, 2, \ldots \quad (3.17)$$

R_m, A_m, B_m and T_m ($m = 0, 1, 2, \ldots$) are unknown complex constants, $k_{mx} = \sqrt{k_m^2 - \mu^2}$ and k_m ($m = 1, 2, 3, \ldots$) are purely imaginary roots of the dispersion relation (3.13).

Again, the velocity potential in the PS region 2 satisfying Equations (3.1), (3.2) and (3.4) can be written as

$$\phi_2 = \left(\frac{ig}{\omega}\right) \sum_{m=0}^{\infty} \left[C_m e^{iq_{mx}x} + D_m e^{-iq_{mx}(x-b)}\right] \mathcal{F}_m \quad \text{for} \quad 0 \leq x \leq b, \; -h \leq y \leq 0, \quad (3.18)$$

where

$$\mathcal{F}_m = \frac{\cosh q_m(z+h)}{\cosh q_m h}, \; m = 0, 1, 2, \ldots \quad (3.19)$$

C_m and D_m ($m = 0, 1, 2, \ldots$) are unknown complex constants, $q_{mx} = \sqrt{q_m^2 - \mu^2}$ and q_m, $m = 0, 1, 2 \ldots$ are the complex roots of the dispersion relation

$$K(m_p + if_p) - q_m \tanh q_m h = 0. \quad (3.20)$$

Finally, in EP region 4, the velocity potential satisfying Equations (3.1), (3.2) and (3.5) can be written as

$$\phi_4 = \left(\frac{ig}{\omega}\right) \sum_{m=-2}^{\infty} \left[E_m e^{i\alpha_{mx}(x-c)} + \mathcal{H}_m e^{-i\alpha_{mx}(x-d)}\right] \mathcal{G}_m \quad \text{for} \quad c \leq x \leq d, \; -h \leq y \leq 0$$

(3.21)

where

$$\mathcal{G}_m = \frac{\cosh \alpha_m(z+h)}{\cosh \alpha_m h} \quad m = -2, -1, 0, 1, 2, \ldots, \quad (3.22)$$

E_m and $\mathcal{H}_m$ ($m = -2, -1, 0, 1, 2, \ldots$) are unknown complex constants, $\alpha_{mx} = \sqrt{\alpha_m^2 - \mu^2}$ and α_m are the complex roots of the form $\pm a + ib$ for $m = -2, -1$, positive real roots for $m = 0$ and purely imaginary roots for $m = 1, 2, \ldots$ for the equation

$$(D\alpha_m^4 + 1 - \epsilon_e K)\alpha_m \tanh \alpha_m h = K. \quad (3.23)$$

Utilizing Equations (3.14)-(3.16), (3.18) and (3.21) along with orthogonality of Ψ_m in matching conditions (3.7)-(3.10), we have

$$U_{0n} + \sum_{m=0}^{\infty} R_m U_{mn} - \sum_{m=0}^{\infty} (m_p + if_p)(C_m + D_m e^{iq_{mx}b}) V_{mn} = 0, \quad (3.24)$$

$$ik_{0x}U_{0n} - \sum_{m=0}^{\infty} ik_{mx}R_m U_{mn} - \sum_{m=0}^{\infty} i\epsilon_p q_{mx}(C_m - D_m e^{iq_{mx}b})V_{mn} = 0, \tag{3.25}$$

$$\sum_{m=0}^{\infty}(A_m + B_m e^{-ik_{mx}(b-c)})U_{mn} - \sum_{m=0}^{\infty}(m_p + if_p)(C_m e^{iq_{mx}b} + D_m)V_{mn} = 0, \tag{3.26}$$

$$\sum_{m=0}^{\infty} ik_{mx}(A_m - B_m e^{-ik_{mx}(b-c)})U_{mn} - \sum_{m=0}^{\infty} i\epsilon_p q_{mx}(C_m e^{iq_{mx}b} - D_m)V_{mn} = 0, \tag{3.27}$$

$$\sum_{m=0}^{\infty}(A_m e^{ik_{mx}(c-b)} + B_m)U_{mn} - \sum_{m=-2}^{\infty}(E_m + \mathcal{H}_m e^{-i\alpha_{mx}(c-d)})W_{mn} = 0, \tag{3.28}$$

$$\sum_{m=0}^{\infty} ik_{mx}(A_m e^{ik_{mx}(c-b)} - B_m)U_{mn} - \sum_{m=-2}^{\infty} i\alpha_{mx}(E_m - \mathcal{H}_m e^{-i\alpha_{mx}(c-d)})W_{mn} = 0, \tag{3.29}$$

$$\sum_{m=-2}^{\infty}(E_m e^{i\alpha_{mx}(d-c)} + \mathcal{H}_m)W_{mn} - \sum_{m=0}^{\infty} T_m \cos k_{mx}(d-p)U_{mn} = 0, \tag{3.30}$$

$$\sum_{m=-2}^{\infty} i\alpha_{mx}(E_m e^{i\alpha_{mx}(d-c)} - \mathcal{H}_m)W_{mn} + \sum_{m=0}^{\infty} T_m k_{mx} \sin k_{mx}(d-p)U_{mn} = 0. \tag{3.31}$$

where

$$U_{mn} = \int_{-h}^{0} \Psi_m \Psi_n dy, \quad V_{mn} = \int_{-h}^{0} \mathcal{F}_m \Psi_n dy, \quad W_{mn} = \int_{-h}^{0} \mathcal{G}_m \Psi_n dy. \tag{3.32}$$

Further, from edge conditions (3.6), we have

$$\sum_{m=-2}^{\infty} \alpha_m(\alpha_{mx}^2 + \nu\mu^2)(E_m + \mathcal{H}_m e^{-i\alpha_{mx}(c-d)}) \tanh \alpha_m h = 0, \tag{3.33}$$

$$\sum_{m=-2}^{\infty} i\alpha_{mx}\alpha_m(\alpha_{mx}^2 + (2-\nu)\mu^2)(E_m - \mathcal{H}_m e^{-i\alpha_{mx}(c-d)}) \tanh \alpha_m h = 0, \tag{3.34}$$

$$\sum_{m=-2}^{\infty} \alpha_m(\alpha_{mx}^2 + \nu\mu^2)(E_m e^{i\alpha_{mx}(d-c)} + \mathcal{H}_m) \tanh \alpha_m h = 0, \tag{3.35}$$

$$\sum_{m=-2}^{\infty} i\alpha_{mx}\alpha_m(\alpha_{mx}^2 + (2-\nu)\mu^2)(E_m e^{i\alpha_{mx}(d-c)} - \mathcal{H}_m) \tanh \alpha_m h = 0. \tag{3.36}$$

In Equations (3.24)-(3.31) and (3.33)-(3.36) keeping up to $m = N$ (i.e. truncating the series after $N + 1$), we get $8N + 12$ equations with $8N + 12$ unknowns and the system is solved numerically by using the Gauss-Elimination method with the help of MATLAB. In this study, the plane wave solution is applied (as considered in Sharma et al. [117]), because for almost all the practical cases, the plane wave approximation is sufficient to describe the wave behaviour as described in Dalrymple et al. [11]. The efficiency of PS and EP to mitigate the wave impact on the sea wall can be studied through wave force (F_w) on the rigid wall, reflection coefficient ($|R_0|$) and dissipation coefficient (k_d) given by Equation (3.44).

Force on rigid wall: The wave force F_w on the rigid wall can be computed using the formula given by

$$F_w = \left| \frac{-i\omega}{gh^2} \int_{-h}^{0} \phi_5(p, y) dy \right|. \tag{3.37}$$

Water elevation in region 5: The water elevation in region 5 is computed by using the formula

$$\eta_5 = \frac{i}{\omega} \frac{\partial \phi_5}{\partial y} \bigg|_{y=0}. \tag{3.38}$$

3.4   Energy Balance Relation

In the present problem, apart from the reflection of waves, a major part of wave energy is dissipated by PS. Thus, for a better understanding of the quantitative behavior of wave reflection and dissipation, an energy identity is derived. The energy identity is derived using the Green's identity which is given by

$$\int_{\mathsf{C}} \left(\phi \frac{\partial \psi}{\partial n} - \psi \frac{\partial \phi}{\partial n} \right) ds = 0,$$

where ψ corresponds to complex conjugate of ϕ and $\frac{\partial}{\partial n}$ corresponds to the outward normal derivative to the boundary C. Consider $\mathsf{C} = \mathsf{C}_1 \cup \mathsf{C}_2 \cup \mathsf{C}_3$, where $\mathsf{C}_1 = \{x = -\mathcal{X}, -h \leq y \leq 0;$ $y = -h, -\mathcal{X} \leq x \leq 0; x = 0, -h \leq y \leq 0; y = 0, -\mathcal{X} \leq x \leq 0\}$, $\mathsf{C}_2 = \{x = 0, -h \leq y \leq 0;$ $y = -h, 0 \leq x \leq b; x = b, -h \leq y \leq 0; y = 0, 0 \leq x \leq b\}$ and $\mathsf{C}_3 = \{x = b, -h \leq y \leq 0;$ $y = -h, b \leq x \leq p; x = p, -h \leq y \leq 0; y = 0, d \leq x \leq p ; y = 0, c \leq x \leq d ;$ $y = 0, b \leq x \leq c \}$. The contribution from the bottom bed $y = -h, -\mathcal{X} \leq x \leq 0;$ $y = -h, 0 \leq x \leq b$ and $y = -h, b \leq x \leq p$ is zero. The contribution from the free surface $y = 0, -\mathcal{X} \leq x \leq 0; y = 0, b \leq x \leq c$ and $y = 0, d \leq x \leq p$ is zero. Due to EP condition and rigid wall condition the contributions from the lines $y = 0, c \leq x \leq d$ and $x = p, -h \leq y \leq 0$ are zero.

The line $x = 0, -h \leq y \leq 0$ contributes

$$\int_{\mathsf{C}} \left(\phi \frac{\partial \psi}{\partial n} - \psi \frac{\partial \phi}{\partial n} \right) ds = \left[\int_{-h}^{0} \left([\epsilon_p(m_p + if_P) - 1] \phi_2 \psi_{2x} - [\epsilon_p(m_p - if_p) - 1] \psi_2 \phi_{2x} \right) dy \right]_{x=0}. \tag{3.39}$$

The line $x = b, -h \leq y \leq 0$ contributes

$$\int_{\mathsf{C}} \left(\phi \frac{\partial \psi}{\partial n} - \psi \frac{\partial \phi}{\partial n} \right) ds = \left[\int_{-h}^{0} \left([\epsilon_p(m_p - if_p) - 1] \psi_2 \phi_{2x} - [\epsilon_p(m_p + if_p) - 1] \phi_2 \psi_{2x} \right) dy \right]_{x=b}. \tag{3.40}$$

The line $y = 0, 0 \leq x \leq b$ contributes

$$\int_{\mathsf{C}} \left(\phi \frac{\partial \psi}{\partial n} - \psi \frac{\partial \phi}{\partial n} \right) ds = \int_{0}^{b} -2iK f_p |\phi_2|^2 dx. \tag{3.41}$$

The contribution from the line $x = -\mathcal{X}, -h \leq y \leq 0$ is

$$\int_C \left(\phi \frac{\partial \psi}{\partial n} - \psi \frac{\partial \phi}{\partial n} \right) ds = (1 - |R_0|^2) \frac{ik_{0x}}{\cosh^2 k_0 h} \left(\frac{\sinh(2k_0 h) + 2k_0 h}{2k_0} \right). \tag{3.42}$$

Adding all the contributions from C_1, C_2 and C_3, the energy balance relation is

$$|R_0|^2 + k_d = 1 \tag{3.43}$$

where

$$k_d = \frac{2k_0 \cosh^2 k_0 h}{ik_{0x}(\sinh 2k_0 h + 2k_0 h)} \left[\int_{-h}^0 \left(\left[\epsilon_p(m_p + if_p) - 1 \right] \phi_2 \psi_{2x} - \left[\epsilon_p(m_p - if_p) - 1 \right] \psi_2 \phi_{2x} \right)_{x=0} dy \right.$$
$$\left. + \int_{-h}^0 \left(\left[\epsilon_p(m_p - if_p) - 1 \right] \psi_2 \phi_{2x} - \left[\epsilon_p(m_p + if_p) - 1 \right] \phi_2 \psi_{2x} \right)_{x=b} dy - \int_0^b \left(2iK f_p |\phi_2|^2 \right)_{y=0} dx \right]. \tag{3.44}$$

$k_0 h$	$|R_0|$	$1 - |R_0|^2$	k_d
0.2	0.8455	0.2851	0.2851
0.4	0.4846	0.7653	0.7652
0.6	0.5972	0.6439	0.6434
0.8	0.6857	0.5306	0.5309
1	0.6730	0.5481	0.5489

Table 3.1: Verification of energy identity.
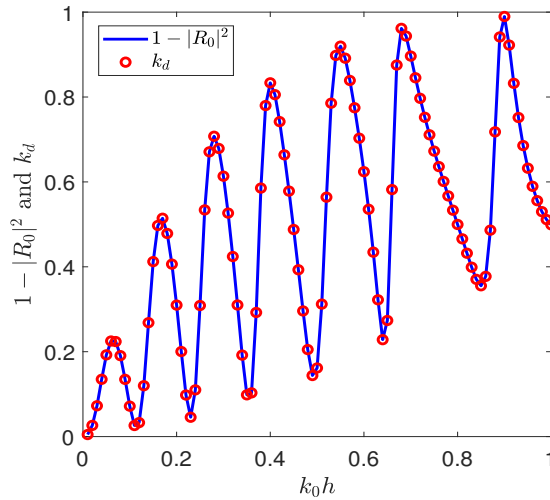
Figure 3.2: Verification of energy identity.

3.5   Results and Discussion

In this section, the efficiency of a thick PS to lessen the wave impact on the rigid wall in the presence of EP is investigated through graphs on wave force (F_w) experienced on rigid wall, reflection coefficient ($|R_0|$), dissipation coefficient (k_d) as defined in Equation (3.44) and free surface elevation (η_5). In the present study, the value of the parameter m_p is taken as 1 and the values of f_p range from 0 to 1, as considered in Dalrymple et al. [11]. Unless otherwise specified, the values of the non-dimensional parameters $k_0h = 1$, $b/h = 1$, $m_p = 1$, $f_p = 0.6$, $\epsilon_p = 0.5$, $\theta = 25^0$, $L_1/h = 8$, $D/h^4 = 50$, $\epsilon_e/h = 0.01$, $L_2/h = 10$ and $L_3/h = 12$ are fixed in this investigation.
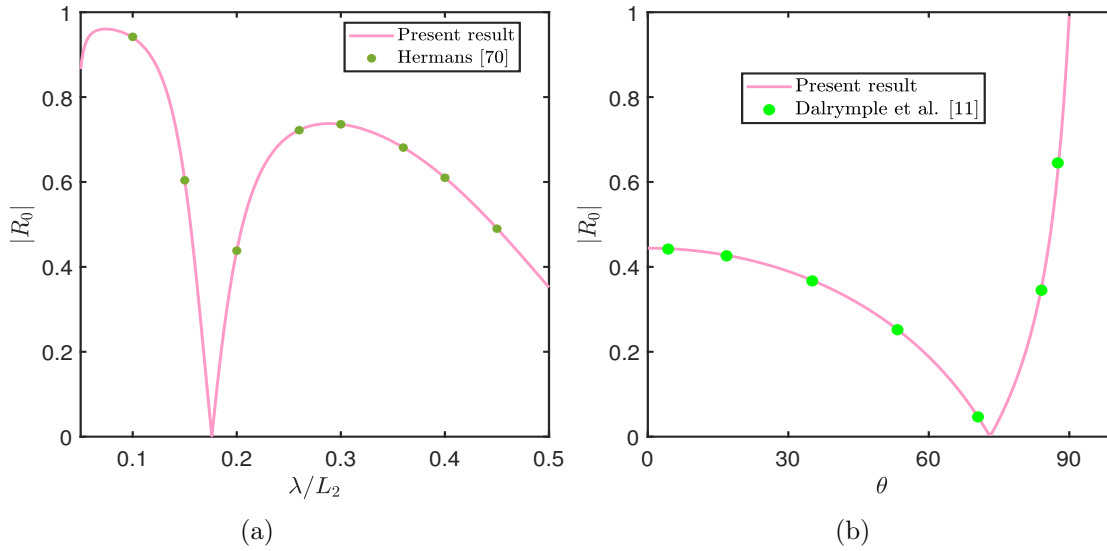
Figure 3.3: Validation of the present results.

3.5.1   Validation

To validate the present numerical results, the energy identity (3.43) involving reflection and dissipation coefficients is verified numerically. The values of k_d and $1 - |R_0|^2$ are tabulated for different values of k_0h in Table 3.1 and plotted in Figure 3.2 against k_0h. From the Table 3.1 and Figure 3.2, it is found that the values of k_d and $1 - |R_0|^2$ are well matched. Hence, the energy balance relation is satisfied, showing the accuracy of the present numerical computations. Further, the present problem reduces to the work of Hermans [70] in the absence of wall and PS and this particular case is illustrated in Figure 3.3a in which the results on $|R_0|$ are well matched with the results of Hermans [70]. In the absence of wall and EP, the present study reduces to scattering of water waves by the thick PS (Dalrymple et al. [11]) and this particular case is illustrated in Figure 3.3b in which the results of $|R_0|$ are well matched with the results of Dalrymple et al. [11].
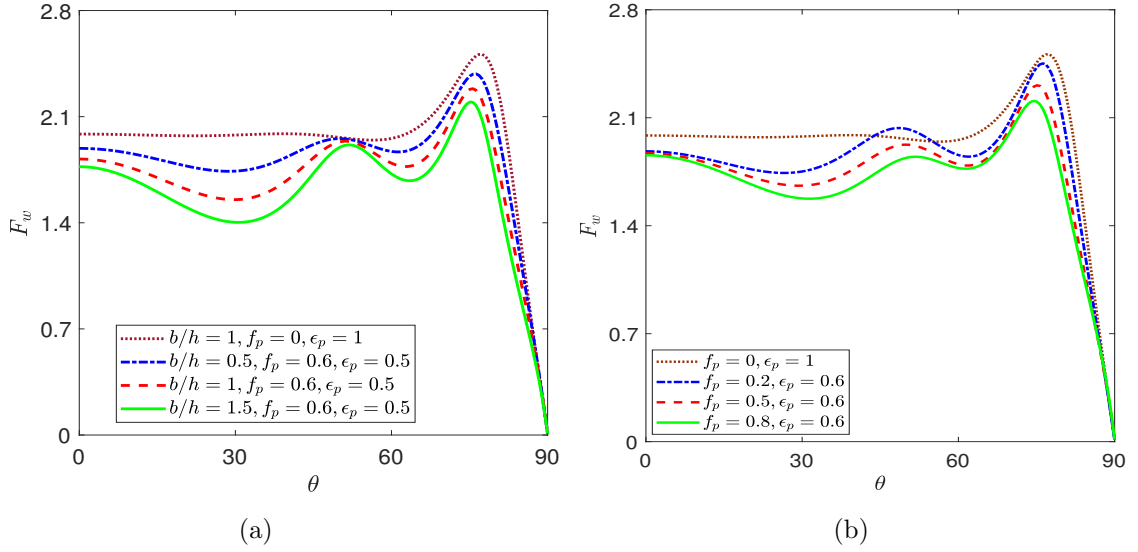
Figure 3.4: F_w vs θ for different values of **(a)** b/h ($k_0h = 0.2$) and **(b)** f_p ($k_0h = 0.2$).
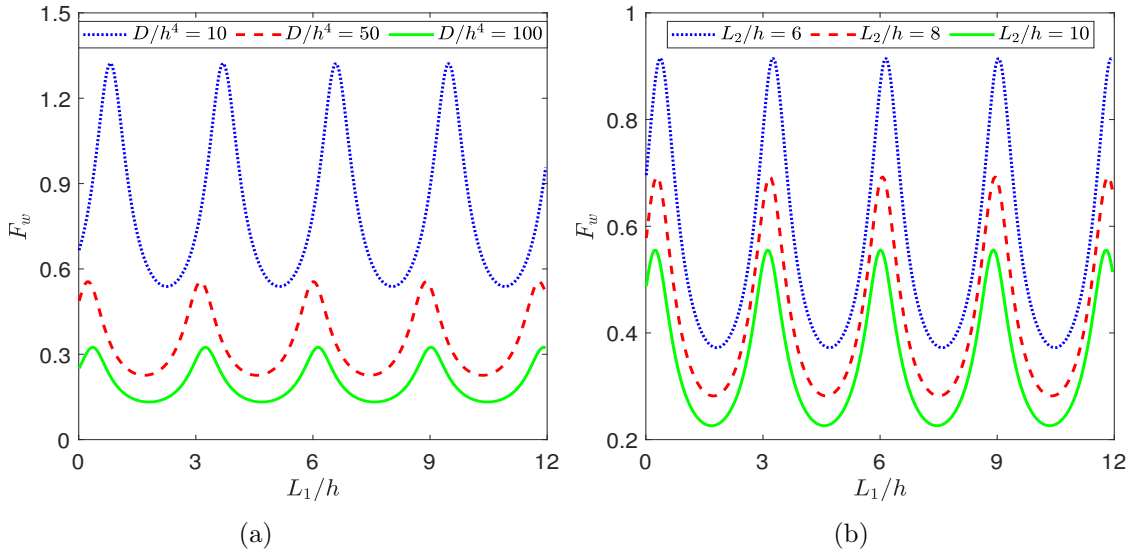
Figure 3.5: F_w vs L_1/h for different values of **(a)** D/h^4 ($k_0h = 1.2$) and **(b)** L_2/h ($k_0h = 1.2$).

3.5.2 Effect of Various Parameter on Force (F_w) Experienced on the Wall, Reflection Coefficient ($|R_0|$), Dissipation Coefficient (k_d) and Free Surface Elevation ($Re(\eta_5)$)

In Figure 3.4, the results of F_w versus angle of incident θ are plotted for different values of b/h and f_p. From the figure, it is observed that F_w exhibits an oscillatory trend for $0° < \theta < 80°$ then after that the oscillatory pattern vanishes and it drops down to zero for $\theta = 90°$ ($\theta = 80°$ is called as the critical angle here). Also, it is seen that the wave force on the sea wall reduces as b/h (or f_p) value increases. This is because, with the increase in b/h (or f_p), PS dissipated more wave energy, and less wave energy is transmitted towards the wall; hence, less wave force is experienced by the wall. It is also observed that in the

presence of PS, the force on the wall is less as compared to the case of absence of PS (i.e. $f_p = 0$ and $\epsilon_p = 1$).

The variations in force F_w versus the gap L_1/h between PS and EP for various values of flexural rigidity D/h^4 and length L_2/h of EP values are depicted in Figure 3.5. It is observed that force displays an oscillatory and periodic as a function of L_1/h. The occurrence of wave force optima is due to the wave trapping between PS and EP, which is important for creating calm zones in the marine environment. Figure 3.5a shows that the force exerted on the wall decreases as the flexural stiffness D/h^4 of EP increases, which is due to more reflection, less transmission of wave by EP and dissipation quality of PS. According to Figure 3.5b, the force experienced by the vertical wall reduces as EP's length L_2/h increases. A long EP enhances wave reflection, resulting in less force being experienced on the wall.
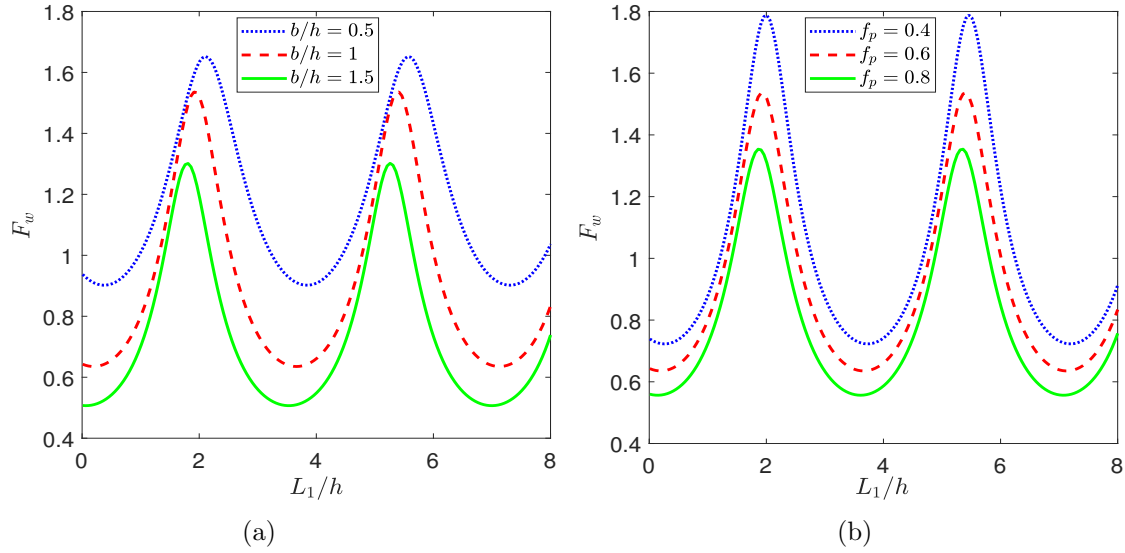
Figure 3.6: F_w vs L_1/h for different values of **(a)** b/h and **(b)** f_p.

Figure 3.6 shows the force F_w versus the gap L_1/h between PS and EP for different width b/h and frictional factor f_p values of PS. It is found that the force is oscillatory and periodic as a function of L_1/h. Figures 3.6a and 3.6b show that the force F_w on the wall decreases as b/h and f_p increase, which is similar to the behavior observed in Figures 3.4a and 3.4b. It is also noted that, F_w is shifted towards the left with an increase in b/h (or f_p). This may be due to the fact that PS with the higher value of b/h (or f_p) dissipates the incident energy more effectively, and also, a major portion of the incident energy is trapped between PS and EP.

The variations in the force F_w vs the gap L_3/h between EP and the wall for various D/h^4 and L_2/h values are shown in Figure 3.7. As a function of L_3/h, F_w is oscillatory and periodic in nature which is due to the trapping of wave in between EP and the wall. Figure 3.7a shows that as D/h^4 increases, the maxima attained by F_w decrease. In Figure 3.7b, it is found that as the length of EP increases, the maxima in F_w decreases. It is also noted that the amplitude in the force F_w curve reduces significantly for EP with

higher flexural rigidity D/h^4 (or length L_2/h). It is apprehended by the fact that with an increase in flexural rigidity D/h^4 (or length L_2/h) of EP, more incident wave is reflected back by EP and less wave is trapped between EP and wall, thereby exerting lesser force on the wall. Further, it is observed in Figure 3.7a that there is a shift towards the right in the force with an increase in D/h^4 and it is noted in Figure 3.7b that there is a shift towards left in the force curves with an increase in L_2/h. The reason for this behavior could be the constructive/destructive interference of incoming waves and reflected waves.

(a)

(b)
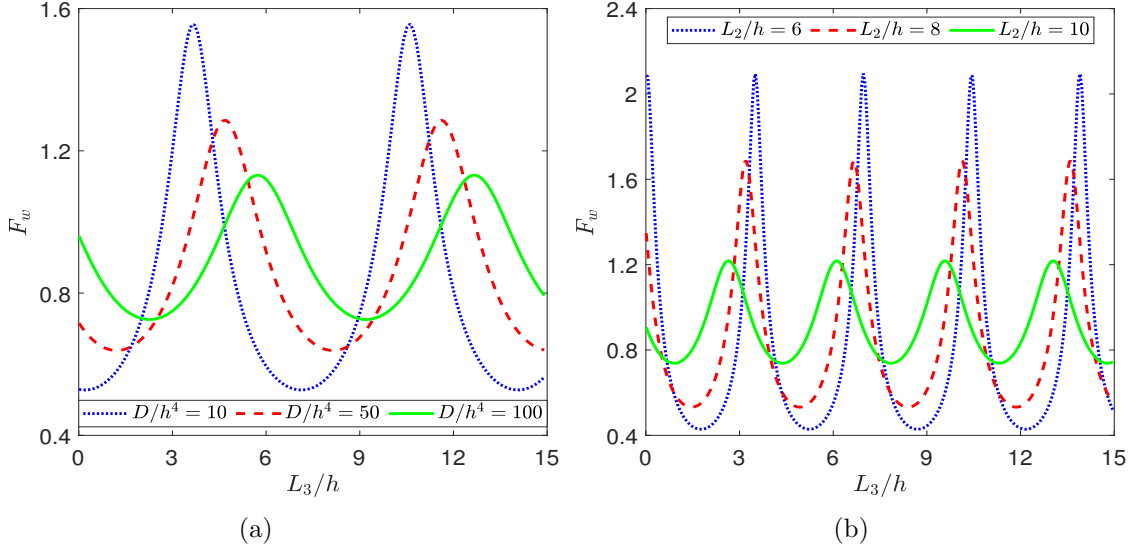
Figure 3.7: F_w vs L_3/h for different values of **(a)** D/h^4 ($b/h = 4$, $k_0h = 0.5$) and **(b)** L_2/h.

(a)

(b)
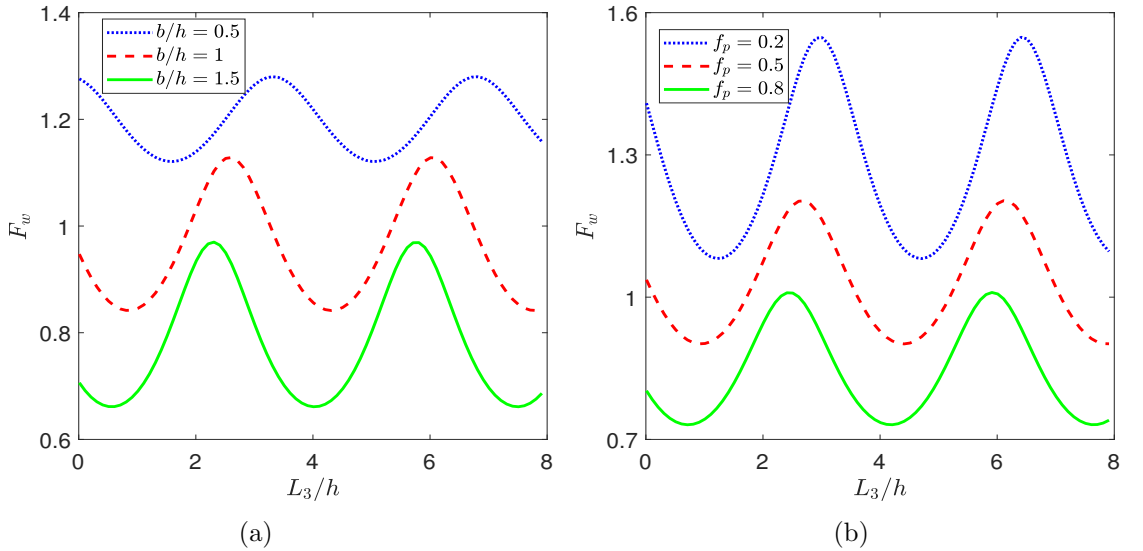
Figure 3.8: F_w vs L_3/h for **(a)** b/h=0.5, 1, 1.5 and **(b)** f_p=0.2, 0.5, 0.8.

The variations in the force F_w versus the gap L_3/h between EP and the wall for different width b/h and friction factor f_p values of PS are shown in Figure 3.8. It is depicted that F_w exhibits a periodic oscillatory pattern as a function of L_3/h. In both

Figures 3.8a and 3.8b, it is noted that, F_w decreases with an increase in b/h (or f_p), as in Figure 3.4. Moreover, with an increase in b/h (or f_p), F_w is shifted towards the left due to a part of energy being dissipated by PS and a part of it being trapped between the gaps between the structures involved in the system.

(a)   (b)
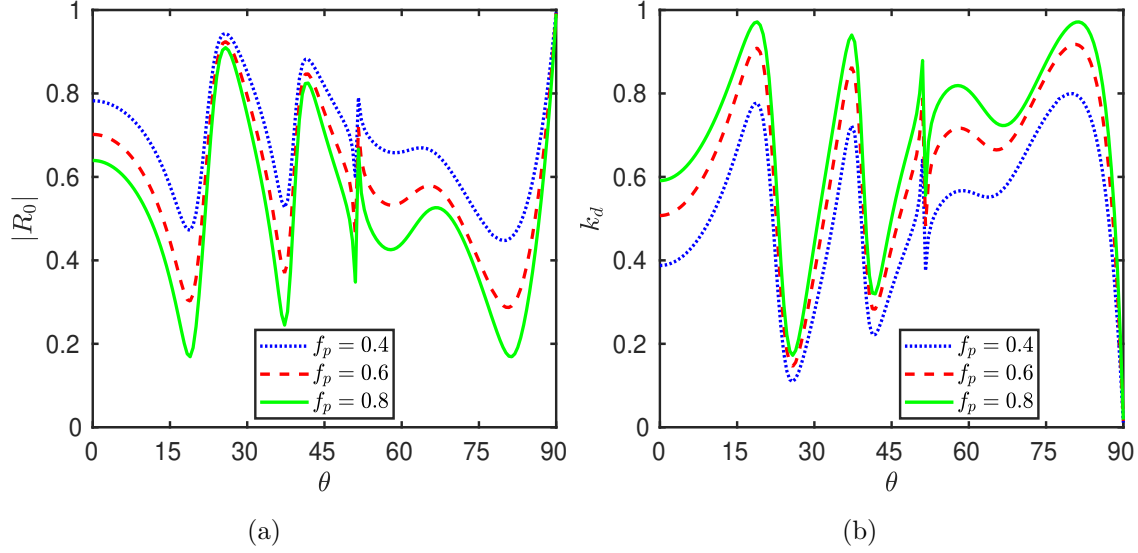
Figure 3.9: $|R_0|$ and k_d vs θ for $f_p = 0.4, 0.6, 0.8$ with $k_0 h = 0.5$.

(a)   (b)
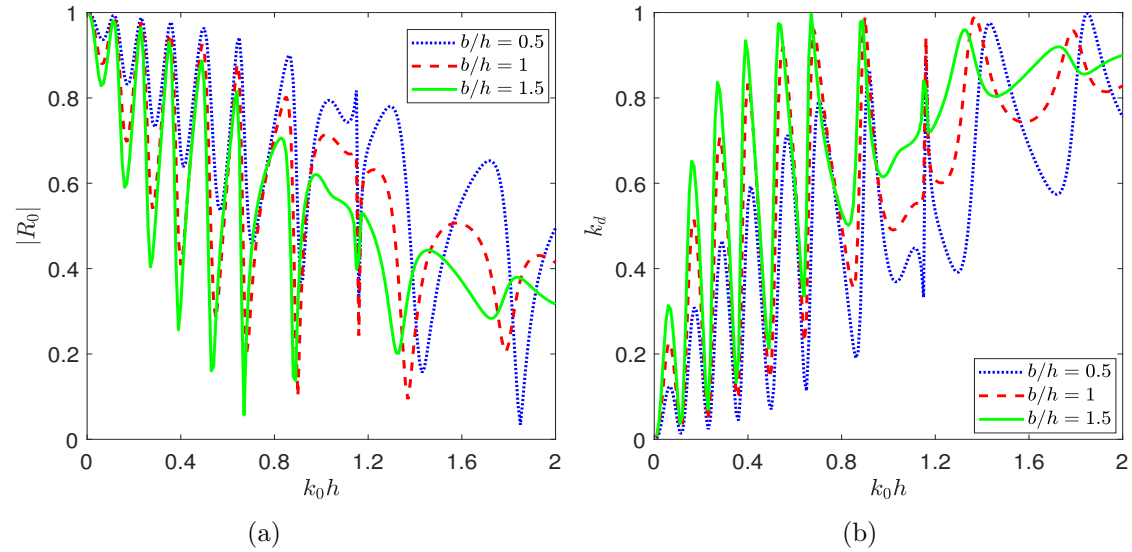
Figure 3.10: $|R_0|$ and k_d vs $k_0 h$ for $b/h = 0.5, 1, 1.5$.

In Figure 3.9, $|R_0|$ and k_d are plotted against angle of incident θ for various values of f_p. It is found that $|R_0|$ and k_d follow an oscillatory pattern with an increase in θ, except $\theta \sim 52°$, where $|R_0|$ and k_d curve is not smooth but when $\theta \sim 80°$, there is a sudden rise in $|R_0|$ and a sudden fall in k_d ($\theta = 80°$ is called as the critical angle, as noticed in Figure 3.4). At $\theta = 90°$, $|R_0|$ becomes unity and k_d becomes zero. It is also noted that $|R_0|$ decreases and k_d increases with an increase in f_p. This is due to the fact that with the increase in f_p, more incident wave energy is dissipated by PS and PS reflects less wave

energy. As with the increase in f_p, more waves are dissipated by PS; fewer waves will transmit through PS towards the wall; hence the wave force experienced by the wall will be less, which is similar to the observation noticed in Figure 3.4b.

Figure 3.10 shows the fluctuations in reflection coefficient $|R_0|$ and dissipation coefficient k_d versus wavenumber $k_0 h$ for various values of width b/h of PS. From Figure 3.10a, it is noted that when $k_0 h$ varies from 0 to 1.1, $|R_0|$ decreases in an oscillatory pattern with sharp oscillations and the minima in the reflection coefficient is also decreasing. When $k_0 h$ is small, the wavelength is large, so the distribution of the energy is more along the water depth. Thus, the mutual interactions of the incoming and the outgoing waves between the wall, EP and PS are influencing the oscillatory behaviour of the reflected wave as observed in the plot. But when $k_0 h \sim 1.1$, the curve is not smooth. Further, with an increase in $k_0 h$, the minima in $|R_0|$ are increasing, and the oscillations become small. Figure 3.10b shows that with the increase in $k_0 h$ $(0 < k_0 h < 1.1)$, k_d increases in an oscillatory pattern with sharp peaks. It is noted that the maxima in k_d increases as $k_0 h$ increases. But when $k_0 h \sim 1.1$, the curve is not smooth, similar to the observation made in Figure 3.10a. As $k_0 h$ further increases, k_d decreases with a decrease in oscillations as well. However, with an increase in b/h, more wave energy is dissipated, and less wave energy is reflected.
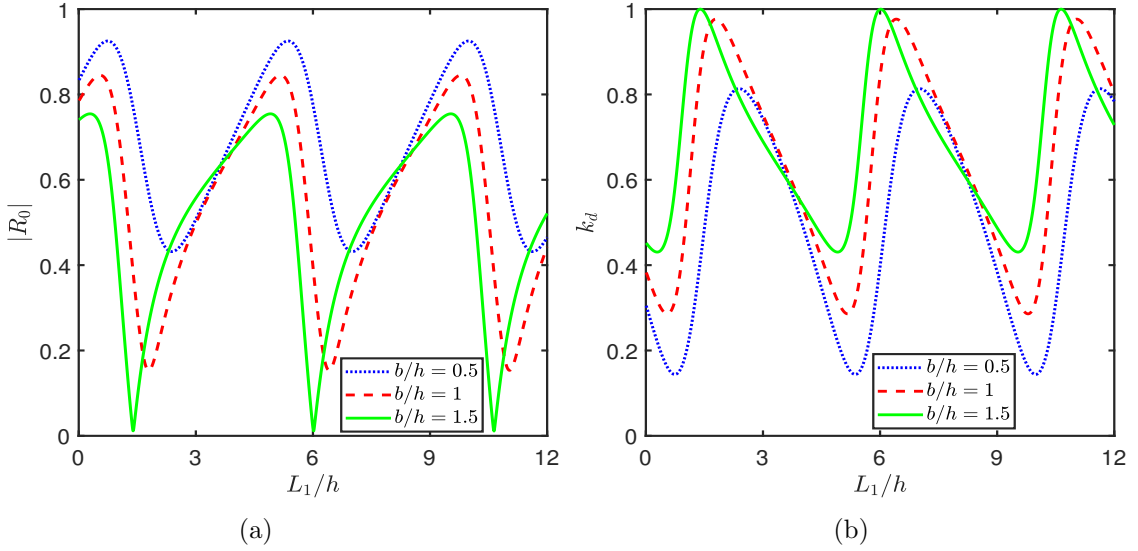
Figure 3.11: $|R_0|$ and k_d vs L_1/h for $b/h = 0.5, 1, 1.5$ with $k_0 h = 0.75$.

Reflection coefficient $|R_0|$ and dissipation coefficient k_d are depicted graphically against length L_1/h of EP for various values of width b/h of PS in Figure 3.11. From the figure, it is found that with an increase in b/h, the wave reflection $|R_0|$ decreases, and energy dissipation k_d increases. This is due to the fact that as the width of PS increases, more wave energy is dissipated by PS, and fewer waves are reflected back. Also, it is found that with an increase in b/h, reflection coefficient $|R_0|$ and dissipation coefficient k_d are shifted towards the left, which is similar to the behavior of Force F_w on the wall found in Figure 3.6a. Furthermore, for higher value of b/h (i.e. for b/h=1.5), energy

dissipation by PS becomes nearly 100% and the wave reflection becomes nearly zero when
$L_1/h = (1.4 + n \times 4.6), n = 0, 1, 2, \ldots$.

(a)

(b)
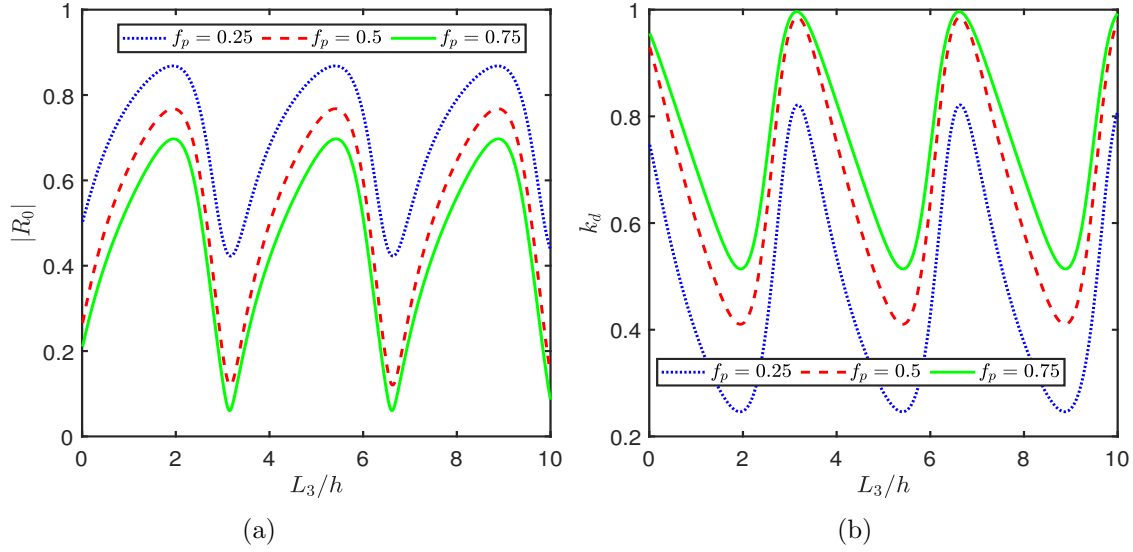
Figure 3.12: $|R_0|$ and k_d vs L_3/h for $f_p = 0.25, 0.5, 0.75$.

(a)

(b)
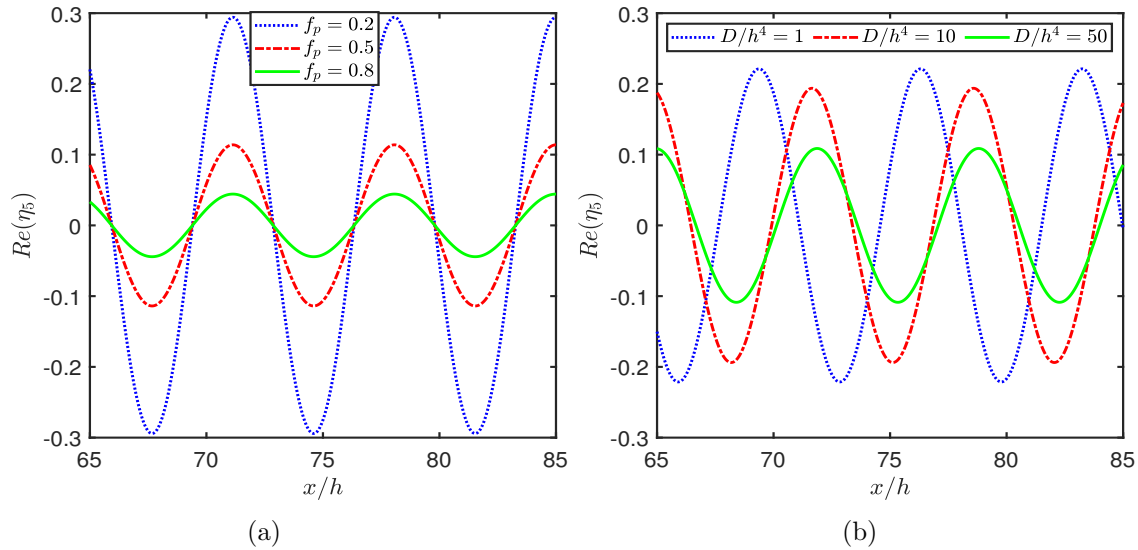
Figure 3.13: $Re(\eta_5)$ for **(a)** $f_p = 0.2$, 0.5 and 0.8 and **(b)** $D/h^4 = 1$, 10 and 50 with
$b/h = 5$, $L_2/h = 30$, $L_1/h = 30$ and $L_3/h = 20$.

The effect of the gap L_3/h between EP and the wall on reflection coefficient $|R_0|$ and
dissipation coefficient k_d for different values of width f_p of PS is plotted on Figure 3.12.
From the figure, it is noted that the wave reflection decreases and energy dissipation k_d
increases, with an increase in f_p. Also, from both Figures 3.12a and 3.12b, it is found that
with an increase in f_p, the curves are slightly shifted towards the left, which is similar
to the behavior of Force F_w on the wall found in Figure 3.6b. It is also found that for a
higher value of f_p (i.e. f_p=0.5 and 0.75), the maxima value of k_d is nearly 1.

Figure 3.13 shows the behavior of free surface elevation η_5 in region 5 for different

values of f_p and D/h^4. From the Figure 3.13a it is observed that with an increase in f_p, the amplitude of free surface elevation η_5 decreases. This is due to the fact that with an increase in f_p, more waves are dissipated by PS, and fewer waves are transmitted towards the wall. Hence, less force is exerted on the wall. Figure 3.13b depicted that with an increase in D/h^4, the amplitude of free surface elevation η_5 decreases. This is due to the fact that with an increase in D/h^4, EP becomes more rigid and more waves are reflected back by EP and fewer waves are transmitted towards the wall. Hence, the wall experiences less force. Thus, PS with a higher f_p value and EP width with a higher D/h^4 value are helpful in creating a tranquility zone for safe navigation.

3.6   Conclusion

In order to safeguard the sea wall, the scattering of oblique water waves by EP placed next to a rigid wall in the presence of PS is investigated in this work. The study uses the governing equation and the boundary conditions to coin a system of equations that can be solved numerically. Plotting the findings for force on the wall, reflection coefficient, dissipation coefficient, and free surface elevation provides a description of the wave motion past the structures. The study shows that the gap between the structures plays a vital role in protecting the sea wall from wave load. It is also found that in the presence of a higher value of length and flexural rigidity of EP, the force acting on the wall is low. In relation to the gaps between PS and EP, and EP and the wall, it is noticed that the force on the wall, the reflection and dissipation coefficients oscillate and follow periodic patterns. From the qualitative behavior of forces acting on the sea wall, the force on the wall shifted to the left due to the effect of the width and frictional factor of PS. Furthermore, for a higher value of the width of PS (i.e., for $b/h=1.5$), energy dissipation by PS becomes nearly 100%, and the wave reflection becomes nearly zero when the gap between PS and EP $L_1/h = (1.4 + n \times 4.6), n = 0, 1, 2, \ldots$. It is also noticed that the free surface elevation between EP and the wall, which aids in the creation of a calm zone, is significantly influenced by the structural characteristics of PS and EP. This study can be very useful in order to build floating structures that can withstand rough wave situations and lessen the impact of waves close to the shore.

Chapter 4

Mitigation of Structural Response on an Elastic Plate by a Truncated Porous Structure

4.1 Introduction

In Chapters 2 and 3, the effectiveness of PS, which extends from top to bottom, in reducing wave response on EP and the sea wall was analyzed. However, in some situations, a full-height porous structure is not practical due to high costs, material requirements, and environmental considerations. As a result, truncated porous structures, such as bottom-standing porous structures (BSPS) and surface-piercing porous structures (SPPS), are often preferred. Therefore, in this chapter, we focus on examining the effectiveness of BSPS and SPPS in reducing the structural response of EP. With the aid of the eigenfunction expansion method, the associated boundary value problem is reduced to a system of linear algebraic equations, which is solved numerically. For both configurations, the effects of various system parameters, such as wavenumber and angle of incidence, are analyzed. The energy balance relation for the given problem is derived to verify the accuracy of the computational results. The study aims to determine the optimal distance between the porous structure and the EP to achieve maximum wave dissipation, thereby reducing the structural response on the EP. The impacts of structural parameters, such as the length, width, porosity, and frictional coefficient of the porous structure, are investigated through graphs of the reflection coefficient, transmission coefficient, dissipation coefficient, free surface elevation, elastic plate deflection, shear force, and strain. A major part of the work presented in this chapter has been published in Sahoo et al. [118].

4.2 Mathematical Formulation

In the contemporary study, scattering of oblique surface gravity wave by EP in the presence of truncated thick porous structures is inspected in the Cartesian coordinate, where y-axis is positive vertically upward, and xz-plane represents the undisturbed free surface of water. The fluid domain is $-\infty < x < \infty, -\infty < z < \infty, -h \leq y \leq 0$, other than EP as shown in Figure 4.1. In this study, the two configurations of homogeneous and isotropic porous

structure, namely, BSPS and partially immersed SPPS, are considered. The notation L_b, L_g, and L_w represent the length of the porous structure, gap, and submerged interface of the structure, respectively. For BSPS $L_b = (0 \le x \le b, -h \le y \le -h + a)$; $L_g = (0 \le x \le b, -h + a \le y \le 0)$ and $L_w = (0 \le x \le b, y = -h + a)$ and for SPPS $L_b = (0 \le x \le b, -a \le y \le 0)$; $L_g = (0 \le x \le b, -h \le y \le -a)$ and $L_w = (0 \le x \le b, y = -a)$, both the structures are assumed to be infinitely long along z-axis and a is the length and b is the width of the porous structure. The porous structure is placed at a L_1 distance from EP in both cases. The position of EP is $c \le x \le d$, $y = 0$, so that the length of EP becomes $L_2 = d - c$. By assuming that the incident wave is propagating along the x-axis with an angel θ, the fluid is incompressible and the flow is irrotational, inviscid and simple harmonic in time with angular frequency ω, the dependence of the potential function in z-direction is chosen to be harmonic throughout, then in each region j there exists the velocity potential of the form $\Phi_j(x, y, z, t) = Re\{\phi_j(x, y)e^{i(\mu z - \omega t)}\}$, satisfying

$$\left(\frac{\partial^2}{\partial x^2} + \frac{\partial^2}{\partial y^2} - \mu^2 \right) \phi_j = 0, \quad \text{in the region } j, \tag{4.1}$$

where $\mu = k_0 \sin \theta$, k_0 is the wavenumber of the incident wave.

The no-flow condition on the rigid bottom is expressed by

$$\frac{\partial \phi_j}{\partial y} = 0, \quad \text{on} \quad y = -h \quad \text{for } j = 1, 3, 4, 5, 6. \tag{4.2}$$

The free-surface condition on the mean free surface is expressed by

$$\frac{\partial \phi_j}{\partial y} - K\phi_j = 0 \quad \text{on} \quad y = 0, \tag{4.3}$$

where $j = 1, 2, 4, 6$ for BSPS and $j = 1, 4, 6$ for SPPS.

For SPPS, the free surface condition in the region 2

$$\frac{\partial \phi_2}{\partial y} - K(m_p + if_p)\phi_2 = 0 \quad \text{on} \quad y = 0, \tag{4.4}$$

with $K = \omega^2/g$, g is the acceleration due to gravity, m_p and f_p are the non-dimensionalized inertial coefficient and frictional coefficient respectively.

The boundary condition on the floating EP is expressed by

$$\left[D \left(\frac{\partial^2}{\partial x^2} - \mu^2 \right)^2 + 1 - \epsilon_e K \right] \phi_{5y} - K\phi_5 = 0 \quad \text{on} \quad y = 0, \tag{4.5}$$

where $D = EI/\rho g$ is the flexural rigidity of EP, with E being the young's modulus, $I = h_0^3/12(1 - \nu^2)$, ν is the Poisson's ratio, ρ is density of the fluid, h_0 is thickness of EP assumed to be small, $\epsilon_e = \rho_s h_0/\rho$ and ρ_s is density of EP.

By assuming that EP is freely floating on the surface of water, the vanishing of bending

moment and shear force at the edges of the EP yield

$$\left(\frac{\partial^2}{\partial x^2} - \nu\mu^2\right)\frac{\partial\phi_5}{\partial y} = 0 \quad \text{and} \quad \frac{\partial}{\partial x}\left(\frac{\partial^2}{\partial x^2} - (2-\nu)\mu^2\right)\frac{\partial\phi_5}{\partial y} = 0 \quad \text{at } (c,0),(d,0). \quad (4.6)$$
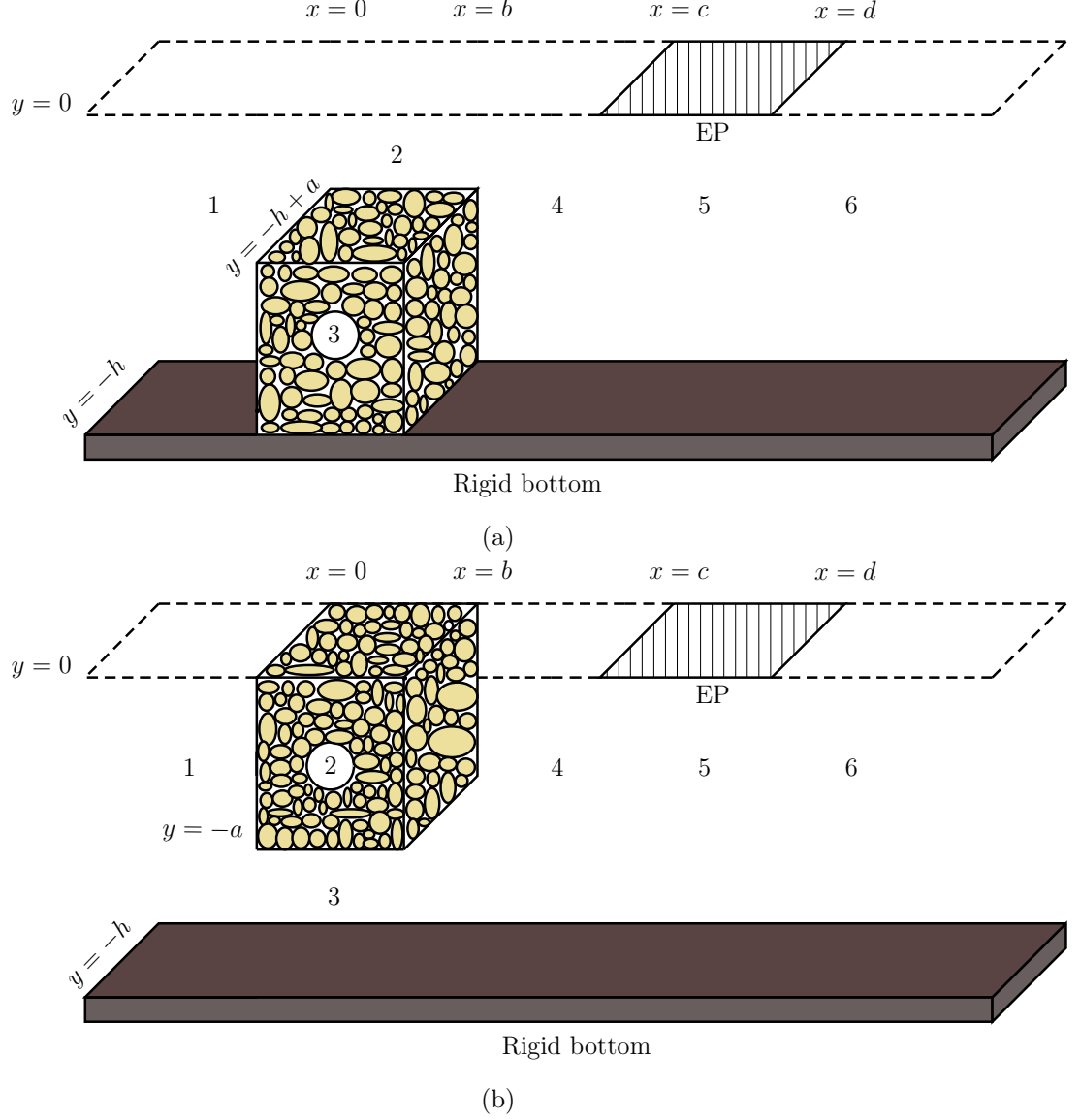
Figure 4.1: Schematic representation of the physical problem (a) BSPS with EP and (b) SPPS with EP.

The boundary conditions on L_w are expressed by

for BSPS: $\quad \phi_2 = (m_p + if_p)\phi_3, \quad \dfrac{\partial\phi_2}{\partial y} = \epsilon_p\dfrac{\partial\phi_3}{\partial y} \quad \text{on} \quad y = -h+a, \quad 0 < x < b, \quad (4.7)$

for SPPS: $\quad \phi_3 = (m_p + if_p)\phi_2, \quad \dfrac{\partial\phi_3}{\partial y} = \epsilon_p\dfrac{\partial\phi_2}{\partial y} \quad \text{on} \quad y = -a, \quad 0 < x < b, \quad (4.8)$

where ϵ_p is a non-dimensionalized quantity denoting the porosity of the porous structure. The conditions of continuity of pressure and velocity along the interfaces between the

regions for BSPS and SPPS are respectively given by

$$\phi_j = \begin{cases} \phi_2 & y \in L_g \\ (m_p + if_p)\phi_3 & y \in L_b \end{cases} \quad \text{and} \quad \frac{\partial \phi_j}{\partial x} = \begin{cases} \frac{\partial \phi_2}{\partial x} & y \in L_g \\ \epsilon_p \frac{\partial \phi_3}{\partial x} & y \in L_b, \end{cases} \tag{4.9}$$

$$\phi_j = \begin{cases} \phi_3 & y \in L_g \\ (m_p + if_p)\phi_2 & y \in L_b \end{cases} \quad \text{and} \quad \frac{\partial \phi_j}{\partial x} = \begin{cases} \frac{\partial \phi_3}{\partial x} & y \in L_g \\ \epsilon_p \frac{\partial \phi_2}{\partial x} & y \in L_b, \end{cases} \tag{4.10}$$

where $j = 1$ on $x = 0$ and $j = 4$ on $x = b$.

The conditions of continuity of velocity and pressure along the interfaces ($x = c, x = d$) of EP region are expressed as

$$\phi_4 = \phi_5, \quad \frac{\partial \phi_4}{\partial x} = \frac{\partial \phi_5}{\partial x} \quad \text{on} \quad x = c, \quad 0 < y < h, \tag{4.11}$$

$$\phi_5 = \phi_6, \quad \frac{\partial \phi_5}{\partial x} = \frac{\partial \phi_6}{\partial x} \quad \text{on} \quad x = d, \quad 0 < y < h. \tag{4.12}$$

The far-field condition is given by

$$\phi_1(x, y) \simeq \left(\frac{ig}{\omega}\right) \frac{\cosh k_0(h + y)}{\cosh k_0 h} \{e^{ik_{0x}x} + R_0 e^{-ik_{0x}x}\} \quad \text{as} \quad x \to -\infty, \tag{4.13}$$

$$\phi_6(x, y) \simeq \left(\frac{ig}{\omega}\right) T_0 \frac{\cosh k_0(h + y)}{\cosh k_0 h} e^{ik_{0x}(x-d)} \quad \text{as} \quad x \to \infty, \tag{4.14}$$

R_0, and T_0 denote the unknown constants associated with reflected and transmitted waves, respectively to be determined here, where $k_{0x} = \sqrt{k_0^2 - \mu^2}$, k_0 is the wavenumber of the incident wave, and it is the positive real root for $n = 0$ of the transcendental equation in k_n as given by

$$K - k_n \tanh k_n h = 0. \tag{4.15}$$

In this problem, the 1/3 singularity (Mandal and Chakrabarti [119]) at the tip of BSPS/SPPS is not considered. This is because the primary interactions occur along the length of the barrier, and the effects of the tip singularity are minimal compared to the overall scattering process. In the next section, the present problem will be solved by utilizing the method of eigenfunction expansion which was used in the work of Sollitt and Cross [5], Dalrymple et al. [11], Losada et al. [18], and Koley et al. [19], where the singularity at the tip of a thick barrier was not taken.

4.3   Method of Solution

For finding the solution of the above boundary value problem, the method of separation of variable is applied in each region and the spatial potential functions are expressed as series solutions in terms of eigenfunctions. The spatial velocity potentials in the open water regions 1, 4 and 6 satisfying Equations (4.1), (4.2), (4.3), (4.13) and (4.14) are

expressed in the forms

$$\phi_1 = \left(\frac{ig}{\omega}\right)\left[e^{ik_{0x}x}\psi_0 + \sum_{n=0}^{\infty} R_n e^{-ik_{nx}x}\psi_n\right] \quad \text{for} \quad -\infty < x \le 0, \ -h \le y \le 0, \quad (4.16)$$

$$\phi_4 = \left(\frac{ig}{\omega}\right)\sum_{n=0}^{\infty}\left[B_n e^{ik_{nx}(x-b)} + C_n e^{-ik_{nx}(x-c)}\right]\psi_n \quad \text{for} \quad b \le x \le c, -h \le y \le 0, \quad (4.17)$$

$$\phi_6 = \left(\frac{ig}{\omega}\right)\sum_{n=0}^{\infty} T_n e^{ik_{nx}(x-d)}\psi_n \quad \text{for} \quad d \le x < \infty, -h \le y \le 0, \quad (4.18)$$

where

$$\psi_n = \frac{\cosh k_n(h+y)}{\cosh k_n h} \quad n = 0, 1, 2\dots. \quad (4.19)$$

R_n, B_n, C_n and T_n are unknown constants, $k_{nx} = \sqrt{k_n^2 - \mu^2}$ with k_0 is the positive real root for $n = 0$ and k_n for $n = 1, 2, 3, \dots$ are purely imaginary roots of the dispersion relation (4.15).

Again, the spatial velocity potentials in the regions 2 and 3 for BSPS satisfying Equations (4.1), (4.2), (4.3) and (4.7) are expressed in the forms

$$\phi_2 = \left(\frac{ig}{\omega}\right)\sum_{n=0}^{\infty}\left[G_n e^{ip_{nx}x} + H_n e^{-ip_{nx}(x-b)}\right]M_n \quad \text{for } 0 \le x \le b, \ -h+a \le y \le 0, \quad (4.20)$$

$$\phi_3 = \left(\frac{ig}{\omega}\right)\sum_{n=0}^{\infty}\left[G_n e^{ip_{nx}x} + H_n e^{-ip_{nx}(x-b)}\right]P_n \quad \text{for } 0 \le x \le b, \ -h \le y \le -h+a, \quad (4.21)$$

whereas for SPPS the spatial velocity potentials satisfying Equations (4.1), (4.2), (4.4) and (4.8) are expressed in the forms

$$\phi_2 = \left(\frac{ig}{\omega}\right)\sum_{n=0}^{\infty}\left[G_n e^{ip_{nx}x} + H_n e^{-ip_{nx}(x-b)}\right]M_n \quad \text{for} \quad 0 \le x \le b, \ -a \le y \le 0, \quad (4.22)$$

$$\phi_3 = \left(\frac{ig}{\omega}\right)\sum_{n=0}^{\infty}\left[G_n e^{ip_{nx}x} + H_n e^{-ip_{nx}(x-b)}\right]Q_n \quad \text{for} \quad 0 \le x \le b, \ -h \le y \le -a, \quad (4.23)$$

where

$$M_n = \frac{\cosh p_n(h+y) - F_n \sinh p_n(h+y)}{\cosh p_n h - F_n \sinh p_n h} \quad n = 0, 1, 2\dots, \quad (4.24)$$

$$P_n = \frac{(1 - F_n \tanh p_n a) \cosh p_n(h+y)}{(m_p + if_p)(\cosh p_n h - F_n \sinh p_n h)} \quad n = 0, 1, 2\dots, \quad (4.25)$$

$$Q_n = \frac{(m_p + if_p)[1 - F_n \tanh p_n(h-a)] \cosh p_n(h+y)}{(\cosh p_n h - F_n \sinh p_n h)} \quad n = 0, 1, 2\dots, \quad (4.26)$$

$$F_n = \begin{cases} \frac{(1-G)\tanh p_n a}{1 - G\tanh^2 p_n a} & \text{for BSPS} \\ \frac{(1-G)\tanh p_n(h-a)}{\tanh^2 p_n(h-a) - G} & \text{for SPPS} \end{cases}, \quad G = \frac{\epsilon_p}{m_p + if_p} \quad (4.27)$$

G_n and H_n are unknown constants, $p_{nx} = \sqrt{p_n^2 - \mu^2}$ and p_n, $n = 0, 1, 2\dots$ are the

complex roots of the dispersion relation

for BSPS: $\quad K - p_n \tanh p_n h - F_n(K \tanh p_n h - p_n) = 0,$ $\qquad$ (4.28)

for SPPS: $\quad K(m_p + i f_p) - p_n \tanh p_n h - F_n[K(m_p + i f_p) \tanh p_n h - p_n] = 0.$ $\quad$ (4.29)

Finally, the spatial velocity potential in EP region 5 satisfying Equations (4.1), (4.2) and (4.5) is expressed in the form

$$\phi_5 = \left(\frac{ig}{\omega}\right) \sum_{n=-2}^{\infty} \left[D_n e^{i\alpha_{nx}(x-c)} + E_n e^{-i\alpha_{nx}(x-d)}\right] \mathcal{G}_n \quad \text{for} \quad c \le x \le d, \ -h \le y \le 0 \ (4.30)$$

where

$$\mathcal{G}_n = \frac{\cosh \alpha_n(h+y)}{\cosh \alpha_n h} \quad n = 0, 1, 2 \ldots, \tag{4.31}$$

D_n and E_n are unknown constants, $\alpha_{nx} = \sqrt{\alpha_n^2 - \mu^2}$ and as in α_n are the complex roots of the form $\pm a + ib$ for $n = -2, -1$, positive real root for $n = 0$ and purely imaginary roots for $n = 1, 2, 3, \ldots$ of the equation

$$(D\alpha_n^4 + 1 - \epsilon_e K)\alpha_n \tanh \alpha_n h = K. \tag{4.32}$$

For BSPS, utilizing Equations (4.16)-(4.18), (4.20), (4.21) and (4.30) along with orthogonality of ψ_n in matching conditions (4.9)-(4.12), we have

$$X_{0m} + \sum_{n=0}^{\infty} R_n X_{nm} - \sum_{n=0}^{\infty} [Y_{nm} + (m_p + i f_p)Z_{nm}](G_n + H_n e^{i p_{nx} b}) = 0, \tag{4.33}$$

$$ik_{0x}X_{om} - \sum_{n=0}^{\infty} ik_{nx}R_n X_{nm} - \sum_{n=0}^{\infty} i p_{nx}[Y_{nm} + \epsilon_p Z_{nm}](G_n - H_n e^{i p_{nx} b}) = 0, \tag{4.34}$$

$$\sum_{n=0}^{\infty} (B_n + C_n e^{-ik_{nx}(b-c)})X_{nm} - \sum_{n=0}^{\infty} [Y_{nm} + (m_p + i f_p)Z_{nm}](G_n e^{i p_{nx} b} + H_n) = 0, \tag{4.35}$$

$$\sum_{n=0}^{\infty} ik_{nx}(B_n - C_n e^{-ik_{nx}(b-c)})X_{nm} - \sum_{n=0}^{\infty} i p_{nx}[Y_{nm} + \epsilon_p Z_{nm}](G_n e^{i p_{nx} b} - H_n) = 0, \tag{4.36}$$

$$\sum_{n=0}^{\infty} (B_n e^{ik_{nx}(c-b)} + C_n)X_{nm} - \sum_{n=-2}^{\infty} (D_n + E_n e^{-i\alpha_{nx}(c-d)})W_{nm} = 0, \tag{4.37}$$

$$\sum_{n=0}^{\infty} ik_{nx}(B_n e^{ik_{nx}(c-b)} - C_n)X_{nm} - \sum_{n=-2}^{\infty} i\alpha_{nx}(D_n - E_n e^{-i\alpha_{nx}(c-d)})W_{nm} = 0, \tag{4.38}$$

$$\sum_{n=-2}^{\infty} (D_n e^{i\alpha_{nx}(d-c)} + E_n)W_{nm} - \sum_{n=0}^{\infty} T_n X_{nm} = 0, \tag{4.39}$$

$$\sum_{n=-2}^{\infty} i\alpha_{nx}(D_n e^{i\alpha_{nx}(d-c)} - E_n)W_{nm} - \sum_{n=0}^{\infty} ik_{nx}T_n X_{nm} = 0. \tag{4.40}$$

For SPPS, among Equations (4.33) and (4.40), the Equations (4.33)-(4.36) will be replaced by the following equations

$$X_{0m} + \sum_{n=0}^{\infty} R_n X_{nm} - \sum_{n=0}^{\infty} [V_{nm} + (m_p + if_p)U_{nm}](G_n + H_n e^{ip_{nx}b}) = 0, \qquad (4.41)$$

$$ik_{0x}X_{om} - \sum_{n=0}^{\infty} ik_{nx}R_n X_{nm} - \sum_{n=0}^{\infty} ip_{nx}[V_{nm} + \epsilon_p U_{nm}](G_n - H_n e^{ip_{nx}b}) = 0, \qquad (4.42)$$

$$\sum_{n=0}^{\infty} (B_n + C_n e^{-ik_{nx}(b-c)})X_{nm} - \sum_{n=0}^{\infty} [V_{nm} + (m_p + if_p)U_{nm}](G_n e^{ip_{nx}b} + H_n) = 0, \quad (4.43)$$

$$\sum_{n=0}^{\infty} ik_{nx}(B_n - C_n e^{-ik_{nx}(b-c)})X_{nm} - \sum_{n=0}^{\infty} ip_{nx}[V_{nm} + \epsilon_p U_{nm}](G_n e^{ip_{nx}b} - H_n) = 0, \quad (4.44)$$

where

$$
\begin{aligned}
X_{nm} &= \int_{-h}^{0} \psi_n \psi_m dy, \quad Y_{nm} = \int_{-h+a}^{0} M_n \psi_m dy, \quad Z_{nm} = \int_{-h}^{-h+a} P_n \psi_m dy, \\
W_{nm} &= \int_{-h}^{0} \mathcal{G}_n \psi_m dy, \quad V_{nm} = \int_{-a}^{0} Q_n \psi_m dy \quad \text{and} \quad U_{nm} = \int_{-h}^{-a} M_n \psi_m dy.
\end{aligned}
\qquad (4.45)
$$

Further, substituting Equation (4.30) in the free edge conditions given by Equation (4.6), we have

$$\sum_{n=-2}^{\infty} \alpha_n (\alpha_{nx}^2 + \nu\mu^2)(D_n + E_n e^{-i\alpha_{nx}(c-d)}) \tanh \alpha_n h = 0, \qquad (4.46)$$

$$\sum_{n=-2}^{\infty} i\alpha_{nx}\alpha_n (\alpha_{nx}^2 + (2-\nu)\mu^2)(D_n - E_n e^{-i\alpha_{nx}(c-d)}) \tanh \alpha_n h = 0, \qquad (4.47)$$

$$\sum_{n=-2}^{\infty} \alpha_n (\alpha_{nx}^2 + \nu\mu^2)(D_n e^{i\alpha_{nx}(d-c)} + E_n) \tanh \alpha_n h = 0, \qquad (4.48)$$

$$\sum_{n=-2}^{\infty} i\alpha_{nx}\alpha_n (\alpha_{nx}^2 + (2-\nu)\mu^2)(D_n e^{i\alpha_{nx}(d-c)} - E_n) \tanh \alpha_n h = 0. \qquad (4.49)$$

After keeping upto $n = N$ (i.e. truncating the series after $N + 1$) in each relation, a system with $(8N + 12)$ number of equations with $(8N + 12)$ number of unknowns given in Equations (4.33)-(4.40) and (4.46)-(4.49) is solved for BSPS where as the system with $(8N + 12)$ number of equations with $(8N + 12)$ number of unknowns given in Equations (4.37)-(4.40), (4.41)-(4.44) and (4.46)-(4.49) is solved for SPPS. Here, this system of equations is solved by the Gauss elimination method with the help of MATLAB. The effectiveness of the porous structure to mitigate the structural response of EP can be studied through reflection coefficient $|R_0|$, transmission coefficient $|T_0|$ and dissipation coefficient k_d given by Equation (4.63).

Force on porous structure: The horizontal wave force k_{f1} on the front face and wave force k_{f2} on the rear face of the porous structure are computed by the respective formulas

given by

$$k_{f1} = \left| \frac{-i\omega}{gh^2} \int_{-h}^{-h+a} [\phi_1(0^-, y)] dy \right|, \tag{4.50}$$

$$k_{f2} = \left| \frac{-i\omega}{gh^2} \int_{-h}^{-h+a} [\phi_4(b^+, y)] dy \right|, \tag{4.51}$$

for BSPS and

$$k_{f1} = \left| \frac{-i\omega}{gh^2} \int_{-a}^{0} [\phi_1(0^-, y)] dy \right|, \tag{4.52}$$

$$k_{f2} = \left| \frac{-i\omega}{gh^2} \int_{-a}^{0} [\phi_4(b^+, y)] dy \right|, \tag{4.53}$$

for SPPS.

Plate deflection: The plate deflection is calculated by using the formula

$$\eta_5 = \frac{i}{\omega} \frac{\partial \phi_5}{\partial y} \bigg|_{y=0}. \tag{4.54}$$

Free surface elevation: The free surface elevation in the respective open water region is computed by using the formula

$$\eta_j = \frac{i}{\omega} \frac{\partial \phi_j}{\partial y} \bigg|_{y=0}, \quad j = 1, 2, 4, 6 \text{ for BSPS} \tag{4.55}$$

$$j = 1, 4, 6 \text{ for SPPS}.$$

Shear force and strain: The shear force S_f and strain S_t on EP are calculated for the normal incident $(\theta = 0°)$ of surface waves by using the formulas

$$S_f = \frac{D}{\omega h} \left| \frac{\partial^4 \phi_5}{\partial x^3 \partial y} \right|_{y=0}, \tag{4.56}$$

$$S_t = \frac{h_0}{2\omega} \left| \frac{\partial^3 \phi_5}{\partial x^2 \partial y} \right|_{y=0}. \tag{4.57}$$

4.4 Energy Balance Relation

In the present problem, apart from the reflection and transmission of waves, a major part of wave energy is dissipated by BSPS/SPPS. Thus, for a better understanding of the quantitative behavior of wave reflection, transmission, and dissipation, an energy identity is derived. The energy identity for the current problem can be derived using the Green's identity, which is given by

$$\int_C \left(\phi \frac{\partial \phi^*}{\partial n} - \phi^* \frac{\partial \phi}{\partial n} \right) ds = 0,$$

where ϕ^* is the complex conjugate of ϕ and $\frac{\partial}{\partial n}$ is the outward normal derivative to the boundary C, $C = C_1 \cup C_2$, where for BSPS $C_1 = \{x = -X, -h \le y \le 0; y = -h, -X \le x \le 0; x = 0, y \in L_b; L_w; x = b, y \in L_b; y = -h, b \le x \le X; x = X, -h \le y \le 0;$

$y = 0, d \leq x \leq X$; $y = 0, c \leq x \leq d$; $y = 0, -X \leq x \leq c$}, C_2={ $x = 0, y \in L_b$; L_w; $x = b, y \in L_b$; $y = -h, 0 \leq x \leq b$ }. Due to the no-flow condition, the contributions from the boundary $y = -h, -X \leq x \leq 0$; $y = -h, b \leq x \leq X$ is zero. The contributions from the boundary $y = 0, d \leq x \leq X$ and $y = 0, -X \leq x \leq c$ are zero because of free surface condition. Due to EP condition, the contribution from the boundary $y = 0, c \leq x \leq d$ is zero. The line $x = 0, y \in L_b$ contributes

$$\int_C \left(\phi \frac{\partial \phi^*}{\partial n} - \phi^* \frac{\partial \phi}{\partial n} \right) ds = \int_{L_b} \left([\epsilon_p(m_p + if_p) - 1] \phi_3 \phi_{3x}^* - [\epsilon_p(m_p - if_p) - 1] \phi_3^* \phi_{3x} \right)_{x=0} dy. \tag{4.58}$$

The line $x = b, y \in L_b$ contributes

$$\int_C \left(\phi \frac{\partial \phi^*}{\partial n} - \phi^* \frac{\partial \phi}{\partial n} \right) ds = \int_{L_b} \left([\epsilon_p(m_p - if_p) - 1] \phi_3^* \phi_{3x} - [\epsilon_p(m_p + if_p) - 1] \phi_3 \phi_{3x}^* \right)_{x=b} dy. \tag{4.59}$$

The line L_w contributes

$$\int_C \left(\phi \frac{\partial \phi^*}{\partial n} - \phi^* \frac{\partial \phi}{\partial n} \right) ds = \int_{L_w} \left([\epsilon_p(m_p - if_p) - 1] \phi_3^* \phi_{3y} - [\epsilon_p(m_p + if_p) - 1] \phi_3 \phi_{3y}^* \right) dx. \tag{4.60}$$

The contribution from the line $x = -X, -h \leq y \leq 0$:

$$\int_C \left(\phi \frac{\partial \phi^*}{\partial n} - \phi^* \frac{\partial \phi}{\partial n} \right) ds = (1 - |R_0|^2) \frac{ik_{0x}}{\cosh^2 k_0 h} \left(\frac{\sinh(2k_0 h) + 2k_0 h}{2k_0} \right). \tag{4.61}$$

The contribution from the line $x = X, -h \leq y \leq 0$:

$$\int_C \left(\phi \frac{\partial \phi^*}{\partial n} - \phi^* \frac{\partial \phi}{\partial n} \right) ds = -(|T_0|^2) \frac{ik_{0x}}{\cosh^2 k_0 h} \left(\frac{\sinh(2k_0 h) + 2k_0 h}{2k_0} \right). \tag{4.62}$$

Adding all contributions from C_1 and C_2, the energy identity is found as

$$|R_0|^2 + |T_0|^2 + k_d = 1 \tag{4.63}$$

where

$$k_d = \frac{2k_0 \cosh^2 k_0 h}{ik_{0x}(\sinh 2k_0 h + 2k_0 h)} \left[\int_{L_b} \left([\epsilon_p(m_p + if_p) - 1] \phi_3 \phi_{3x}^* - [\epsilon_p(m_p - if_p) - 1] \phi_3^* \phi_{3x} \right)_{x=0} dy \right.$$

$$+ \int_{L_b} \left([\epsilon_p(m_p - if_p) - 1] \phi_3^* \phi_{3x} - [\epsilon_p(m_p + if_p) - 1] \phi_3 \phi_{3x}^* \right)_{x=b} dy$$

$$\left. + \int_{L_w} \left([\epsilon_p(m_p - if_p) - 1] \phi_3^* \phi_{3y} - [\epsilon_p(m_p + if_p) - 1] \phi_3 \phi_{3y}^* \right) dx \right]. \tag{4.64}$$

Similarly, by taking the suitable choice of contour along SPPS, the energy identity can be derived as $|R_0|^2 + |T_0|^2 + k_d = 1$, where

$$k_d = \frac{2k_0 \cosh^2 k_0 h}{ik_{0x}(\sinh 2k_0 h + 2k_0 h)} \left[\int_0^b -2iK f_p |\phi_2|^2 dx \right.$$

$$+ \int_{L_b} \left(\left[\epsilon_p(m_p + if_p) - 1 \right] \phi_2 \phi_{2x}^* - \left[\epsilon_p(m_p - if_p) - 1 \right] \phi_2^* \phi_{2x} \right)_{x=0} dy$$

$$+ \int_{L_b} \left(\left[\epsilon_p(m_p - if_p) - 1 \right] \phi_2^* \phi_{2x} - \left[\epsilon_p(m_p + if_p) - 1 \right] \phi_2 \phi_{2x}^* \right)_{x=b} dy$$

$$\left. + \int_{L_w} \left(\left[\epsilon_p(m_p + if_p) - 1 \right] \phi_2 \phi_{2y}^* - \left[\epsilon_p(m_p - if_p) - 1 \right] \phi_2^* \phi_{2y} \right) dx \right].$$

$$(4.65)$$

4.5 Results and Discussion

In this section, the usefulness of BSPS/SPPS to reduce the structural response on Ep is studied through the reflection coefficient ($|R_0|$), transmission coefficient ($|T_0|$), dissipation coefficient (k_d), hydrodynamics forces on the porous structure (k_{f1} and k_{f2}), plate deflection ($Re(\eta_5)$), shear force (S_f) and strain (S_t) on EP. The structural and system parameters are non-dimensionalized using the length scale of water depth (h). The values of the non-dimensional parameters $D/h^4 = 10^2$, $\epsilon_e/h = 0.01$, $L_2/h = 5$, $L_1/h = 4$, $a/h = 0.5$, $b/h = 0.6$, $f_p = 0.5$ and $m_p = 1$ are kept fixed in this investigation unless otherwise mentioned. Several computational results are performed to investigate the effect of various structural parameters, but in this section, few results are shown to avoid the repetition.

$k_0 h$	BSPS						SPPS					
	$N = 4$		$N = 5$		$N = 6$		$N = 4$		$N = 5$		$N = 6$	
	$|R_0|$	$|T_0|$	$|R_0|$	$|T_0|$	$|R_0|$	$|T_0|$	$|R_0|$	$|T_0|$	$|R_0|$	$|T_0|$	$|R_0|$	$|T_0|$
0.2	0.0092	0.9977	0.0092	0.9977	0.0092	0.9977	0.0479	0.9633	0.048	0.9633	0.048	0.9633
0.4	0.0291	0.9951	0.0292	0.9951	0.0291	0.9951	0.0932	0.9673	0.0931	0.9671	0.0931	0.9671
0.6	0.0902	0.9908	0.0902	0.9907	0.0902	0.9907	0.1717	0.9525	0.1718	0.9525	0.1718	0.9525
0.8	0.2094	0.9671	0.2095	0.9671	0.2095	0.9671	0.24	0.9519	0.2392	0.9516	0.2392	0.9516
1	0.4151	0.9020	0.4152	0.9020	0.4152	0.9020	0.5893	0.7807	0.5882	0.78	0.5882	0.78
1.2	0.5187	0.8467	0.5188	0.8467	0.5188	0.8467	0.3727	0.8654	0.3789	0.8701	0.3789	0.8701

Table 4.1: Convergence for N through $|R_0|$ and $|T_0|$ for BSPS and SPPS with $\epsilon_p = 0.437$, $a/h = 0.2$, $f_p = 0.25$ and $\theta = 0^0$.

4.5.1 Convergence Study for N

From the Table 4.1, the convergence of series is studied where the value of $|R_0|$ and $|T_0|$ are tabulated against wavenumber $k_0 h$ for various values of $N = 4, 5$ and 6 with fixed value of $\epsilon_p = 0.437$, $a/h = 0.2$, $f_p = 0.25$ and $\theta = 0^0$. Here it is observed from the table that the accuracy upto 4th decimal point is achieved in the values of $|R_0|$ and $|T_0|$ for $N = 5$ for all values of $k_0 h$. However, in the present study, all the graphs are generated

for $N = 0$ (as considered in Sharma et al. [117]), because for almost all the practical cases, the plane wave approximation is sufficient to describe the wave behaviour as described in Dalrymple et al. [11].

k_0h	$N = 1$		$N = 3$		$N = 5$		$N = 7$		$N = 9$		$N = 11$	
	$|R_0|$	C	$|R_0|$	C	$|R_0|$	C	$|R_0|$	C	$|R_0|$	C	$|R_0|$	C
0.9	0.3218749541	-	0.3221564263	1.1019	0.3222401146	0.5527	0.3222621048	1.1159	0.3222726105	-	0.3222772176	-
1	0.4145041116	-	0.4151271186	0.5272	0.4152389381	1.1037	0.4152926222	0.7624	0.4153165071	-	0.4153293889	-
1.1	0.4745089758	-	0.4750188686	0.8772	0.4751482654	05321	0.4751871250	1.1702	0.4752135192	-	0.4752249201	-

Table 4.2: Order of convergence for various value of N for BSPS.

To find the order of convergence, we first find the numerical values of $|R_0|$ for various values of N=1,3,5,7,9 and 11, denoted as $|R_0|_N$, N=1,3,5,7,9, 11 and for various values of k_0h which are tabulated in Table 4.2. As given by Equation (2.61), the order of convergence denoted by 'C' can be defined by the formula

$$C = \frac{\log\left|\frac{|R_0|_{N+4}-|R_0|_{N+2}}{|R_0|_{N+2}-|R_0|_N}\right|}{\log\left|\frac{|R_0|_{N+2}-|R_0|_N}{|R_0|_N-|R_0|_{N-2}}\right|}, N = 3, 5, 7. \tag{4.66}$$

From Table 4.2, it is concluded that the order convergence lies between 0.5 and 1.2.

4.5.2 Validation

To validate the present methodology and results, it may be noted that the present problem reduces to the work of Hermans [70] on considering the parameter value as $m_p = 1$, $f_p = 0$, $\epsilon_p = 1$ (absence of porous structure) and $D/h^4 = 10^{-3}$. Figure 4.2a illustrates, the present results for $|R_0|$ and $|T_0|$ are well matched with the results of Hermans [70]. In the absence of EP (i.e. $D/h^4 = 0$, $\epsilon_e = 0$), the present study reduces to scattering of water waves by the porous structure. Figure 4.2b illustrates, the present results of $|R_0|$ and $|T_0|$ for BSPS ($k_0h = 0.68$, $\epsilon_p = 0.4$, $b/h = 1$, $f_p = 0.5$ and $a/h = 0.3$) are well-matched with the results of Losada et al. [18]. Figure 4.2c illustrates the present results of $|R_0|$ for SPPS ($Kh = 0.2012$, $\epsilon_p = 0.4$, $b/h = 1$, $f_p = 1$ and $a/h = 1$) in the absence of EP are well-matched with the results of Dalrymple et al. [11]. When the length a/h of the porous structure is equal to 1, the present problem reduces to the problem of Chapter 2. From the Figure 4.2d it is observed that the results of $|R_0|$ are well-matched with the results of Chapter 2 (Figure 2.3a). Further, to verify the energy identity given in relation (4.63), the values of k_d and $1 - |R_0|^2 - |T_0|^2$ are tabulated for different values of k_0h in Table 4.3 for both the cases of BSPS and SPPS and plotted in Figure 4.3 against k_0h for the case of BSPS. From the Table 4.3 and Figure 4.3, it is found that the values of k_d and $1 - |R_0|^2 - |T_0|^2$ are well matched. Hence, the energy balance relation is satisfied, showing the accuracy of the present numerical computations.
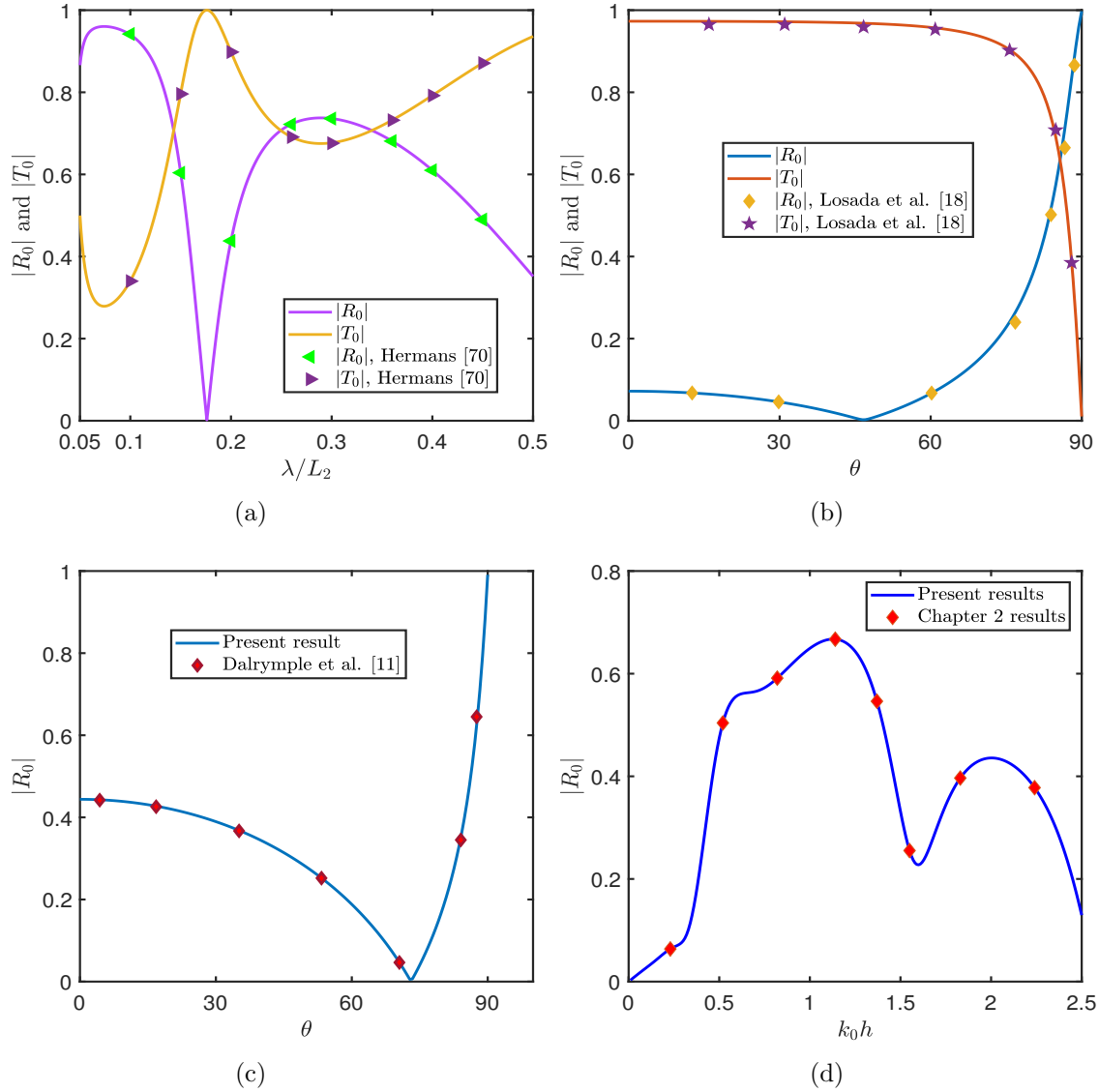
Figure 4.2: Validation of present results with results of (a) Hermans [70] (b) Losada et al. [18], (c) Dalrymple et al. [11] and (d) Chapter 2.

4.5.3   Effect of BSPS on Reflection Coefficient ($|R_0|$), Transmission Coefficient ($|T_0|$), Dissipation Coefficient (k_d), Force Experienced on BSPS (k_{f1} and k_{f2}), Plate Deflection ($Re(\eta_5)$) and Free Surface Elevation ($Re(\eta_j), j = 1, 2, 4, 6$)

In this section, the influence of BSPS on $|R_0|$, $|T_0|$, k_d, k_{f1}, k_{f2}, $Re(\eta_5)$ and $Re(\eta_j), j = 1, 2, 4, 6$ is studied through different graphs for different parameters as described below.

Figure 4.4, gives the behaviour of $|R_0|$, $|T_0|$ and k_d versus the wavenumber $k_0 h$ for different values of flexural rigidity D/h^4. From the figure, it is observed that as the $k_0 h$ value increases, the reflection coefficient $|R_0|$ and dissipation coefficient k_d increase, while the transmission coefficient $|T_0|$ decreases. It is also observed that with an increase in flexural rigidity, the reflection coefficient increases. This is because as flexural rigidity increases, the rigidity of the structure increases, and more waves are reflected.

$k_0 h$	BSPS				SPPS			
	$|R_0|$	$|T_0|$	$1 - |R_0|^2 - |T_0|^2$	k_d	$|R_0|$	$|T_0|$	$1 - |R_0|^2 - |T_0|^2$	k_d
0.2	0.0245	0.9876	0.024	0.024	0.0490	0.9266	0.1389	0.1384
0.4	0.0599	0.9770	0.0418	0.0418	0.3158	0.8338	0.2051	0.2051
0.6	0.1426	0.9472	0.0825	0.0825	0.4193	0.7367	0.2814	0.2819
0.8	0.3877	0.8854	0.0657	0.0658	0.246	0.7629	0.3575	0.3562
1	0.4556	0.8537	0.0634	0.0636	0.3332	0.6439	0.4743	0.478
1.2	0.5075	0.7492	0.1805	0.1811	0.54	0.4729	0.4848	0.4852

Table 4.3: Verification of energy identity with $\epsilon_p = 0.55$ and $\theta = 10^0$.
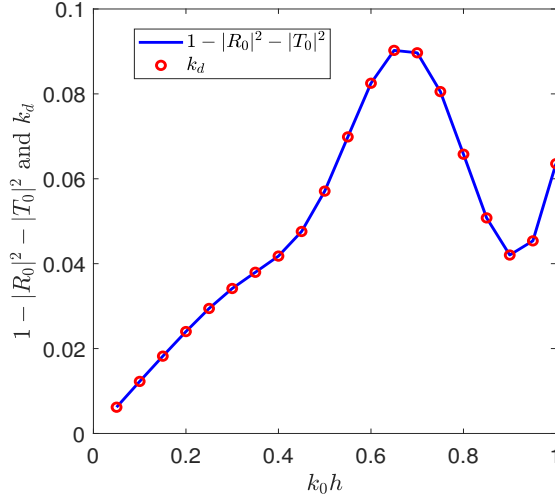
Figure 4.3: Verification of energy identity for BSPS case with $\epsilon_p = 0.55$, $\theta = 10^0$.

(a)   (b)   (c)
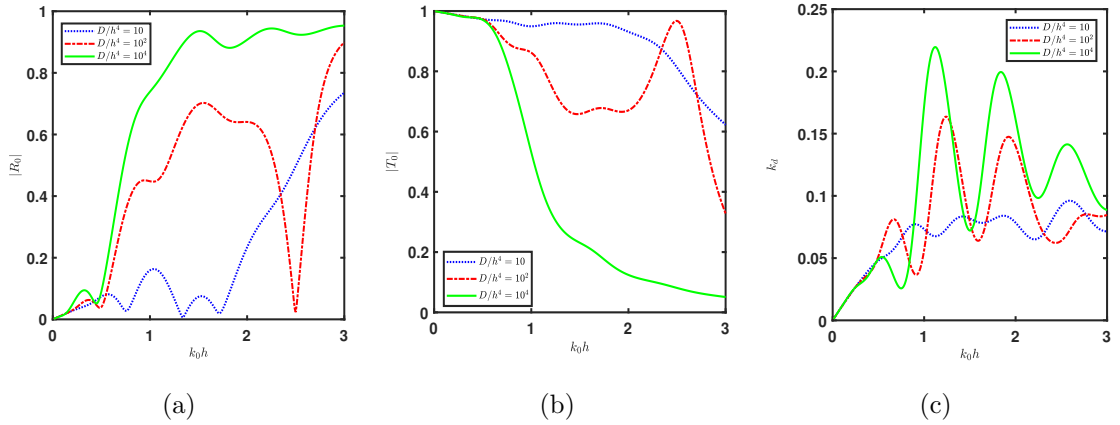
Figure 4.4: $|R_0|$, $|T_0|$ and k_d vs $k_0 h$ for different values of $D/h^4 = 10$, 10^2 and 10^4 with $\epsilon_p = 0.437$, $\theta = 10^0$.

Figures 4.5 - 4.6, give the behaviour of $|R_0|$, $|T_0|$ and k_d versus the wavenumber $k_0 h$ for different values of structural length a/h and width b/h, respectively. Both the figures depict that the behavior of $|R_0|$, $|T_0|$ and k_d values are the same with respect to $k_0 h$ as observed in Figure 4.4 for $D/h^4 = 10^2$. With the increase in length a/h and width b/h, energy dissipation by BSPS increases, and consequently, there is a decrease in reflection coefficient $|R_0|$ and transmission coefficient $|T_0|$.

Figures 4.7 - 4.8, give the behaviour of $|R_0|$, $|T_0|$ and k_d versus distance L_1/h between

BSPS and EP for different values of structural length a/h and width b/h, respectively. It is observed that wave reflection, transmission and dissipation are periodic and oscillatory. The maximum/minimum of wave reflection may be due to the constructive/destructive interface of the incident and reflected waves.

(a)   (b)   (c)

Figure 4.5: $|R_0|$, $|T_0|$ and k_d vs $k_0 h$ for different values of $a/h = 0.2$, 0.5 and 0.8 with $\epsilon_p = 0.437$, $\theta = 10^0$.

(a)   (b)   (c)

Figure 4.6: $|R_0|$, $|T_0|$ and k_d vs $k_0 h$ for different values of $b/h = 0.4$, 0.6 and 0.8 with $\epsilon_p = 0.437$, $\theta = 10^0$.

Figure 4.9 gives the behavior of $|R_0|$, $|T_0|$ and k_d versus L_1/h for different values of porosity ϵ_p. It is observed that as the porosity of the structure increases, more wave energy is dissipated by the structure, causing the values of reflection and transmission coefficients to decrease.

Figure 4.10 shows the behavior of $|R_0|$, $|T_0|$ and k_d versus L_1/h for different values of flexural rigidity D/h^4. It is noted that as the rigidity of the structure increases, the reflection coefficient increases and the transmission coefficient decreases. This is because as the rigidity of the structure increases, it becomes rigid, and most of the wave energy concentrated on the free surface is reflected back by EP, and less wave energy is transmitted.

Figure 4.11 gives the behavior of $|R_0|$, $|T_0|$ and k_d versus L_1/h for different values of frictional coefficient f_p. The reflection, transmission, and dissipation coefficients

are periodic and oscillatory, as observed in Figure 4.10. Further, with an increase in the frictional coefficient, the reflection and transmission coefficients decrease, and the dissipation coefficient increases.

(a)   (b)   (c)
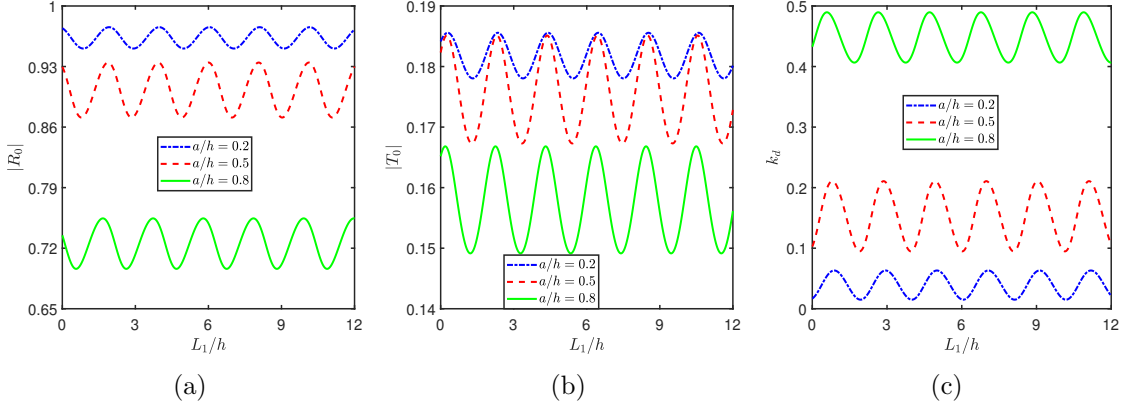
Figure 4.7: $|R_0|$, $|T_0|$ and k_d vs L_1/h for different values of $a/h = 0.2, 0.5$ and 0.8 with $\epsilon_p = 0.437$, $\theta = 20^0$, $Kh = 1.5$.

(a)   (b)   (c)
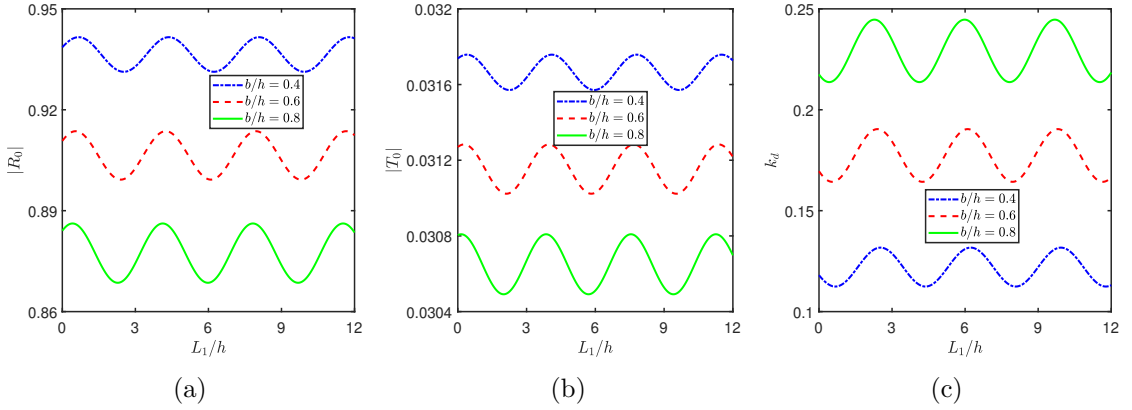
Figure 4.8: $|R_0|$, $|T_0|$ and k_d vs L_1/h for different values of $b/h = 0.4, 0.6$ and 0.8 with $\epsilon_p = 0.437$, $\theta = 45^0$, $Kh = 1$.

(a)   (b)   (c)
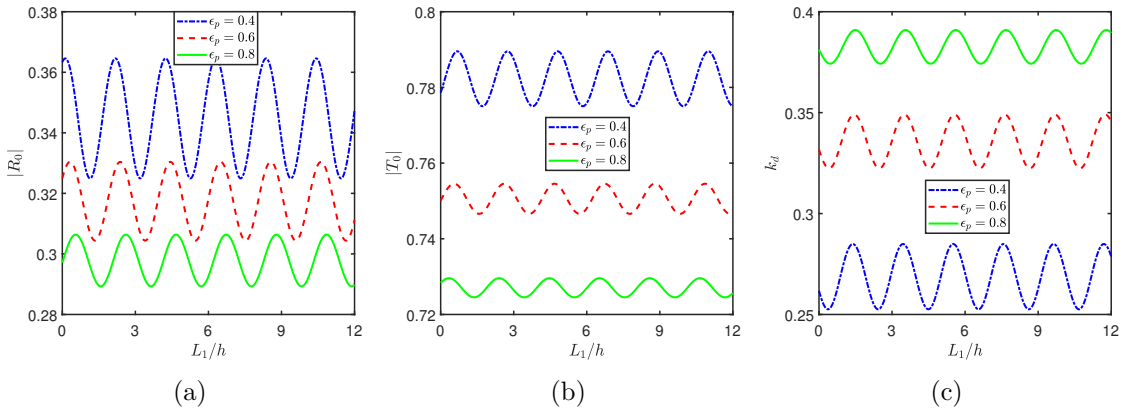
Figure 4.9: $|R_0|$, $|T_0|$ and k_d vs L_1/h for different values of $\epsilon_p = 0.4, 0.6$ and 0.8 with $D/h^4 = 10$, $\theta = 20^0$, $b/h = 2$, $Kh = 1.5$.

Figure 4.10: $|R_0|$, $|T_0|$ and k_d vs L_1/h for different values of $D/h^4 = 10, 10^2$ and 10^4 with $\epsilon_p = 0.437$, $\theta = 10^0$, $Kh = 0.5$.
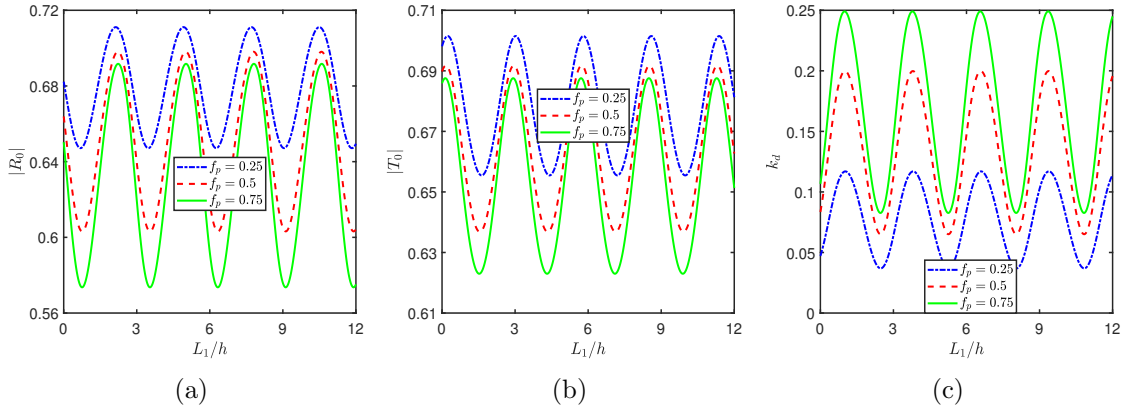
Figure 4.11: $|R_0|$, $|T_0|$ and k_d vs L_1/h for different values of $f_p = 0.25, 0.5$ and 0.75 with $\epsilon_p = 0.55$, $\theta = 20^0$, $Kh = 1$.
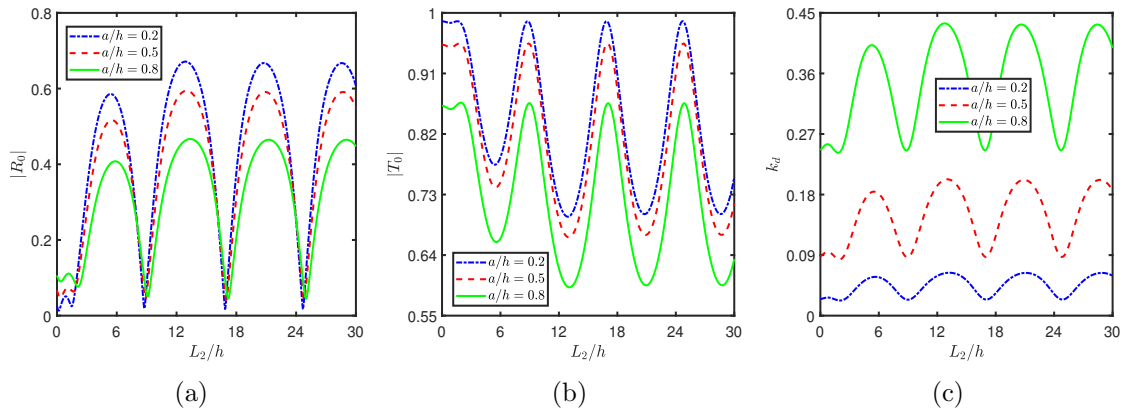
Figure 4.12: $|R_0|$, $|T_0|$ and k_d vs L_2/h for different values of $a/h = 0.2, 0.5$ and 0.8 with $\epsilon_p = 0.55$, $\theta = 10^0$, $Kh = 1$.

Figures 4.12 - 4.13 give the behavior of $|R_0|$, $|T_0|$ and k_d versus L_2/h for different values of structural length a/h and width b/h. From the figures, it is noted that the maxima of the reflection coefficient increases as the length of EP increases, but after a certain EP length, the maximum value of the reflection coefficient becomes constant. In

the transmission case, the opposite behavior is observed.

(a)   (b)   (c)

Figure 4.13: $|R_0|$, $|T_0|$ and k_d vs L_2/h for different values of $b/h = 0.4, 0.6$ and 0.8 with $\epsilon_p = 0.55$, $\theta = 10^0$, $Kh = 1$.

(a)   (b)   (c)

Figure 4.14: $|R_0|$, $|T_0|$ and k_d vs L_2/h for different values of $D/h^4 = 10, 10^2$ and 10^4 with $\epsilon_p = 0.437$, $\theta = 10^0$, $Kh = 0.5$.

(a)   (b)

Figure 4.15: $|R_0|$, $|T_0|$ and k_d vs θ for different values of $f_p = 0.25, 0.5$ and 0.75 with $\epsilon_p = 0.437$, $Kh = 0.5$.

Figure 4.14 gives the behavior of $|R_0|$, $|T_0|$ and k_d versus L_2/h for different values of flexural rigidity D/h^4. In this figure, it is observed that the number of nodes and antinodes

in $|R_0|$, $|T_0|$ and k_d are decreased with an increase in D/h^4 value of EP, this may be due to the formation of standing wave. In addition, it is observed that as the flexural rigidity increases, the reflection coefficient increases and the transmission coefficient decreases.

In Figure 4.15, the behavior of $|R_0|$, $|T_0|$ and k_d versus θ for different values of frictional coefficient f_p is presented. Here, optima in wave reflection and wave transmission are observed due to the change in the phase of the incident and reflected waves. Moreover, as the frictional coefficient f_p increases, the dissipation coefficient also increases.

(a)   (b)   (c)

Figure 4.16: $|R_0|$, $|T_0|$ and k_d vs b/h for different values of $a/h = 0.2$, 0.5 and 0.8 with $\epsilon_p = 0.437$, $\theta = 10^0$, $Kh = 0.5$.

(a)   (b)   (c)

Figure 4.17: $|R_0|$, $|T_0|$ and k_d vs b/h for different values of $f_p = 0.25$, 0.5 and 0.75 with $\epsilon_p = 0.437$, $\theta = 10^0$, $Kh = 0.5$.

Figures 4.16 - 4.17 give the behaviour of $|R_0|$, $|T_0|$ and k_d versus structural width b/h for different values of structural length a/h and frictional coefficient f_p respectively. It is observed that the reflection coefficient decreases in an oscillating pattern with an increase in structural width. Further, for the higher values of structural width, the reflection coefficient becomes constant. Here, the phenomenon of the resonating pattern may be due to the multiple wave interaction between BSPS and EP. It is also observed that the transmission coefficient decreases with an increase in structural width, and dissipation of energy increases with an increase in structural width.

The behavior of force k_{f1} acting on the front face and force k_{f2} acting on the rear

face of BSPS vs L_1/h for different values of structural length a/h and structural width b/h respectively are investigated in Figures 4.18 - 4.19. From the figure, it is noted that the wave forces k_{f1} and k_{f2} increase with an increase in the structural length a/h. With an increase in structural width b/h, the wave force k_{f1} is increasing, but the force k_{f2} is decreasing.

(a) (b)
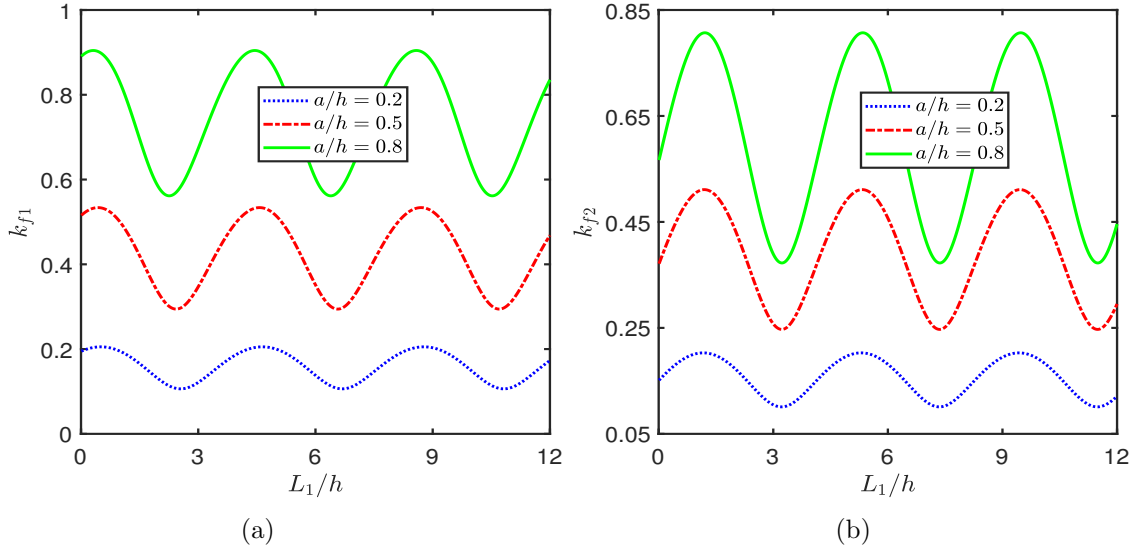
Figure 4.18: k_{f1} and k_{f2} vs L_1/h for different values of $a/h = 0.2$, 0.5 and 0.8 with $\epsilon_p = 0.437$, $\theta = 10^0$, $Kh = 0.5$.

(a) (b)
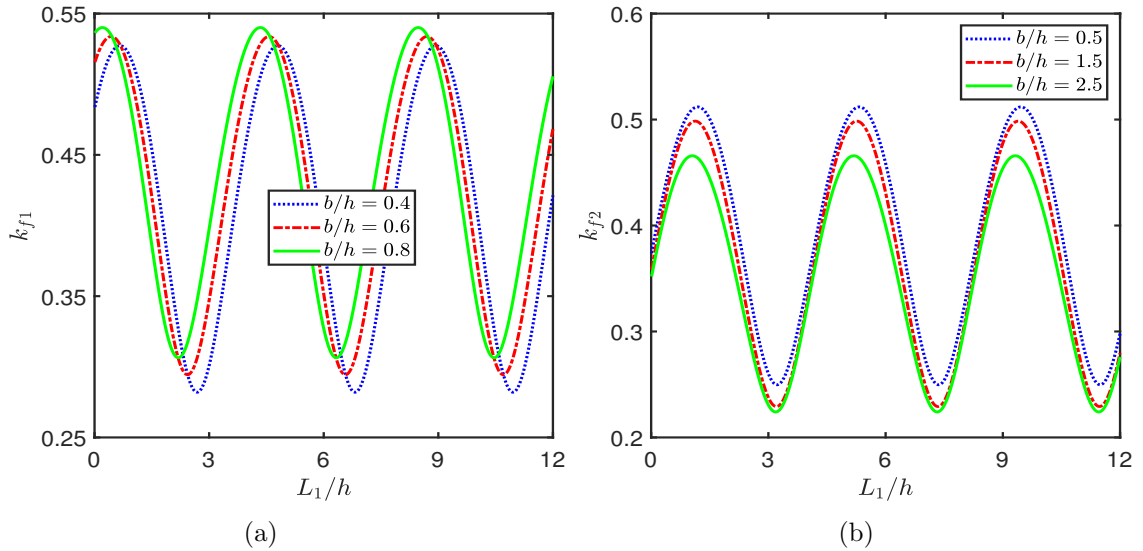
Figure 4.19: k_{f1} and k_{f2} vs L_1/h for different values of b/h with $\epsilon_p = 0.437$, $\theta = 10^0$, $Kh = 0.5$.

Figure 4.20 depicts the graphs of the free surface elevation η_1, η_2, η_4, η_6, and plate deflection η_5, for different values of length a/h, porosity ϵ_p and frictional coefficient f_p of BSPS. Figure 4.20a shows that as structural length a/h increases, the free surface elevation in regions 2, 4 and 6 and EP deflection decrease significantly. This is because as BSPS

length increases, most of the incident wave energy is dissipated, yielding to lesser energy transmitted by EP. Hence, a decrease in EP deflection and free surface elevation in the lee side of the structure is observed. Figure 4.20b shows that as porosity ϵ_p increases, the free surface elevation and EP deflection decrease. This is primarily due to the increased dissipation of wave energy with an increase in porosity ϵ_p values. Hence, a structure with large porosity ϵ_p effectively attenuates the structural response of EP by reducing EP deflection. Figure 4.20c shows that as the frictional coefficient f_p increases, the free surface elevation and EP deflection decrease. The observation and the related reasons are similar as observed in Figure 4.20b.

(a)   (b)   (c)
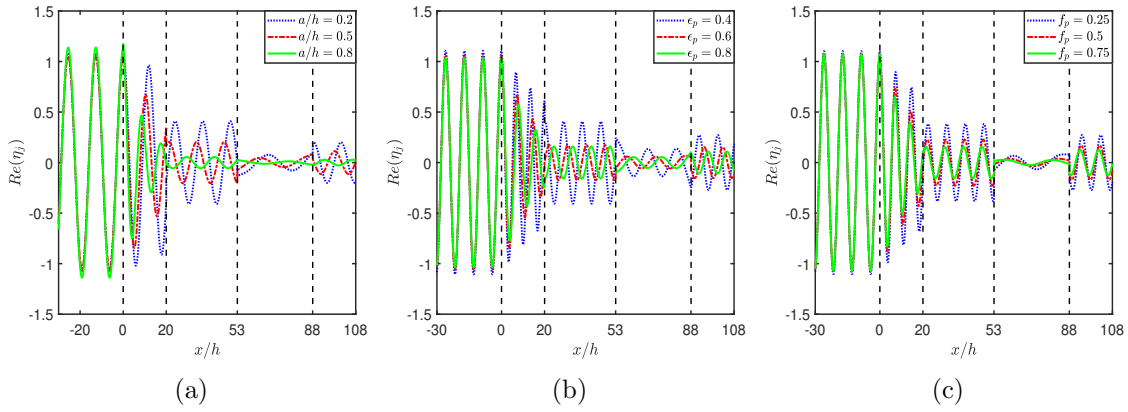
Figure 4.20: Free surface elevation $Re(\eta_j), j = 1, 2, 4, 6$ and plate deflection $Re(\eta_5)$ for different values of **(a)** $a/h = 0.2$, 0.5 and 0.8 ($Kh = 0.25$) , **(b)** $\epsilon_p = 0.4$, 0.6 and 0.8 ($D/h^4 = 10$, $Kh = 0.5$) and **(c)** $f_p = 0.25$, 0.5 and 0.75 ($Kh = 0.5$) with $b/h = 20$, $L_1/h = 33$, $L_2/h = 35$, $\epsilon_p = 0.437$, $\theta = 20^0$.

(a)   (b)
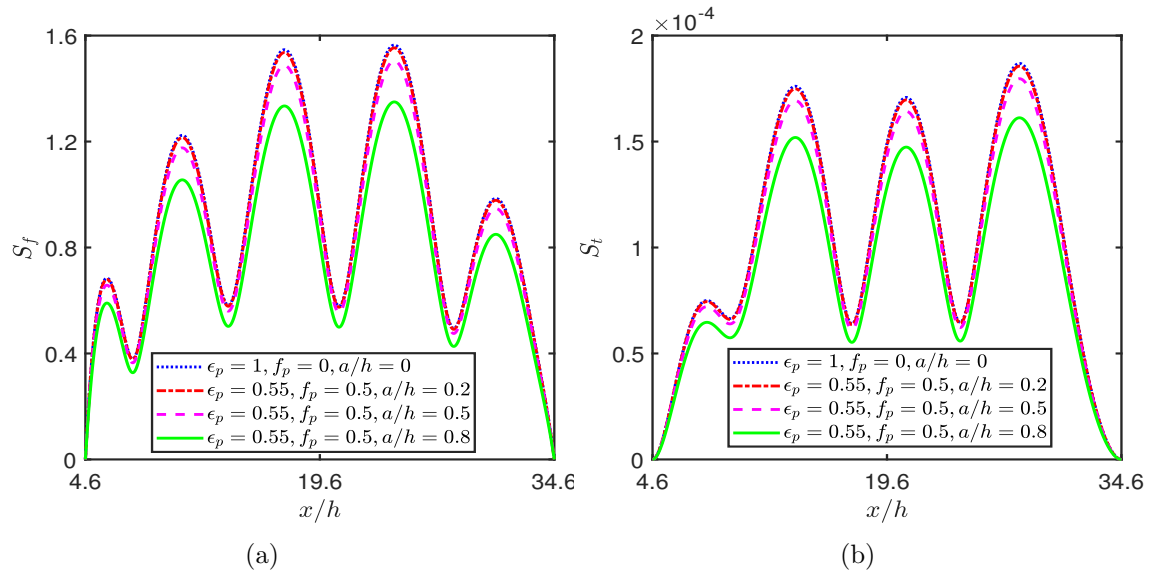
Figure 4.21: S_f and S_t in the absence of BSPS ($f_p = 0$, $\epsilon_p = 1$, $a/h = 0$) and presence of BSPS for different values of a/h with $f_p = 0.5$, $\epsilon_p = 0.5$, $\theta = 0^0$, $Kh = 1$, $L_1/h = 4$, $L_2/h = 30$.

Figure 4.21 gives the shear force S_f and strain S_t for different values of structural

length a/h of BSPS. From this figure, it is noted that at the ends of EP the shear force and the strain are zero which is due to the assumption of free edge behaviour at both the ends of EP and the variation of shear force S_f & strain S_t follows an oscillatory pattern. Further, it is depicted that the S_f and S_t for the case of absence of BSPS ($f_p = 0$, $\epsilon_p = 1$, $a/h = 0$) is more as compared to the other cases where BSPS is present ($f_p = 0.5$ and $\epsilon_p = 0.55$). Thus BSPS is highly effective in reducing the S_f and S_t experienced by EP. As the structural length a/h increases amplitude of the shear force and strain of EP decrease. This is due to the fact that as the structural length a/h increases, more wave energy is dissipated by BSPS, as observed in Figure 4.7c.
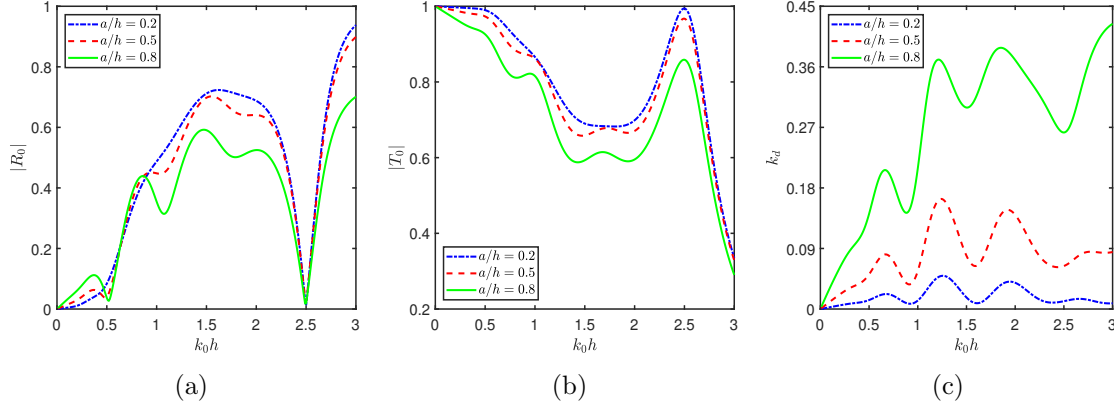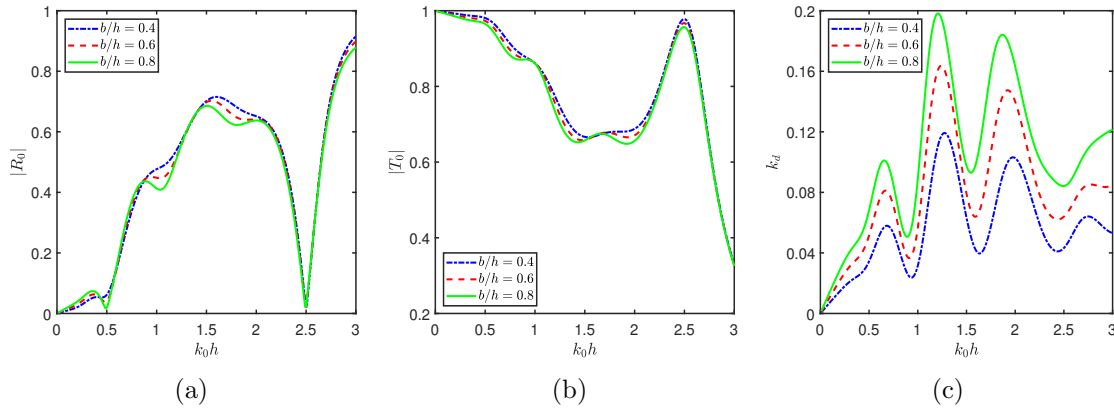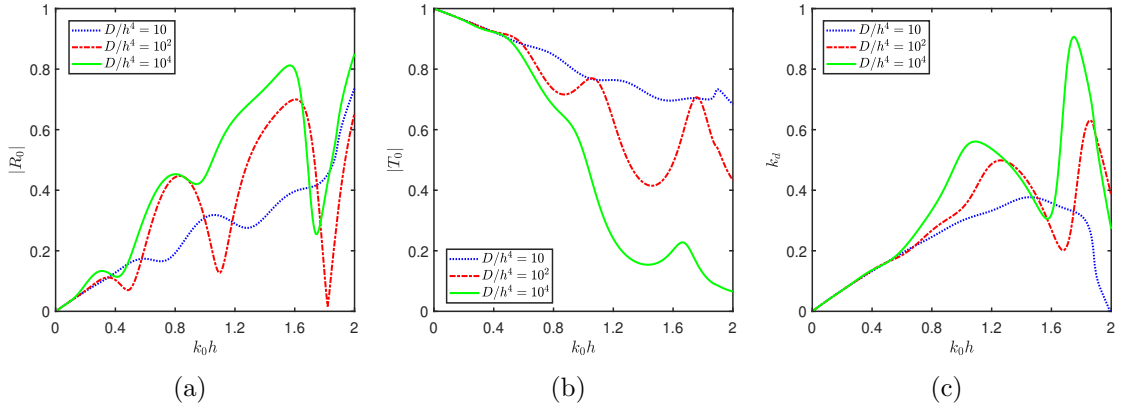

Figure 4.22: $|R_0|$, $|T_0|$ and k_d vs k_0h for different values of $D/h^4 = 10$, 10^2 and 10^4 with $\epsilon_p = 0.437$, $\theta = 10^0$.

4.5.4   Effect of SPPS on Reflection Coefficient ($|R_0|$), Transmission Coefficient ($|T_0|$), Dissipation Coefficient (k_d), Force Experienced on SPPS (k_{f1} and k_{f2}), Plate Deflection ($Re(\eta_5)$) and Free Surface Elevation ($Re(\eta_j)$, $j = 1, 4, 6$)

In this section, the numerical results for $|R_0|$, $|T_0|$, k_d, k_{f1}, k_{f2}, $Re(\eta_5)$ and $Re(\eta_j)$, $j = 1, 4, 6$ are plotted through graphs for different parameters by replacing BSPS with SPPS.

In Figure 4.22, the behavior of $|R_0|$, $|T_0|$ and k_d versus wavenumber k_0h for different values of flexural rigidity D/h^4 is presented. In Figure 4.22a, it is observed that with an increase in flexural rigidity D/h^4, the wave reflection is increasing. This is because as flexural rigidity D/h^4 increases, EP becomes rigid, causing more reflection. It is also observed that as flexural rigidity D/h^4 increases, oscillation in reflection decreases. In Figure 4.22b, it is observed that the wave transmission decreases as flexural rigidity D/h^4 increases. Figure 4.22c shows that as flexural rigidity D/h^4 increases, the dissipation coefficient increases. This is due to an increased mutual interaction between SPPS and EP, which increases the dissipation of energy. As compared to BSPS case, more wave energy is dissipated in SPPS case.

The behavior of $|R_0|$, $|T_0|$ and k_d versus distance L_1/h between SPPS and EP are examined for different values of structural length a/h, width b/h and porosity ϵ_p,

respectively in Figures 4.23, 4.24 and 4.25. It is noted that the behavior of the curves is similar to the behavior of BSPS as in Figures 4.7, 4.8 and 4.9. But, the wave reflection and transmission in SPPS case are less as compared to BSPS case. This is due to the fact that SPPS dissipates more wave energy, which is concentrated near the free surface, than BSPS.

(a)   (b)   (c)
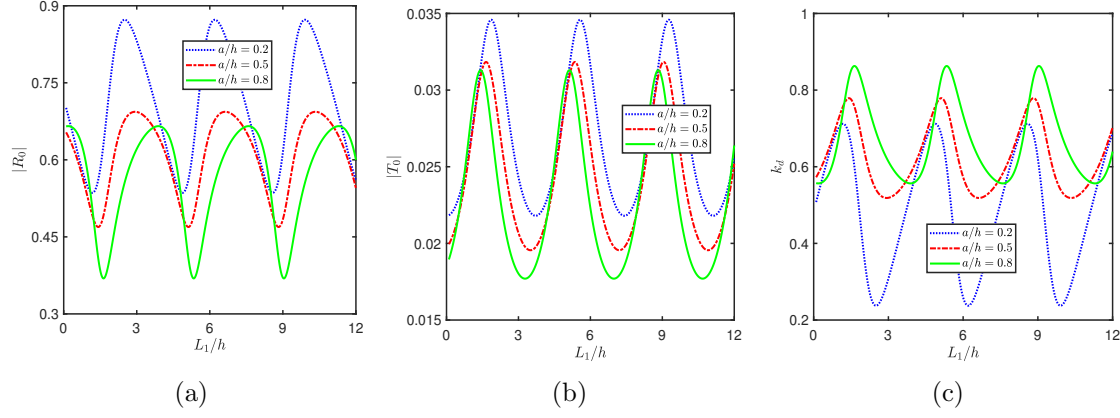
Figure 4.23: $|R_0|$, $|T_0|$ and k_d vs L_1/h for different values of $a/h = 0.2$, 0.5 and 0.8 with $\epsilon_p = 0.437$, $\theta = 20^0$, $Kh = 1.5$.

(a)   (b)   (c)
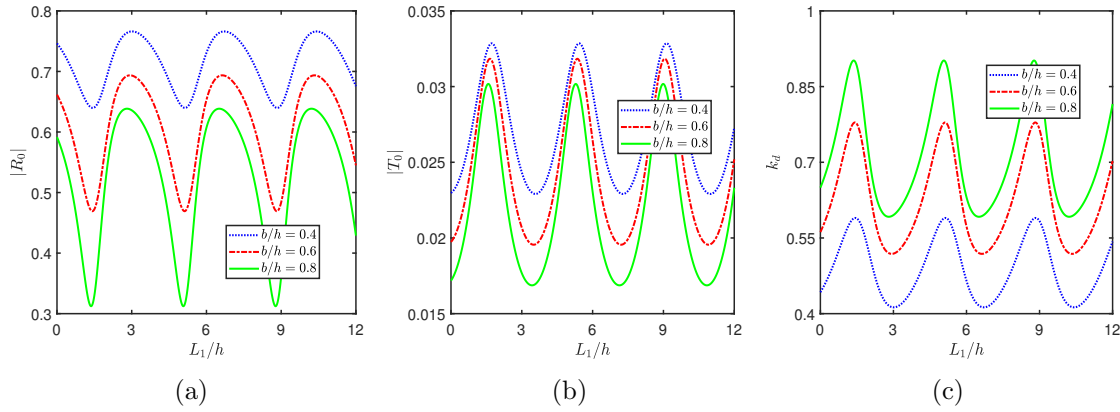
Figure 4.24: $|R_0|$, $|T_0|$ and k_d vs L_1/h for different values of $b/h = 0.4$, 0.6 and 0.8 with $\epsilon_p = 0.437$, $\theta = 45^0$, $Kh = 1$.

Figure 4.26 gives the behavior of $|R_0|$, $|T_0|$ and k_d versus L_2/h for different values of flexural rigidity D/h^4. From Figure 4.26a, it is observed that as flexural rigidity D/h^4 increases, reflection of the wave energy increases. Further, the number of oscillations decreases as flexural rigidity D/h^4 increases. This is due to reduced flexure of EP caused by increased flexural rigidity D/h^4 values. Moreover, an opposite behaviour is observed in transmission of wave energy in Figure 4.26b. As flexural rigidity D/h^4 increases, transmission decreases. Figure 4.26c shows that as flexural rigidity D/h^4 increases, dissipation of energy increases. This is because, SPPS dissipates wave energy more efficiently that is concentrated near the free surface.

Figure 4.27 gives the behavior of $|R_0|$, $|T_0|$ and k_d versus θ for different values of frictional coefficient f_p. The general shape and the behavior of the plots of $|R_0|$, $|T_0|$ and

k_d are similar to that of Figure 4.15. However, the wave reflection and the wave dissipation are more by SPPS as compared to BSPS in Figure 4.15.

(a) (b) (c)
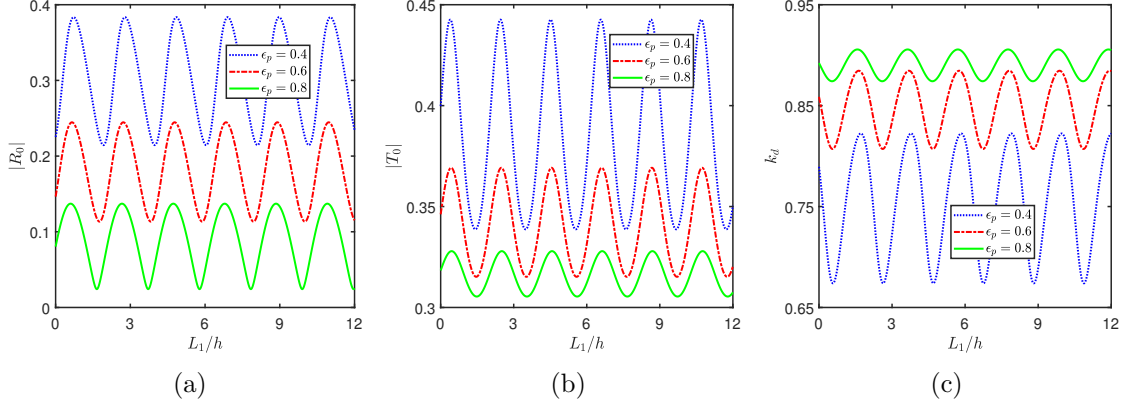
Figure 4.25: $|R_0|$, $|T_0|$ and k_d vs L_1/h for different values of $\epsilon_p = 0.4$, 0.6 and 0.8 with $D/h^4 = 10$, $\theta = 20^0$, $b/h = 2$, $Kh = 1.5$.
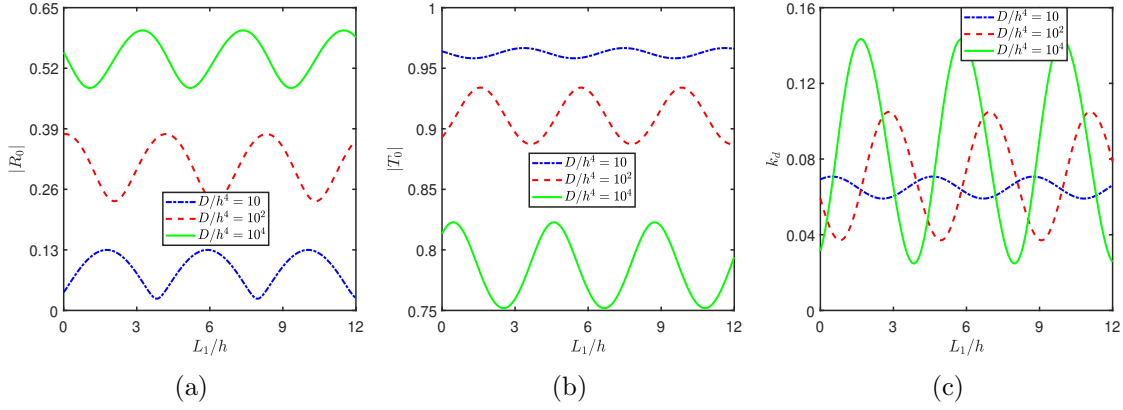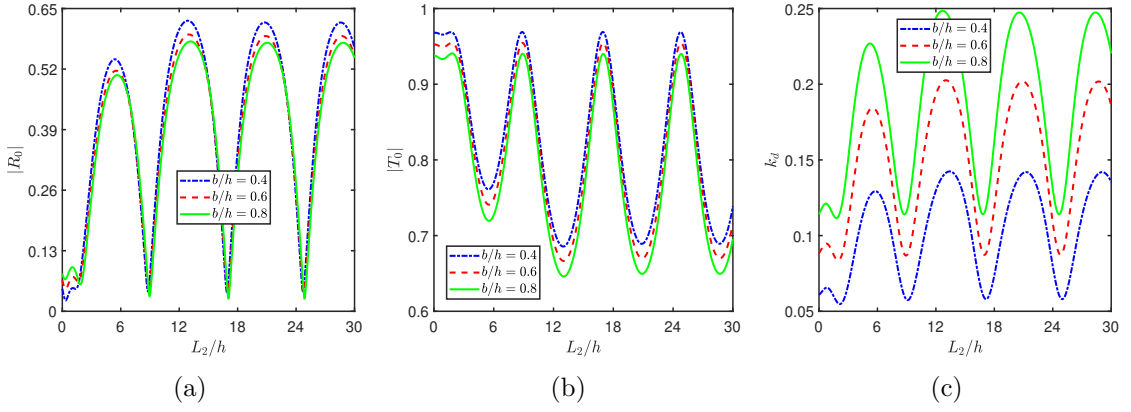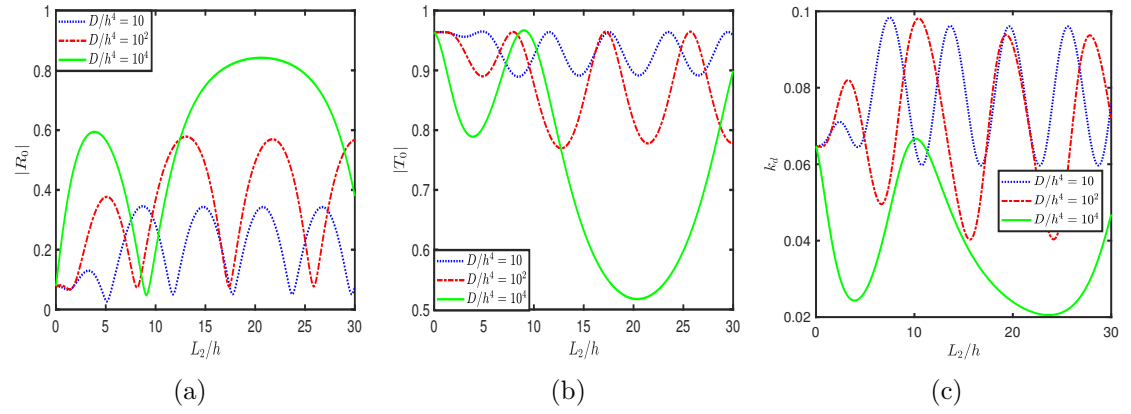

(a) (b) (c)
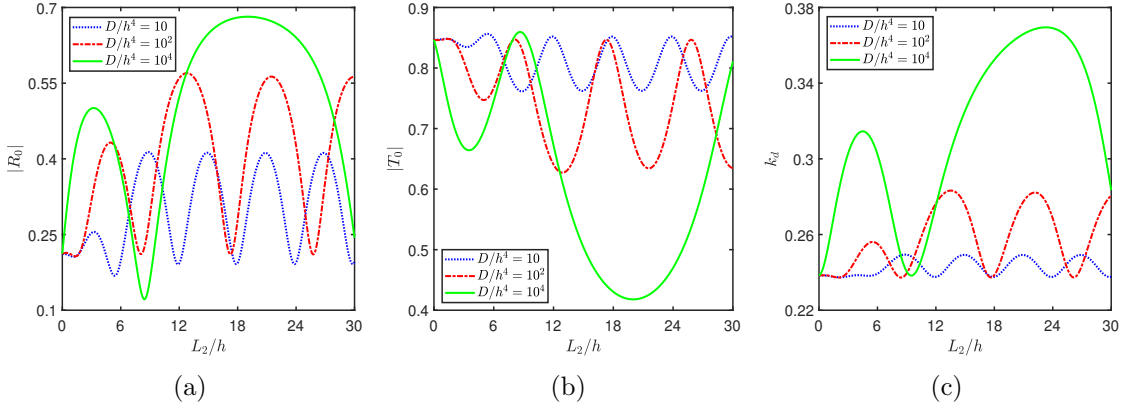
Figure 4.26: $|R_0|$, $|T_0|$ and k_d vs L_2/h for different values of $D/h^4 = 10$, 10^2 and 10^4 with $\epsilon_p = 0.437$, $\theta = 10^0$, $Kh = 0.5$.
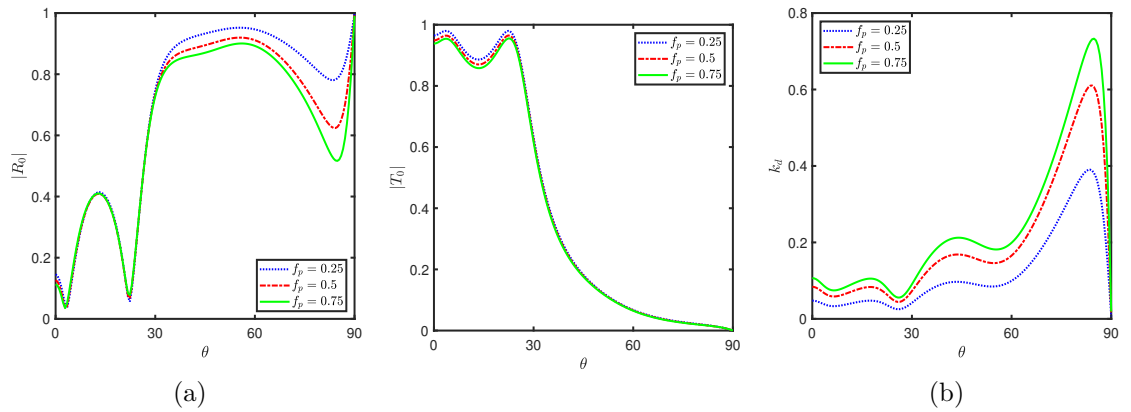

(a) (b)
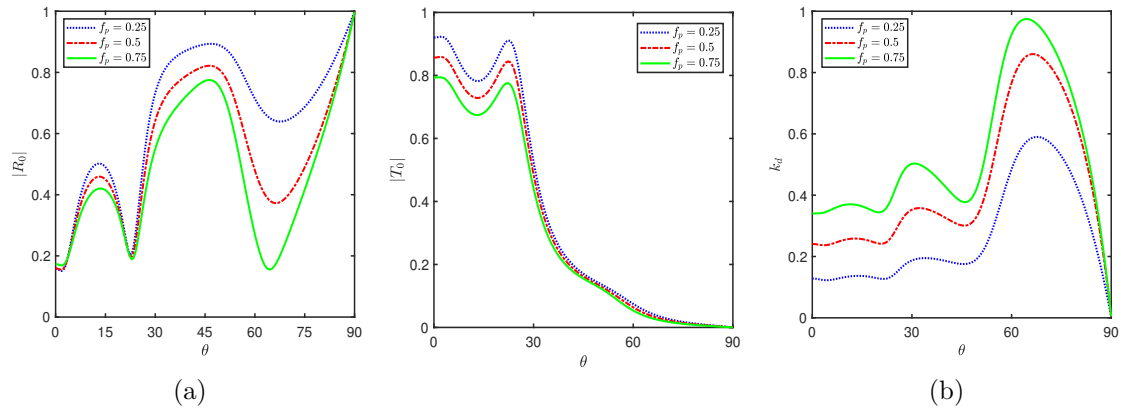
Figure 4.27: $|R_0|$, $|T_0|$ and k_d vs θ for different values of $f_p = 0.25$, 0.5 and 0.75 with $\epsilon_p = 0.437$, $Kh = 0.5$.

Figure 4.28 shows the behaviour of $|R_0|$, $|T_0|$ and k_d versus structural width b/h

for different values of frictional coefficient f_p. From the figure, it is revealed that the behavior of curves is similar to that of Figure 4.17. The oscillatory pattern in the reflection coefficient decreases with an increase in structural width, and for the higher value of structural width, the reflection coefficient becomes constant. However, the number of oscillations is less as compared to BSPS. Further as frictional coefficient f_p increases, reflection and transmission decrease which is similar to Figure 4.17. In Figure 4.28c, it is observed that as the frictional coefficient f_p increases, the dissipation of wave energy increases.
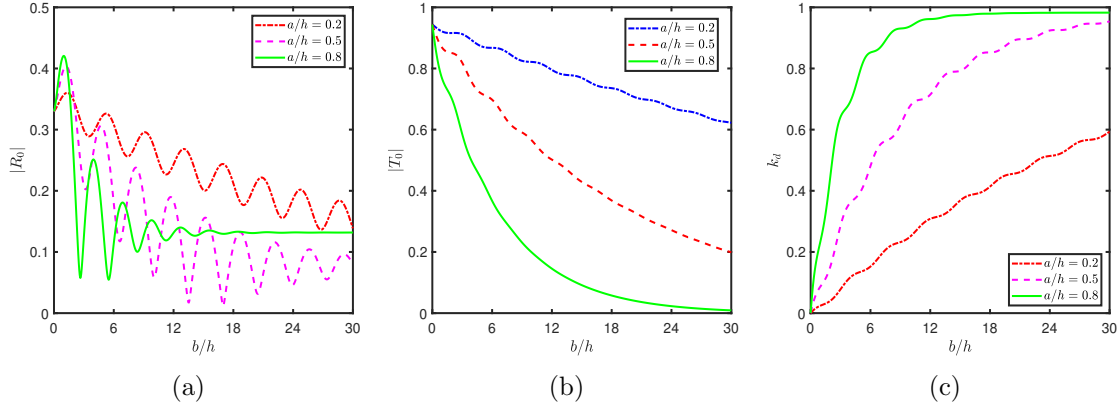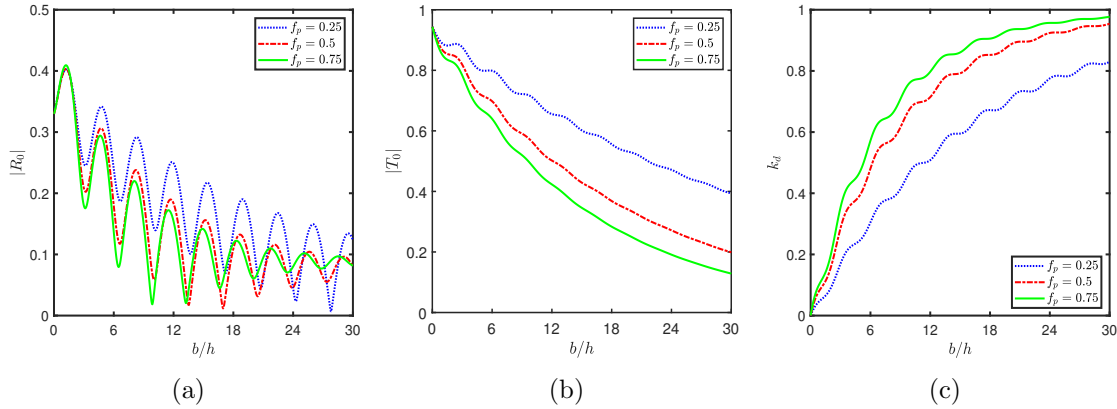

| (a) | (b) | (c) |
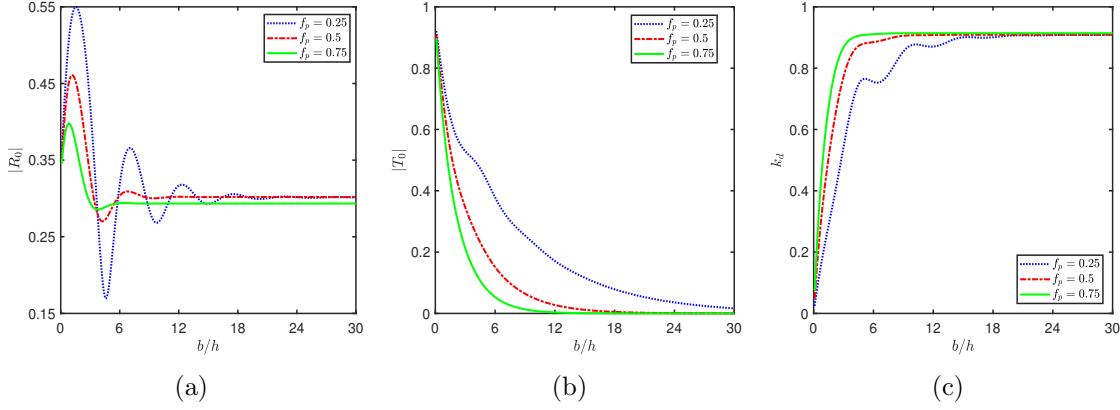
Figure 4.28: $|R_0|$, $|T_0|$ and k_d vs b/h for different values of $f_p = 0.25$, 0.5 and 0.75 with $\epsilon_p = 0.437$, $\theta = 10^0$, $Kh = 0.5$.

| (a) | (b) |
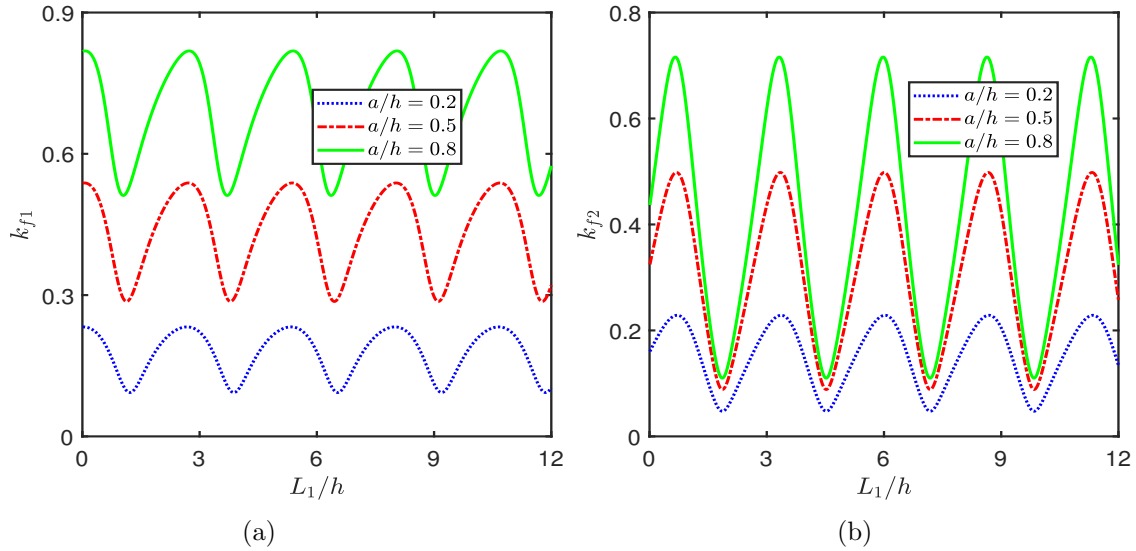
Figure 4.29: k_{f1} and k_{f2} vs L_1/h for different values of $a/h = 0.2$, 0.5 and 0.8 with $\epsilon_p = 0.437$, $\theta = 10^0$, $Kh = 1$.

Figure 4.29 presents the behaviour of wave force k_{f1} acting on the front face and wave force k_{f2} acting on the rear face vs L_1/h for different values of structural length a/h. It is revealed that wave forces k_{f1} and k_{f2} are both periodic and oscillatory, as observed in Figure 4.18 for BSPS. Further, it is also observed that with an increase in length a/h of

SPPS, k_{f1} and k_{f2} increases. This may be due to the fact that with an increase in a/h, more wave energy interacts with SPPS.

Figure 4.30 gives the free surface elevation and plate deflection for different values of length a/h, porosity ϵ_p and frictional coefficient f_p of SPPS. Similar behavior is noticed as in Figure 4.20. Fig 4.30a depicts that plate deflection and free surface elevation in the lee side decreases with increase in structural length a/h. Fig 4.30b shows that with an increase in porosity ϵ_p, plate deflection and free surface elevation in the lee side decrease. Figure 4.30c shows that as frictional coefficient f_p increases, plate deflection and free surface elevation in the lee side decrease.

(a)	(b)	(c)
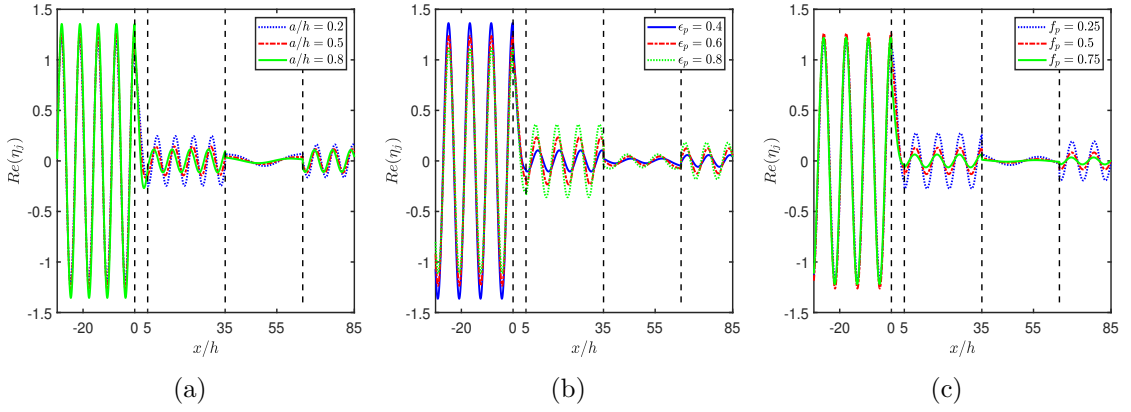
Figure 4.30: Free surface elevation $Re(\eta_j), j = 1, 2, 4, 6$ and plate deflection $Re(\eta_5)$ for different values of **(a)** $a/h = 0.2$, 0.5 and 0.8 ($\theta = 20^0$, $Kh = 0.7$), **(b)** $\epsilon_p = 0.4$, 0.6 and 0.8 ($D/h^4 = 10$, $\theta = 10^0$, $Kh = 0.5$) and **(c)** $f_p = 0.25$, 0.5 and 0.75 ($\theta = 20^0$, $Kh = 0.5$) with $b/h = 5$, $L_1/h = 30$, $L_2/h = 30$, $\epsilon_p = 0.437$.

(a)	(b)
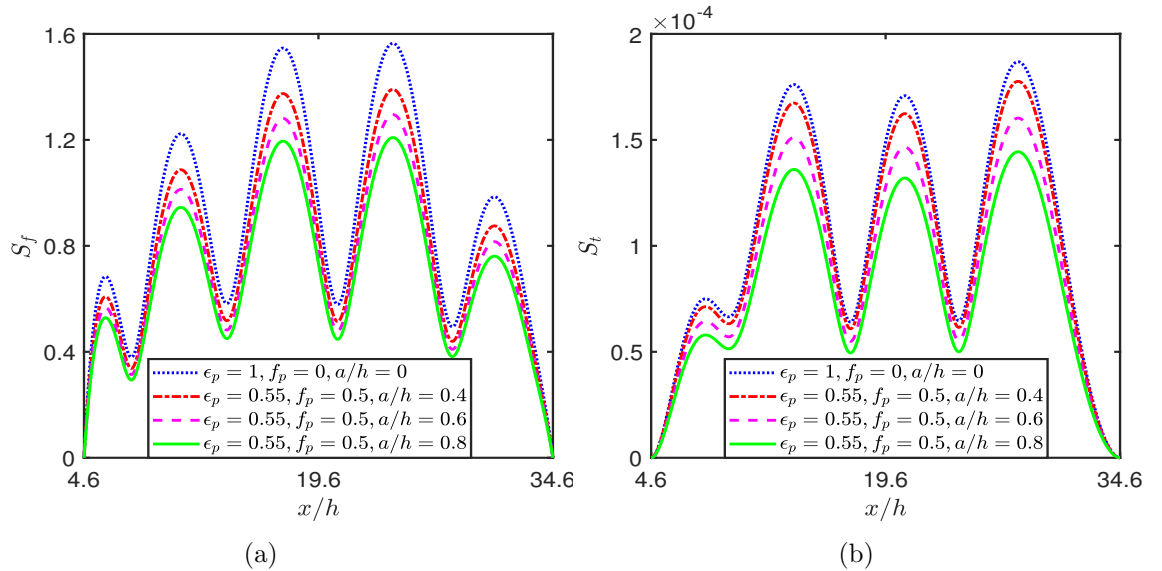
Figure 4.31: S_f and S_t for in the absence SPPS ($a/h = 0$, $f_p = 0$ and $\epsilon_p = 1$) and in the presence of SPPS ($f_p = 0.5$ and $\epsilon_p = 0.55$) for different values of a/h with , $\theta = 0^0$, $Kh = 1$, $L_1/h = 4$, $L_2/h = 30$.

In Figure 4.31, the shear force S_f and strain S_t for different values of length a/h of

SPPS are presented. Here also, as in Figure 4.21, it is observed that S_f and S_t experienced by EP in the absence of SPPS (i.e. $a/h = 0$, $f_p = 0$ and $\epsilon_p = 1$) is more as compared to the case of in the presence of SPPS ($f_p = 0.5$ and $\epsilon_p = 0.55$). Further, the amplitude of shear force/strain is less in SPPS as compared to BSPS.

4.6   Conclusion

The ability to reduce the oblique surface wave impact on EP by a truncated thick porous structure located at a finite distance from EP is analyzed. The related boundary value problem gives rise to a system of linear algebraic equations by using the eigenfunction expansion method and orthogonality of eigenfunction, which is solved numerically to determine the unknown constants corresponding to reflection and transmission coefficients. The dissipation coefficient related to wave energy dissipation is determined through the energy balance relation. This study shows that as the length, porosity, and frictional factor of BSPS/SPPS increase, energy dissipation increases, resulting in a decrease in wave reflection and transmission. With an increase in the width of the porous structure, the reflection coefficient decreases in an oscillating pattern, and for the higher value of structural width, the reflection coefficient becomes constant. The porous structure's structural length, porosity, and friction factors play an important role in reducing plate deflection and free surface elevation on the lee side of EP. With an increase in structural length the shear force and strain on EP decrease. The effect of the wavenumber of incident waves, the gap between the porous structure and elastic plate, and flexural rigidity and length of EP are also analyzed. It is found that SPPS dissipates more wave energy which is concentrated near the free surface, as compared to the BSPS case. Therefore, it can be concluded that with suitable adjustment on truncated thick porous structure and EP, a better coastal protection system can be designed by coastal engineers to diminish the wave impact structural response of EP.

Chapter 5

Mitigation of Wave Load on a Sea Wall by a Truncated Porous Structure in the Presence of an Elastic Plate

5.1 Introduction

In Chapter 4, the mitigation of the structural response of EP in the presence of BSPS and SPPS was analyzed. In Chapter 5, we have extended the problem of Chapter 4 to examine the effectiveness of BSPS/SPPS in reducing wave load on a sea wall in the presence of EP. The physical problem is formulated mathematically and the boundary value problem is solved using the eigenfunction expansion method, which coins to a system of equation through the application of orthogonality of eigenfunctions associated to the free surface region. This system of equations are solved numerically to determine the reflection and dissipation coefficients. The energy identity derived and verified numerically to check the accuracy of the numerical results. The wave response on the wall is analyzed through the wave force experienced by the wall, as well as the reflection and dissipation coefficients. The influence of structural and wave parameters is examined through various graphs. A major part of the work presented in this chapter has been published in Sahoo et al. [120].

5.2 Mathematical Formulation

The problem is formulated in the three-dimensional Cartesian coordinate system under the assumption that the fluid is inviscid, incompressible and the flow is irrotational and simple harmonic in time with angular frequency ω. The y-axis is chosen vertically upward and xz-plane represents the undisturbed free surface of the fluid. The whole fluid region is divided into 6 regions, as in Figure 5.1. The EP ($c \leq x \leq d$ and $y = 0$) of length $L_2 = d - c$ is placed at a distance L_1 from the porous structure and at a distance L_3 from the rigid wall. Here two types of configuration of porous structure, namely (a) BSPS and (b) SPPS, which are isotropic and homogeneous in nature are considered. The areas covered by the porous structure and the gap regions are denoted by L_p and L_g, respectively and the submerged interface of the porous structure represent by L_m where

for BSPS $L_p = (0 \leq x \leq b, \ -h \leq y \leq -h + a)$, $L_g = (0 \leq x \leq b, \ -h + a \leq y \leq 0)$ and $L_m = (0 \leq x \leq b, \ y = -h + a)$ and for SPPS $L_p = (0 \leq x \leq b, \ -a \leq y \leq 0)$, $L_g = (0 \leq x \leq b, \ -h \leq y \leq -a)$ and $L_m = (0 \leq x \leq b, \ y = -a)$. To make sure that the matching conditions at vertical interfaces are satisfied, it is considered that the solution variations in each region are identical (using Snell's law). Since the motion is time harmonic, it can be expressed by $\Phi_j(x, y, z, t) = Re\{\phi_j(x, y)e^{i(\mu z - \omega t)}\}$, satisfying

$$\left(\frac{\partial^2}{\partial x^2} + \frac{\partial^2}{\partial y^2} - \mu^2 \right) \phi_j = 0, \ \text{in each region } j, \tag{5.1}$$

where $\mu = k_0 \sin \theta$ and k_0 is the wavenumber of the propagating wave, which make an angle θ with the x-axis.
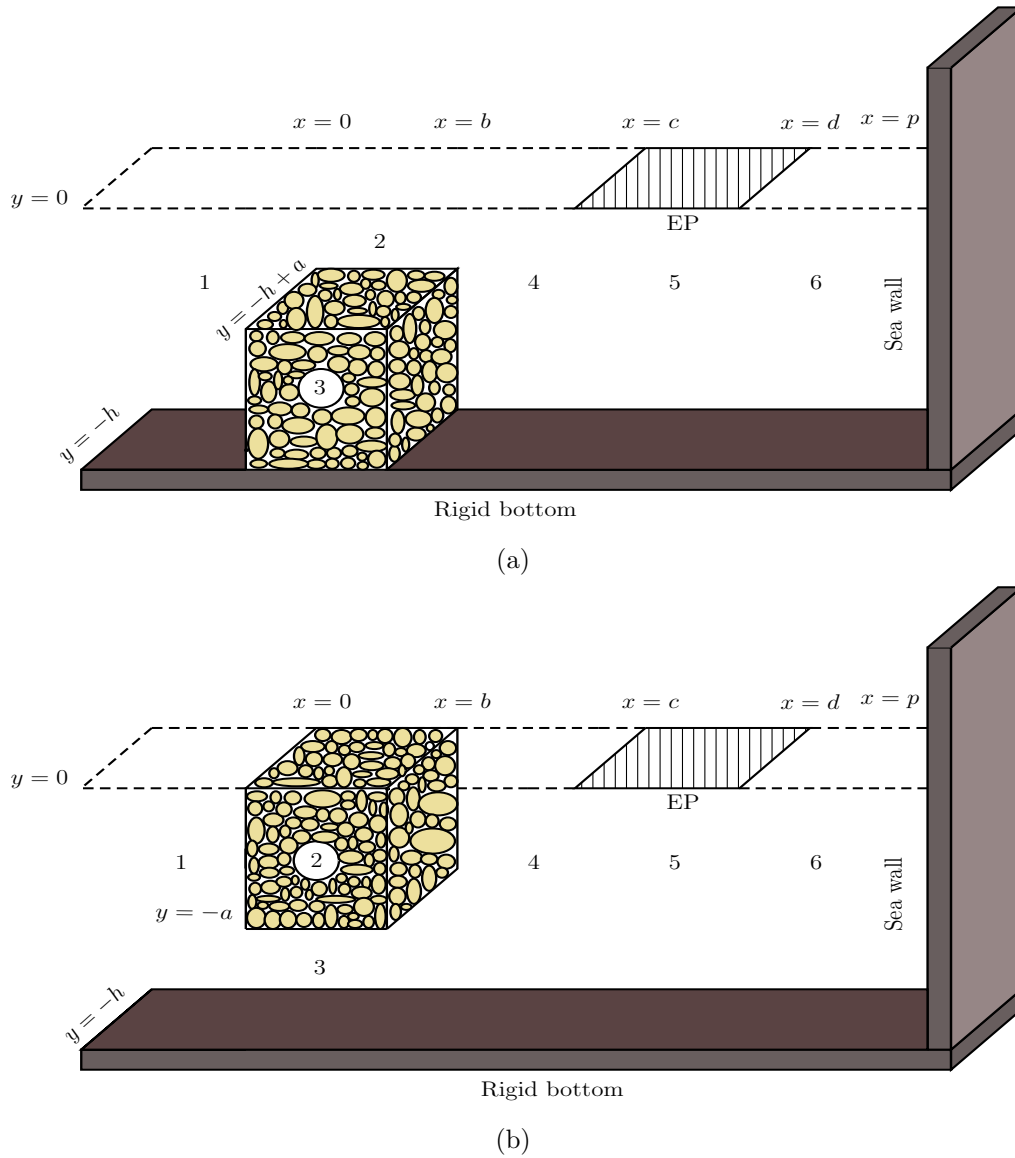
Figure 5.1: Schematic representation of the physical problem in the presence of (a) BSPS and (b)SPPS.

The rigid bottom condition is given as

$$\frac{\partial \phi_j}{\partial y} = 0, \text{ on } y = -h \text{ for } j = 1, 3, 4, 5, 6. \tag{5.2}$$

The condition on the free-surface is represented by

$$\frac{\partial \phi_j}{\partial y} - K\phi_j = 0 \text{ on } y = 0, \tag{5.3}$$

with $K = \omega^2/g$, g is the acceleration due to gravity, $j = 1, 2, 4, 6$ for BSPS and $j = 1, 4, 6$ for SPPS.

For SPPS, the free-surface condition in region 2 is represented by

$$\frac{\partial \phi_j}{\partial y} - K(m_p + if_p)\phi_j = 0 \text{ on } y = 0, \text{ for } j = 2, \tag{5.4}$$

where the non-dimensionalized parameters m_p and f_p stand for the inertial coefficient and frictional factor, respectively.

The boundary condition on EP is used to express by

$$\left[D\left(\frac{\partial^2}{\partial x^2} - \mu^2\right)^2 + 1 - \epsilon_e K \right] \phi_{5y} - K\phi_5 = 0 \text{ on } y = 0, \tag{5.5}$$

where $D = EI/\rho_s g$ is the flexural rigidity of the plate, E is the young's modulus, $I = h_1^3/12(1 - \nu^2)$, h_1 is thickness of EP assumed to be small, ν is the Poisson's ratio, $\epsilon_e = \rho_e h_1/\rho_s$, ρ_s is density of the fluid and ρ_e is density of EP.

By considering EP to be floated freely on the water's surface, the bending moment and shear force at EP's edges will vanish, which yield

$$\left(\frac{\partial^2}{\partial x^2} - \nu\mu^2\right)\frac{\partial \phi_5}{\partial y} = 0 \text{ and } \frac{\partial}{\partial x}\left(\frac{\partial^2}{\partial x^2} - (2 - \nu)\mu^2\right)\frac{\partial \phi_5}{\partial y} = 0 \text{ at } (c, 0) \text{ and } (d, 0). \tag{5.6}$$

The expression for boundary conditions on L_m are given as,

$$\text{for BSPS: } \phi_2 = (m_p + if_p)\phi_3, \ \frac{\partial \phi_2}{\partial y} = \epsilon_p \frac{\partial \phi_3}{\partial y} \text{ on } y = -h + a, \ 0 \leq x \leq b, \tag{5.7}$$

$$\text{for SPPS: } \phi_3 = (m_p + if_p)\phi_2, \ \frac{\partial \phi_3}{\partial y} = \epsilon_p \frac{\partial \phi_2}{\partial y} \text{ on } y = -a, \ 0 \leq x \leq b, \tag{5.8}$$

where ϵ_p is the porosity of BSPS/SPPS. The pressure and velocity continuity conditions, along the interfaces at $x = 0$ and $x = b$ are given as

$$\text{for BSPS: } \phi_j = \begin{cases} \phi_2, & y \in L_g \\ (m_p + if_p)\phi_3, & y \in L_p \end{cases} \text{ and } \frac{\partial \phi_j}{\partial x} = \begin{cases} \frac{\partial \phi_2}{\partial x}, & y \in L_g \\ \epsilon_p \frac{\partial \phi_3}{\partial x}, & y \in L_p, \end{cases} \tag{5.9}$$

$$\text{for SPPS: } \phi_j = \begin{cases} \phi_3, & y \in L_g \\ (m_p + if_p)\phi_2, & y \in L_p \end{cases} \text{ and } \frac{\partial \phi_j}{\partial x} = \begin{cases} \frac{\partial \phi_3}{\partial x}, & y \in L_g \\ \epsilon_p \frac{\partial \phi_2}{\partial x}, & y \in L_p, \end{cases} \tag{5.10}$$

where $j = 1$ at $x = 0$ and $j = 4$ at $x = b$.

For both BSPS and SPPS, the conditions for continuity of pressure and velocity along interfaces at $x = c$ and $x = d$ in the EP region are expressed as

$$\phi_4 = \phi_5, \quad \frac{\partial \phi_4}{\partial x} = \frac{\partial \phi_5}{\partial x} \text{ on } x = c, \ -h \leq y \leq 0, \tag{5.11}$$

$$\phi_5 = \phi_6, \quad \frac{\partial \phi_5}{\partial x} = \frac{\partial \phi_6}{\partial x} \text{ on } x = d, \ -h \leq y \leq 0. \tag{5.12}$$

The rigid wall causes the horizontal velocity component to vanish, which results in

$$\frac{\partial \phi_6}{\partial x} = 0 \text{ on } x = p, \ -h \leq y \leq 0. \tag{5.13}$$

The radiation condition is expressed as

$$\phi_1(x, y) \sim \left(\frac{ig}{\omega} \right) \frac{\cosh k_0(h + y)}{\cosh k_0 h} \{ e^{ik_{0x}x} + R_0 e^{-ik_{0x}x} \} \text{ as } x \to -\infty, \tag{5.14}$$

where $k_{0x} = \sqrt{k_0^2 - \mu^2}$, R_0 is the unknown complex constant associated with reflective wave. In this problem, the singularity at the tip of BSPS/SPPS is not considered.

5.3 Method of Solution

Using the variable separable method to the Helmholtz equation in conjunction with rigid bottom condition and free surface condition, the velocity potential in each region is expressed in terms of eigenfunctions. The velocity potential in regions 1, 4 and 6, satisfying Equations (5.1), (5.2), (5.3), (5.13) and (5.14) can be formulated as follows:

$$\phi_1 = \left(\frac{ig}{\omega} \right) \left[e^{ik_{0x}x} \hat{\psi}_0 + \sum_{m=0}^{\infty} R_m e^{-ik_{mx}x} \hat{\psi}_m \right] \text{ for } -\infty < x \leq 0, \ -h \leq y \leq 0, \tag{5.15}$$

$$\phi_4 = \left(\frac{ig}{\omega} \right) \sum_{m=0}^{\infty} \left[C_m e^{ik_{mx}(x-b)} + D_m e^{-ik_{mx}(x-c)} \right] \hat{\psi}_m \text{ for } b \leq x \leq c, \ -h \leq y \leq 0, \tag{5.16}$$

$$\phi_6 = \left(\frac{ig}{\omega} \right) \sum_{m=0}^{\infty} T_m \cos k_{mx}(x-p) \hat{\psi}_m \text{ for } d \leq x \leq p, \ -h \leq y \leq 0, \tag{5.17}$$

where

$$\hat{\psi}_m = \frac{\cosh k_m(h + y)}{\cosh k_m h}, \ m = 0, 1, 2, \ldots, \tag{5.18}$$

are the eigenfunctions in the free surface region, R_m, C_m, D_m and T_m are unknown complex constants, $k_{mx} = \sqrt{k_m^2 - \mu^2}$ and k_0 is the positive real root and k_m, $m = 1, 2, 3 \ldots$ are the purely imaginary roots of the dispersion relation

$$K - k_m \tanh k_m h = 0. \tag{5.19}$$

For BSPS, in regions 2 and 3, the velocity potential ϕ_2 and ϕ_3 can be given in the forms

$$\phi_2 = \left(\frac{ig}{\omega}\right) \sum_{m=0}^{\infty} \left[F_m e^{ip_{mx}x} + G_m e^{-ip_{mx}(x-b)}\right] Q_m \text{ for } 0 \le x \le b, \ -h+a \le y \le 0, \quad (5.20)$$

$$\phi_3 = \left(\frac{ig}{\omega}\right) \sum_{m=0}^{\infty} \left[F_m e^{ip_{mx}x} + G_m e^{-ip_{mx}(x-b)}\right] M_m \text{ for } 0 \le x \le b, \ -h \le y \le -h+a, \quad (5.21)$$

where as for SPPS, these ϕ_2 and ϕ_3 can be expressed in the forms

$$\phi_2 = \left(\frac{ig}{\omega}\right) \sum_{m=0}^{\infty} \left[F_m e^{ip_{mx}x} + G_m e^{-ip_{mx}(x-b)}\right] Q_m \text{ for } 0 \le x \le b, \ -a \le y \le 0, \quad (5.22)$$

$$\phi_3 = \left(\frac{ig}{\omega}\right) \sum_{m=0}^{\infty} \left[F_m e^{ip_{mx}x} + G_m e^{-ip_{mx}(x-b)}\right] P_m \text{ for } 0 \le x \le b, \ -H \le y \le -a, \quad (5.23)$$

where

$$Q_m = \frac{\cosh p_m(h+y) - \mathcal{A}_m \sinh p_m(h+y)}{\cosh p_m h - \mathcal{A}_m \sinh p_m h}, \ m = 0, 1, 2, \ldots, \quad (5.24)$$

$$M_m = \frac{(1 - \mathcal{A}_m \tanh p_m a) \cosh p_m(h+y)}{(m_p + if_p)(\cosh p_m h - \mathcal{A}_m \sinh p_m h)}, \ m = 0, 1, 2, \ldots, \quad (5.25)$$

$$P_m = \frac{(m_p + if_p)[1 - \mathcal{A}_m \tanh p_m(h-a)] \cosh p_m(h+y)}{(\cosh p_m h - \mathcal{A}_m \sinh p_m h)}, \ m = 0, 1, 2, \ldots, \quad (5.26)$$

$$\mathcal{A}_m = \begin{cases} \frac{(1-G)\tanh p_m a}{1 - G \tanh^2 p_m a} & \text{for BSPS} \\ \frac{(1-G)\tanh p_m(h-a)}{\tanh^2 p_m(h-a) - G} & \text{for SPPS} \end{cases}, \ G = \frac{\epsilon_p}{m_p + if}, \quad (5.27)$$

F_m and G_m are unknown complex constants, $p_{mx} = \sqrt{p_m^2 - \mu^2}$ and $p_m, \ m = 1, 2, 3, \ldots$ are complex roots of the of the equation:

for BSPS: $K - p_m \tanh p_m h - \mathcal{A}_m(K \tanh p_m h - p_m) = 0,$ \quad (5.28)

for SPPS: $K(m_p + if_p) - p_m \tanh p_m h - \mathcal{A}_m[K(m_p + if_p)\tanh p_m h - p_m] = 0.$ \quad (5.29)

Finally, in EP region 5, the velocity potential satisfying Equations (5.1), (5.2) and (5.5) can be expressed in the form

$$\phi_5 = \left(\frac{ig}{\omega}\right) \sum_{m=-2}^{\infty} \left[B_m e^{i\alpha_{mx}(x-a)} + E_m e^{-i\alpha_{mx}(x-d)}\right] \mathcal{F}_m \text{ for } c \le x \le d, \ -h \le y \le \le 0 \quad (5.30)$$

where

$$\mathcal{F}_m = \frac{\cosh \alpha_m(h+y)}{\cosh \alpha_m h}, \ m = -2, -1, 0, 1, 2, \ldots, \quad (5.31)$$

B_m and E_m are unknown constants, $\alpha_{mx} = \sqrt{\alpha_m^2 - \mu^2}$ and α_m are the complex roots of the form $\pm a_1 + ia_2$ for $m = -2, -1$, positive real root for $m = 0$ and purely imaginary

roots for $m = 1, 2, 3, \ldots$ of the dispersion relation given by

$$(D\alpha_m^4 + 1 - \epsilon_e K)\alpha_m \tanh \alpha_m h = K. \tag{5.32}$$

For BSPS, utilizing Equations (5.15)-(5.17), (5.20), (5.21) and (5.30) along with orthogonality of $\hat{\psi}_m$ in matching conditions (5.9)-(5.12), we have

$$U_{0n} + \sum_{m=0}^{\infty} R_m U_{mn} - \sum_{m=0}^{\infty} [V_{mn} + (m_p + if_p)Y_{mn}](F_m + G_m e^{ip_{mx}b}) = 0, \tag{5.33}$$

$$ik_{0x}U_{0n} - \sum_{m=0}^{\infty} R_m ik_{mx}U_{mn} - \sum_{m=0}^{\infty} ip_{mx}[V_{mn} + \epsilon_p Y_{mn}](F_m - G_m e^{ip_{mx}b}) = 0, \tag{5.34}$$

$$\sum_{m=0}^{\infty} (C_m + D_m e^{-ik_{mx}(b-c)})U_{mn} - \sum_{m=0}^{\infty} [V_{mn} + (m_p + if_p)Y_{mn}](F_m e^{ip_{mx}b} + G_m) = 0, \tag{5.35}$$

$$\sum_{m=0}^{\infty} ik_{mx}(C_m - D_m e^{-ik_{mx}(b-c)})U_{mn} - \sum_{m=0}^{\infty} ip_{mx}[V_{mn} + \epsilon_p Y_{mn}](F_m e^{ip_{mx}b} - G_m) = 0, \tag{5.36}$$

$$\sum_{m=0}^{\infty} (C_m e^{ik_{mx}(c-b)} + D_m)U_{mn} - \sum_{m=-2}^{\infty} (B_m + E_m e^{-i\alpha_{mx}(c-d)})X_{mn} = 0, \tag{5.37}$$

$$\sum_{m=0}^{\infty} ik_{mx}(C_m e^{ik_{mx}(c-b)} - D_m)U_{mn} - \sum_{m=-2}^{\infty} i\alpha_{mx}(B_m - E_m e^{-i\alpha_{mx}(c-d)})X_{mn} = 0, \tag{5.38}$$

$$\sum_{m=-2}^{\infty} (B_m e^{i\alpha_{mx}(d-c)} + E_m)X_{mn} - \sum_{m=0}^{\infty} T_m \cos k_{mx}(d-p)U_{mn} = 0, \tag{5.39}$$

$$\sum_{m=-2}^{\infty} i\alpha_{mx}(B_m e^{i\alpha_{mx}(d-c)} - E_m)X_{mn} + \sum_{m=0}^{\infty} k_{mx}T_m \sin k_{mx}(d-p)U_{mn} = 0. \tag{5.40}$$

For SPPS, among Equations (5.33) and (5.40), the Equations (5.33)-(5.36) will be replaced by

$$U_{0n} + \sum_{m=0}^{\infty} R_m U_{mn} - \sum_{m=0}^{\infty} [Z_{mn} + (m_p + if_p)W_{mn}](F_m + G_m e^{ip_{mx}b}) = 0, \tag{5.41}$$

$$U_{0n} - \sum_{m=0}^{\infty} R_m ik_{mx}U_{mn} - \sum_{m=0}^{\infty} ip_{mx}[Z_{mn} + \epsilon_p W_{mn}](F_m - G_m e^{ip_{mx}b}) = 0, \tag{5.42}$$

$$\sum_{m=0}^{\infty} (C_m + D_m e^{-ik_{mx}(b-c)})U_{mn} - \sum_{m=0}^{\infty} [Z_{mn} + (m_p + if_p)W_{mn}](F_m e^{ip_{mx}b} + G_m) = 0, \tag{5.43}$$

$$\sum_{m=0}^{\infty} ik_{mx}(C_m - D_m e^{-ik_{mx}(b-c)})U_{mn} - \sum_{m=0}^{\infty} ip_{mx}[Z_{mn} + \epsilon_p W_{mn}](F_m e^{ip_{mx}b} - G_m) = 0, \tag{5.44}$$

where

$$U_{mn} = \int_{-h}^{0} \hat{\psi}_m \hat{\psi}_n, \ V_{mn} = \int_{-h+a}^{0} Q_m \hat{\psi}_n dy, \ Y_{mn} = \int_{-h}^{-h+a} M_m \hat{\psi}_n dy,$$

$$X_{mn} = \int_{-h}^{0} \mathcal{F}_m \hat{\psi}_n dy, \ Z_{mn} = \int_{-a}^{0} P_m \hat{\psi}_n dy \text{ and } W_{mn} = \int_{-h}^{-a} Q_m \hat{\psi}_n dy. \tag{5.45}$$

Moreover, by using Equation (5.30) in Equation (5.6) (free edge conditions of EP), we have

$$\sum_{m=-2}^{\infty} \alpha_m (\alpha_{mx}^2 + \nu\mu^2)(B_m + E_m e^{-i\alpha_{mx}(c-d)}) \tanh \alpha_m h = 0, \tag{5.46}$$

$$\sum_{m=-2}^{\infty} i\alpha_{mx}\alpha_m (\alpha_{mx}^2 + (2-\nu)\mu^2)(B_m - E_m e^{-i\alpha_{mx}(c-d)}) \tanh \alpha_m h = 0, \tag{5.47}$$

$$\sum_{m=-2}^{\infty} \alpha_m (\alpha_{mx}^2 + \nu\mu^2)(B_m e^{i\alpha_{mx}(d-c)} + E_m) \tanh \alpha_m h = 0, \tag{5.48}$$

$$\sum_{m=-2}^{\infty} i\alpha_{mx}\alpha_m (\alpha_{mx}^2 + (2-\nu)\mu^2)(B_m e^{i\alpha_{mx}(d-c)} - E_m) \tanh \alpha_m h = 0. \tag{5.49}$$

After keeping upto $m = N$ (i.e. truncating the series after $N + 1$), a system with $(8N + 12)$ number of equations with $(8N + 12)$ number of unknowns given in Equations (5.33)-(5.40) and (5.46)-(5.49) is solved for BSPS where as the system with $(8N + 12)$ number of equations with $(8N+12)$ number of unknowns given in Equations (5.37)-(5.40), (5.41)-(5.44) and (5.46)-(5.49) is solved for SPPS. Here, these equations are solved by Gauss elimination method with the help of MATLAB. In this study, plane wave solution is applied (as considered in Sharma et al. [117]), because for almost all the practical cases the plane wave approximation is sufficient to describe the wave behaviour as described in Dalrymple et al. [11]. Once the unknowns are determined, utilizing the velocity potential in the respective region, the force experienced by the wall, EP deflection and free surface elevation can be obtained by the following formulas.

Force experienced by the wall: The wave-induced force F_w on the rigid wall is computed using the integral given by

$$F_w = \left| \frac{-i\omega}{gh^2} \int_{-h}^{0} \phi_6(p, y) dy \right|. \tag{5.50}$$

Plate deflection: The formula for calculating EP deflection is given by

$$\eta_5 = \frac{i}{\omega} \frac{\partial \phi_5}{\partial y} \bigg|_{y=0}. \tag{5.51}$$

Free surface elevation: The formula for calculating free surface elevation is given by

$$\eta_j = \frac{i}{\omega} \frac{\partial \phi_j}{\partial y}\bigg|_{y=0}, \ j = 1,2,4,6 \text{ for BSPS} \tag{5.52}$$

$$j = 1,4,6 \text{ for SPPS.}$$

5.4 Energy Balance Relation

In the present problem, apart from the reflection of waves, a major part of wave energy is dissipated by BSPS/SPPS. Thus, for a better understanding of the quantitative behavior of wave reflection and dissipation, an energy identity is derived. Using the Green's identity, the energy identity for this study can be determined which is represented by

$$\int_{\mathcal{C}} \left(\phi \frac{\partial \hat{\phi}}{\partial n} - \hat{\phi} \frac{\partial \phi}{\partial n} \right) ds = 0, \tag{5.53}$$

where $\hat{\phi}$ is the complex conjugate of ϕ and $\frac{\partial}{\partial n}$ is the outward normal derivative to the boundary $\mathcal{C}$, $\mathcal{C} = \mathcal{C}_1 \cup \mathcal{C}_2$, where for BSPS $\mathcal{C}_1 = \{x = -\mathsf{X}, -h \leq y \leq 0; \ y = -h, -\mathsf{X} \leq x \leq 0; \ x = 0, y \in L_p; \ L_m; \ x = b, y \in L_p; \ y = -h, b \leq x \leq p; \ x = p, -h \leq y \leq 0; \ y = 0, d \leq x \leq p; \ y = 0, c \leq x \leq d; \ y = 0, -\mathsf{X} \leq x \leq c\}$, $\mathcal{C}_2 = \{ x = 0, y \in L_p; \ L_m; \ x = b, y \in L_p; \ y = -h, 0 \leq x \leq b \}$. The contribution from $\mathcal{C}_1$ and $\mathcal{C}_2$ (except the line $x = p, -h \leq y \leq 0$) will be same as in Section 4.4. The line $x = p, -h \leq y \leq 0$ contributes

$$\int_{\mathcal{C}} \left(\phi \frac{\partial \hat{\phi}}{\partial n} - \hat{\phi} \frac{\partial \phi}{\partial n} \right) ds = 0. \tag{5.54}$$

By combining all the contributions from $\mathcal{C}_1$ and $\mathcal{C}_2$, the energy identity is derived as

$$|R_0|^2 + k_d = 1 \tag{5.55}$$

where

$$k_d = \frac{2k_0 \cosh^2 k_0 h}{ik_{0x}(\sinh 2k_0 h + 2k_0 h)} \left[\int_{L_p} \left([\epsilon_p(m_p + if_p) - 1] \phi_3 \phi_{3x}^* - [\epsilon_p(m_p - if_p) - 1] \phi_3^* \phi_{3x} \right) dy \bigg|_{x=0} \right.$$

$$+ \int_{L_p} \left([\epsilon_p(m_p - if_p) - 1] \phi_3^* \phi_{3x} - [\epsilon_p(m_p + if_p) - 1] \phi_3 \phi_{3x}^* \right) dy \bigg|_{x=b}$$

$$+ \left. \int_{L_m} \left([\epsilon_p(m_p - if_p) - 1] \phi_3^* \phi_{3y} - [\epsilon_p(m_p + if_p) - 1] \phi_3 \phi_{3y}^* \right) dx \right]. \tag{5.56}$$

Similarly, by selecting the appropriate contour along SPPS, the energy identity can be

found as $|R_0|^2 + k_d = 1$, where

$$k_d = \frac{2k_0 \cosh^2 k_0 h}{ik_{0x}(\sinh 2k_0 h + 2k_0 h)} \left[\int_0^r -2iK f_p |\phi_2|^2 dx \right.$$
$$+ \int_{L_p} \left([\epsilon_p(m_p + if_p) - 1] \phi_2 \phi_{2x}^* - [\epsilon_p(m_p - if_p) - 1] \phi_2^* \phi_{2x} \right)_{x=0} dy$$
$$+ \int_{L_p} \left([\epsilon_p(m_p - if_p) - 1] \phi_2^* \phi_{2x} - [\epsilon_p(m_p + if_p) - 1] \phi_2 \phi_{2x}^* \right)_{x=b} dy$$
$$+ \left. \int_{L_m} \left([\epsilon_p(m_p + if_p) - 1] \phi_2 \phi_{2y}^* - [\epsilon_p(m_p - if_p) - 1] \phi_2^* \phi_{2y} \right) dx \right].$$

(5.57)

5.5 Results and Discussion

In this section, the usefulness of a thick porous structure to minimize the wave effect on a rigid wall in the presence of EP is studied through reflection coefficient $|R_0|$, dissipation coefficient k_d, wave force (F_w) experienced by the wall, free surface elevation ($Re(\eta_1)$, $Re(\eta_j)$) and plate deflection (η_5). Unless otherwise specified, the non-dimensional parameters $k_0 h = 1$, $b/h = 0.6$, $a/h = 0.5$, $m_p = 1$, $f_p = 0.5$, $\epsilon_p = 0.5$, $\theta = 20^0$, $L_1/h = 4$, $\epsilon_e/h = 0.01$, $L_2/h = 5$, $D/h^4 = 50$ and $L_3/h = 6$ will remain fixed throughout this study. In this section, several computations are done, but to avoid repetition, few results are presented.

5.5.1 Convergence Study for N

Within the context of our study, Table 5.1 investigates the convergence of the number of evanescent modes, denoted as N. The table provides a detailed record of $|R_0|$ associated with various values of $k_0 h$, considering different N values, specifically $N = 0$, 2, 4, 6, and 8. Significantly, a consistent trend emerges wherein the precision of $|R_0|$ calculations extends reliably up to the fourth decimal point when N is fixed at 4, regardless of the chosen $k_0 h$ values. But in Figure 5.2, it is observed that the behavior of the curve for the reflection coefficient corresponding to plane wave solution is similar to the curve for the full wave solution for $N = 4$. Since the plane-wave approximation is sufficient to describe the wave behavior as mentioned by Dalrymple et al. [11], we have taken $N = 0$ for plotting all graphs.

$k_0 h$	$N=0$	$N=2$	$N=4$	$N=6$	$N=8$
0.25	0.9979	0.9973	0.9973	0.9973	0.9973
0.5	0.9933	0.9913	0.991	0.991	0.991
0.75	0.9947	0.9936	0.9935	0.9935	0.9935
1	0.9956	0.9945	0.9944	0.9944	0.9944
1.25	0.9791	0.9726	0.9717	0.9717	0.9717
1.5	0.9942	0.9920	0.9918	0.9918	0.9918

Table 5.1: Convergence of N through $|R_0|$ with $f_p = 0.25$ and $a/h = 0.2$.
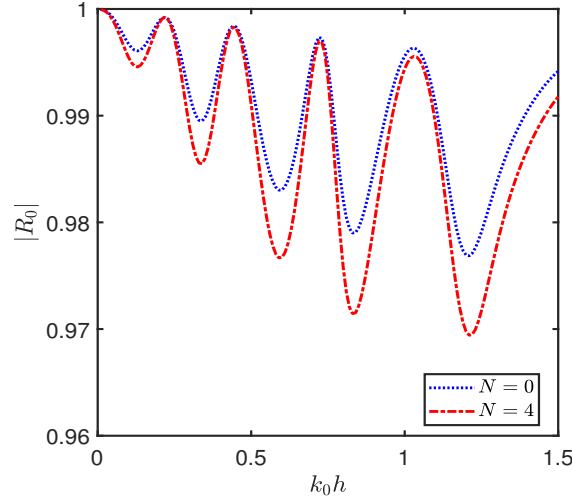
Figure 5.2: Comparison between plane wave solution ($N = 0$) and full wave solution ($N = 4$) with $f_p = 0.25$ and $a/h = 0.2$.

5.5.2 Validation

For the validation of the current numerical results with the existing literature, it is noted that without the presence of EP, the present problem is equivalent to the work by Koley et al. [19]. Table 5.2 and Figure 5.3a depicts the outcomes of the current problem without the presence of EP (i.e. $D/h^4 = 0$, $\epsilon_e/h = 0$) with $\epsilon_p = 0.437$, $a/h = 0.2$, $f_p = 0.5$, $\theta = 10^0$ and $L/\lambda = 1$ ($L = L_1 + L_2 + L_3$ and $\lambda = 2\pi/k_0$), which shows a close agreement with the results of Koley et al. [19]. It may be noted that when the length a/h of the porous structure is equal to 1, the present problem reduces to the problem of Chapter 3. From the Figure 5.3b it is observed that the results of $|R_0|$ are well-matched with the results of Chapter 3 (Figure 3.12a). Further, to verify the energy identity given by Equation (5.55), the values of k_d and $1 - |R_0|^2$ are calculated numerically for various values of k_0h and tabulated in Table 5.3. It is revealed from Table 5.3 that the energy identity relation holds with close agreement for both cases (BSPS and SPPS).

N	a/h	Koley et al. (2015) ($|R_0|$)	Present Study ($|R_0|$)
1	0.2	0.99870	0.999
	0.5	0.99288	0.996
	0.8	0.96334	0.965
3	0.2	0.99917	0.9993
	0.5	0.99462	0.9939
	0.8	0.96483	0.965
5	0.2	0.99918	0.9991
	0.5	0.99623	0.9968
	0.8	0.965	0.965

Table 5.2: Comparison of present results with Koley et al. [19] for $|R_0|$ for a porous structure in the presence of a sea wall and in the absence of elastic plate for different values of a/h.

(a)
(b)
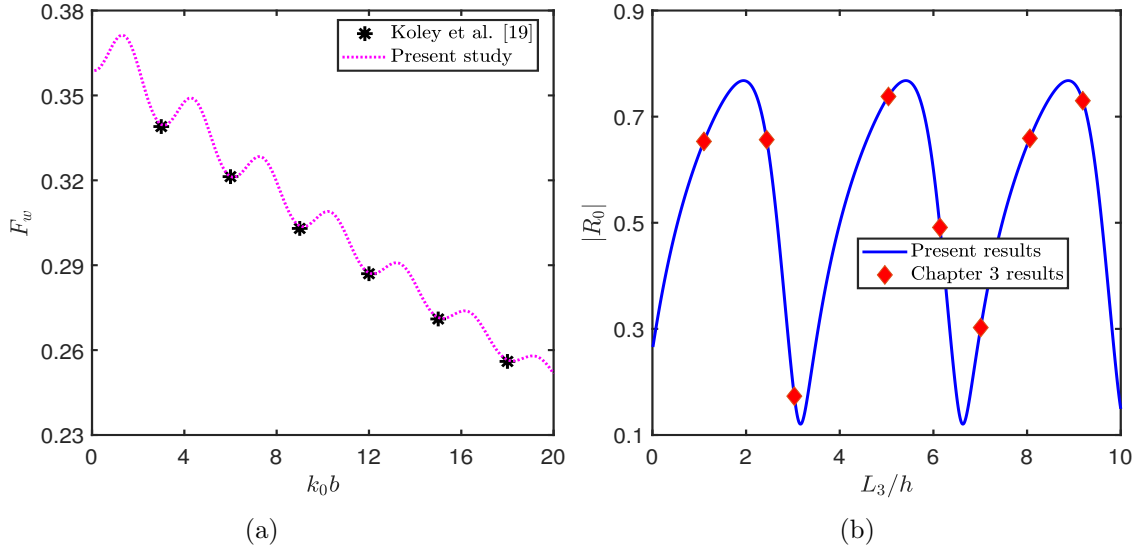
Figure 5.3: Validation of the numerical results with results of **(a)** Koley et al. [19] with $\epsilon_p = 0.437$, $a/h = 0.2$, $f_p = 0.5$, $\theta = 10^0$ and $L/\lambda = 1$ ($L = L_1 + L_2 + L_3$ and $\lambda = 2\pi/k_0$) and **(b)** Chapter 3 with $k_0h = 1$, $a/h = 1$, $b/h = 1$, $m_p = 1$, $f_p = 0.5$, $\epsilon_p = 0.5$, $\theta = 25^0$, $L_1/h = 8$, $D/h^4 = 50$, $\epsilon_e/h = 0.01$, $L_2/h = 10$ and $L_3/h = 12$.

k_0h	BSPS			SPPS		
	$\lvert R_0 \rvert$	$1 - \lvert R_0 \rvert^2$	k_d	$\lvert R_0 \rvert$	$1 - \lvert R_0 \rvert^2$	k_d
0.25	0.9867	0.0263	0.0263	0.8962	0.1968	0.1968
0.5	0.9546	0.0887	0.0887	0.8054	0.3513	0.3512
0.75	0.9629	0.0729	0.0728	0.7180	0.4845	0.4843
1	0.9670	0.0649	0.0647	0.7383	0.4549	0.4547
1.25	0.8833	0.2194	0.2192	0.6660	0.5565	0.5562
1.5	0.9468	0.1032	0.1031	0.7415	0.4502	0.4500

Table 5.3: Verification of energy identity.
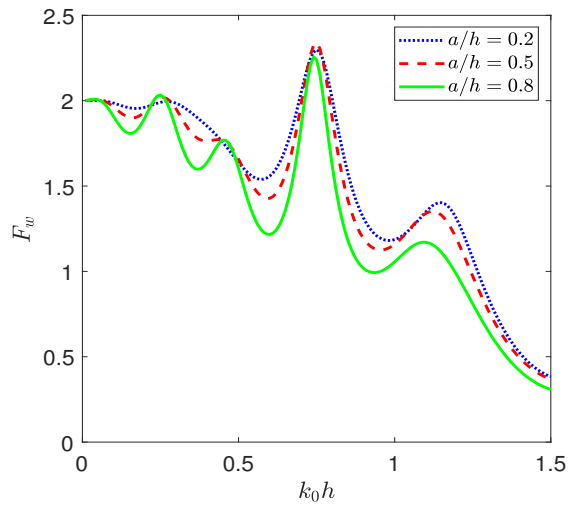
Figure 5.4: Force F_w versus wavenumber k_0h for various values of a/h of BSPS with $b/h = 1$.

5.5.3 Effect of BSPS on Force (F_w) Experienced on the Wall, Reflection Coefficient ($|R_0|$), Dissipation Coefficient (k_d), Plate Deflection ($Re(\eta_5)$) and Free Surface Elevation ($Re(\eta_j), j = 1, 2, 4, 6$)

In this section, the influence of BSPS on F_w, $|R_0|$, k_d, $Re(\eta_5)$ and $\eta_j, j = 1, 2, 4, 6$ is studied through different graphs for different parameters as described below.

Figure 5.4 shows the behavior of the force F_w experienced by the wall versus wavenumber k_0h for various values of length a/h of BSPS. The figure shows that with an increase in k_0h, the force F_w experienced by the wall decreases in an oscillatory pattern. It is also noted that with an increase in a/h, the force F_w decreases. This may be because, as a/h increases, more wave energy is dissipated and reflected by BSPS, and fewer waves are transmitted toward the wall.

Figure 5.5a shows the force F_w versus L_1/h variations for different flexural rigidity D/h^4 values. It is viewed that the force experienced by the vertical wall diminishes as EP's flexural rigidity increases. This is because the increase in flexural rigidity of EP makes it more rigid, implying more incident waves are reflected back and less incident waves are transmitted below EP (as observed in Sahoo et al. [68]), causing less force experienced by the wall. Figure 5.5b shows the force F_w versus L_1/h for different lengths L_2/h of EP. It is observed that with an increase in L_2/h, the force experienced by the wall decreases. This may be because the longer EP reflects more incident waves, causing less wave impact on the wall. Furthermore, in both the Figures 5.5a and 5.5b, force shows oscillatory and periodic patterns with respect to L_1/h. The occurrence of optima in wave force may be due to the of constructive and destructive interference between the incident wave and reflective wave, as discussed by Koley et al. [19].
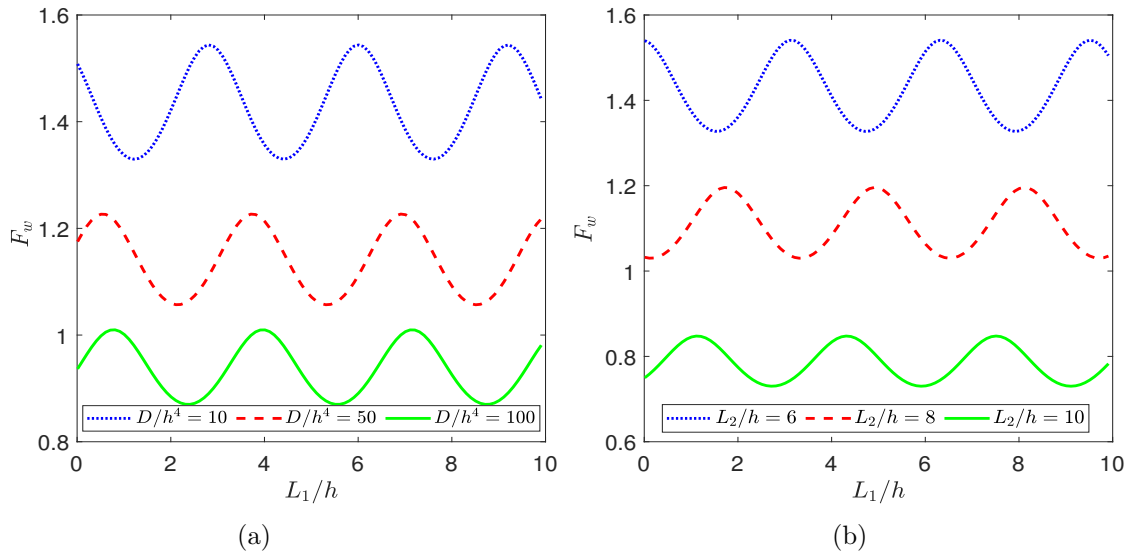
Figure 5.5: Force F_w versus gap L_1/H between BSPS and EP for various values of **(a)** flexural rigidity D/h^4 ($\theta = 10^0$) and **(b)** length L_2/h of EP ($\theta = 10^0$).

Figures 5.6a and 5.6b show the force F_w versus L_1/h for different lengths (a/h) and widths (b/h) of BSPS, respectively. The force F_w demonstrates an oscillatory and periodic

pattern with varying L_1/h, as illustrated in Figure 5.5. It is observed that as a/h (or b/h) increases, the force F_w on the wall decreases. This is because when a/h (or b/h) increases, energy dissipation by the porous structure increases; thereby, the transmission of energy towards the wall decreases, implying less force experienced by the wall; hence the wall is protected. Further, it is highlighted that the minima in wave force F_w are observed when the gap (L_1) between BSPS and EP is approximately an odd integral multiple of the depth of water (h).
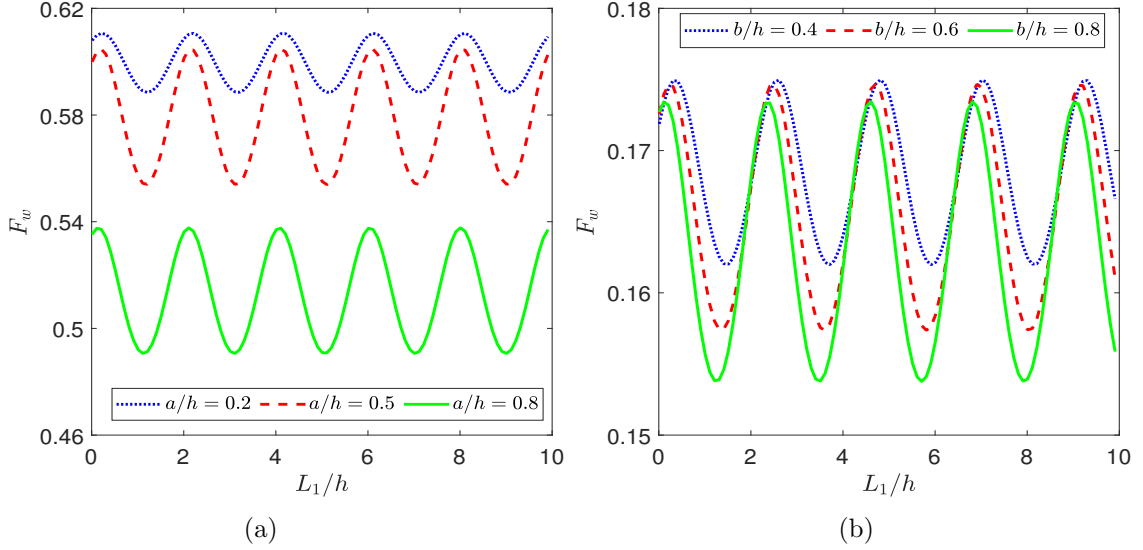
Figure 5.6: Force F_w versus gap L_1/H between BSPS and EP for various values of **(a)** length a/h ($k_0 h = 1.7$ and $D/h^4 = 100$) and **(b)** width b/h of BSPS ($k_0 h = 1.5$ and $D/h^4 = 100$).
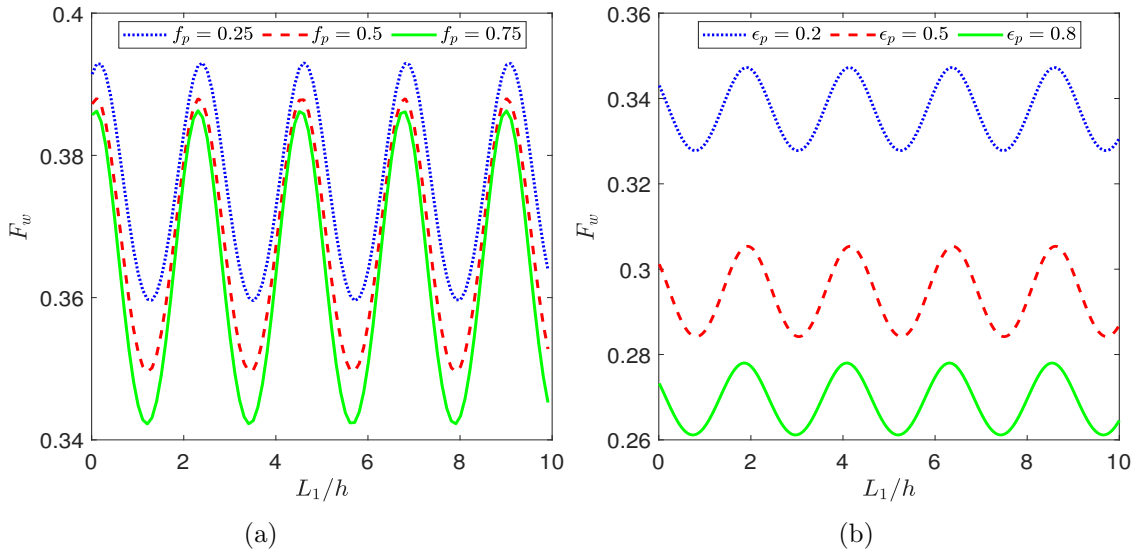
Figure 5.7: Force F_w versus gap L_1/h between BSPS and Ep for various values of **(a)** frictional factor f_p ($k_0 h = 1.5$) and **(b)** porosity ϵ_p of BSPS ($k_0 h = 1.5$ and $b/h = 3.5$).

Figures 5.7a and 5.7b show the force F_w versus L_1/h for different frictional coefficient

f_p and porosity ϵ_p values of BSPS, respectively. From both the Figures 5.7a and 5.7b, it is observed that the force F_w exhibits oscillatory and periodic behavior with respect to L_1/h and the minima in wave force F_w on the vertical wall are observed when the gap (L_1) between the porous structure and EP is approximately odd integral multiple of depth of water (h), as seen in Figure 5.6. It is also found that the force experienced by the wall diminishes as f_p (or ϵ_p) increases because the porous structure dissipates more energy as f_p (or ϵ_p) increases, which results in less energy being transmitted towards the wall, yielding less force experienced by the wall.
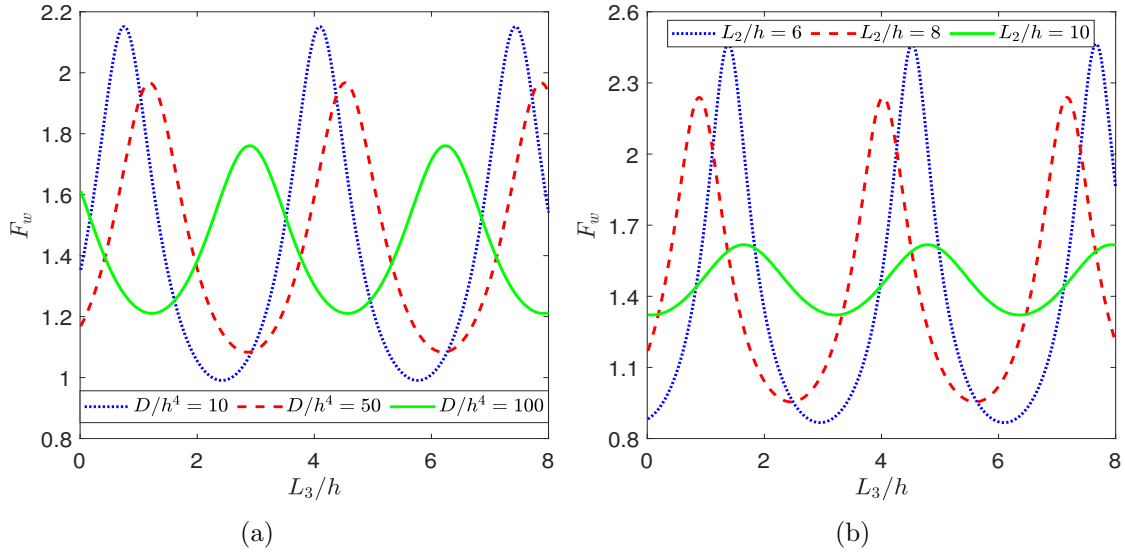
Figure 5.8: Force F_w versus gap L_3/h between EP and sea wall for various values of **(a)** flexural rigidity D/h^4 ($L_1/h = 6$) and **(b)** length L_2/h of EP ($\theta = 0^0$ and $D/h^4 = 10$).

Figures 5.8a and 5.8b depict the variations in force F_w versus L_3/h for different flexural rigidity D/h^4 and length L_2/h values of EP, respectively. It is observed that the Force F_w is oscillatory and periodic in nature with respect to the gap L_3/h between EP and the wall. Figure 5.8a shows that as D/h^4 increases, the maximum value of F_w decreases. However, the maxima are shifted towards the right for an increase in D/h^4 values. In Figure 5.8b, it is found that as the length of EP increases, the maximum value of F_w decreases. It is also noted that the amplitude of force F_w reduces significantly for EP with higher flexural rigidity D/h^4, which is supported by the fact that as D/h^4 value increases, the plate behaves more like a rigid plate, thereby reflecting more wave energy and thus reducing the force experienced by the wall. When L_2/h (length of EP) increases, more wave energy is reflected back by EP and less wave energy is transmitted towards the wall.

Figures 5.9a and 5.9b show force F_w versus L_3/h variations for different f_p and ϵ_p values, respectively. Force F_w follows an oscillatory and periodic pattern with respect to L_3/h, as found in Figure 5.8. From both Figures 5.9a and 5.9b, it is noted that as f_p (or ϵ_p) increases, force F_w is slightly reduced. This may be with an increase in f_p (or ϵ_p), a major part of the wave energy is dissipated by the porous structure. Hence less

wave trapped in between EP and vertical wall. Additionally, by observing Figure 5.9b, it becomes evident that the force experienced by the wall is greater when there is no porous structure ($\epsilon_p = 1$ and $f_p = 0$) compared to when a porous structure is present.
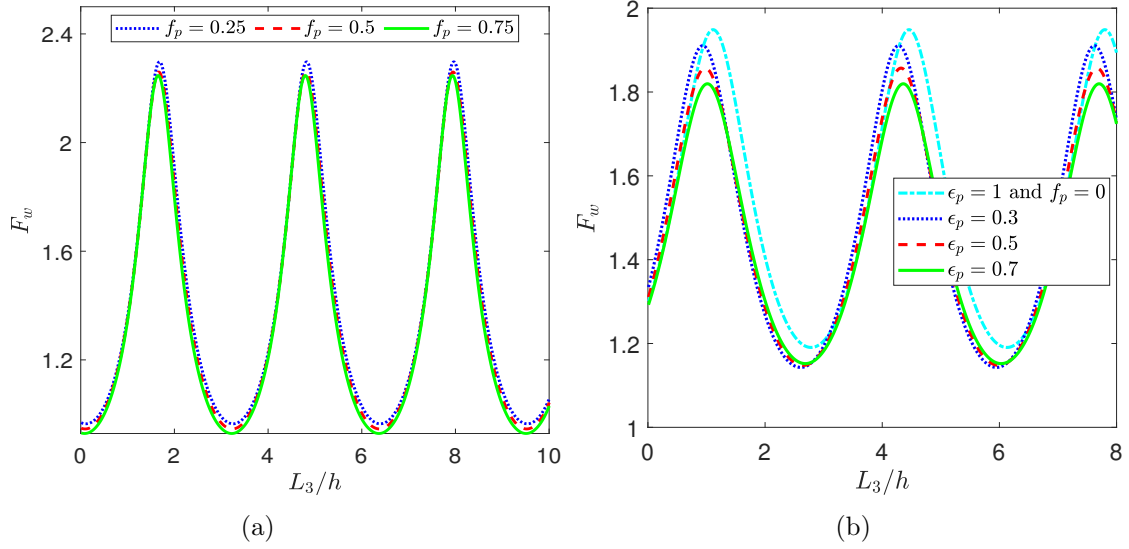
Figure 5.9: Force F_w versus gap L_3/h between EP and sea wall for various values of **(a)** frictional factor f_p ($D/h^4 = 10$ and $\theta = 0^0$) and **(b)** porosity ϵ_p of BSPS.
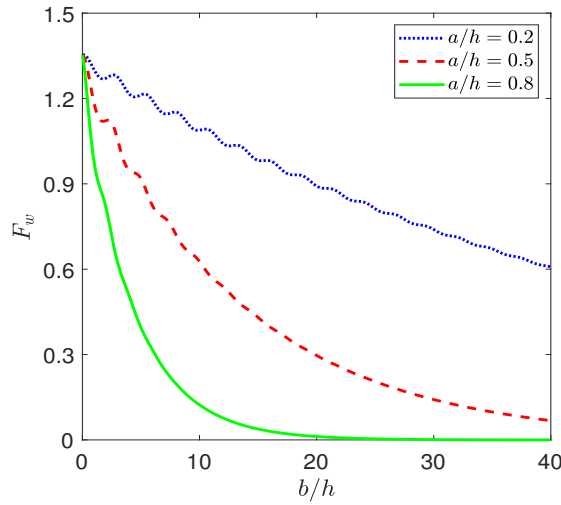
Figure 5.10: Force F_w versus width b/h for various values of a/h of BSPS with $k_0 h = 1.2$.

Figure 5.10 shows the variation of F_w versus b/h for different values of a/h. From the figure it is found that with an increase in b/h, force F_w on the rigid wall decreases and for higher values of b/h, force F_w goes to zero. This may be due to the fact that the porous structure with higher width b/h absorbs all the incident waves and no wave is transmitted towards the wall. It is also found that for smaller values of a/h the oscillatory pattern in F_w appears upto certain values of b/h and for higher values of a/h the oscillatory pattern vanishes.

Figure 5.11 depicts the variations in reflection coefficient $|R_0|$ and dissipation

coefficient k_d versus wavenumber $k_0 h$ for different values of porosity ϵ_p. From Figure 5.11a, it is noted that with the increase in $k_0 h$ ($0 < k_0 h < 1.7$), $|R_0|$ decreases in an oscillatory pattern and the amplitude of oscillation increases. But when $k_0 h \sim 1.7$, the curve is not smooth. After that, with the increase in $k_0 h$, $|R_0|$ increases in an oscillatory pattern and the amplitude of oscillations decreases. Figure 5.11b shows that when $k_0 h$ varies from 0 to 1.7, k_d increases in an oscillatory pattern and amplitude oscillation also increases. But when $k_0 h \sim 1.7$, the curve is not smooth, as in Figure 5.11a. After that, with the increase in $k_0 h$, k_d decreases and the amplitude of oscillations also decreases. However, with an increase in ϵ_p more wave energy is dissipated and less wave energy is reflected.
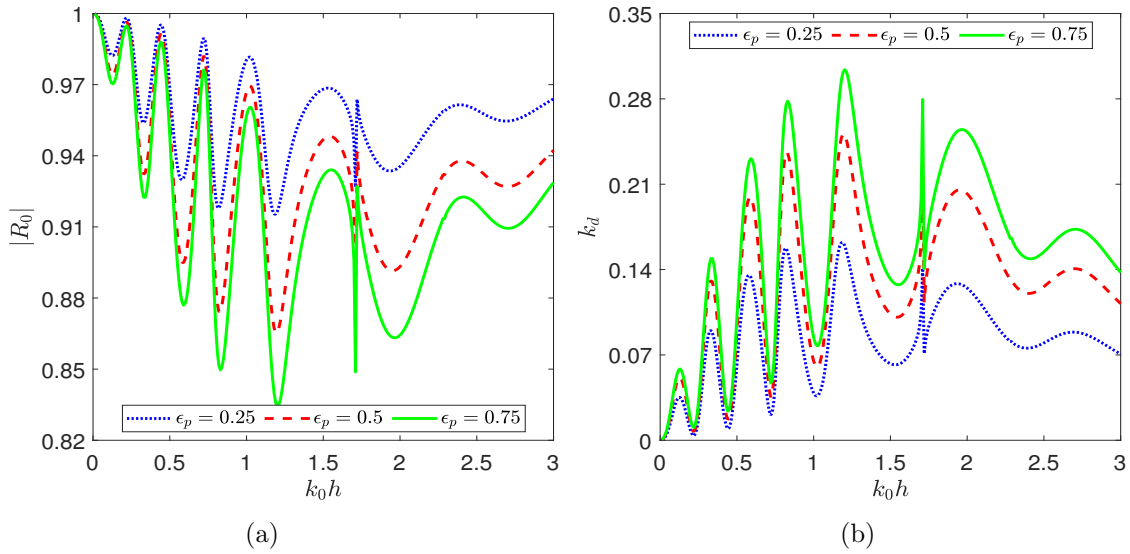
Figure 5.11: Reflection coefficient $|R_0|$ and dissipation coefficient k_d versus wave number $k_0 h$ for various values of porosity ϵ_p of BSPS.

Figure 5.12 illustrates the behavior of $|R_0|$ and k_d versus L_1/h for various values of a/h. In this figure, $|R_0|$ and k_d show an oscillatory and periodic pattern with L_1/h, similar to the pattern of force F_w versus L_1/h, as in Figure 5.6a. This optimum in wave reflection may be due to the resonating interaction of waves in a confined zone between BSPS and EP. Further, it is highlighted that minima in wave reflection $|R_0|$ are observed when the distance L_1 between BSPS and EP is approximate to the odd integral multiple of the depth of water (h). In addition, the wave reflection $|R_0|$ (and dissipation k_d) reaches a minimum value in between two maximum values. It is also noted that with an increase in a/h, the wave reflection decreases and dissipation increases. Comparing Figure 5.6a with Figure 5.12a, it is found that the optimum in wave reflection corresponds to optima in wave force experienced by the wall.

The distribution of reflection coefficient $|R_0|$ and dissipation coefficient k_d against L_3/h for different values of f_p are plotted in Figures 5.13a and 5.13b, respectively. In these figures, $|R_0|$ and k_d follow a periodic and oscillatory pattern with L_3/h, similar to the pattern of force F_w versus L_3/h, as in Figure 5.9a. The optimum in wave reflection

may be due to the constructive and destructive interference between the incident wave and the reflected wave. It is also found that with an increase in f_p, the porous structure dissipates more wave energy; consequently, wave reflection decreases.
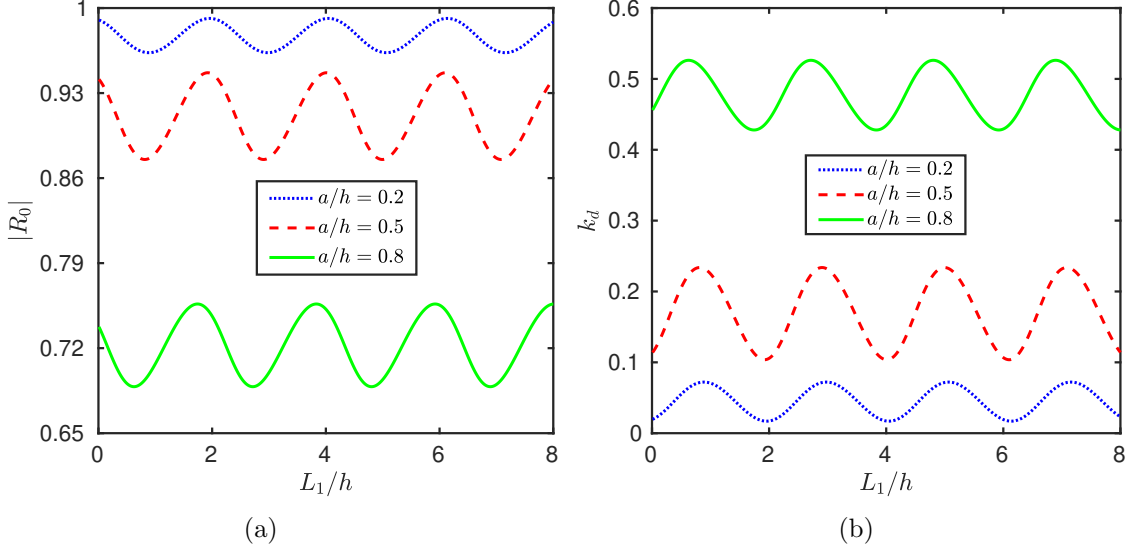
Figure 5.12: Reflection coefficient $|R_0|$ and dissipation coefficient k_d versus gap L_1/h between BSPS and EP for various values of length a/h of BSPS with $k_0 h = 1.7$ and $D/h^4 = 100$.

Figure 5.13: Reflection coefficient $|R_0|$ and dissipation coefficient k_d versus gap L_3/h between EP and sea wall for various values of frictional coefficient f_p of BSPS.

In Figure 5.14, reflection coefficient $|R_0|$ and dissipation coefficient k_d versus angle of incidence θ are plotted for different values for b/h. The figure illustrates that for $0^0 < \theta < 60^0$ (close to 60^0), $|R_0|$ and k_d follow an oscillatory pattern. When $\theta \sim 60^0$, there is a sudden fall in $|R_0|$ and a sudden rise in k_d. However, when $\theta \sim 87^0$, there is a sudden rise in $|R_0|$ and it becomes unity when $\theta = 90^0$ for all values of b/h. Also, there is

a sudden fall in k_d for $\theta \sim 87^0$ and k_d becomes zero when $\theta = 90^0$ for all values of b/h. The angle $\theta = 87^0$, where the reflection coefficient reaches its global minimum, is identified as the critical angle. Further, the figure shows that the global minima of $|R_0|$ decreases and the global maxima of k_d increases with an increase in b/h.

(a)   (b)

Figure 5.14: Reflection coefficient $|R_0|$ and dissipation coefficient k_d versus angle of incident θ for width b/h of BSPS.

(a)   (b)
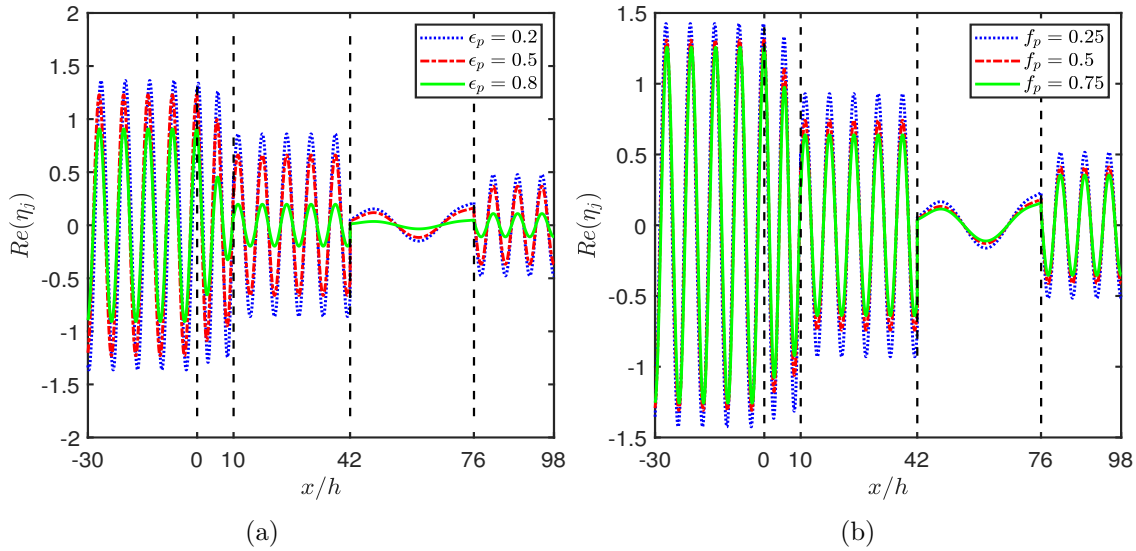
Figure 5.15: Plate deflection $(Re(\eta_5))$ and free surface elevation $(Re(\eta_j), j = 1, 2, 4, 6)$ for various values of **(a)** porosity ϵ_p $(D/h^4 = 10)$ and **(b)** frictional factor f_p $(\epsilon_p = 0.437, D/h^4 = 10^2)$ with $b/h = 10$, $L_1/h = 32$, $L_2/h = 34$, $L_3/h = 22$.

Figures 5.15a and 5.15b show the behavior of plate deflection $(Re(\eta_5))$ and free surface elevation $(Re(\eta_j), j = 1, 2, 4, 6)$ for different values of ϵ_p and f_p, respectively. From these figures, it is noted that the free surface elevation $(Re(\eta_6))$ in Region 6 and the EP deflection $(Re(\eta_5))$ in Region 5 are less than the free surface elevation (η_1) in Region 1 for fixed

values of ϵ_p and f_p due to the fact that the porous structure dissipates a major part of the wave energy and less wave energy is transmitted towards EP and vertical wall. Further, from Figure 5.15a, it is noted that as ϵ_p increases, the amplitude of free surface elevation ($Re(\eta_6)$) is reduced in the region 6 between EP and wall, creating a calm zone for safe navigation. From Figure 5.15b, it is noted that as f_p increases, the amplitude of oscillation is reduced in Region 6 between EP and wall, thus creating a calm zone for the marine environment.

(a) (b)
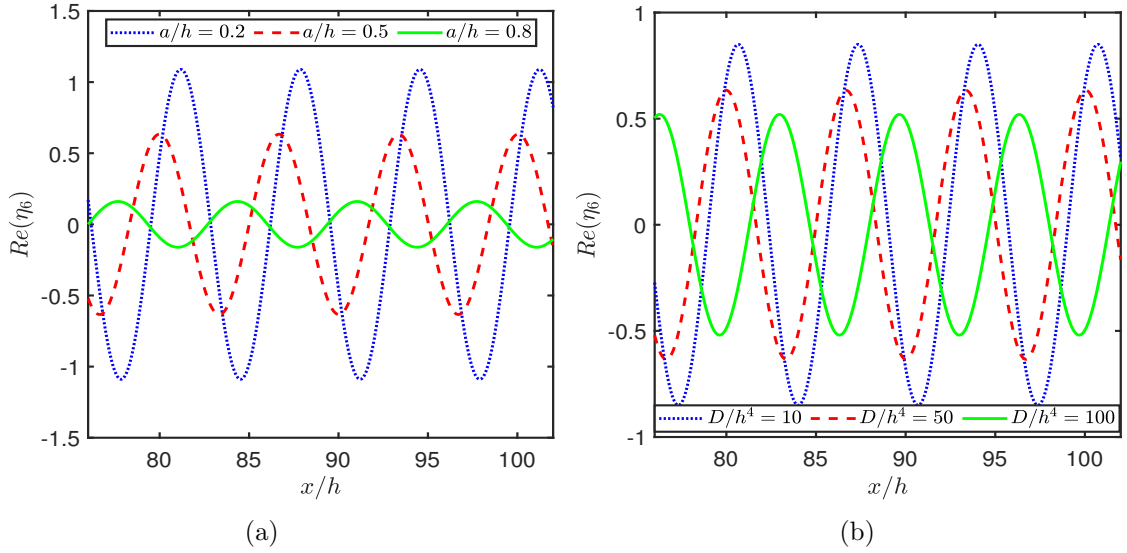
Figure 5.16: $Re(\eta_6)$ for various values of **(a)** length a/h and **(b)** flexural rigidity D/h^4 with $b/h = 10$, $L_1/h = 32$, $L_2/h = 34$ and $L_3/h = 26$.
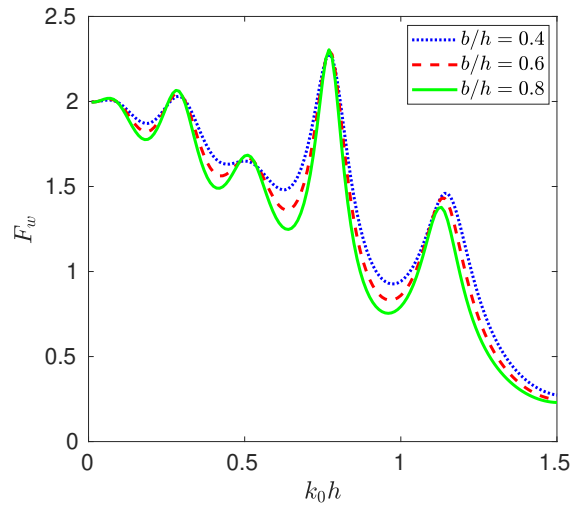
Figure 5.17: Force F_w versus wavenumber $k_0 h$ for various values of b/h of SPPS.

Figure 5.16 show the variations of free surface elevation $Re(\eta_6)$ in region 6 for different a/h and D/h^4. In Figures 5.16a and 5.16b, the patterns observed here are oscillatory and periodic. In Figure 5.16a, it is found that with an increase in a/h, $Re(\eta_6)$ decreases. This is because with an increase in a/h, dissipation of wave energy by porous structure

increases and less wave energy is transmitted towards the vertical wall, which creates a calm zone for safe navigation. Further, in Figure 5.16b, it is found that as D/h^4 value increases, $Re(\eta_6)$ decreases, and thus a calm zone is created in region 6. This is due to the fact that as D/h^4 value increases, EP becomes more rigid, thus more wave energy is reflected by EP and less wave energy is transmitted towards the vertical wall. Therefore, an EP with higher value flexural rigidity helps in creating a tranquility zone, which is the objective of the study. From these Figures 5.15 and 5.16, it can be concluded that the porous structure with higher values of ϵ_p, f_p, a/h and EP with higher values of D/h^4 plays a significant role in protecting the rigid wall.

5.5.4 Effect of SPPS on Force (F_w) Experienced on the Wall, Reflection Coefficient ($|R_0|$), Dissipation Coefficient (k_d), Plate Deflection ($Re(\eta_5)$) and Free Surface Elevation ($Re(\eta_j), j = 1, 4, 6$)

In this section, the numerical results for F_w, $|R_0|$, k_d, $Re(\eta_5)$ and $Re(\eta_j), j = 1, 4, 6$ are plotted through graphs for different parameters by replacing BSPS with SPPS.

Figure 5.17 shows the behavior of the force F_w experienced by the wall versus wavenumber k_0h for various values of width b/h of SPPS. From the figure, it can be found that F_w decreases in an oscillatory pattern with an increase in k_0h, as observed for the case of BSPS (see Figure 5.4). Further, it is observed that with an increase in b/h, the force experienced by the wall decreases. This may be due to the fact that with an increase in b/h, more wave energy is reflected and dissipated by the SPPS.
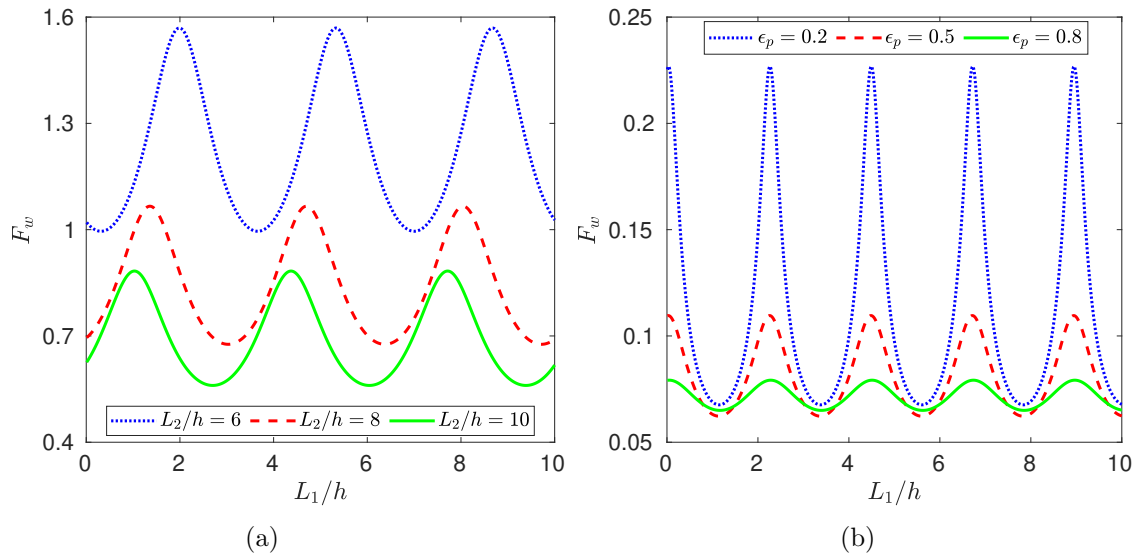
Figure 5.18: Force F_w versus gap L_1/h between SPPS and EP for various values of **(a)** length L_2/h ($D/h^4 = 100$) and **(b)** porosity ϵ_p ($k_0h = 1.5$, $b/h = 3.5$).

Figure 5.18 gives the behavior of force F_w versus L_1/h for different values of L_2/h and ϵ_p. From the Figures 5.18a and 5.18b, it is observed that with respect to L_1/h, force F_w follows an oscillatory and periodic pattern and also found that with an increase in L_2/h (or ϵ_p), the force F_w on the wall decreases, which is similar to the results in the presence

of BSPS, as in Figures 5.5b and 5.7b. Comparing Figure 5.7b with Figure 5.18b, it can be seen that wave force F_w on the wall is less in the case of SPPS in comparison to the case of BSPS. This may be due to, SPPS dissipating more wave energy concentrated at the free surface as compared to BSPS.

(a)	(b)
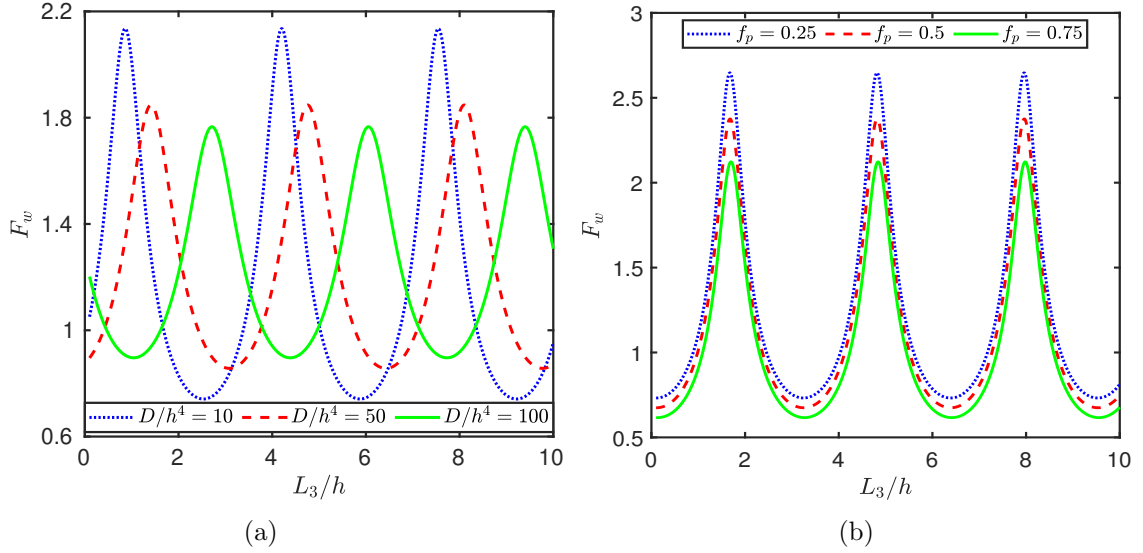
Figure 5.19: Force F_w versus gap L_3/h between EP and sea wall for various values of **(a)** flexural rigidity D/h^4 ($L_1/h = 6$) and **(b)** frictional factor f_p.
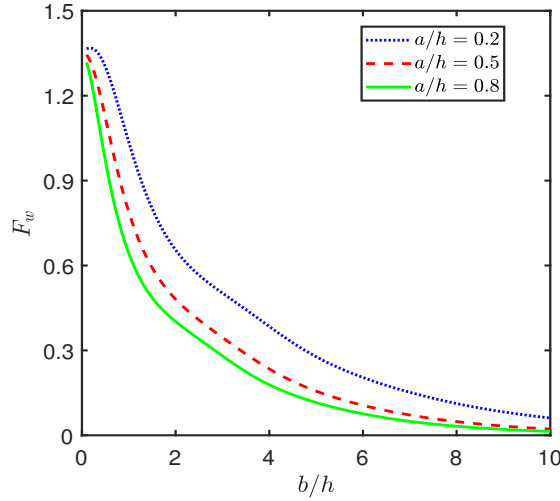
Figure 5.20: Force F_w versus width b/h of SPPS for various values of length a/h with $k_0 h = 1.2$.

Figure 5.19 shows the force F_w versus L_3/h variations for different D/h^4 and f_p values. It is observed that with respect to L_3/h, the force is oscillatory and periodic in nature. In Figure 5.19a, the maximum value of the force F_w on the wall decreases as D/h^4 increases. Further, there is a shift towards the right with an increase in D/h^4 which may be due to as D/h^4 increases, more wave energy is reflected by EP and another amount of wave energy is trapped between EP and vertical wall, as in Figure 5.8a. However, Figure 5.19b

shows that as f_p increases, the force F_w experienced by the wall is slightly reduced.

Force F_w versus b/h for different values of a/h is plotted in Figure 5.20. It depicts that when b/h increases, the force F_w on the wall slowly decreases and becomes zero for higher values of b/h. But, by comparing Figure 5.10 with Figure 5.20, it can be seen that for protecting the vertical wall, SPPS is more effective as compared to BSPS, and it is also noted that with an increase in a/h, the force F_w on the wall decreases.
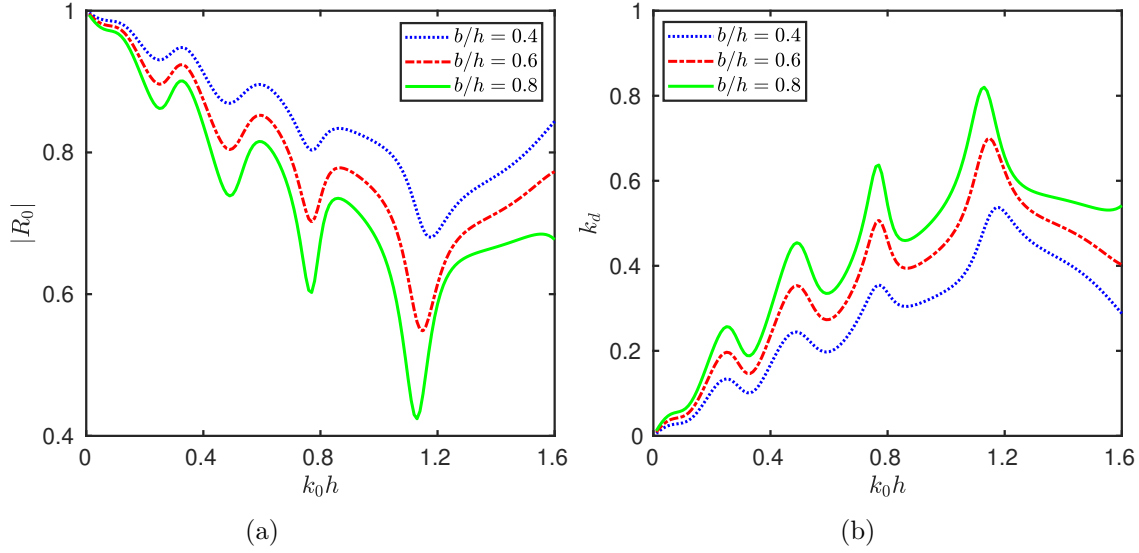
Figure 5.21: Reflection coefficient $|R_0|$ and dissipation coefficient k_d versus wave number $k_0 h$ for various values of width b/h.
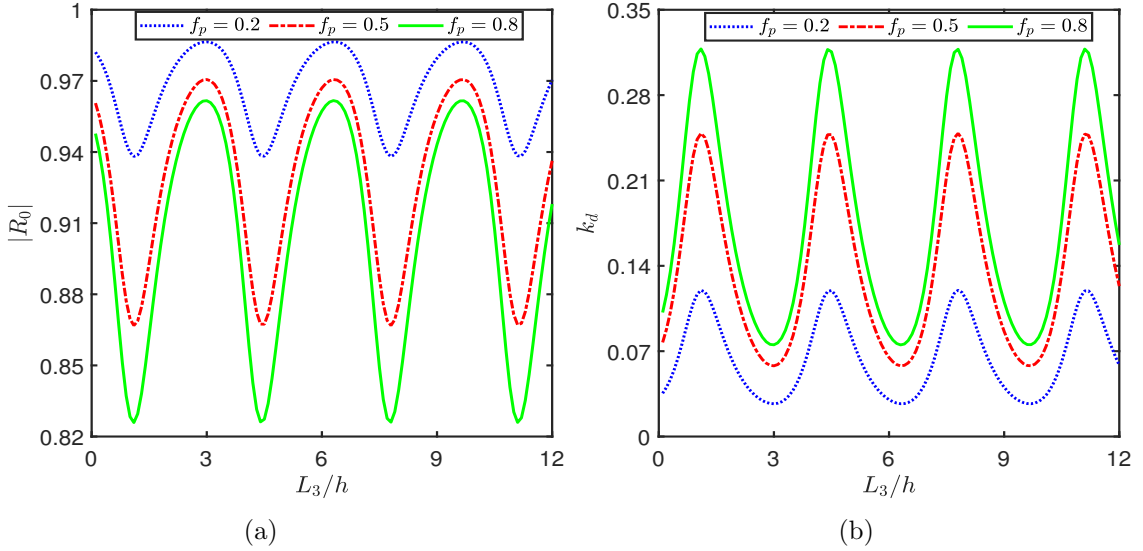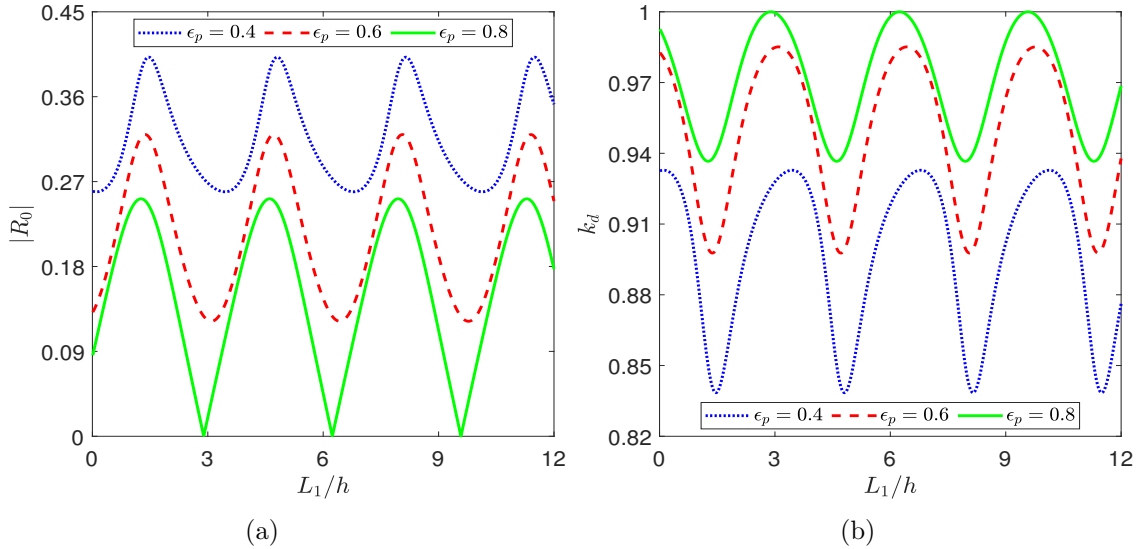

Figure 5.22: Reflection coefficient $|R_0|$ and dissipation coefficient k_d versus gap L_1/h between SPPS and EP for various values of porosity ϵ_p with $b/h = 3.5$.

The behavior of reflection coefficient $|R_0|$ and dissipation coefficient k_d versus $k_0 h$ are examined for different values of b/h in Figure 5.21. From the figure it is found that when $k_0 h$ increases, wave reflection decreases in an oscillatory pattern but the wave

energy dissipation increases in an oscillatory pattern. As $k_0 h$ increases the amplitude of oscillations increases in both cases. However, with an increase in b/h, $|R_0|$ increases and k_d decreases. This is due to the fact that the porous structure dissipates more incident wave energy as its width b/h increases and less wave energy is reflected back.

(a)   (b)
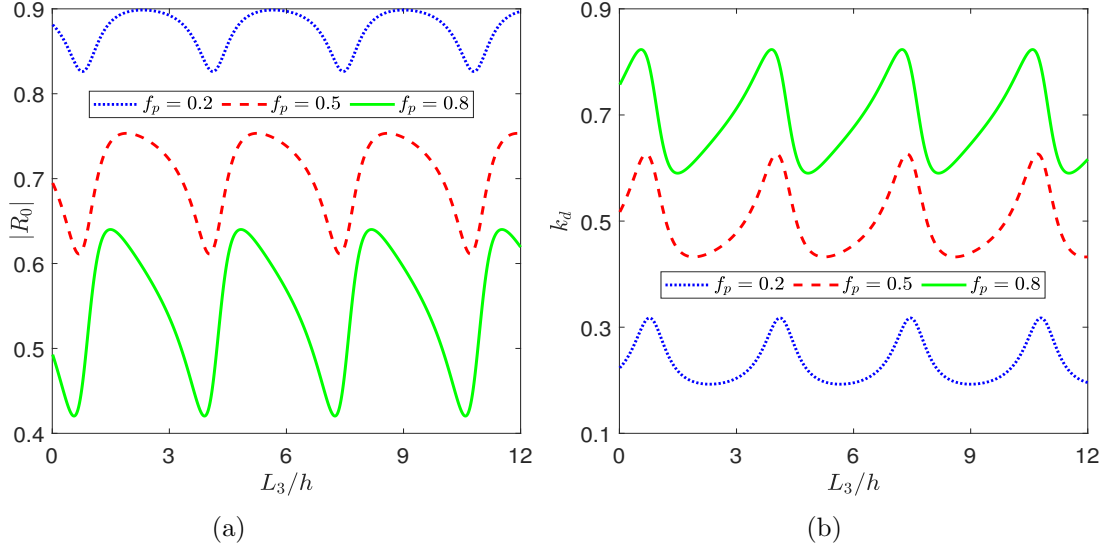
Figure 5.23: Reflection coefficient $|R_0|$ and dissipation coefficient k_d versus gap L_3/h between SPPS and EP and sea wall for various values of frictional coefficient f_p.

(a)   (b)

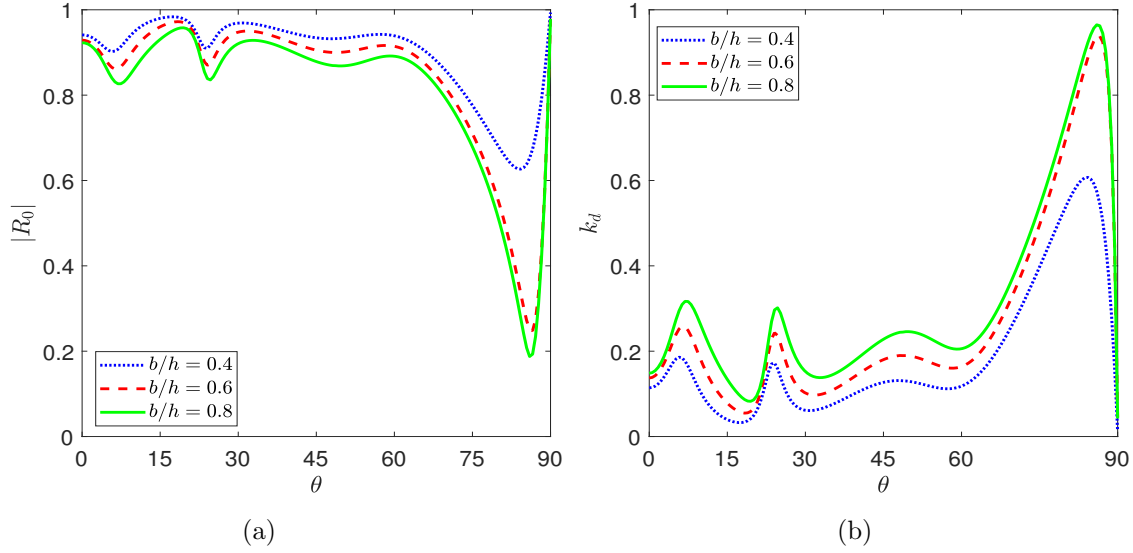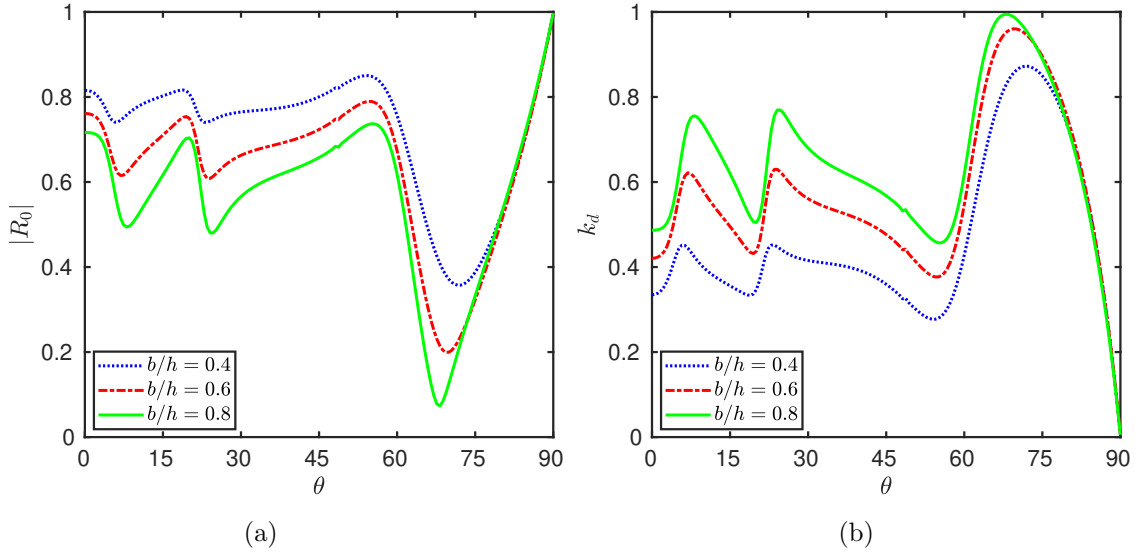Figure 5.24: Reflection coefficient $|R_0|$ and dissipation coefficient k_d versus angle of incident θ for width b/h.

Figure 5.22 shows the variations in reflection coefficient $|R_0|$ and dissipation coefficient k_d versus L_1/h for different ϵ_p. From Figure 5.22a, it is noted that as ϵ_p increases, wave reflection decreases in an oscillatory and periodic pattern. Further, the occurrence of zero minima is observed for ϵ_p=0.8, this may be due to the π-phase shift between the incident wave and reflected wave. Figure 5.22b shows the variations in k_d versus L_1/h for different

ϵ_p values. As ϵ_p increases, the wave dissipation increases in an oscillatory and periodic pattern, and this behavior is opposite to that observed for the reflection coefficient.

Figure 5.23 shows the variations in reflection coefficient $|R_0|$ and dissipation coefficient k_d versus L_3/h for various values of f_p. From Figure 5.23a, it is observed that as f_p increases, wave reflection decreases in an oscillatory and periodic pattern, where the maxima are shifting towards the left for a higher value of f_p which may be due to the porous structure is dissipating a large amount of wave energy and another amount of may be trapped between EP and wall. Figure 5.23b shows the variations in k_d versus L_3/h for different f_p values. As f_p increases, the wave dissipation increases with a significant increase in the amplitude of oscillation.

Figure 5.24 shows the variations in reflection coefficient $|R_0|$ and dissipation coefficient k_d versus θ for different values of b/h. It is found that $|R_0|$ decreases and k_d increases in an oscillatory pattern for $0^0 \le \theta \le 60^0$, then there is a sudden fall in $|R_0|$ and a sudden rise in k_d when $\theta \sim 60^0$, as in Figure 5.14. However, when $\theta \sim 70^0$, there is a sudden rise in $|R_0|$ and a sudden fall in k_d. Here, the angle $\theta = 70^0$ is termed as the critical angle, where the reflection coefficient reaches its global minimum. Comparison between Figure 5.14 and Figure 5.24 depicts that the wave dissipation is more and wave reflection is less by SPPS as compared to BSPS. From Figure 5.18b and Figure 5.24 it can be concluded that SPPS is more useful in protecting the rigid wall as compared to BSPS.
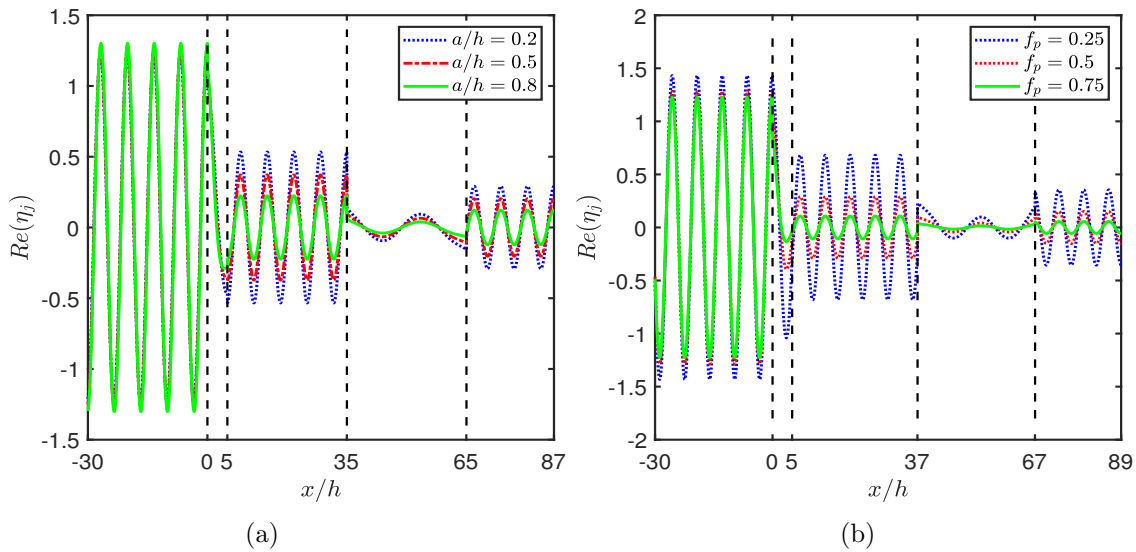
Figure 5.25: Plate deflection $(Re(\eta_5))$ and free surface elevation $(Re(\eta_j), j = 1, 2, 4, 6)$ for various values of **(a)** length a/h $(L_1/h = 30)$ and **(b)** frictional factor f_p $(L_1/h = 32, \theta = 10^0)$ with $b/h = 5, L_2/h = 30, L_3/h = 20$.

Figures 5.25a and 5.25b show the variations in Plate deflection $(Re(\eta_5))$ and free surface elevation $(Re(\eta_j), j = 1, 2, 4, 6)$ for different a/h and f_p, respectively. In these figures, it is noted that the free surface elevation (η_6) in Region 6 and plate deflection (η_5) in Region 5 are less than the free surface elevation (η_1) in Region 1 for fixed values of a/h and f_p due to the fact that the porous structure dissipates a major part of the wave energy

and transmits less amount of wave energy, which is similar to the observation obtained in Figure 5.15. From Figures 5.25a and 5.25b, it is noted that as a/h (or f_p) increases, the amplitude of free surface elevation (η_6) is reduced in the region 6 between EP and the wall. Thus a calm zone is created for safe navigation.

Figure 5.26 shows the behavior of free surface elevation in region 6 for different a/h and D/h^4. Figures 5.26a and 5.26b depict that with an increase in a/h and D/h^4, the η_6 curves decrease in an oscillatory and periodic pattern, as observed in Figure 5.16. Thus, the porous structure with a higher a/h value and EP with a higher D/h^4 value are helpful in creating a tranquility zone for safe navigation.
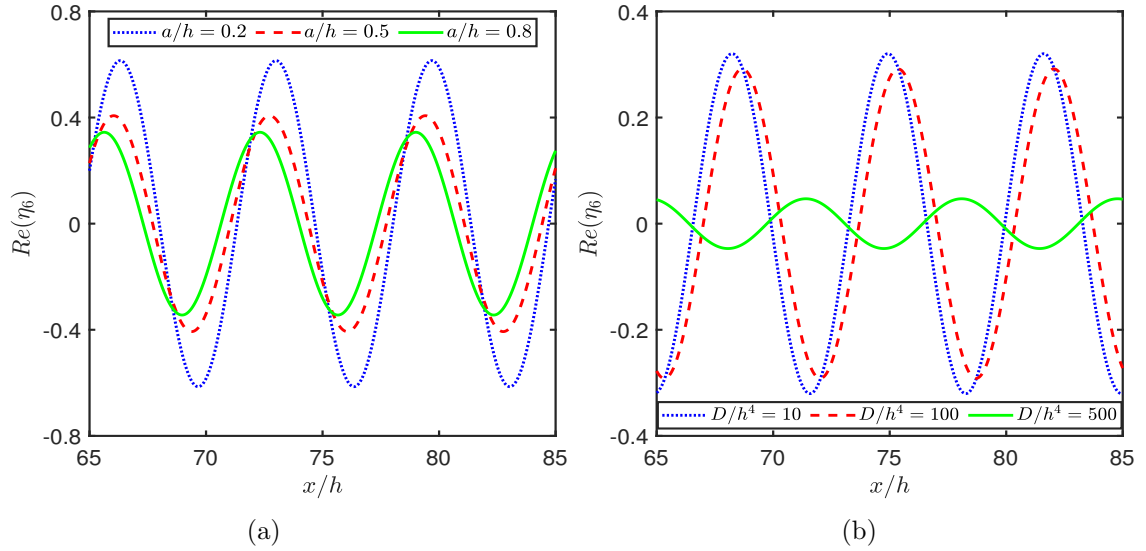
Figure 5.26: $Re(\eta_6)$ for various values of **(a)** length a/h and **(b)** flexural rigidity D/h^4 with $b/h = 5$, $L_1/h = 30$, $L_2/h = 30$ and $L_3/h = 20$.

Figure 5.27a and Figure 5.27b, respectively, show the behavior of force F_w experienced by the wall and energy dissipation coefficient k_d versus k_0h for the three cases namely, (i) EP alone, (ii) BSPS and EP and (iii) SPPS and EP. Analysis of Figure 5.27a reveals that F_w is higher in the presence of EP alone (i.e. in the absence of BSPS and SPPS) as compared to the presence of BSPS/SPPS with EP. Moreover, at $k_0h = 0.85$, F_w is 60% lower in the presence of SPPS than in the presence of BSPS. This observation can be attributed to the fact that in the absence of a porous structure, the energy dissipation coefficient k_d is zero and significant changes in the k_d are obtained after introducing the truncated porous structure. The installation position of the porous structure such as bottom standing or surface piercing plays an evident role in dissipating the wave energy. EP with SPPS shows the ultimate wave damping (nearly 90%) with increasing harmonic oscillatory pattern against the k_0h (Figure 5.27b). Consequently, a smaller portion of the wave is transmitted towards the wall and the wall experiences minimal force, as depicted in Figure 5.27b. The wave-damping performance of BSPS is evident when compared with the EP alone. However, the higher wave damping is obtained by SPPS as compared to BSPS, and the variation between them is 50% at $k_0h = 0.85$ because the 80% of incident wave

energy is concentrated near the first 10% of the water depth as mentioned in Venkateswarlu and Karmakar [9]. Thus the present study strongly suggests an SPPS with EP to control the wave force experienced by vertical rigid wall.
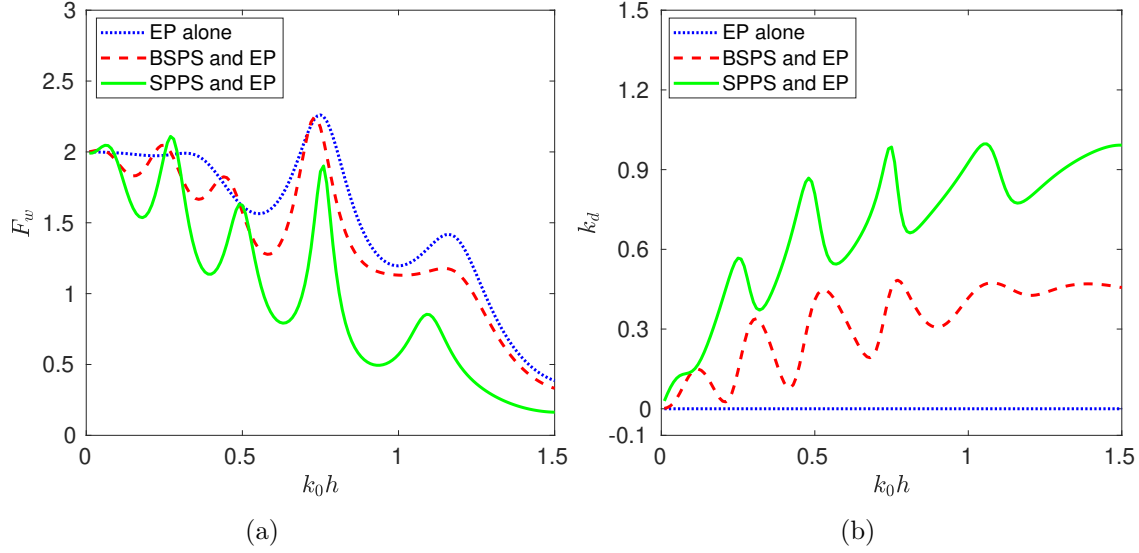
Figure 5.27: Comparison between three cases such as absence of BSPS and SPPS (i.e., EP alone), presence of BSPS ($b/h=2$) and presence of SPPS ($b/h=2$) for **(a)** F_w and **(b)** k_d vs k_0h.

5.6   Conclusion

In this paper, the interaction of oblique water waves by EP placed near a sea wall in the presence of a porous structure (BSPS/SPPS) is studied for the protection of the sea wall. The expressions in terms of eigenfunction expansion for velocity potentials coin the boundary value problem into an algebraic system which is solved numerically. The wave motion past the structures is characterized by plotting the results for force experienced by the wall, reflection and dissipation coefficients. From this study, it is found that when the distance between BSPS and EP is an odd multiple of the depth of water, the wave force experienced by the wall is minimum and this minimum value of the wave force corresponds to the minimum value of the reflection coefficient. Also, periodic harmonic oscillations are observed in the reflection coefficient, dissipation coefficient and force experienced by the wall with respect to variation of the gap length between PS and EP and also gap length between EP and vertical wall. There is a 60% reduction in force and 50% enhancement in damping coefficient after installing the SPPS when compared with the BSPS. Hence, from the cost-effective viewpoint, SPPS is suggested over BSPS in the presence of EP to protect the rigid wall against unprecedented gravity waves.

Chapter 6

Mitigation of Wave Load on a Sea Wall by a Submerged Porous Structure in the Presence of Step Type Bottom

6.1 Introduction

In Chapters 3 and 5, the effectiveness of thick porous structures of different configurations, such as (i) complete porous structure extending from top to bottom, (ii) bottom-standing porous structure, and (iii) surface-piercing porous structure, is analyzed to mitigate the wave load on a sea wall. However, these three types of configurations may not be practical in some situations. The complete and surface-piercing porous structures may not be useful for creating safe navigation channels or harbors in natural environments. In addition, the construction of a bottom-mounted porous structure is challenging in some situations. Therefore, we propose the use of a submerged thick porous structure with a finite width that is neither bottom-standing nor surface-piercing. This novel structure could be a valuable addition to breakwater types and offer solutions to various ocean engineering challenges. To model mathematically, Sollitt and Cross model is used to model the flow past submerged porous structure (SPS). The eigenfunction expansion method along with orthogonality of eigenfunction is developed to solve the boundary value problem. The energy balance relation is derived to verify the accuracy of the computational results and to provide quantitative information about wave energy dissipation. Additionally, the present results are validated against known results produced by Koley et al. [19]. Hydrodynamic factors such as wave force experienced on the wall, reflection coefficient, dissipation coefficient, and free surface elevation are analyzed for various wave and structural parameters. A major part of this work is communicated to a journal for publication.

6.2 Mathematical Formulation

In this section, we present a problem that involves the scattering of oblique waves by thick submerged porous structure (SPS) within the context of a step-type bottom in the

presence of a sea wall under the linear water wave theory. The problem is formulated within a three-dimensional Cartesian coordinate system, where it is assumed that the fluid is inviscid and incompressible and that the flow is irrotational and simple harmonic in time with an angular frequency ω. The y-axis is oriented in a vertically upward direction and the xz-plane is designated as the undisturbed water surface. This problem considers that SPS is to be fixed at a submergence depth a, following submerged thick rigid structure work by Kanoria et al. [121]. Also, this structure can be fixed by using the method of mooring lines (see Karmakar and Soares [122]), although this aspect is not considered in the current situation. SPS ($0 \leq x \leq l$ and $-b \leq y \leq -a$) with width l is placed at a distance $L_1 = r_1 - l$ from the first step (see Figure 6.1). SPS is assumed to be infinitely long along the z-axis. The two successive steps, each characterized by heights $s_1 = h - H_1$ and $s_2 = h - H_2$, and widths $L_2 = r_2 - r_1$ and $L_3 = r_3 - r_2$, are respectively positioned at depths H_1 and H_2, as shown in Figure 6.1. The entire fluid region is divided into 7 regions. The whole fluid domain is divided into 7 regions R_1, R_2, R_3, R_4, R_5, R_6 and R_7 as mentioned in Figure 6.1.
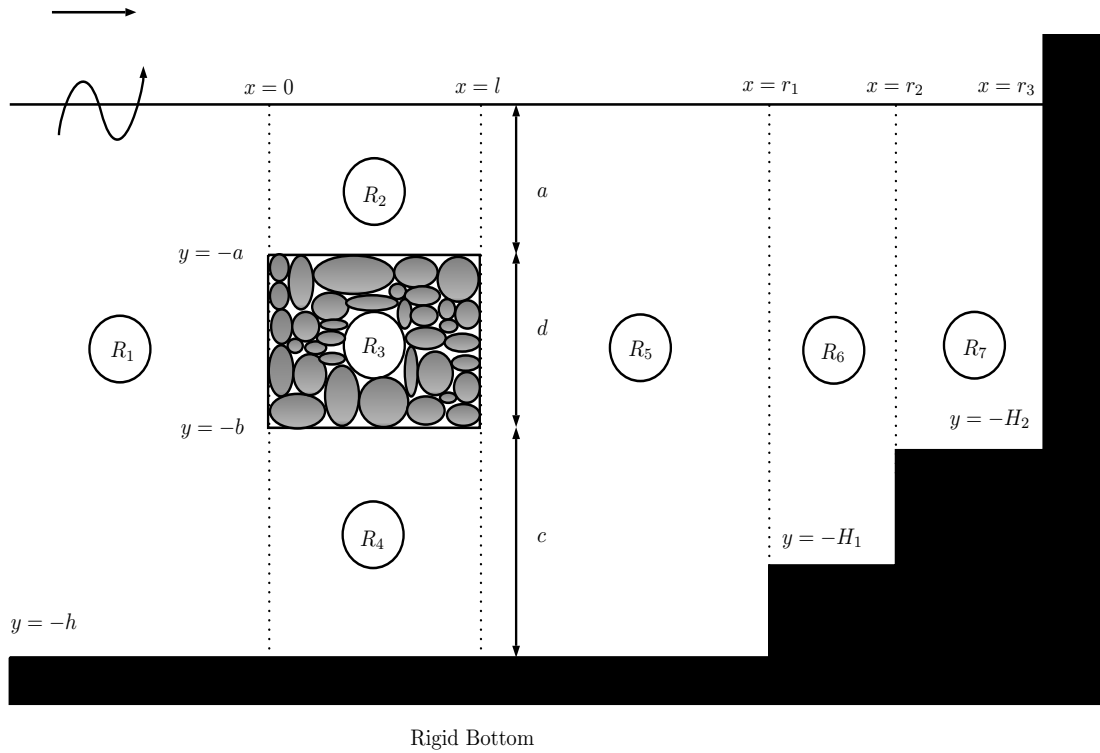
Figure 6.1: SPS kept at a finite distance from the sea wall over two stepped bottom.

The fluid motion can be described by the velocity potential $\Phi_j(x, y, z, t) = Re\{\phi_j(x, y)e^{i(\beta z - \omega t)}\}$, satisfying

$$\left(\frac{\partial^2}{\partial x^2} + \frac{\partial^2}{\partial y^2} - \beta^2 \right) \phi_j = 0, \text{ in each region } R_j, \tag{6.1}$$

where $\beta = k \sin\theta$ and k representing the wavenumber of the incidence wave and θ representing the angle between the wave's direction and the x-axis.

The rigid bottom condition is given by

$$\frac{\partial \phi_j}{\partial y} = 0 \text{ on } y = -h \text{ for } j = 1, 4, 5, \tag{6.2}$$

$$\frac{\partial \phi_6}{\partial y} = 0 \text{ on } y = -H_1, \tag{6.3}$$

$$\frac{\partial \phi_7}{\partial y} = 0 \text{ on } y = -H_2. \tag{6.4}$$

In the free-surface, the undisturbed water surface condition is expressed by

$$\frac{\partial \phi_j}{\partial y} - K\phi_j = 0 \text{ on } y = 0 \text{ for } j = 1, 2, 5, 6, 7, \tag{6.5}$$

with $K = \omega^2/g$, g is the acceleration due to gravity.

The conditions for continuity of pressure and velocity along the interfaces of SPS are expressed as

$$\phi_2 = (m + if)\phi_3, \ \frac{\partial \phi_2}{\partial y} = \epsilon \frac{\partial \phi_3}{\partial y} \text{ on } y = -a, \ 0 \leq x \leq l, \tag{6.6}$$

$$\phi_4 = (m + if)\phi_3, \ \frac{\partial \phi_4}{\partial y} = \epsilon \frac{\partial \phi_3}{\partial y} \text{ on } y = -b, \ 0 \leq x \leq l, \tag{6.7}$$

$$\phi_1 = (m + if)\phi_3, \ \frac{\partial \phi_1}{\partial x} = \epsilon \frac{\partial \phi_3}{\partial x} \text{ on } x = 0, \ -b \leq y \leq -a, \tag{6.8}$$

$$\phi_5 = (m + if)\phi_3, \ \frac{\partial \phi_5}{\partial x} = \epsilon \frac{\partial \phi_3}{\partial x} \text{ on } x = l, \ -b \leq y \leq -a, \tag{6.9}$$

where the non-dimensionalized quantities m, f and ϵ respectively represent the inertial coefficient, frictional factor and porosity of SPS.

The conditions for continuity of pressure and velocity along the mutual vertical interfaces at $x = 0$ and $x = l$ are expressed as

$$\phi_j = \begin{cases} \phi_2, -a \leq y \leq 0 \\ \phi_4, -h \leq y \leq -b \end{cases} \text{ and } \frac{\partial \phi_j}{\partial x} = \begin{cases} \frac{\partial \phi_2}{\partial x}, -a \leq y \leq 0 \\ \frac{\partial \phi_4}{\partial x}, -h \leq y \leq -b \end{cases} \tag{6.10}$$

where $j = 1$ on $x = 0$ and $j = 5$ on $x = l$.

The continuity of pressure and velocity along the mutual interfaces $x = r_1$ and $x = r_2$ are used to express by

$$\phi_5 = \phi_6, \ \frac{\partial \phi_5}{\partial x} = \frac{\partial \phi_6}{\partial x} \text{ on } x = r_1, \ -H_1 \leq y \leq 0, \tag{6.11}$$

$$\phi_6 = \phi_7, \ \frac{\partial \phi_6}{\partial x} = \frac{\partial \phi_7}{\partial x} \text{ on } x = r_2, \ -H_2 \leq y \leq 0. \tag{6.12}$$

The conditions at the steps are expressed as

$$\frac{\partial \phi_5}{\partial x} = 0 \quad \text{on} \quad x = r_1, \quad -h \leq y \leq -H_1, \tag{6.13}$$

$$\frac{\partial \phi_6}{\partial x} = 0 \quad \text{on} \quad x = r_2, \quad -H_1 \leq y \leq -H_2. \tag{6.14}$$

The condition on the rigid sea wall at $x = r_3$ is expressed as

$$\frac{\partial \phi_7}{\partial x} = 0 \quad \text{on} \quad x = r_3, \quad -H_2 \le y \le 0. \tag{6.15}$$

The far-field condition is given by

$$\phi_1(x,y) \simeq \left(\frac{ig}{\omega}\right) \frac{\cosh k(h+y)}{\cosh kh}\{e^{ik_x x} + R_0 e^{-ik_x x}\} \text{ as } x \to -\infty, \tag{6.16}$$

where $|R_0|$ is commonly referred as the reflection coefficient and $k_x = \sqrt{k^2 - \beta^2}$, k is the positive real root of the transcendental equation in k given by

$$K - k \tanh kh = 0. \tag{6.17}$$

In this problem, the singularity at the tip of SPS is not considered.

6.3   Method of Solution

In the study, the Helmholtz equation is solved using the variable separable method. This approach enables to write the expression of the velocity potential in each region in terms of eigenfunctions. The study also utilizes the plane wave solution, which is similar to the approach taken in the Sharma et al. [117]. The spatial potential in the region R_1, R_5, R_6 and R_7, satisfying Equations (6.1)-(6.5) and (6.13)-(6.16), can be expressed in the form

$$\phi_1 = \left(\frac{ig}{\omega}\right)\left[e^{ik_x x} + R_0 e^{-ik_x x}\right]\mathcal{F}_1(y) \text{ for } -\infty < x \le 0, \ -h \le y \le 0, \tag{6.18}$$

$$\phi_5 = \left(\frac{ig}{\omega}\right)\left[Ae^{ik_x(x-l)} + Be^{-ik_x(x-r_1)}\right]\mathcal{F}_1(y) \text{ for } l \le x \le r_1, \ -h \le y \le 0, \tag{6.19}$$

$$\phi_6 = \left(\frac{ig}{\omega}\right)\left[Ce^{iq_{1x}(x-r_1)} + De^{-iq_{1x}(x-r_2)}\right]\mathcal{F}_2(y) \text{ for } r_1 \le x \le r_2, \ -H_1 \le y \le 0, \tag{6.20}$$

$$\phi_7 = \left(\frac{ig}{\omega}\right) \mathsf{E}\cos q_{2x}(x-r_3)\mathcal{F}_3(y) \text{ for } r_2 \le x \le r_3, \ -H_2 \le y \le 0, \tag{6.21}$$

where

$$\mathcal{F}_1(y) = \frac{\cosh k(h+y)}{\cosh kh}, \mathcal{F}_2(y) = \frac{\cosh q_1(H_1+y)}{\cosh q_1 H_1}, \mathcal{F}_3(y) = \frac{\cosh q_2(H_2+y)}{\cosh q_2 H_2}, \tag{6.22}$$

R_0, A, B, C, D and E are unknown complex constants, $q_{1x} = \sqrt{q_1^2 - \beta^2}$ and $q_{2x} = \sqrt{q_2^2 - \beta^2}$ with q_1 and q_2 are the positive real roots of the relations respectively given by

$$K - q_1 \tanh q_1 H_1 = 0 \text{ and } K - q_2 \tanh q_2 H_2 = 0. \tag{6.23}$$

In regions R_2, R_3 and R_4, satisfying Equations (6.1)-(6.7), can be expressed in the form

$$\phi_2 = \left(\frac{ig}{\omega}\right)\left[\mathcal{G}e^{ip_x x} + \mathcal{H}e^{-ip_x(x-l)}\right]M(y) \text{ for } 0 \le x \le l, \ -b \le y \le 0, \tag{6.24}$$

$$\phi_3 = \left(\frac{ig}{\omega}\right)\left[\mathcal{G}e^{ip_x x} + \mathcal{H}e^{-ip_x(x-l)}\right]P(y) \text{ for } 0 \le x \le l, \ -c \le y \le -b, \tag{6.25}$$

$$\phi_4 = \left(\frac{ig}{\omega}\right)\left[\mathcal{G}e^{ip_x x} + \mathcal{H}e^{-ip_x(x-l)}\right]Q(y) \text{ for } 0 \le x \le l, \ -h \le y \le -c, \tag{6.26}$$

where

$$M(y) = \frac{(1-\alpha\beta)\cosh p(h+y) - (\beta-\alpha\gamma)\sinh p(h+y)}{(1-\alpha\beta)\cosh ph - (\beta-\alpha\gamma)\sinh ph}, \tag{6.27}$$

$$P(y) = \frac{[1-\beta\tanh p(h-a)][\cosh p(h+y) - \alpha\sinh p(h+y)]}{(m+if)[(1-\alpha\beta)\cosh ph - (\beta-\alpha\gamma)\sinh ph]}, \tag{6.28}$$

$$Q(y) = \frac{[1-\beta\tanh p(h-a)][1-\alpha\tanh p(h-b)]\cosh p(h+y)}{(1-\alpha\beta)\cosh ph - (\beta-\alpha\gamma)\sinh ph}, \tag{6.29}$$

$$\alpha = \frac{(1-G)\tanh p(h-b)}{\tanh^2 p(h-b) - G}, \beta = \frac{(1-G)\tanh p(h-a)}{1-G\tanh^2 p(h-a)}, \tag{6.30}$$

$$\gamma = \frac{\tanh^2 p(h-a) - G}{1-G\tanh^2 p(h-a)}, G = \frac{\epsilon}{(m+if)}, \tag{6.31}$$

$\mathcal{G}$ and $\mathcal{H}$ are unknown complex constants, $p_x = \sqrt{p^2 - ß^2}$ and p is the complex root for the most progressive mode (least damped, see Dalrymple et al. [11]) of the relation given by

$$[p(1-\alpha\beta) + K(\beta-\alpha\gamma)]\tanh ph - p(\beta-\alpha\gamma) - K(1-\alpha\beta) = 0. \tag{6.32}$$

It may be noted that in the absence of SPS (i.e. when $m = 1$, $\epsilon = 1$ and $f = 0$, then $G = 1$, $\alpha = 0$, $\beta = 0$ and $\gamma = -1$), Equation (6.32) reduces to the free surface transcendental equation in p, given by $K - p\tanh ph = 0$, which is same as Equation (6.17).

Now, by utilizing the conditions given in Equations (6.8)-(6.14) and taking advantage of the orthogonality of the eigenfunction $\mathcal{F}_1(y)$ in $-h \le y \le 0$, we can arrive at the following set of equations

$$(1+R)Z_1 - [U + (m+if)V + W](\mathcal{G} + \mathcal{H}e^{ip_x l}) = 0, \tag{6.33}$$

$$ik_x(1-R)Z_1 - ip_x[U + \epsilon V + W](\mathcal{G} - \mathcal{H}e^{ip_x l}) = 0, \tag{6.34}$$

$$[U + (m+if)V + W](\mathcal{G}e^{ip_x l} + \mathcal{H}) - [A + Be^{-ik_x(l-r_1)}]Z_1 = 0, \tag{6.35}$$

$$ip_x[U + \epsilon V + W](\mathcal{G}e^{ip_x l} - \mathcal{H}) - ik_x[A - Be^{-ik_x(l-r_1)}]Z_1 = 0, \tag{6.36}$$

$$[Ae^{ik_x(r_1-l)} + B]Z_2 - [C + De^{-iq_{1x}(r_1-r_2)}]X_1 = 0, \tag{6.37}$$

$$ik_x[Ae^{ik_x(r_1-l)} - B]Z_1 - iq_{1x}[C + De^{-iq_{1x}(r_1-r_2)}]X_1 = 0, \tag{6.38}$$

$$[Ce^{iq_{1x}(r_2-r_1)} + D]X_2 - T\cos q_{2x}(r_2 - r_3)Y = 0, \tag{6.39}$$

$$iq_{1x}[Ce^{iq_{1x}(r_2-r_1)} + D]X_1 + q_{2x}T\sin q_{2x}(r_2 - r_3)Y = 0, \tag{6.40}$$

where

$$Z_1 = \int_{-h}^{0} \mathcal{F}_1(y)\mathcal{F}_1(y)dy, \ U = \int_{-b}^{0} M(y)\mathcal{F}_1(y)dy, \ V = \int_{-c}^{-b} P(y)\mathcal{F}_1(y)dy, \quad (6.41)$$

$$X = \int_{-H}^{-c} Q(y)\mathcal{F}_1(y)dy, Z_2 = \int_{-H_1}^{0} \mathcal{F}_1(y)\mathcal{F}_1(y)dy, \ X_1 = \int_{-H_1}^{0} \mathcal{F}_2(y)\mathcal{F}_1(y)dy,$$

$$X_2 = \int_{-H_2}^{0} \mathcal{F}_2(y)\mathcal{F}_1(y)dy \text{ and } Y = \int_{-H_2}^{0} \mathcal{F}_3(y)\mathcal{F}_1(y)dy.$$

Thus, we obtain a system of 8 equations with 8 unknowns R_0, A, B, C, D, E, $\mathcal{G}$ and $\mathcal{H}$. This system has been solved numerically using the Gauss-Elimination method with the help of MATLAB. The reflection coefficient ($|R_0|$), energy dissipation coefficient k_d (see Equation (6.50)) in Section 6.4 by SPS and force (F_w) experienced by the wall can be determined.

Force experienced by the wall: The wave-induced force F_w by the rigid wall is computed using the integral given by

$$F_w = \left| \frac{-i\omega}{gh^2} \int_{-h}^{0} \phi_7(r_3, y)dy \right|. \tag{6.42}$$

6.4   Energy Balance Relation

In the present problem, apart from the reflection of waves, a major part of wave energy is dissipated by SPS. Thus, for better understanding of the quantitative behaviour of wave reflection and dissipation, an energy identity is derived. By employing Green's identity, the energy identity for this study can be determined, which is expressed by

$$\int_{\mathcal{C}} \left(\phi_j \frac{\partial \hat{\phi}_j}{\partial n} - \hat{\phi}_j \frac{\partial \phi_j}{\partial n} \right) ds = 0, \tag{6.43}$$

where $\hat{\phi}_j$ represents the complex conjugate of ϕ_j and $\frac{\partial}{\partial n}$ denotes the outward normal derivative to the boundary $\mathcal{C}$, $\mathcal{C} = \mathcal{C}_1 \cup \mathcal{C}_2 \cup \mathcal{C}_3 \cup \mathcal{C}_4 \cup \mathcal{C}_5$, where $\mathcal{C}_1 = \{x = -\mathsf{X}, -h \leq y \leq 0;$ $y = -h, -\mathsf{X} \leq x \leq 0; x = 0, -h \leq y \leq 0; y = 0, -\mathsf{X} \leq x \leq 0;\}$, $\mathcal{C}_2 = \{ x = 0, -a \leq y \leq 0;$ $y = -a, 0 \leq x \leq l; x = l, -a \leq y \leq 0; y = 0, 0 \leq x \leq l \}$, $\mathcal{C}_3 = \{ x = 0, -b \leq y \leq -a;$ $y = -b, 0 \leq x \leq l; x = l, -b \leq y \leq -a; y = -a, 0 \leq x \leq l \}$, $\mathcal{C}_4 = \{ x = 0, -h \leq y \leq -b;$ $y = -h, 0 \leq x \leq l; x = l, -h \leq y \leq -b; y = -b, 0 \leq x \leq l \}$ and $\mathcal{C}_5 = \{ x = l, -h \leq y \leq 0;$ $y = -h, l \leq x \leq r_1; x = r_1, -h \leq y \leq -H_1; y = -H_1, r_1 \leq x \leq r_2; x = r_2, -H_1 \leq y \leq -H_2; y = -H_2, r_2 \leq x \leq r_3; x = r_3, -H_2 \leq y \leq 0; y = 0, l \leq x \leq r_3$. The contribution from the flat bottom $y = -h, -\mathsf{X} \leq x \leq 0; y = -h, 0 \leq x \leq l; y = -h, l \leq x \leq r_1$ is zero. Due to the steps,the contribution from the steps $x = r_1, -h \leq y \leq -H_1; y = -H_1, r_1 \leq x \leq r_2; x = r_2, -H_1 \leq y \leq -H_2; y = -H_2, r_2 \leq x \leq r_3$ are zero. Due to the free surface condition, the contribution from the boundary $y = 0, -\mathsf{X} \leq x \leq 0, y = 0, 0 \leq x \leq l$ and $y = 0, l \leq x \leq r_3$ is zero. The contribution from the sea wall $x = r_3, -H_2 \leq y \leq 0$ is zero.

Due to SPS, the vertical line $x = 0, -b \leq y \leq -a$ contributes

$$\int_{\mathcal{C}} \left(\phi_j \frac{\partial \hat{\phi}_j}{\partial n} - \hat{\phi}_j \frac{\partial \phi_j}{\partial n} \right) ds = \int_{-b}^{-a} \left([\epsilon(m+if) - 1] \phi_3 \phi_{3x}^* - [\epsilon(m-if) - 1] \phi_3^* \phi_{3x} \right)_{x=0} dy \quad (6.44)$$

and on $x = l, -b \leq y \leq -a$

$$\int_{\mathcal{C}} \left(\phi_j \frac{\partial \hat{\phi}_j}{\partial n} - \hat{\phi}_j \frac{\partial \phi_j}{\partial n} \right) ds = \int_{-b}^{-a} \left([\epsilon(m-if) - 1] \phi_3^* \phi_{3x} - [\epsilon(m+if) - 1] \phi_3 \phi_{3x}^* \right)_{x=l} dy. \quad (6.45)$$

Similarly, on the horizontal line $y = -a, 0 \leq x \leq l$

$$\int_{\mathcal{C}} \left(\phi_j \frac{\partial \hat{\phi}_j}{\partial n} - \hat{\phi}_j \frac{\partial \phi_j}{\partial n} \right) ds = \int_0^l \left([\epsilon(m-if) - 1] \phi_3^* \phi_{3y} - [\epsilon(m+if) - 1] \phi_3 \phi_{3y}^* \right)_{y=-a} dx \quad (6.46)$$

and on $y = -b, 0 \leq x \leq l$

$$\int_{\mathcal{C}} \left(\phi_j \frac{\partial \hat{\phi}_j}{\partial n} - \hat{\phi}_j \frac{\partial \phi_j}{\partial n} \right) ds = \int_0^l \left([\epsilon(m+if) - 1] \phi_3 \phi_{3y}^* - [\epsilon(m-if) - 1] \phi_3^* \phi_{3y} \right)_{y=-b} dx. \quad (6.47)$$

On the line $x = -\mathsf{X}, -h \leq y \leq 0$

$$\int_{\mathcal{C}} \left(\phi_j \frac{\partial \hat{\phi}_j}{\partial n} - \hat{\phi}_j \frac{\partial \phi_j}{\partial n} \right) ds = (1 - |R_0|^2) \frac{ik}{\cosh^2 kh} \left(\frac{\sinh(2kh) + 2kh}{2k} \right). \quad (6.48)$$

By consolidating all contributions from $\mathcal{C}_1, \mathcal{C}_2, \mathcal{C}_3, \mathcal{C}_4$ and $\mathcal{C}_5$, the energy identity is deduced as

$$|R_0|^2 + k_d = 1 \quad (6.49)$$

where

$$k_d = \frac{2k \cosh^2 kh}{ik(\sinh 2kh + 2kh)} \left[\int_{-b}^{-a} \left([\epsilon(m+if) - 1] \phi_3 \phi_{3x}^* - [\epsilon(m-if) - 1] \phi_3^* \phi_{3x} \right)_{x=0} dy \right.$$

$$+ \int_{-b}^{-a} \left([\epsilon(m-if) - 1] \phi_3^* \phi_{3x} - [\epsilon(m+if) - 1] \phi_3 \phi_{3x}^* \right)_{x=l} dy$$

$$+ \int_0^l \left([\epsilon(m-if) - 1] \phi_3^* \phi_{3y} - [\epsilon(m+if) - 1] \phi_3 \phi_{3y}^* \right)_{y=-a} dx$$

$$+ \left. \int_0^l \left([\epsilon(m+if) - 1] \phi_3 \phi_{3y}^* - [\epsilon(m-if) - 1] \phi_3^* \phi_{3y} \right)_{y=-b} dx \right].$$

$$(6.50)$$

6.5   Results and Discussion

In this section, the study evaluates how well SPS and the bottom steps mitigate the wave load on the sea wall. The investigation centers on multiple parameters, specifically F_w, $|R_0|$ and k_d. The values of non-dimensional factors such as $kh = 1$, $a/h = 0.2$, $d/h = 0.45$, $l/h = 2$, $L_1/h = 8$, $L_2/h = 7$, $L_3/h = 6$, $s_1/h = 0.2$, $s_2/h = 0.4$, and the other parameters $m = 1$, $f = 0.6$, $\epsilon = 0.5$ and $\theta = 25°$ are kept fixed throughout the investigation unless stated otherwise. While several computations are performed, only selected results are presented to prevent redundancy.

6.5.1 Validation

For the validation of the current numerical results with the existing literature, it is noted that without the presence of steps (i.e. when $H_1 = H_2 = h$) and the gap between SPS and bottom is zero (i.e. $c = h - b = 0$), the present problem is equivalent to the work "interaction of water waves with bottom-standing porous structure in the presence of a wall" by Koley et al. [19]. For the fixed value of $d/h = 0.5$, $\epsilon = 0.437$, $f = 0.25$, $\theta = 10°$ and $L/\lambda = 1$ ($L = L_1 + L_2 + L_3$), Figure 6.2 shows a close agreement with the results of Koley et al. [19]. In addition to this, to verify the energy identity derived in Equation (6.49), the numerical data of k_d and $1 - |R_0|^2$ for different kh values are tabulated in Table 6.1, which demonstrates a consistent agreement between k_d and $1 - |R_0|^2$ validating the energy identity.
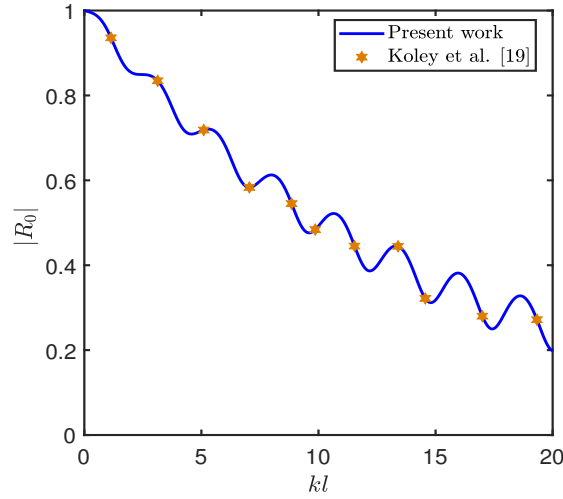
Figure 6.2: Validation of the present results with Koley et al.[19].

kh	$|R_0|$	$1 - |R_0|^2$	k_d
0.2	0.9367	0.1226	0.1226
0.4	0.9865	0.0265	0.0269
0.6	0.9634	0.0719	0.0722
0.8	0.7852	0.3835	0.3837
1	0.8203	0.3271	0.3275

Table 6.1: Verification of energy identity.

6.5.2 Effect of Various Parameters on Force (F_w) Experienced by the Wall

Figure 6.3 explores a surface plot depicting the force experienced by the wall F_w across different a/h and d/h values. Within the ranges of $0.1 < a/h < 0.3$ and $0.1 < d/h < 0.6$, the wave force consistently remains below 59%. However, at $a/h = 0.1$ and $d/h = 0.6$, the

wave force is notably lower, recorded as 37%, but the implication of a SPS with $a/h = 0.1$, indicating the SPS's proximity to the free surface, potentially obstructing vessel movement, underscores the need to avoid such configurations. Based on these findings, this study advocates for the selection of $a/h = 0.2$ alongside $d/h = 0.45$, because this combination yields a force of approximately 52%, balancing mitigation of wave load on the wall and preserving optimal vessel maneuverability.
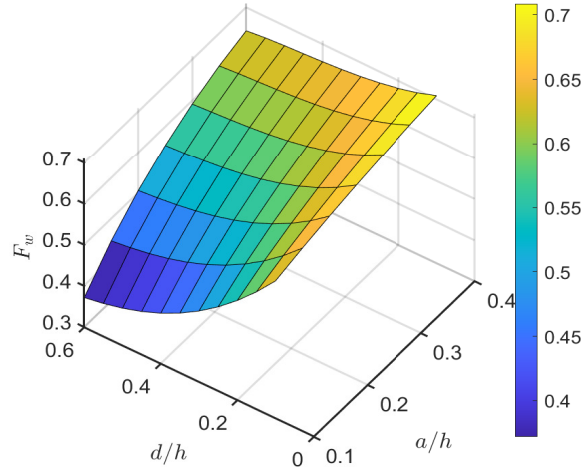
Figure 6.3: Surface plot of Force F_w versus d/h and a/h.
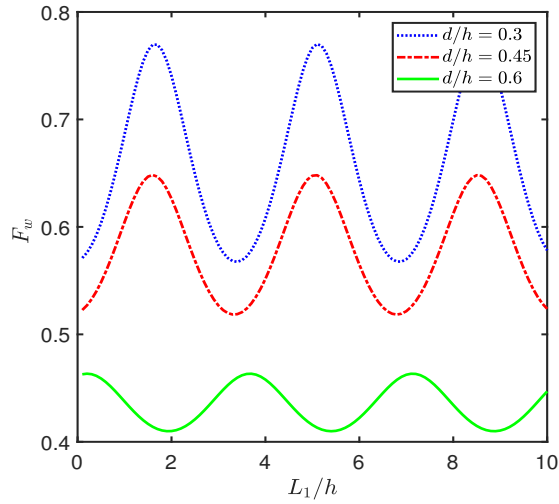
Figure 6.4: Force F_w versus L_1/h for different values of d/h.

Figure 6.4 shows the behavior of F_w versus gap L_1/h between SPS and steps for different values of d/h. The figure shows that with respect to L_1/h, F_w follows an oscillatory and periodic pattern, with periodicity $L_1/h = 3.4$. The optimum value may be due to the constructive and destructive interface between the incident and reflected wave. It is found that with an increase in d/h from 0.3 to 0.6, F_w decreases. This may be with an increase in the length d/h of SPS, more wave energy is dissipated by SPS. Moreover, it has been observed that for certain values of L_1/h, F_w curves reach maxima for $d/h = 0.3$

and 0.45, whereas at the same L_1/h points, minima are attained for $d/h = 0.6$. Similarly, there are certain values of L_1/h, the F_w curves achieve minima for $d/h = 0.3$ and 0.45, while for $d/h = 0.6$, maxima are observed at the same points of L_1/h. This may be due to the different phase angle between the incident wave and reflected wave for the cases of lower and higher values of d/h.
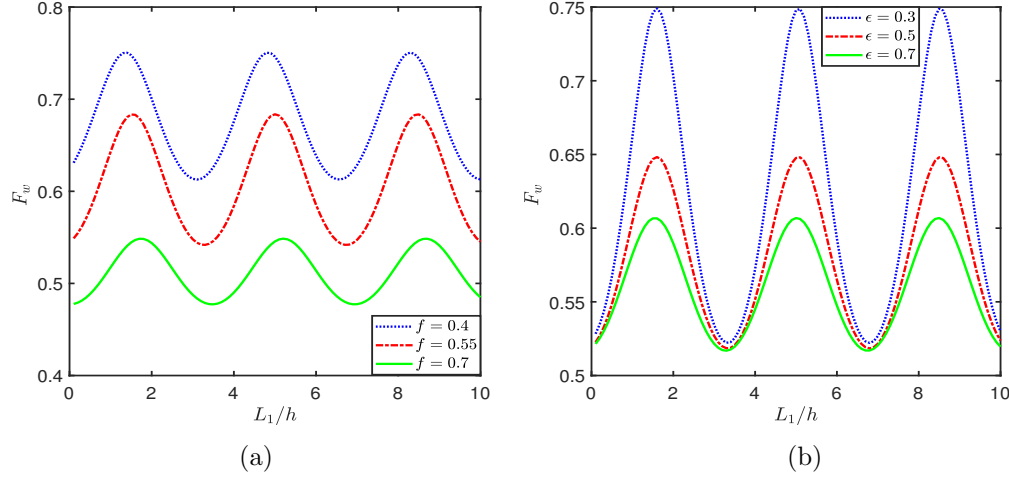
Figure 6.5: Force F_w versus L_1/h for different values of (a) f and (b) ϵ.
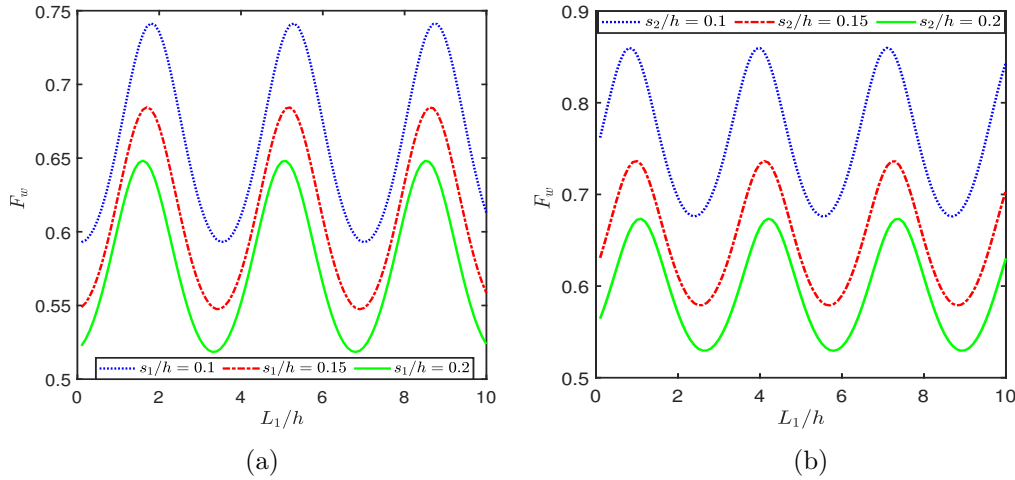
Figure 6.6: Force F_w versus L_1/h for different values of (a) s_1/h and (b) s_2/h.

Figure 6.5 demonstrates the behavior of F_w versus gap L_1/h between SPS and steps for different values of frictional coefficient f and porosity ϵ of SPS. Form the figure, F_w follows an oscillatory and periodic pattern with respect to $L_1 h$, as observed in Figure 6.4. In Figure 6.5a, it is observed that Max F_w decreases from 75% to 55% as f increases from 0.4 to 0.7, and the F_w curve shifts towards the right. These trends in F_w may be attributed to the rise in the dissipation coefficient as f increases. It is noticed that when f varies from 0.55 to 0.7, Min F_w will be in between 55% to 48%, which is in the desired range of F_w. From Figure 6.5b, it is evident the same effect, an increase in ϵ from 0.3 to 0.7 corresponds to a decrease in Max F_w from 75% to 60%. This phenomenon is likely

a consequence of the heightened dissipation coefficient as ϵ increases, leading to reduced interaction of waves with the wall. Furthermore, it has been observed that for some points of L_1/h, the minima values of F_w are attained which do not change with the increase in ϵ value, however, there is a decrease in the maxima values of F_w. For values of porosity falling between 0.5 and 0.7, where F_w is within the range of 52% to less than 65%, advising to take for a moderate porosity. In the rest of the computations, $\epsilon = 0.5$ is chosen as it ensures here Min F_w 52% and $f = 0.6$ is chosen as it ensures here Min F_w 55%, where both are less than 60%, the feasible range to protect the wall.
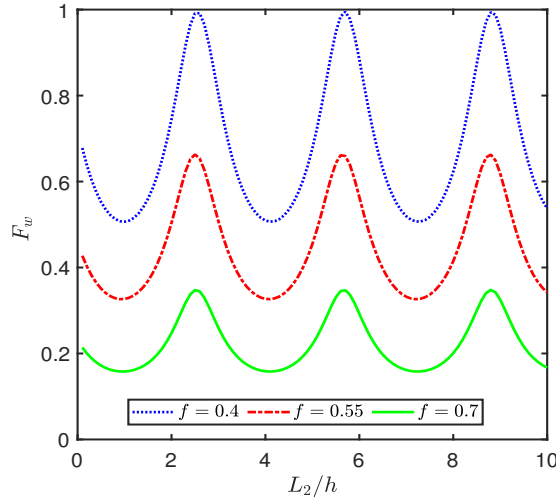
Figure 6.7: Force F_w versus L_2/h for different values of f with fixed value $l/h = 8$.

Figure 6.6 illustrates the behavior of F_w versus gap L_1/h between SPS and steps for different values of steps height s_1/h or s_2/h. As observed in Figure 6.4, here, F_w also follows an oscillatory and periodic versus L_1/h. From the figure, it is also concluded that as step height s_1/h (or s_2/h) increases, F_w decreases. This may be with an increase in s_1/h (or s_2/h), the step reflects more wave energy, and the wall experiences less wave force.

Figure 6.7 illustrates the variation in F_w versus the width L_2/h of step-1 for different values of f. The graph reveals that F_w follows an oscillatory and periodic trend with a periodicity of $L_2/h = 3.1$. The optimal points in F_w can be attributed to constructive and destructive interference between the incident and reflected waves. From the figure, it has been observed that certain values of L_2/h result in F_w curves reaching their maxima, similarly, there exist certain values of L_2/h where the opposite behavior is observed. Thus, it can be concluded that the value of L_2/h plays an important role. Also, it is found that with the increase in f, the amplitude of F_w oscillations decreases. This phenomenon could be attributed to SPS effectively dissipating a significant portion of the wave energy while another portion becomes trapped within the trapping chamber.

In Figure 6.8, the variation of F_w with width L_3/h of step-2 is graphically represented for different values of d/h and ϵ. The figure demonstrates that F_w exhibits an oscillatory and periodic behavior as L_3/h changes, with a periodicity of $L_3/h = 2.7$. The optimal

points in F_w are a result of constructive and destructive interference between incident and reflected waves. As observed in Figure 6.7, F_w attains maxima for certain values of L_3/h and there exist certain values of L_3/h, where it attains minima, implying the width of L_3/h of step-2 also plays an important role in reducing the value of F_w. Additionally, it is observed that an increase in d/h from 0.3 to 0.6 leads to a decrease in Max F_w from 97% to 20% and for an increases in ϵ from 0.3 to 0.7 leads to a decrease in Max F_w from 76% to 49%. Further, it is also observed that with the increase in d/h (or ϵ), there is a reduction in the amplitude of the curve of F_w. This phenomenon could be attributed to SPS effectively dissipating a significant portion of the wave energy while another portion becomes trapped within the trapping chamber.
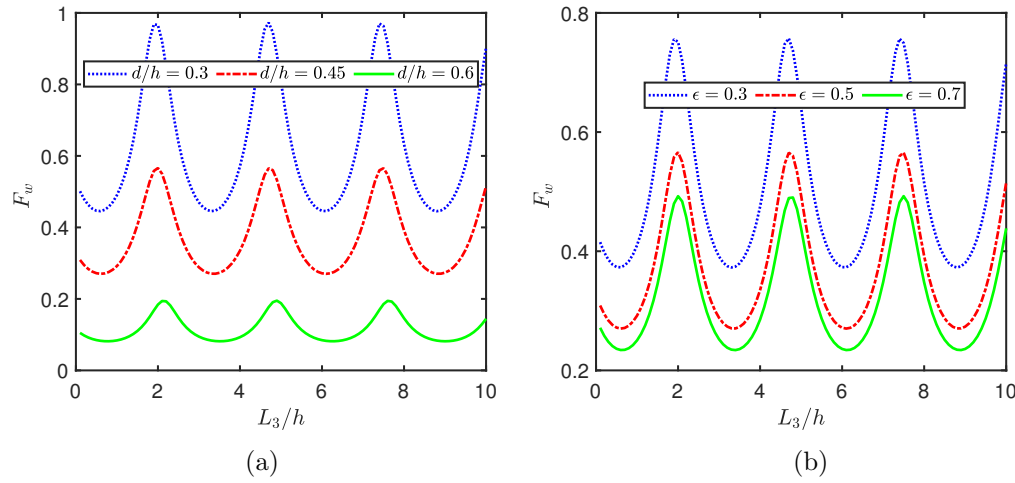
Figure 6.8: Force F_w versus L_3/h for different values of (a) d/h and (b) ϵ with fixed value $l/h = 8$.
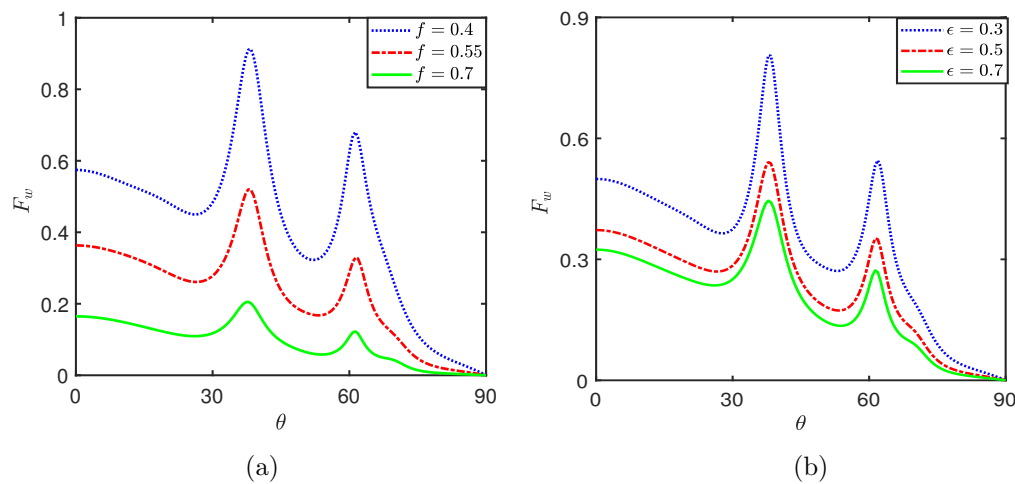
Figure 6.9: Force F_w versus θ for different values of (a) f with fixed $l/h = 10$ and (b) ϵ with fixed $l/h = 8$.

Figure 6.9 illustrates the relationship between F_w and θ for various values of f and ϵ. The figure reveals that for all values of f and ϵ, in the range $0° < \theta < 30°$ the force

F_w experienced on the wall decreases gradually whereas in the range $30° < \theta < 65°$ the force F_w is an oscillatory pattern and after this range of θ it decreases monotonically and reaches to zero at $\theta = 90°$. F_w shows a harmonic peak at $\theta = 38°$ and $\theta = 61°$. Hence it is observed that for $0° \leq \theta \leq 30°$, F_w is less than 60%.

Figure 6.10 depicts the relationship between F_w and width l/h of SPS for various values of s_1/h and s_2/h. With respect to the width l/h, F_w exhibits an oscillatory pattern for smaller l/h values, which diminishes as l/h increases. Subsequently, it decreases monotonically and approaches zero for higher l/h values. This may be due to the fact that for larger values of l/h, nearly all wave energy is dissipated by SPS. It's observed that for higher l/h values, F_w value remains constant regardless of s_1/h and s_2/h value. This suggests that with a larger width of SPS, the influence of step height becomes negligible.
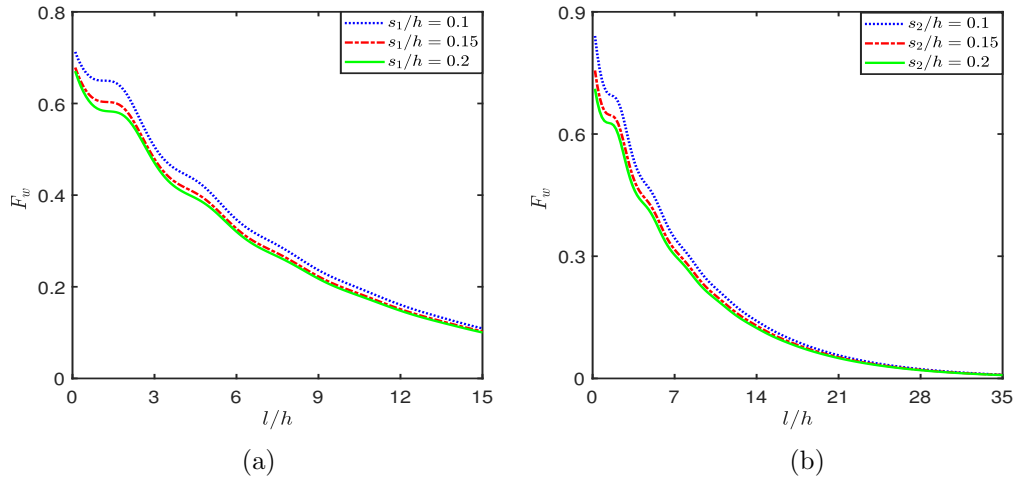
Figure 6.10: Force F_w versus l/h for different values of (a) s_1/h and (b) s_2/h.
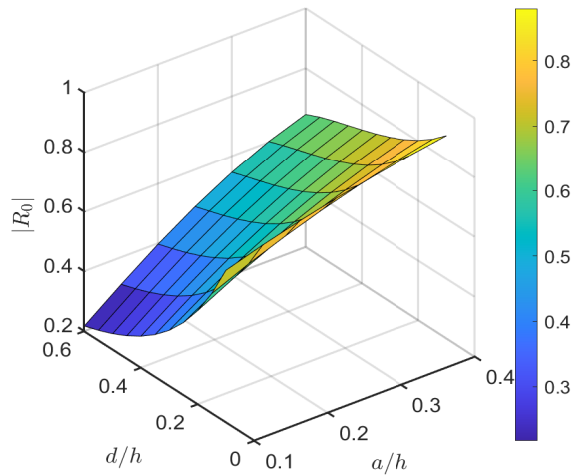
Figure 6.11: Surface plot of Reflection coefficient $|R_0|$ versus d/h and a/h.

6.5.3 Effect of Various Parameter on Reflection Coefficient ($|R_0|$) and Dissipation Coefficient (k_d)

Figure 6.11 presents a surface plot depicting $|R_0|$ across different a/h and d/h values. Analysis of the depicted data reveals a clear trend: within the ranges of $0.1 < a/h < 0.3$ and $0.1 < d/h < 0.6$, wave reflection consistently registers at less than 54%. However, at $a/h = 0.1$ and $d/h = 0.6$, wave reflection is notably lower at 21%. It's crucial to highlight that $a/h = 0.1$ implies SPS is positioned close to the free surface, potentially hindering vessel movement. Thus, configurations with $a/h = 0.1$ should be avoided. Based on these observations from Figures 6.3 and 6.11, this study advocates for selecting $a/h = 0.2$ alongside $d/h = 0.45$, as this combination yields a wave reflection of approximately 45%, balancing reflection of incident wave energy and preserving optimal vessel maneuverability.
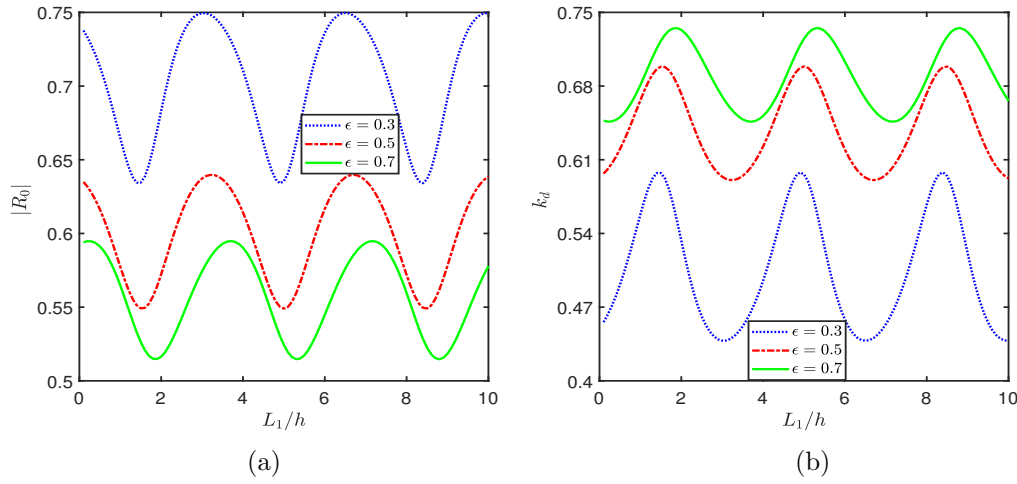
Figure 6.12: (a) Reflection coefficient $|R_0|$ and (b) dissipation coefficient k_d versus L_1/h for different values ϵ.

In Figure 6.12, the behavior of the reflection coefficient $|R_0|$ and dissipation coefficient k_d is presented with respect to L_1/h for various values of ϵ. The results reveal an oscillatory and periodic pattern in both $|R_0|$ and k_d with respect to L_1/h, with periodicity $L_1/h = 3.4$, as observed in Figure 6.4. The maxima in wave reflection and minima in wave dissipation are attributed to constructive interference between the incident and reflected waves, while the minima in wave reflection and maxima in wave dissipation result from destructive interference between these waves. It is noteworthy that an increase in ϵ correlates with a decrease in the reflection coefficient $|R_0|$ and an increase in the dissipation coefficient k_d. This trend can be explained by the heightened porosity ϵ of SPS, leading to increased wave energy dissipation and reduced wave interaction with the wall. Thus less wave is reflected back by the wall. Furthermore, it is observed that as ϵ increases, $|R_0|$ and k_d curves shifted towards the right. Notably, the Max $|R_0|$ decreases from 64% to 49% and Max k_d increases from 70% to 74% for an increase in ϵ values from 0.5 to 0.7.

In Figure 6.13, the graph illustrates the relationship between the reflection coefficient $|R_0|$ and the dissipation coefficient k_d concerning L_2/h for various d/h values of SPS.

The findings showcase an oscillatory and periodic (with a periodicity $L_2/h = 3.1$) pattern in both $|R_0|$ and k_d. Peaks in wave reflection and troughs in wave dissipation result from constructive interference between incident and reflected waves, while troughs in wave reflection and peaks in wave dissipation stem from destructive interference. Notably, an increase in d/h corresponds to a decrease in the reflection coefficient $|R_0|$ and an increase in the dissipation coefficient k_d. This behavior is rationalized by the heightened length (d/h) of SPS, leading to enhanced wave energy dissipation and diminished wave reflection by the wall. Further, it is also noted that for the higher value $d/h = 0.45$ and 0.6, the minima of the curves $|R_0|$ and the maxima of the curve k_d shifted towards the right, while for smaller value $d/h = 0.3$, the maxima of the curves $|R_0|$ and the minima of the curve k_d shifted towards the left.
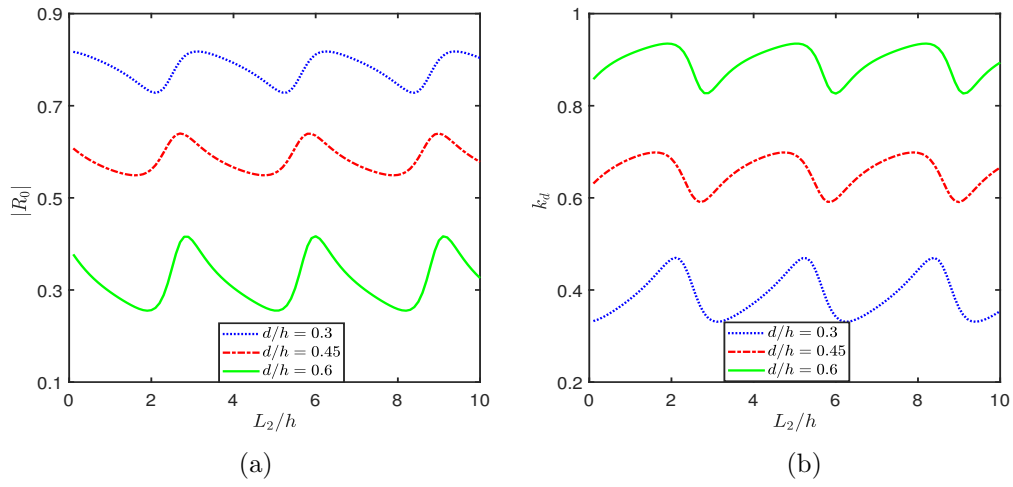
Figure 6.13: (a) Reflection coefficient $|R_0|$ and (b) dissipation coefficient k_d versus L_2/h for different values of d/h.
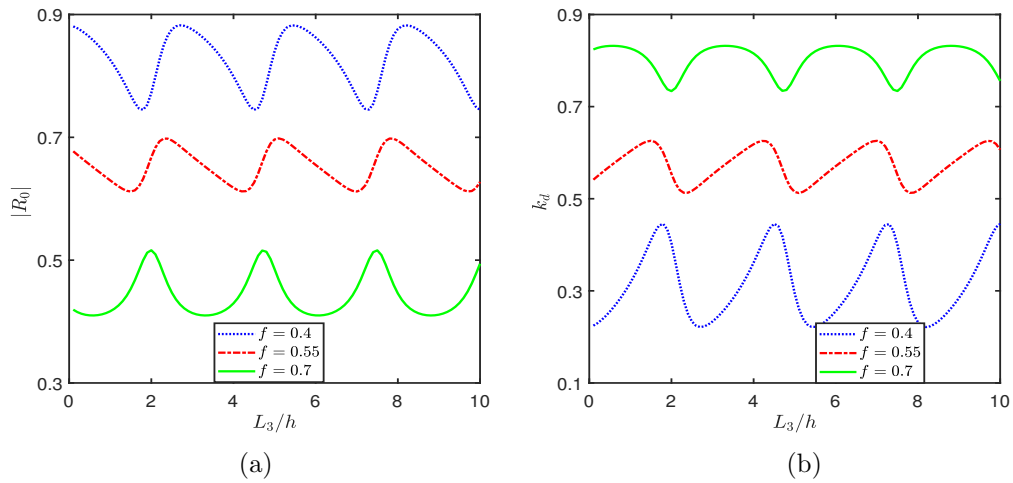
Figure 6.14: (a) Reflection coefficient $|R_0|$ and (b) dissipation coefficient k_d versus L_3/h for different values of f.

In Figure 6.14, the graph depicts the correlation between the reflection coefficient

$|R_0|$ and the dissipation coefficient k_d with L_3/h for various f values of SPS. As observed in Figure 6.8, with respect to L_3/h, a repetitive and oscillatory pattern is also observed in both $|R_0|$ and k_d curves, with periodicity $L_3/h = 2.7$. Peaks in wave reflection and troughs in wave dissipation arise from constructive interference between incident and reflected waves, while troughs in wave reflection and peaks in wave dissipation result from destructive interference. Additionally, an increase in the frictional coefficient f corresponds to a decrease in the reflection coefficient $|R_0|$ and an increase in the dissipation coefficient k_d. This trend can be explained by a higher value of f, leading to higher wave energy dissipation and reduces wave reflection by the wall. Moreover, it is also noted that for the smaller values $f = 0.4$ and 0.55, the maxima in wave reflection and minima in wave dissipation are shifted towards the left.
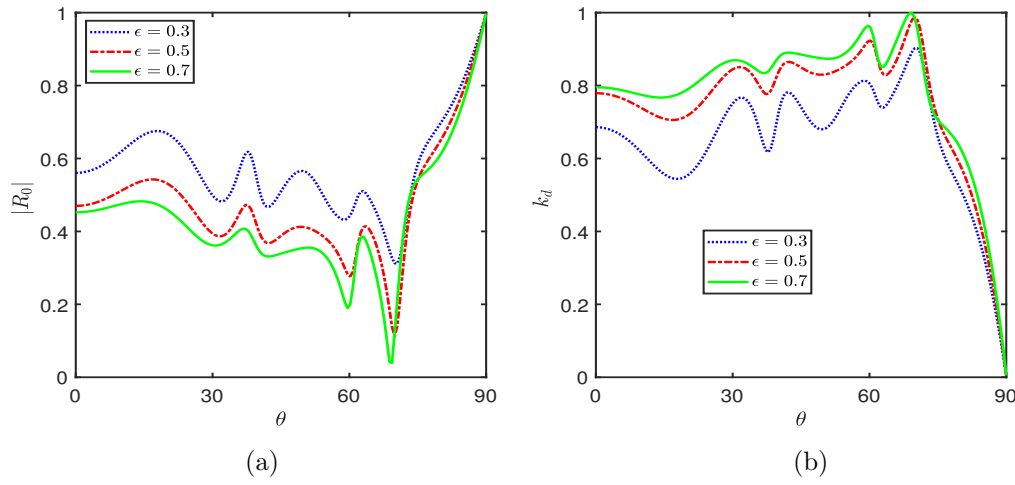
Figure 6.15: (a) Reflection coefficient $|R_0|$ and (b) dissipation coefficient k_d versus θ for different values of ϵ.
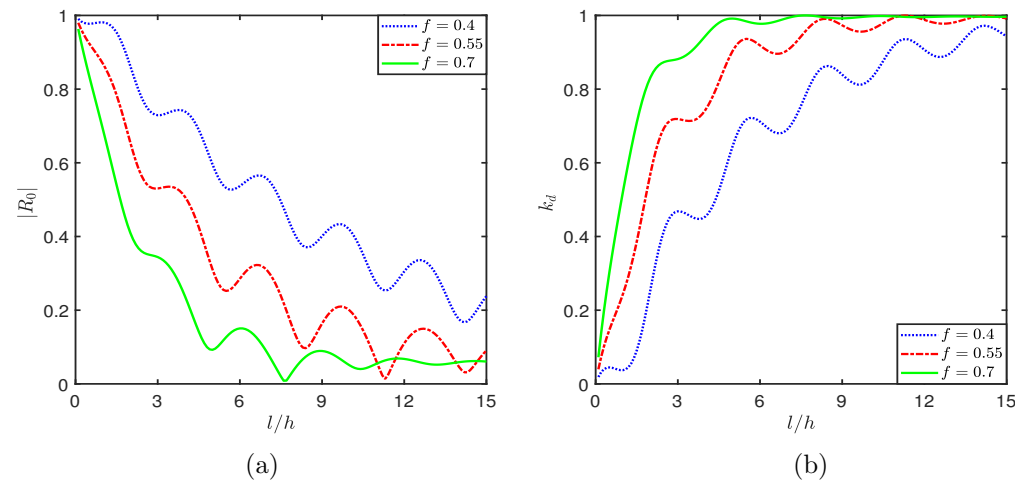
Figure 6.16: (a) Reflection coefficient $|R_0|$ and (b) dissipation coefficient k_d versus l/h for different f.

In Figure 6.15, the graph illustrates the relationship between the reflection coefficient

$|R_0|$ and the dissipation coefficient k_d with respect to θ for various ϵ values of SPS. The figure demonstrates that as θ increases from $0°$ to $67°$, the reflection coefficient $|R_0|$ follows a diminishing oscillatory pattern, while the dissipation coefficient k_d exhibits an increasing oscillatory trend. At $\theta = 67°$, the SPS dissipates almost all wave energy, particularly for higher values of $\epsilon = 0.5$ and 0.7, resulting in significantly reduced wave reflection. However, beyond $\theta = 67°$, there is a sudden increase in wave reflection, reaching unity at $\theta = 90°$, and a simultaneous abrupt decrease in energy dissipation to zero at $\theta = 90°$, regardless of SPS parameter values. Here, $\theta = 67°$ is referred to as the critical angle.

Figure 6.16 shows the variation of the reflection coefficient $|R_0|$ and the dissipation coefficient k_d with respect to l/h for various f values of SPS. The figure shows that $|R_0|$ decreases sharply and k_d increases sharply for the range $0 < l/h < 2.5$. But both coefficients follow an oscillatory pattern for the range $2.5 < l/h < 15$. Moreover, it has been observed that with a higher width $l/h > 12$ and $f = 0.4, 0.55, 0.7$, almost 100% of the incident wave energy is dissipated by SPS, thereby preventing the incident wave energy from transmitting towards the wall.
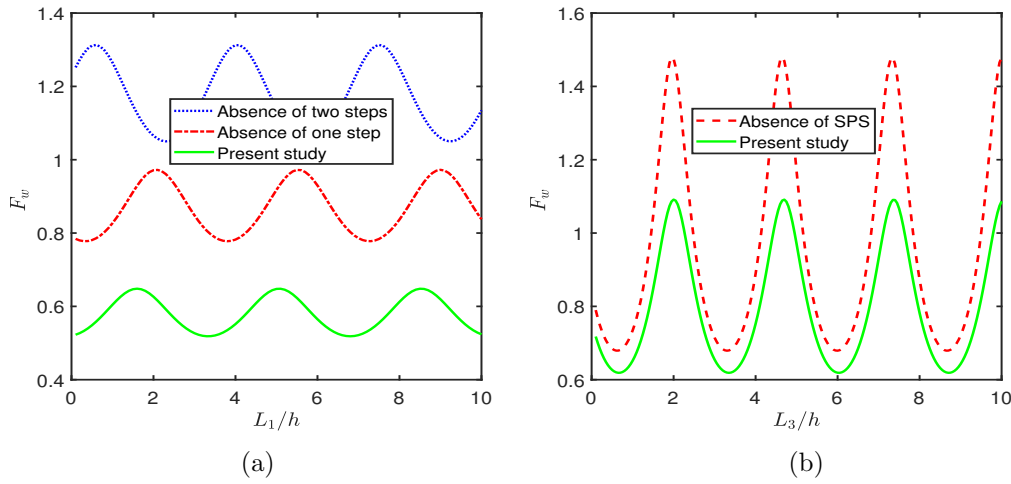
Figure 6.17: Force F_w vs (a) L_1/h and (b) L_3/h ($\theta = 20°$, $d/h = 0.5$).

6.5.4 Comparison Study

Figure 6.17a demonstrates the effect of force F_w versus L_1/h, for three cases: (A1) in the absence of two steps, (A2) in the absence of one step and (A3) present study. From the figure, it has been observed that certain values of L_1/h result in F_w curves reaching their maxima for Case A1, but they result minima for Cases A2 and A3. However, there exist certain values of L_1/h where the opposite behavior is observed: minima are attained for Case A1, whereas maxima are achieved for Cases A2 and A3. This may be because the phase angle between the incident wave and reflected wave for Cases A2 and A3 differs from Case A1. This figure further suggests that F_w experiences a reduction of approximately 37% by Case A2, while the reduction in F_w is about 57% by Case A3, as compared to Case A1. Hence, it can be concluded that Case A3 mitigates wave action more than Cases A1

and A2 by reflecting more wave energy. Figure 6.17b demonstrates the effect of force F_w versus L_3/h for two cases: (B1) in the absence of SPS and (B2) present study. The figure indicates that F_w experiences a reduction of approximately 26% by Case B2, as compared to Case B1. Thus, from this study, it can be concluded that both SPS and the two steps play a crucial role in reducing the wave load on the sea wall.

6.6   Conclusion

To safeguard the sea wall, this paper investigates the interaction of oblique water waves with SPS near a sea wall and also in the presence of two steps. The related boundary value problem gives rise to a system of linear algebraic equations by using the eigenfunction expansion method and orthogonality of eigenfunction, which is solved numerically. From the study, it is observed that within the ranges of $0.1 < a/h < 0.3$ and $0.1 < d/h < 0.6$ with fixed value of $kh = 1$, $l/h = 2$, $L_1/h = 8$, $L_2/h = 7$, $L_3/h = 6$, $s_1/h = 0.2$, $s_2/h = 0.2$, $m = 1$, $f = 0.6$, $\epsilon = 0.5$ and $\theta = 25°$, the wave reflection and force experienced on the wall consistently register at less than 54% and 59%, respectively. For fixed values of $a/h = 0.2$ and $d/h = 0.45$, the wave reflection and force experienced on the wall are nearly 45% and 52%, respectively. Further, it is suggested that SPS with the porosity from 0.5 to 0.7 with fixed $kh = 1$, $a/h = 0.2$, $d/h = 0.45$, $l/h = 2$, $L_2/h = 7$, $L_3/h = 6$, $s_1/h = 0.2$, $s_2/h = 0.2$, $m = 1$ and $\theta = 25°$, F_w decreases from 65% to 52% and with the frictional coefficient from 0.55 to 0.7, Min F_w decreases from 55% to 48% with respect to L_1/h. Moreover, periodic harmonic oscillations are noted in hydrodynamic coefficients of engineering significance concerning variations in the confined water region between SPS and the steps, as well as the width of step-1 and step-2. Also, it is found that at angles $\theta = 38°$ and $\theta = 61°$, force on the wall exhibits harmonic peaks, and for the reflection coefficient and the dissipation coefficient, $\theta = 67°$ is denoted as the critical angle. Further, Compared to when SPS is not present, the present study recorded 26% reduction in the force experienced on the wall. Compared to the absence of both steps, the problem with SPS and wall over one step reduces the force on the wall by 37%, and the problem with SPS and wall over two steps reduces the force by 57%. The effect of the steps' height becomes negligible for a larger width of SPS.

Chapter 7

Mitigation of Wave Response on an Elastic Plate by Multiple Bottom-Standing Porous Structure

7.1 Introduction

In Chapters 2-5, we examine the effectiveness of various configurations of a single thick porous structure such as PS extended from top to bottom, BSPS and SPPS, to mitigate the wave response on an elastic plate (EP) or on a sea wall in the presence of EP, whereas in Chapter 6, we examine the effectiveness of a thick submerged porous structure (SPS) to mitigate the wave response on the sea wall in the presence of two steps bottom. In this chapter, we focus on analyzing the effectiveness of multiple bottom-standing porous structures (BSPS) in reducing the wave response on a floating elastic plate. The study formulates the governing equation and boundary conditions within the potential flow theory framework. Though this problem may be handled by employing scattering matrix approach as in Biggs and Porter [123] (who examined wave acattering by an array of periodic barriers) but we have solved it here by utilizing the eigenfunction expansion method along with orthogonality of eigenfunctions which gives rise to a system of algebraic equations. These equations are subsequently solved to examine several factors, including plate deflection, shear force, strain of EP, and coefficients related to reflection, transmission, and dissipation. The investigation underscores the significance of BSPS parameters, such as length, porosity, and frictional coefficient, in reducing plate deflection, shear force, and strain on the EP. Additionally, the present results are validated against known results produced by Losada et al. [18] and Hermans [70]. The major part of this work is communicated to a journal for publication.

7.2 Mathematical Formulation

The current investigation examines the scattering of surface gravity waves by a floating elastic structure in the presence of multiple bottom-standing porous structures within a Cartesian coordinate system. The elastic plate (EP) thickness is assumed to be small. The fluid domain is $-\infty < x < \infty$, $-h \le y \le 0$, other than EP as shown in Figure 7.1. This study considers n number of BSPS denoted by PS_m, $m = 1, 2, 3, \ldots, n$ counted

from left to right. The notation LP_m, represents the position of PS_m, defined by LP_m : $d_m \leq x \leq b_m, -h \leq y \leq -h + a_m$ ($m = 1, 2, 3, \ldots, n$), where as $l_m = d_{m+1} - b_m$ ($m = 1, 2, 3, \ldots, n-1$) denotes the gap between m^{th} and $(m+1)^{th}$ of BSPS and $c_m = b_m - d_m$ is the width of BSPS. The position of EP is $b_{n+1} \leq x \leq b_{n+2}, y = 0$, so that the length of EP becomes $L = b_{n+2} - b_{n+1}$ and the gap between PS_n and EP becomes $l_n = b_{n+1} - b_n$. Assuming the incident wave travels at an angle $\theta = 0°$ along the x-axis, and considering an incompressible, inviscid fluid with the irrotational and simple harmonic flow in time with angular frequency ω, within each region denoted by R_j ($j = 3m-2, 3m-1, 3m$ ($m = 1, 2, 3, \ldots, n$), $3n+1, 3n+2, 3n+3$) as described in Figure 7.1, there exists a velocity potential expressed in the form $\Phi_j(x, y, t) = Re\{\phi_j(x, y)e^{-i\omega t}\}$, satisfying

$$\left(\frac{\partial^2}{\partial x^2} + \frac{\partial^2}{\partial y^2}\right)\phi_j = 0, \quad \text{in the region } R_j. \tag{7.1}$$
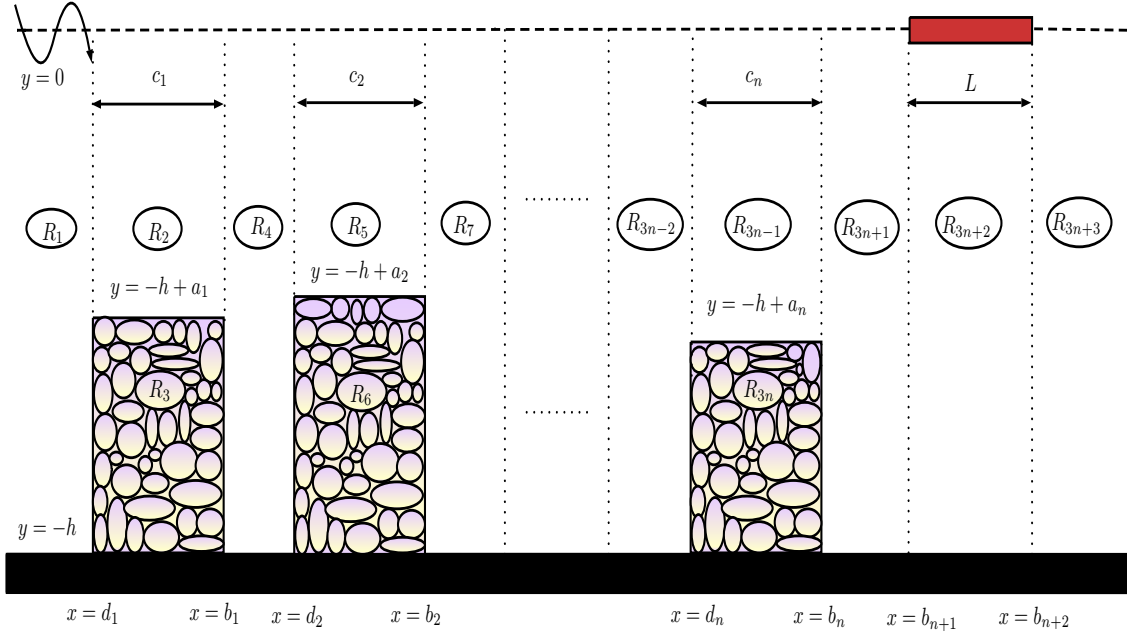
Figure 7.1: Schematic representation of scattering of water wave in the presence of multiple BSPS and EP.

The impermeable bottom condition is given by

$$\frac{\partial \phi_j}{\partial y} = 0, \text{ on } y = -h \text{ for } j = 3m-2, 3m \text{ } (m = 1, 2, 3, \ldots, n), 3n+1, 3n+2, 3n+3. \tag{7.2}$$

The free-surface condition is expressed by

$$\frac{\partial \phi_j}{\partial y} - K\phi_j = 0 \text{ on } y = 0 \text{ for } j = 3m-2, 3m-1 \text{ } (m = 1, 2, 3, \ldots, n), 3n+1, 3n+3, \tag{7.3}$$

with $K = \omega^2/g$, and g is the acceleration due to gravity.

The boundary condition on the floating EP is expressed by

$$\left[D\frac{\partial^4}{\partial x^4} + 1 - \epsilon_e K\right]\frac{\partial\phi_{3n+2}}{\partial y} - K\phi_{3n+2} = 0 \quad \text{on} \quad y = 0, \tag{7.4}$$

where $D = EI/\rho g$ is the flexural rigidity of EP, with E being the Young's modulus, $I = h_0^3/12(1-\nu^2)$, ν is the Poisson's ratio, ρ is the density of the fluid, $\epsilon_e = \rho_s h_0/\rho$, h_0 is the thickness of EP assumed to be small and ρ_s is the density of EP. It may be noted that in the absence of EP (i.e. $D = 0$ and $\epsilon_e = 0$), the Equation (7.4) reduces to the free surface condition in ϕ_{3n+2}, given by $\frac{\partial\phi_{3n+2}}{\partial y} - K\phi_{3n+2} = 0$.

By assuming that EP is freely floating on the surface of water, the vanishing of bending moment and shear force at the edges of EP yield

$$\frac{\partial^3\phi_{3n+2}}{\partial x^2\partial y} \to 0 \quad \text{and} \quad \frac{\partial^4\phi_{3n+2}}{\partial x^3\partial y} \to 0 \quad \text{at } (b_{n+1}, 0) \text{ and } (b_{n+2}, 0). \tag{7.5}$$

Due to the continuity of pressure and velocity along the mutual interfaces of PS_m, $(m = 1, 2, 3,\ldots, n)$ are expressed by

$$\phi_{3m-1} = (s_m + if_m)\phi_{3m}, \quad \frac{\partial\phi_{3m-1}}{\partial y} = \epsilon_m\frac{\partial\phi_{3m}}{\partial y} \quad \text{on } y = -h + a_m, \ d_m \leq x \leq b_m, \tag{7.6}$$

$$\phi_{3m-2} = (s_m + if_m)\phi_{3m}, \quad \frac{\partial\phi_{3m-2}}{\partial x} = \epsilon_m\frac{\partial\phi_{3m}}{\partial x} \quad \text{on} \quad x = d_m, \ -h \leq y \leq -h + a_m, \tag{7.7}$$

$$\phi_{3m+1} = (s_m + if_m)\phi_{3m}, \quad \frac{\partial\phi_{3m+1}}{\partial x} = \epsilon_m\frac{\partial\phi_{3m}}{\partial x} \quad \text{on} \quad x = b_m, \ -h \leq y \leq -h + a_m, \tag{7.8}$$

where s_m, f_m and ϵ_m are the inertial coefficient, frictional coefficient and porosity of the permeable material PS_m, respectively.

The conditions of continuity of pressure and velocity along the vertical interfaces at $x = d_m$ and $x = b_m$ are expressed as

$$\phi_{3m-2} = \phi_{3m-1}, \quad \frac{\partial\phi_{3m-2}}{\partial x} = \frac{\partial\phi_{3m-1}}{\partial x} \quad \text{on} \quad x = d_m, \quad -h + a_m \leq y \leq 0, \tag{7.9}$$

$$\phi_{3m-1} = \phi_{3m+1}, \quad \frac{\partial\phi_{3m-1}}{\partial x} = \frac{\partial\phi_{3m+1}}{\partial x} \quad \text{on} \quad x = b_m, \quad -h + a_m \leq y \leq 0. \tag{7.10}$$

The conditions of continuity for pressure and velocity along the interfaces of R_{3n+2} (EP is present) are given as

$$\phi_{3n+1} = \phi_{3n+2}, \quad \frac{\partial\phi_{3n+1}}{\partial x} = \frac{\partial\phi_{3n+2}}{\partial x} \quad \text{on} \quad x = b_{n+1}, \quad -h \leq y \leq 0, \tag{7.11}$$

$$\phi_{3n+2} = \phi_{3n+3}, \quad \frac{\partial\phi_{3n+2}}{\partial x} = \frac{\partial\phi_{3n+3}}{\partial x} \quad \text{on} \quad x = b_{n+2}, \quad -h \leq y \leq 0. \tag{7.12}$$

The far-field condition is given by

$$\phi_1(x, y) \simeq \left(\frac{ig}{\omega}\right)\frac{\cosh k(h+y)}{\cosh kh}\{e^{ik(x-d_1)} + R_0 e^{-ik(x-d_1)}\} \quad \text{as} \quad x \to -\infty, \tag{7.13}$$

$$\phi_{3n+3}(x, y) \simeq \left(\frac{ig}{\omega}\right)T_0\frac{\cosh k(h+y)}{\cosh kh}e^{ik(x-b_{n+2})} \quad \text{as} \quad x \to \infty, \tag{7.14}$$

where R_0 and T_0 denote the unknown constants associated with reflected and transmitted wave, respectively to be determined here. In this problem, the singularity at the tip of each BSPS is not considered.

7.3 Method of Solution

To solve the boundary value problem described above, the method of separation of variables is employed within each region, expressing the spatial potential functions in terms of eigenfunctions. The spatial velocity potentials in the open water regions R_1, R_{3n+3} and R_{3m+1} $(m = 1, 2, 3, \ldots, n)$ satisfying Equations (7.1), (7.2), (7.3), (7.13) and (7.14) are expressed in the forms

$$\phi_1 = \left(\frac{ig}{\omega}\right)\left[e^{ik(x-d_1)} + R_0 e^{-ik(x-d_1)}\right]\psi(y) \quad \text{for} \quad -\infty < x \le 0, \ -h \le y \le 0, \quad (7.15)$$

$$\phi_{3n+3} = \left(\frac{ig}{\omega}\right)T_0 e^{ik(x-b_{n+2})}\psi(y) \quad \text{for} \quad b_{n+2} \le x < \infty, -h \le y \le 0, \quad (7.16)$$

$$\phi_{3m+1} = \left(\frac{ig}{\omega}\right)\left[A_m e^{ik(x-b_m)} + B_m e^{-ik(x-d_{m+1})}\right]\psi(y) \quad \text{for } b_m \le x \le d_{m+1}, -h \le y \le 0, \quad (7.17)$$

where

$$\psi(y) = \frac{\cosh k(h + y)}{\cosh kh}. \quad (7.18)$$

R_0, A_m, B_m and T_0 are unknown constants and k is the positive real root of the dispersion relation

$$K - k\tanh kh = 0. \quad (7.19)$$

Again, the spatial velocity potentials in the porous regions R_{3m-1} and R_{3m} $(m = 1, 2, 3, \ldots, n)$ satisfying Equations (7.1), (7.2), (7.3) and (7.6) are expressed in the forms

$$\phi_{3m-1} = \left(\frac{ig}{\omega}\right)\left[E_m e^{ip_m(x-d_m)} + H_m e^{-ip_m(x-b_m)}\right]P_m(y) \quad \text{for} \quad d_m \le x \le b_m, \ -h + a_m \le y \le 0, \quad (7.20)$$

$$\phi_{3m} = \left(\frac{ig}{\omega}\right)\left[E_m e^{ip_m(x-d_m)} + H_m e^{-ip_m(x-b_m)}\right]Q_m(y) \quad \text{for} \quad d_m \le x \le b_m, \ -h + a_m \le y \le 0, \quad (7.21)$$

where

$$P_m(y) = \frac{\cosh p_m(h + y) - \mathcal{F}_m \sinh p_m(h + y)}{\cosh p_m h - \mathcal{F}_m \sinh p_m h}, \quad (7.22)$$

$$Q_m(y) = \frac{(1 - \mathcal{F}_m \tanh p_m a_m)\cosh p_m(h + y)}{(s_m + if_m)(\cosh p_m h - \mathcal{F}_m \sinh p_m h)}, \quad (7.23)$$

$$\mathcal{F}_m = \frac{(1 - G_m)\tanh p_m a_m}{1 - G_m \tanh^2 p_m a_m}, \quad G_m = \frac{\epsilon_m}{s_m + if_m}, \quad (7.24)$$

E_m and H_m, are unknown constants and p_m are the complex root of the dispersion relation

$$K - p_m \tanh p_m h - \mathcal{F}_m(K \tanh p_m h - p_m) = 0, \tag{7.25}$$

corresponding to PS_m. Finally, the spatial velocity potential in the region R_{3n+2} (EP is present) is satisfying Equations (7.1), (7.2) and (7.4) is expressed in the form

$$\phi_{3n+2} = \left(\frac{ig}{\omega}\right) \sum_{q=-2}^{0} \left[\mathcal{C}_q e^{i\alpha_q(x-b_{n+1})} + \mathcal{D}_q e^{-i\alpha_q(x-b_{n+2})}\right] \mathcal{G}_q(y) \quad \text{for} \quad b_{n+1} \leq x \leq b_{n+2}, \ -h \leq y \leq 0 \tag{7.26}$$

where

$$\mathcal{G}_q(y) = \frac{\cosh \alpha_q(h+y)}{\cosh \alpha_q h} \quad q = -2, -1, 0, \tag{7.27}$$

$\mathcal{C}_q$ and $\mathcal{D}_q$ are unknown constants and α_q are the complex roots of the form $\pm\beta_1 + i\beta_2$ for $q = -1, -2$ and positive real root for $q = 0$ of the equation

$$(D\alpha_q^4 + 1 - \epsilon_e K)\alpha_q \tanh \alpha_q h = K. \tag{7.28}$$

Using matching conditions as given in Equations (7.7)-(7.12), in conjunction with the orthogonality of eigenfunctions $\psi(y)$ in $-h \leq y \leq 0$, we have for $m = 2, 3, 4, \ldots, n$

$$(1 + R_0)X - [Y_1 + (s_1 + if_1)Z_1](E_1 + H_1 e^{-ip_1(d_1-b_1)}) = 0, \tag{7.29}$$

$$ik(1 - R_0)X - ip_1[Y_1 + \epsilon_1 Z_1](E_1 - H_1 e^{-ip_1(d_1-b_1)}) = 0, \tag{7.30}$$

$$(A_1 + B_1 e^{-ik(b_1-d_2)})X - [Y_1 + (s_1 + if_1)Z_1](E_1 e^{ip_1(b_1-d_1)} + H_1) = 0, \tag{7.31}$$

$$ik(A_1 - B_1 e^{-ik(b_1-d_2)})X - ip_1[Y_1 + \epsilon_1 Z_1](E_1 e^{ip_1(b_1-d_1)} - H_1) = 0, \tag{7.32}$$

$$(A_{m-1} e^{ik(d_m-b_{m-1})} + B_{m-1})X - [Y_m + (s_m + if_m)Z_m](E_m + H_m e^{-ip_m(d_m-b_m)}) = 0, \tag{7.33}$$

$$ik(A_{m-1} e^{ik(d_m-b_{m-1})} - B_{m-1})X - ip_m[Y_m + \epsilon_m Z_m](E_m - H_m e^{-ip_m(d_m-b_m)}) = 0, \tag{7.34}$$

$$(A_{m+1} + B_{m+1} e^{-ik(b_m-d_{m+1})})X - [Y_m + (s_m + if_m)Z_m](E_m e^{ip_m(b_m-d_m)} + H_m) = 0, \tag{7.35}$$

$$ik(A_{m+1} - B_{m+1} e^{-ik(b_m-d_{m+1})})X - ip_m[Y_m + \epsilon_m Z_m](E_m e^{ip_m(b_m-d_m)} - H_m) = 0, \tag{7.36}$$

$$(A_{n+1} e^{ik(b_{n+1}-b_n)} + B_{n+1})X - \sum_{q=-2}^{0} (\mathcal{C}_q + \mathcal{D}_q e^{-i\alpha_q(b_{n+1}-b_{n+2})})W_q = 0, \tag{7.37}$$

$$ik(A_{n+1} e^{ik(b_{n+1}-b_n)} - B_{n+1})X - \sum_{q=-2}^{0} i\alpha_q(\mathcal{C}_q - \mathcal{D}_q e^{-i\alpha_q(b_{n+1}-b_{n+2})})W_q = 0, \tag{7.38}$$

$$\sum_{q=-2}^{0} (\mathcal{C}_q e^{i\alpha_q(b_{n+2}-b_{n+1})} + \mathcal{D}_q)W_q - T_0 X = 0, \tag{7.39}$$

$$\sum_{q=-2}^{0} i\alpha_q(\mathcal{C}_q e^{i\alpha_q(b_{n+2}-b_{n+1})} - \mathcal{D}_q)W_q - ikT_0 X = 0, \tag{7.40}$$

where

$$X = \int_{-h}^{0} \psi(y)\psi(y)dy, \quad Y_m = \int_{-h+a_m}^{0} P_m(y)\psi(y)dy,$$

$$Z_m = \int_{-h}^{-h+a_m} Q_m(y)\psi(y)dy, \quad W_q = \int_{-h}^{0} \mathcal{G}_q(y)\psi(y)dy. \tag{7.41}$$

Further, the free edge conditions (7.5), gives

$$\sum_{q=-2}^{0} \alpha_q^3 (\mathcal{C}_q + \mathcal{D}_q e^{-i\alpha_q(b_{n+1}-b_{n+2})}) \tanh \alpha_q h = 0, \tag{7.42}$$

$$\sum_{q=-2}^{0} i\alpha_q^4 (\mathcal{C}_q - \mathcal{D}_q e^{-i\alpha_q(b_{n+1}-b_{n+2})}) \tanh \alpha_q h = 0, \tag{7.43}$$

$$\sum_{q=-2}^{0} \alpha_q^3 (\mathcal{C}_q e^{i\alpha_q(b_{n+2}-b_{n+1})} + \mathcal{D}_q) \tanh \alpha_q h = 0, \tag{7.44}$$

$$\sum_{q=-2}^{0} i\alpha_q^4 (\mathcal{C}_q e^{i\alpha_q(b_{n+2}-b_{n+1})} - \mathcal{D}_q) \tanh \alpha_q h = 0. \tag{7.45}$$

Equations (7.29)-(7.45) represents a system of $(4n + 12)$ equations for the determination of $(4n + 12)$ unknowns R_0, T_0, A_m, B_m, E_m, H_m, $\mathcal{C}_q$ and $\mathcal{D}_q$ ($m = 1, 2, \ldots, n$), which is solved numerically by Gauss elimination method with the help of MATLAB. The effectiveness of thick porous structure to mitigate the structural response of EP can be studied through the plate deflection, shear force, strain, reflection coefficient $|R_0|$, transmission coefficient $|T_0|$ and dissipation coefficient $K_D = 1 - |R_0|^2 - |T_0|^2$.

Plate deflection: The plate deflection is calculated by using the formula

$$\eta_E = \frac{i}{\omega} \frac{\partial \phi_{3n+2}}{\partial y}\bigg|_{y=0}. \tag{7.46}$$

Shear force and strain: The shear force S_F and strain S_T on EP surface are calculated by

$$S_F = \frac{D}{h\omega} \left| \frac{\partial^4 \phi_{3n+2}}{\partial x^3 \partial y} \right|_{y=0}, \tag{7.47}$$

$$S_T = \frac{h_0}{2\omega} \left| \frac{\partial^3 \phi_{3n+2}}{\partial x^2 \partial y} \right|_{y=0}. \tag{7.48}$$

7.4 Results and Discussion

In this section, the usefulness of n number of BSPS to minimize the wave effect on EP is studied through plate deflection $(Re(\eta_E))$, shear force (S_F), strain (S_T) reflection coefficient $|R_0|$, transmission coefficient $|T_0|$ and dissipation coefficient K_D. Unless otherwise specified, the non-dimensional parameters $kh = 1$, $a_m/h = 0.5$, $c_m/h = 1$, $s_m = 1$, $f_m = 0.5$, $\epsilon_m = 0.5$, $l_1/h = 4$, $l_m/h = 8$, $\epsilon_e/h = 0.01$, $D/h^4 = 100$ and $L/h = 20$

will remain fixed throughout this study. In this section, several computations are done, but few results are presented to avoid repetition. The analysis is carried out to mitigate high wave load on EP in the presence of different combinations of BSPS such as (i) one BSPS, (ii) two BSPS, (iii) three BSPS and (iv) four BSPS.

7.4.1 Validation

To validate the present methodology and results, it is noted that for $n = 1$ and without the presence of EP, the present problem is equivalent to the work "interaction of water waves with a single BSPS" by Losada et al. [18]. Figure 7.2a shows the results of the present problem in the absence of EP (i.e. $D/h^4 = 0$, $\epsilon_e/h = 0$) and with $kh = 0.68$, $\epsilon_1 = 0.4$, $f_1 = 0.5$, $a_1/h = 0.3$, which are well matched with the result of Losada et al. [18]. Further, on considering the parameter value as $s_m = 1$, $f_m = 0$, $\epsilon_m = 1$ (absence of porous structures) and $D/h^4 = 10^{-3}$, the present problem reduces to the work "scattering of water waves in the presence of EP" by Hermans [70]. Figure 7.2b illustrates the results on $|R_0|$ and $|T_0|$, which are also well matched with the results of Hermans [70].
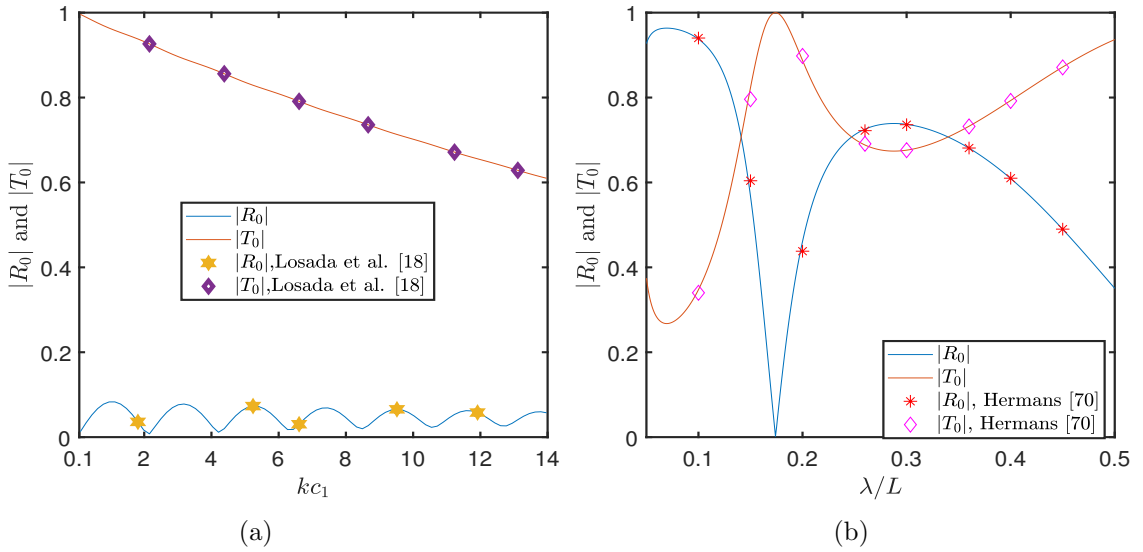
Figure 7.2: Validation of the numerical code for **(a)** Presence of one BSPS only and **(b)** Presence of EP only.

7.4.2 Effect of Two BSPS on Plate Deflection ($Re(\eta_E)$), Shear Force (S_F), Strain (S_T), Reflection Coefficient ($|R_0|$), Transmission Coefficient ($|T_0|$) and Dissipation Coefficient (K_D)

Figure 7.3 illustrates the variations in plate deflection (η_E) concerning different values of the length a_1/h and the frictional coefficient (f_1) of PS_1. Figure 7.3a shows that with an increase in the length a_1/h, there is a notable decrease in plate deflection. This decline can be attributed to the heightened dissipation of incident wave energy as the length of PS_1 increases, resulting in diminished energy transmission towards EP. Consequently, a

reduction in the plate deflection is evident. In Figure 7.3b, the relationship between f_1 and plate deflection is examined. It is evident that as f_1 increases, there is a corresponding decrease in plate deflection. This phenomenon can be primarily attributed to the amplified dissipation of wave energy associated with higher values of f_1. Consequently, PS_1, characterized by a larger frictional coefficient (f_1), effectively mitigates the structural response of EP by reducing plate deflection.

(a)

(b)
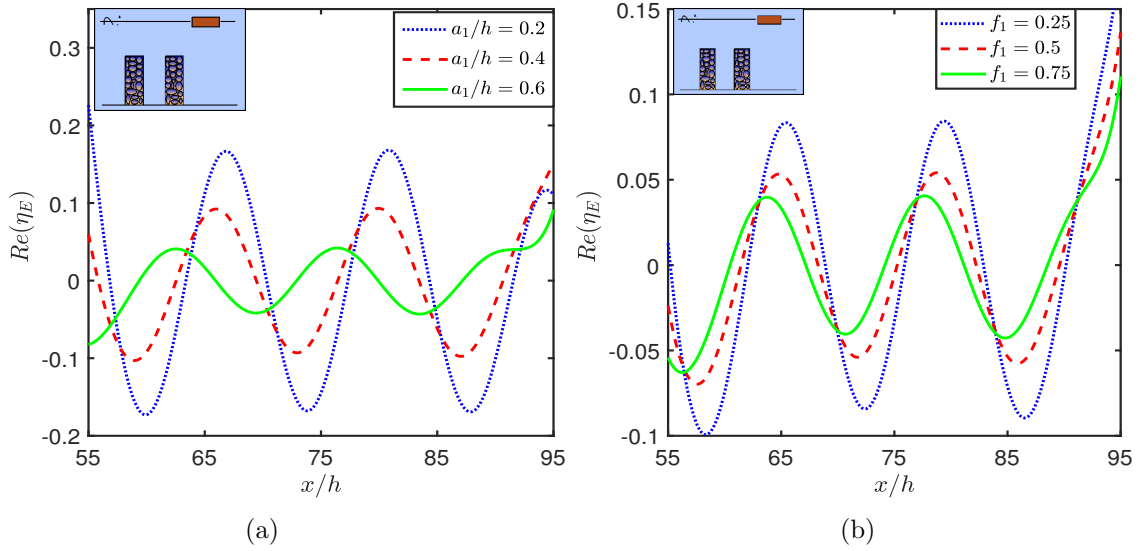
Figure 7.3: $Re(\eta_E)$ for different values of a_1/h and f_1 with $c_m/h = 10$, $l_1/h = 15$, $l_2/h = 20$, $D/h^4 = 75$ and $L/h = 40$.

(a)

(b)
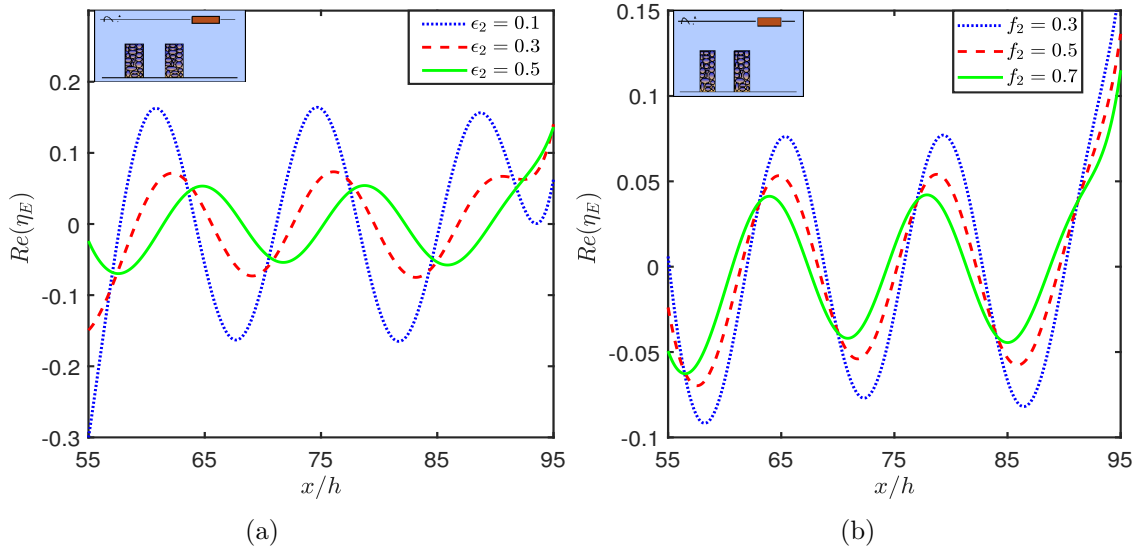
Figure 7.4: $Re(\eta_E)$ for different values of ϵ_2 and f_2 with $c_m/h = 10$, $l_1/h = 15$, $l_2/h = 20$, $D/h^4 = 75$ and $L/h = 40$.

Figure 7.4 illustrates the plate deflection (η_E) across various values of the porosity (ϵ_2) and the frictional coefficient (f_2) of PS_2. Figure 7.4a shows that an increase in ϵ_2 significantly decreases plate deflection, as a result of change in the wave damping.

The porous structures offer minimal wave damping for low values of BSPS porosity (Venkateswarlu et al. [124]), and it increases after increasing the BSPS porosity. Figure 7.4b examines the relationship between the f_2 and plate deflection. It is observed that an increase in the f_2 corresponds to a decrease in plate deflection. This decrease can be attributed to the heightened dissipation of incident wave energy as ϵ_2 and f_2 of PS_2 increases, reducing energy transmission towards EP. Consequently, it effectively mitigates the structural response of EP by reducing plate deflection. In both cases (Figure 7.4a and Figure 7.4b), the plate deflection pattern is oscillatory, and the magnitude is highly influenced by ϵ_2 and f_2 due to change in wave damping.
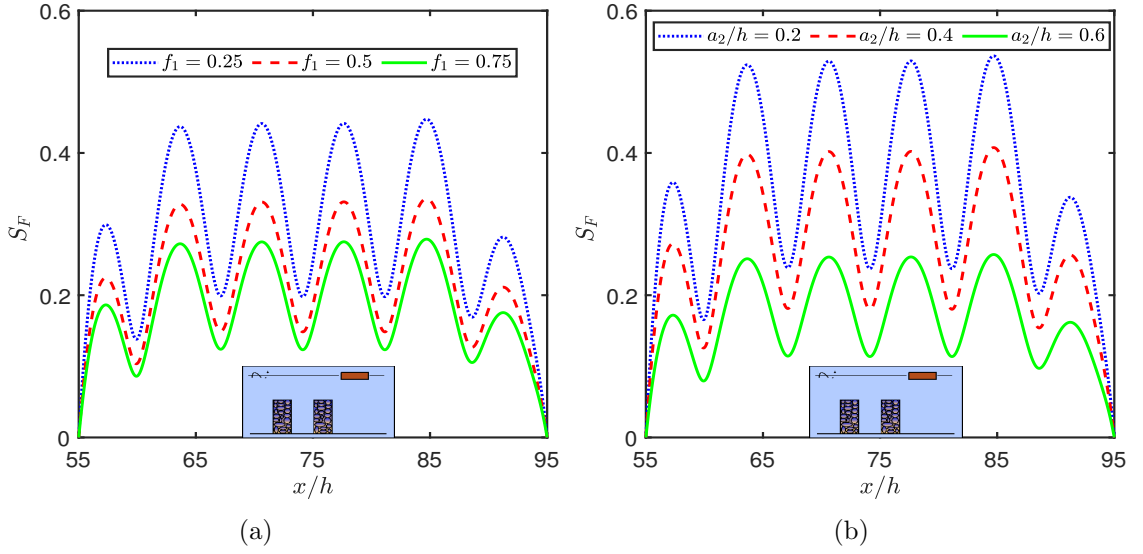
Figure 7.5: S_F for different values of f_1 and a_2/h with $c_m/h = 10$, $l_1/h = 15$, $l_2/h = 20$, $D/h^4 = 75$ and $L/h = 40$.
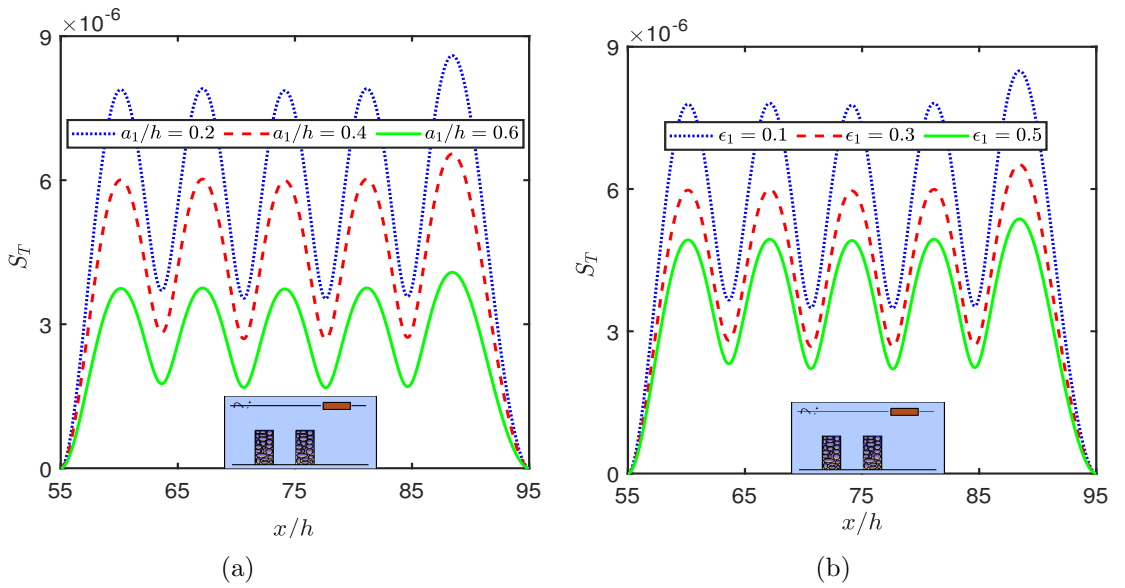
Figure 7.6: S_T for different values of a_1/h and ϵ_1 with $c_m/h = 10$, $l_1/h = 15$, $l_2/h = 20$, $D/h^4 = 75$ and $L/h = 40$.

In Figure 7.5, the shear force (S_F) is presented to illustrate the influence of frictional coefficient f_1 of PS_1 and the length a_2/h of PS_2, on the structural response of EP. Notably, the shear force at the ends of EP is zero, aligning with the assumption of free edge behavior. Additionally, the variation of S_F exhibits an oscillatory pattern, indicating dynamic changes in the structural response. Interestingly, as both f_1 of PS_1 and a_2/h of PS_2 increase, there is a decrease in the amplitude of the shear force of EP. This trend suggests that heightened values of these parameters contribute to reduced S_F and enhanced damping characteristics of the system. Such behavior is attributed to the increased wave energy dissipation by PS_1 and PS_2, as observed and analyzed in Figure 7.3.

Figure 7.6 provides a comprehensive analysis of strain (S_T) dynamics across a range of values for both the length (a_1/h) and the porosity (ϵ_1) within PS_1. Noteworthy is the observation that the strain is zero at the ends of EP, aligning with the assumed free edge behavior. Additionally, the variation of strain S_T is characterized by an oscillatory pattern, suggesting dynamic fluctuations in the structural response. Furthermore, an intriguing correlation emerges between the increase in both a_1/h and ϵ_1 and the subsequent decrease in strain amplitude within EP. This fascinating phenomenon underscores the heightened wave energy dissipation facilitated by PS_1, as analyzed in Figures 7.3 and 7.5.
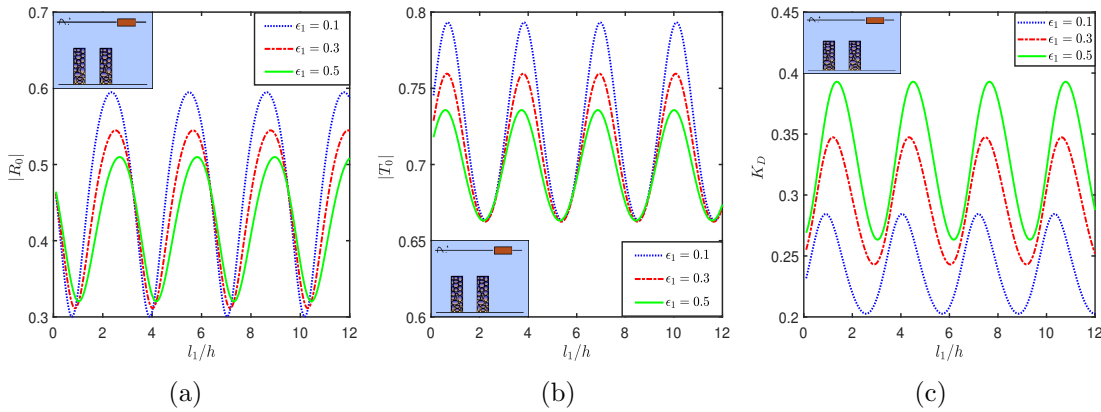
Figure 7.7: $|R_0|$, $|T_0|$ and K_D vs l_1/h for different values of ϵ_1.

The graphical representations in Figure 7.7 illustrate the variations in reflection coefficient $|R_0|$, transmission coefficient $|T_0|$ and dissipation coefficient K_D with respect to l_1/h for various porosity levels ϵ_1 of PS_1. These figures reveal a periodic and oscillatory behavior of $|R_0|$, $|T_0|$ and K_D as l_1/h changes. The presence of peaks and troughs in wave reflection suggests the occurrence of constructive and destructive interference between incident and reflected waves, respectively. Additionally, an increase in ϵ_1 of PS_1 leads to greater wave energy dissipation within the PS_1, as analyzed in Figure 7.6b, consequently resulting in decreased wave reflection and transmission. This observation underscores the crucial role of porosity in influencing wave energy dissipation and subsequent wave reflection and transmission properties. The role of BSPS is significant in dissipating the incident wave energy, and the remaining wave energy i.e., transmitted from the second porous structure is being reflected by EP, as it is fixed near the free surface. This

phenomenon amplifies the fluid resonance, which may lead to standing wave formation as a result of wave-wave interaction in the gap region.

Several authors (Vijay et al. [31]; Dhanunjaya et al. [125]) reported that the maximum part of wave energy is focused near the free surface (approximately 80%). Thus, the selection of breakwater length is partially dependent upon the level of EP protection. An attempt has been made in the present study to understand the fluid behavior against BSPS length. Figure 7.8 presents the distribution of reflection coefficient $|R_0|$, transmission coefficient $|T_0|$ and dissipation coefficient K_D across different values of the length a_2/h of PS_2 plotted against l_1/h. These figures reveal a periodic and oscillatory trend in $|R_0|$, $|T_0|$ and K_D as l_1/h varies, consistent with the patterns observed in Figure 7.7. Moreover, it is noted that an increase in a_2/h of PS_2 induces greater wave energy dissipation by PS_2, as evidenced in Figure 7.5b. Consequently, this amplified dissipation leads to a decrease in wave reflection and transmission.

Figure 7.8: $|R_0|$, $|T_0|$ and K_D vs l_1/h for different values of a_2/h.
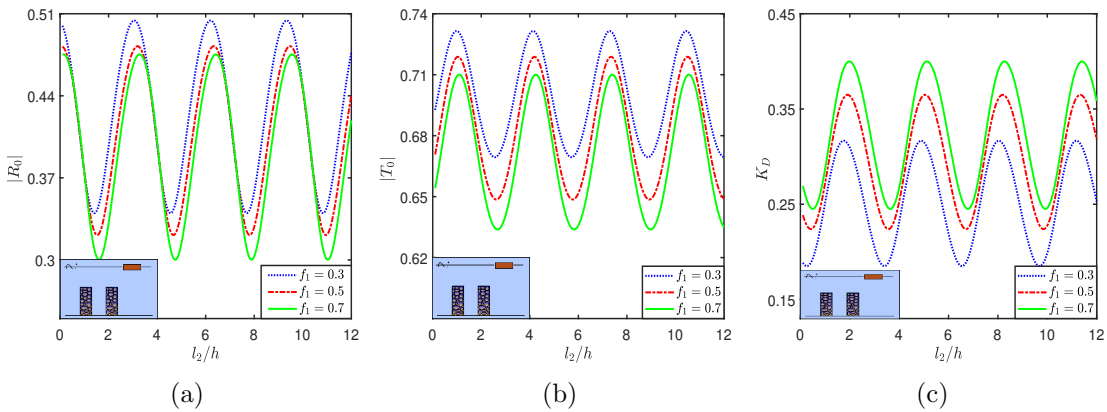
Figure 7.9: $|R_0|$, $|T_0|$ and K_D vs l_2/h for different values of f_1.

Figure 7.9 illustrates the variations in the reflection coefficient $|R_0|$, transmission coefficient $|T_0|$ and dissipation coefficient K_D across different frictional coefficient (f_1) of PS_1 plotted against l_2/h. These plots reveal a periodic and oscillatory pattern in $|R_0|$, $|T_0|$ and K_D as l_2/h changes. Additionally, it is observed that increasing the value of f_1

of PS_1 results in higher wave energy dissipation by PS_1, as demonstrated in Figures 7.3b and 7.5a. Consequently, this heightened dissipation leads to a reduction in wave reflection and transmission.

Figure 7.10 depicts the variations in the reflection coefficient $|R_0|$, transmission coefficient $|T_0|$ and dissipation coefficient K_D across the different length (a_1/h) of PS_1 plotted against l_2/h. These plots exhibit a periodic and oscillatory trend in $|R_0|$, $|T_0|$ and K_D as l_2/h varies. Moreover, it is noted that increasing a_1/h of PS_1 results in increased wave energy dissipation by PS_1, and magnitude of harmonic oscillations as evidenced in Figures 7.3a and 7.6a. Consequently, this heightened dissipation leads to a decrease in wave reflection and transmission. Particularly, when BSPS length approaches $a_1/h = 0.8$, the value of wave transmission is below 0.6, which strongly suggests an optimal protection of EP against the incident wave stroke.
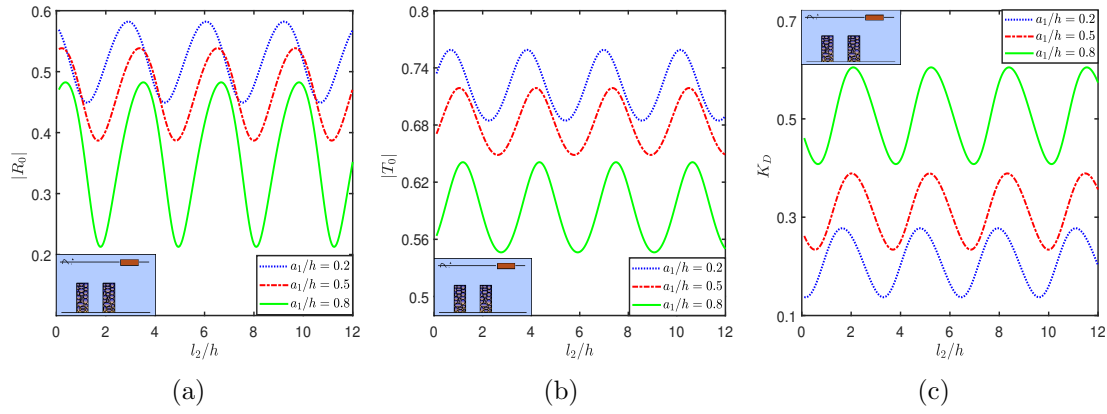
Figure 7.10: $|R_0|$, $|T_0|$ and K_D vs l_2/h for different values of a_1/h.
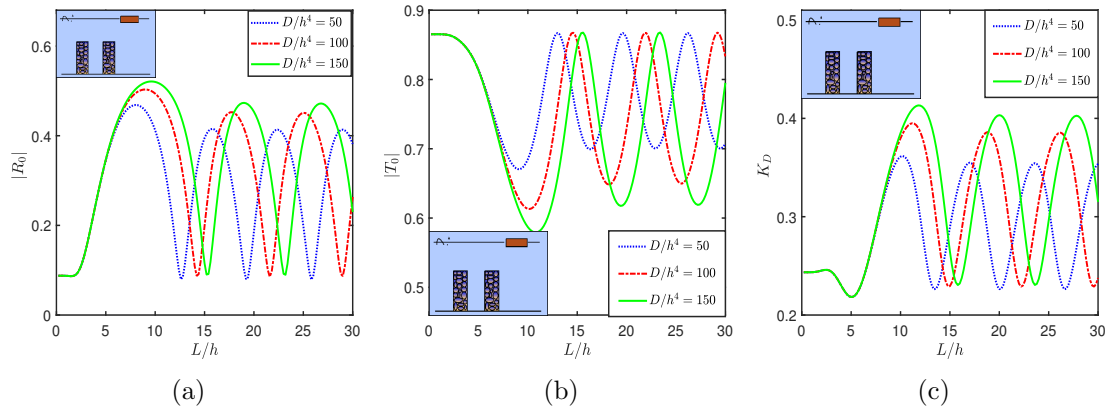
Figure 7.11: $|R_0|$, $|T_0|$ and K_D vs L/h for different values of D/h^4.

Figure 7.11 showcases the fluctuations of the reflection coefficient $|R_0|$, transmission coefficient $|T_0|$ and dissipation coefficient K_D across various flexural rigidity values (D/h^4) plotted against L/h. These graphs reveal an oscillatory pattern in $|R_0|$, $|T_0|$ and K_D as L/h changes. Additionally, it's worth noting that as D/h^4 rises, the reflection coefficient increases while the transmission coefficient decreases. This trend occurs because as the

structure becomes more rigid, more wave energy is reflected back by EP, resulting in reduced transmission of wave energy through the structure.

Figure 7.12 illustrates the dynamic changes in the reflection coefficient $|R_0|$, transmission coefficient $|T_0|$ and dissipation coefficient K_D across different frictional coefficient values (f_2) plotted against L/h. These plots unveil an oscillatory behavior in $|R_0|$, $|T_0|$ and K_D as L/h undergoes variation, same with the observations in Figure 7.11. Moreover, an escalation in f_2 leads to heightened dissipation of incident wave energy, consequently resulting in decreased values of $|R_0|$ and $|T_0|$. The predicted values of $|T_0|$ at each of the harmonic troughs are evident while designing the BSPS to secure the EP and shore-side regions against the incident wave stroke.
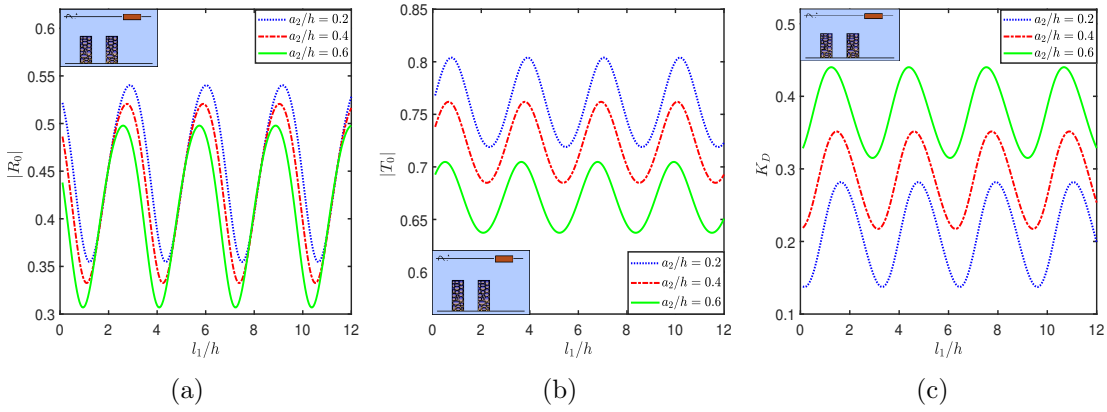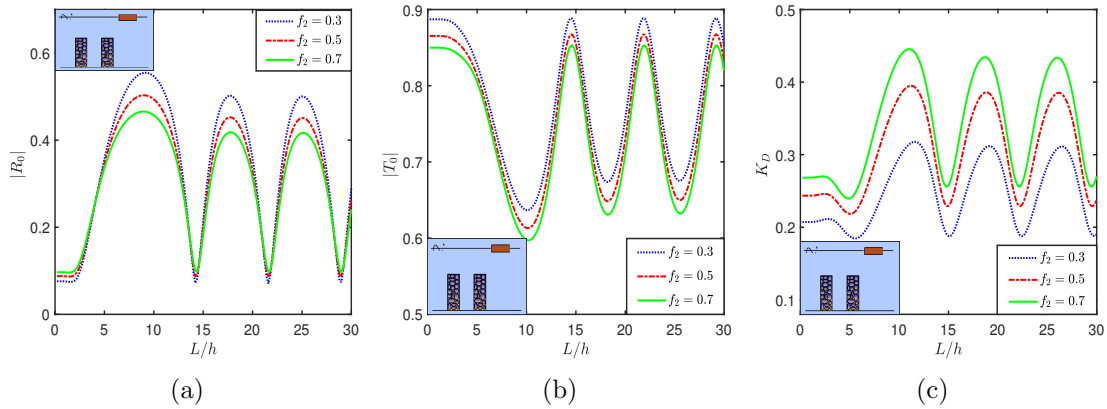

Figure 7.12: $|R_0|$, $|T_0|$ and K_D vs L/h for different values of f_2.
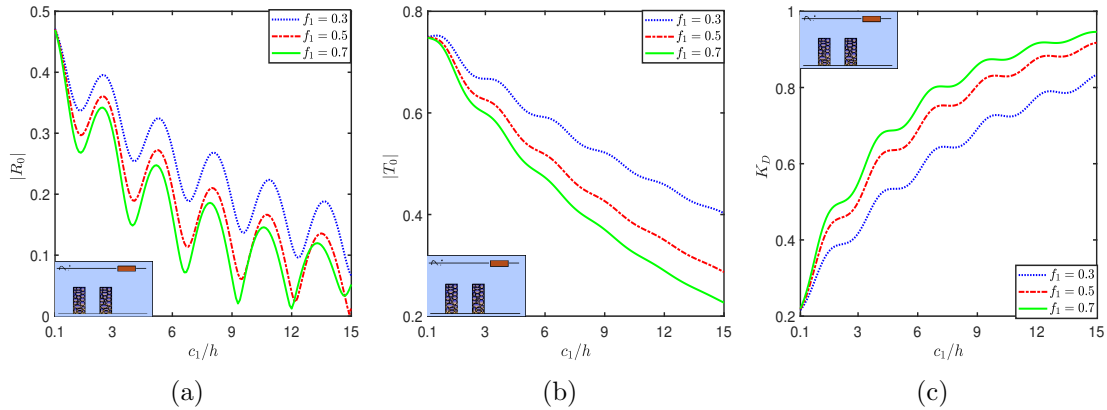
Figure 7.13: $|R_0|$, $|T_0|$ and K_D vs c_1/h for different values of f_1.

Figure 7.13 illustrates the relationship between $|R_0|$, $|T_0|$ and K_D in relation to the BSPS width c_1/h across various frictional coefficient values f_1 of PS_1. The depicted trend reveals that $|R_0|$ follows an oscillating pattern and this oscillating pattern decreases as the width of PS_1 expands. This phenomenon of resonating patterns may be due to the multiple wave interactions between BSPS and EP. Additionally, it is evident from the figures that both the reflection and transmission coefficients decrease as the width increases, while concurrently, there is a notable increase in energy dissipation. In this

case, the role of EP is evident, as the reflection starts nearly $|R_0| = 0.48$ when BSPS width $c_1/h = 0.1$. The transmission coefficient is observed to be $|T_0| < 0.5$ when $c_1/h = 4$ and $f_1 = 0.7$. Here, it is concluded that the BSPS with width $c_1/h = 4$ along with length $a_1/h = 0.5$ gives $|T_0| < 0.5$, which agrees with the results of Venkateswarlu et al. [126] who reported that $c_1/h = 2$ is sufficient to obtain $|T_0| < 0.5$ as the breakwater is fully extended from the bottom to the free surface ($a_1/h = 1$). In the present case, the length of the breakwater is $a_1/h = 0.5$, which is 50% in the fully extended breakwater. This concludes that the primary cost of construction is less affected as the quantity of rock required to develop BSPS is less in line with the fully extended breakwater. The additional advantage of BSPS is that this kind of breakwater experiences minimal fluid force compared to the fully extended breakwater.
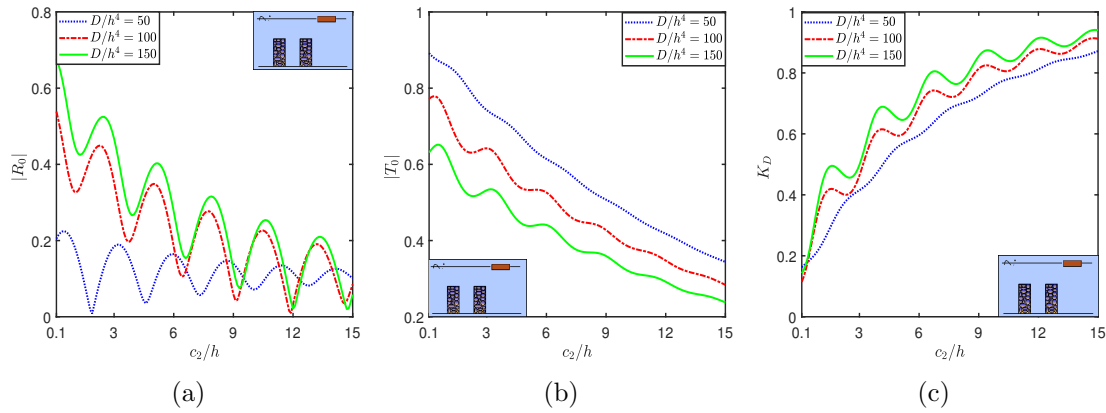
Figure 7.14: $|R_0|$, $|T_0|$ and K_D vs c_2/h for different values of D/h^4.

Figure 7.14 depicts the behavior of $|R_0|$, $|T_0|$ and K_D concerning the width c_2/h of PS_2 across various values of the flexural rigidity D/h^4. The figure demonstrates that the reflection coefficient decreases in an oscillating pattern with an increasing width c_2/h of PS_2. This resonating behavior likely arises from the intricate interactions of incident waves between BSPS and EP. Moreover, it is also observed that both the reflection and transmission coefficients decrease as the width expands, leading to increased dissipation of energy, consistent with the findings in Figure 7.13. Additionally, it is noteworthy that with higher structural rigidity, the transmission coefficient decreases while the reflection coefficient increases for smaller c_2/h and minor increases for larger c_2/h.

7.4.3 Effect of Three BSPS on Plate Deflection ($Re(\eta_E)$), Shear Force (S_F), Strain (S_T), Reflection Coefficient ($|R_0|$), Transmission Coefficient ($|T_0|$) and Dissipation Coefficient (K_D)

Figure 7.15a illustrates the impact of varying lengths (a_3/h) of PS_3 on plate deflection (η_E), revealing a significant decrease in deflection with increasing values of a_3/h. Meanwhile, Figure 7.15b explores the correlation between the porosity (ϵ_3) of PS_3 and η_E, observing a decrease in deflection as ϵ_3 increases. This trend is attributed to the increased dissipation of incident wave energy as both a_3/h and ϵ_3 of PS_3 rise, reducing

energy transmission towards EP. Consequently, this mechanism effectively mitigates the structural response of EP by diminishing plate deflection.

Figure 7.16 presents an analysis of shear force (S_F) showcasing the impact of the length a_3/h and the frictional coefficient f_3 of PS_3 on the behavior of EP. Notably, the S_F remains zero at the ends of EP, consistent with the assumption of free edge behavior. Moreover, S_F exhibits a distinct oscillatory pattern. Remarkably, an increase in both f_3 and a_3/h corresponds to a noticeable reduction in the amplitude of the S_F of EP. This trend suggests that higher values of these parameters contribute to decrease S_F. This behavior is attributed to the enhanced wave energy dissipation by PS_3, as evidenced and analyzed in Figure 7.15.
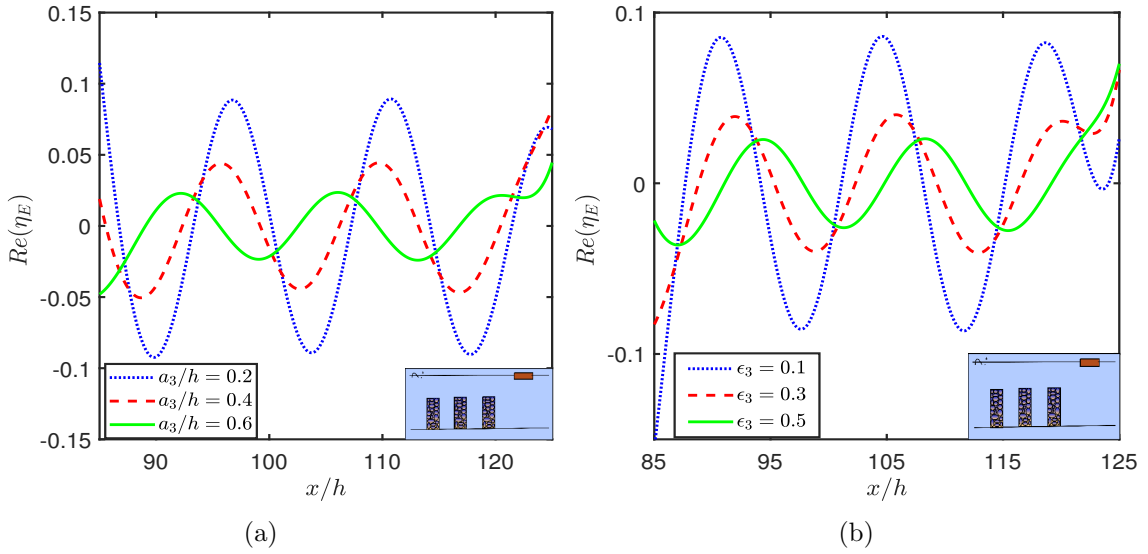
Figure 7.15: $Re(\eta_E)$ for different values of a_3/h and ϵ_3 with $c_m/h = 10$, $l_1/h = 15$, $l_2/h = 15$, $l_3/h = 20$, $D/h^4 = 75$ and $L/h = 40$.

Figure 7.17 depicts the strain (S_T) across different values of the porosity (ϵ_3) and frictional coefficient (f_3) of PS_3. Notably, at the ends of EP, S_T is zero, reflecting the assumption of free edge behavior. Additionally, the variation of S_T follows an oscillatory pattern. Furthermore, an increase in both ϵ_3 and f_3 correlates with a decrease in the amplitude of the strain of EP. This phenomenon is attributed to the enhanced wave energy dissipation by PS_3, as analyzed in Figures 7.15 and 7.16.

Figure 7.18 illustrates the changes in the reflection coefficient $|R_0|$, transmission coefficient $|T_0|$ and dissipation coefficient K_D across varying frictional coefficient (f_3) of PS_3 plotted against l_3/h. These graphs display a periodic and oscillatory pattern in $|R_0|$, $|T_0|$, and K_D as l_3/h changes, which is due to the presence of free-gap regions. Additionally, it's observed that increasing the frictional coefficient f_3 of PS_3 leads to greater wave energy dissipation by PS_3. Consequently, this heightened dissipation results in a reduction in both wave reflection and transmission. BSPS experience minimal wave force when the $|R_0|$, and $|T_0|$ are minimum, and this condition is obtained at each of the harmonic trough, which would enhance the working period of BSPS.
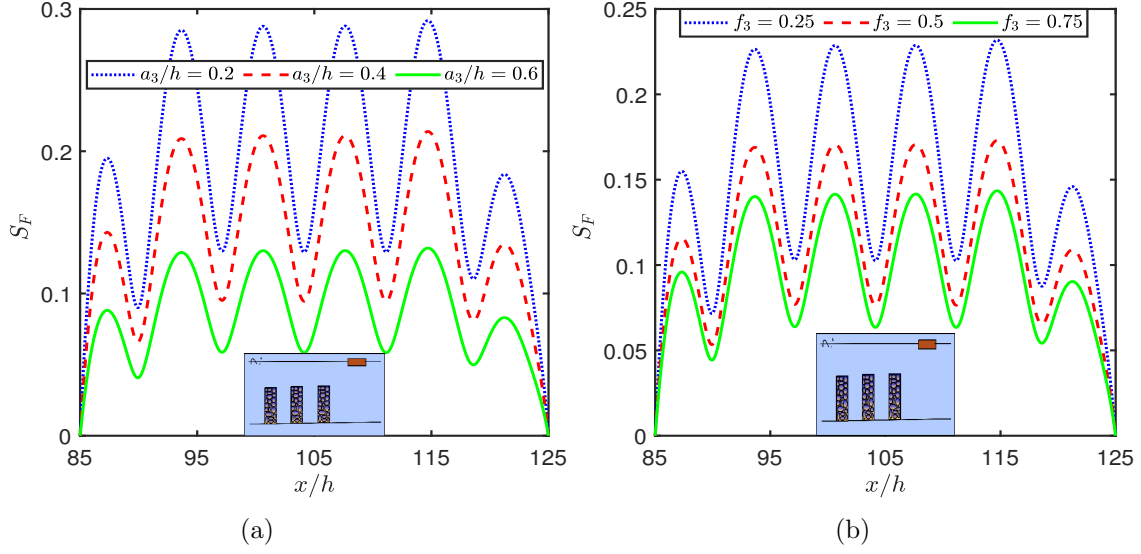
Figure 7.16: S_F for different values of a_3/h and f_3 with $c_m/h = 10$, $l_1/h = 15$, $l_2/h = 15$, $l_3/h = 20$, $D/h^4 = 75$ and $L/h = 40$.
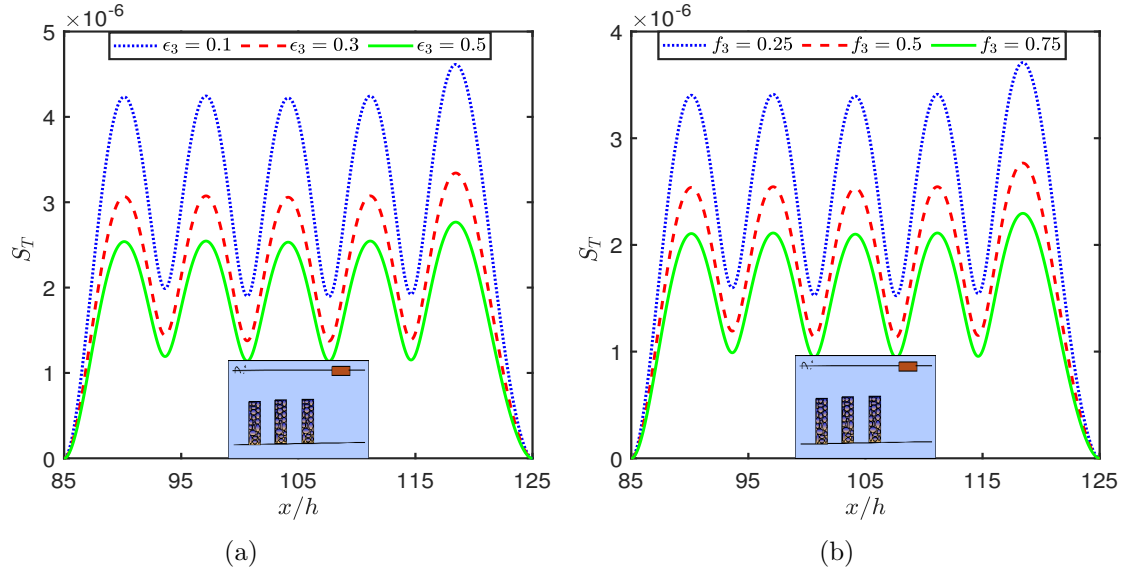
Figure 7.17: S_T for different values of ϵ_3 and f_3 with $c_m/h = 10$, $l_1/h = 15$, $l_2/h = 15$, $l_3/h = 20$, $D/h^4 = 75$ and $L/h = 40$.

Figure 7.19 depicts the correlation between $|R_0|$, $|T_0|$ and K_D concerning the width c_3/h across various length values a_3/h of PS_3. The illustrated pattern shows that $|R_0|$ exhibits oscillations and this oscillatory behavior diminishes as c_3/h of PS_3 expands. This resonance phenomenon is likely attributable to the complex interactions between BSPS and EP waves. Furthermore, the figures suggest that both $|R_0|$ and $|T_0|$ decrease as c_3/h increases, accompanied by a notable rise in energy dissipation. Moreover, an increase in the length a_3/h of PS_3 leads to a higher dissipation coefficient, resulting in decreased $|R_0|$ and $|T_0|$.
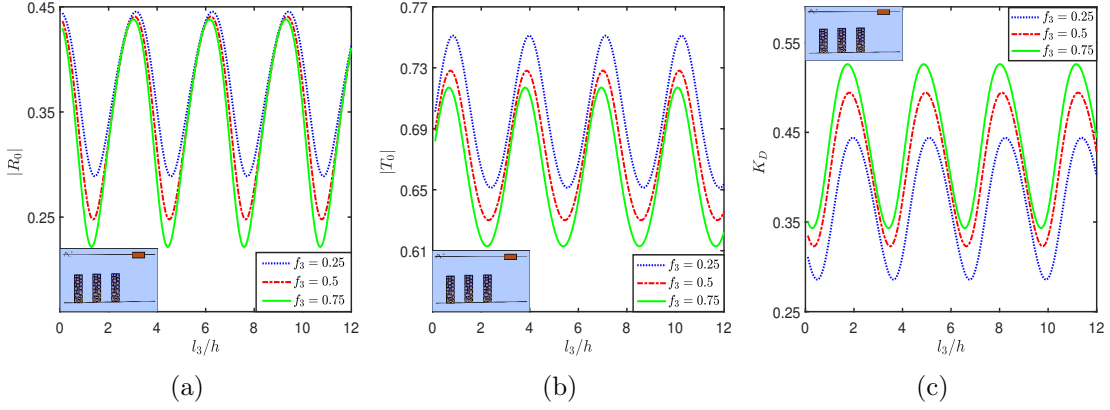
Figure 7.18: $|R_0|$, $|T_0|$ and K_D vs l_3/h for different values of f_3.
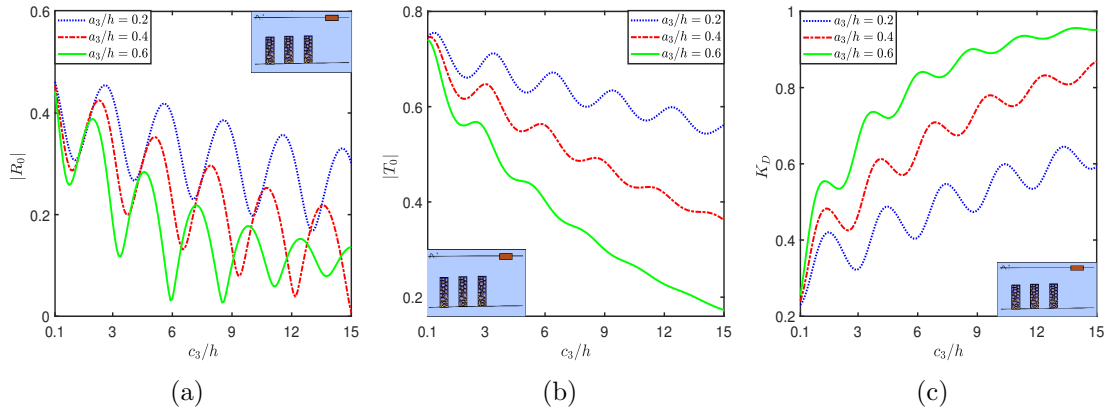
Figure 7.19: $|R_0|$, $|T_0|$ and K_D vs c_3/h for different values of a_3/h.

7.4.4   Comparative Study Between Multiple BSPS with EP

A comparative study is conducted to evaluate the mitigation of the structural response of EP in the presence of different number of BSPS.

Figure 7.20 illustrates the relationship between the reflection coefficient ($|R_0|$) and the wavenumber (kh) for various numbers of BSPS, where (a) considers cases where n is an odd number and (b) considers cases where n is even. It is found that for $n = 1$, the harmonic peak magnitude decreases with an increase in kh, but for the $n = 2, 3, 4, 5, 6$, within the range of $0.1 < kh < 1$ there are three peaks, which may be treated as a major peak followed by multiple minor peaks. The major peak magnitude is more than all the other minor peaks, and the second peak magnitude is less than the third peak, but within the range of $1 < kh < 3$, the magnitude of the harmonic peak decreases with an increase in kh. It is also noted that $n = 1$ and $n = 2$ have no sub-harmonic peak between the two harmonic peaks. But for other values of n, there are $n-2$ numbers of sub-harmonic peaks between two harmonic peaks. However, the bandwidth of each harmonic peak (major and minor) is observed to be the same, which may be due to the presence of multiple gap regions. Now from Figure 7.20a, by comparing the curves for $n = 3$ and $n = 5$, it is noted that the harmonic peaks for $n = 5$ show a right shift for the first, third, fifth, seventh and

ninth number of harmonic peaks and a left shift for the second, fourth, sixth and eighth number of harmonic peaks. Similar observations are also identified in Figure 7.20b for $n = 4$ and $n = 6$. As a comparison, when EP is placed far away from a single BSPS, $|R_0|$ is highly oscillatory and bandwidth is almost identical. The multiple zero minima are observed after each of the harmonic peaks against the relative wavenumber. But, in the presence of two BSPS, the oscillations are non-identical and the sub-peaks are identified in $|R_0|$ pattern. Almost 100% increment of $|R_0|$ is observed in the presence of two BSPS when compared with the presence of one BSPS with EP, which may be due to the change in wave damping. Thus the present study suggests an even number of BSPS for enhanced reflection and an odd number of BSPS for well-balanced scattering coefficients. Further, from the $|R_0|$ pattern, it is identified that with an increase in n, $|R_0|$ increases. This may be because as the number of BSPS increases, more incident wave energy is reflected back by the BSPS.
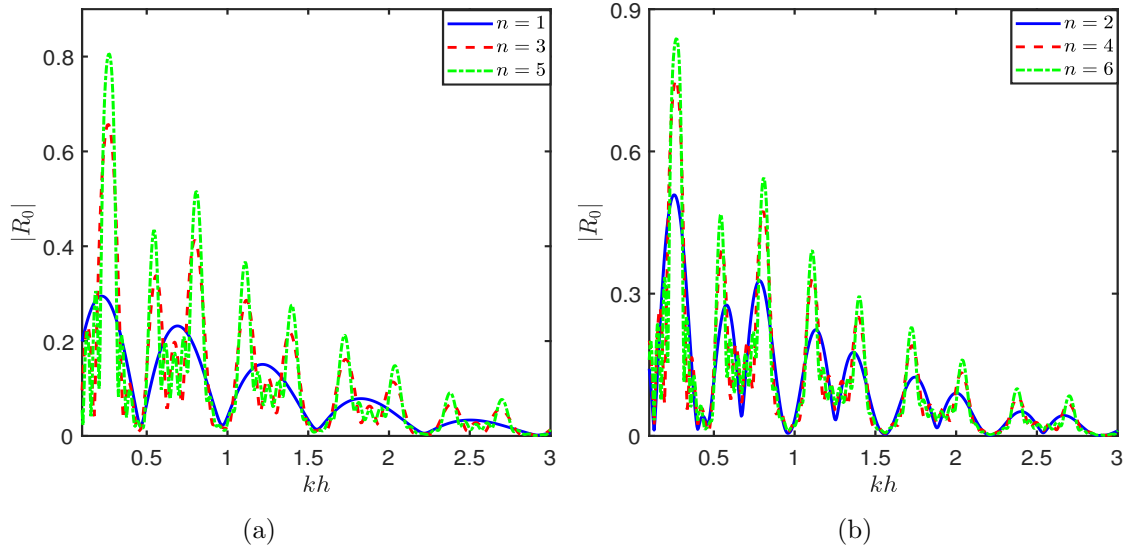
Figure 7.20: $|R_0|$ vs kh for number of BSPS (a) $n = 1, 3$ and 4 and (b) $n = 2, 4$ and 6 (with $a_m/h = 0.5$, $c_m/h = 5$, $f_m = 1$, $\epsilon_m = 0.1$ $l_4/h = 5$ and $L/h = 20$).

Figures 7.21a and 7.21b present the dynamics of the energy dissipation coefficient K_D and plate deflection $Re(\eta_E)$, respectively, for five distinct scenarios: (i) EP alone, (ii) one BSPS with EP, (iii) two BSPS with EP, (iv) three BSPS with EP, and (v) four BSPS with EP. An analysis of Figure 7.21a indicates that K_D is lower in the sole presence of EP (without BSPS) compared to other configurations with BSPS and EP. Moreover, K_D is nearly 21%, 37%, 53%, and 65% in configurations with one, two, three, and four BSPS with EP, respectively. This difference highlights the significant impact of BSPS introduction on altering K_D, as K_D is zero in the absence of BSPS. This disparity underscores the substantial impact of BSPS installations on enhancing wave energy dissipation. Notably, the number of BSPS installations significantly influences K_D, with the setup involving four BSPS achieving the highest wave damping (nearly 65%). Consequently, a smaller portion of the wave energy is transmitted towards EP, resulting in minimal plate deflection,

as depicted in Figure 7.21b. The effectiveness of BSPS in wave damping is clearly demonstrated when contrasted with EP alone. Furthermore, the superior wave damping capability is evident with four BSPS and EP compared to scenarios involving fewer BSPS installations, with differences of nearly 36%, 18%, and 8% observed for configurations with one, two, and three BSPS with EP, respectively. Overall, the number BSPS is purely dependent upon the level of protection of EP against incident wave stroke.

(a)   (b)
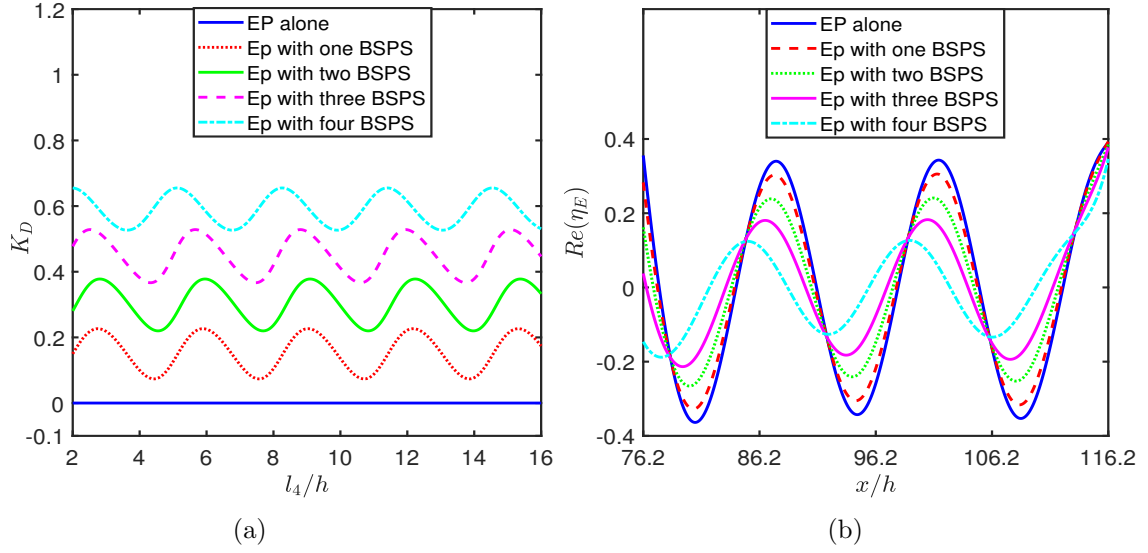
Figure 7.21: (a) K_D and (b) $Re(\eta_E)$ for the cases where only EP (absence of BSPS), EP with one BSPS, EP with two BSPS, EP with three BSPS and EP with four BSPS (with $c_m/h = 10$, $l_1/h = 15$, $l_2/h = 20$, $l_3/h = 15$, $l_4/h = 20$, $D/h^4 = 75$ and $L/h = 40$).

(a)   (b)
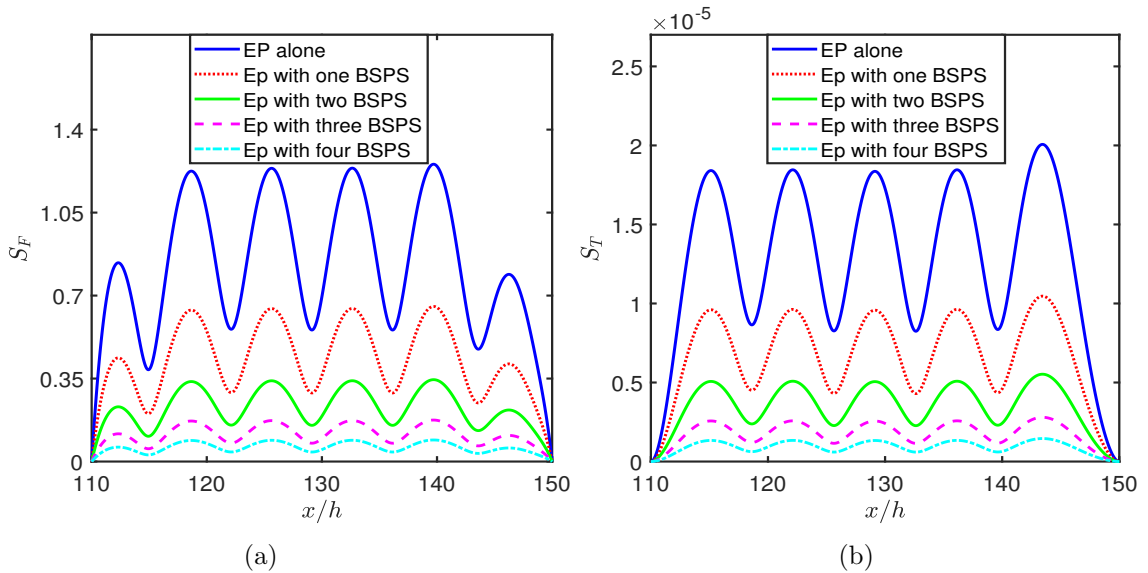
Figure 7.22: (a) S_F and (b) S_T for the cases where only EP (absence of BSPS), EP with one BSPS, EP with two BSPS, EP with three BSPS and EP with four BSPS (with $c_m/h = 10$, $l_1/h = 15$, $l_2/h = 20$, $l_3/h = 15$, $l_4/h = 20$, $D/h^4 = 75$ and $L/h = 40$).

Figures 7.22a and 7.22b present shear force S_F and strain S_T, respectively, for five

distinct scenarios: (i) EP alone, (ii) EP with one BSPS, (iii) EP with two BSPS, (iv) EP with three BSPS, and (v) EP with four BSPS. Analysis of these figures reveals that S_F and S_T are more in the absence of BSPS (EP alone) compared to the presence of BSPS and EP. Furthermore, S_F is approximately 49%, 74%, 88%, and 94% lower in configurations with one, two, three, and four BSPS with EP, respectively, compared to EP alone. However, S_T is approximately 48%, 72%, 86%, and 92% lower in configurations with one, two, three, and four BSPS with EP, respectively, compared to EP alone. This observation can be attributed to the fact that in the absence of BSPS, the energy dissipation coefficient K_D is zero, and significant changes in K_D occur after introducing the BSPS, as observed in Figure 7.21a. The effectiveness of BSPS in damping waves is evident when compared to EP alone. However, S_F and S_T achieved the lowest with four BSPS and EP compared to one BSPS with EP, two BSPS with EP, and three BSPS with EP. Thus, the number of BSPS installations plays a crucial role in mitigating the structural response on EP by dissipating a large amount of incident waves by BSPS. From Figures 7.21 and 7.22, it is recommended that three BSPS with EP will be suitable to secure the shoreside regions against the incident wave stroke.

(a) (b) (c)
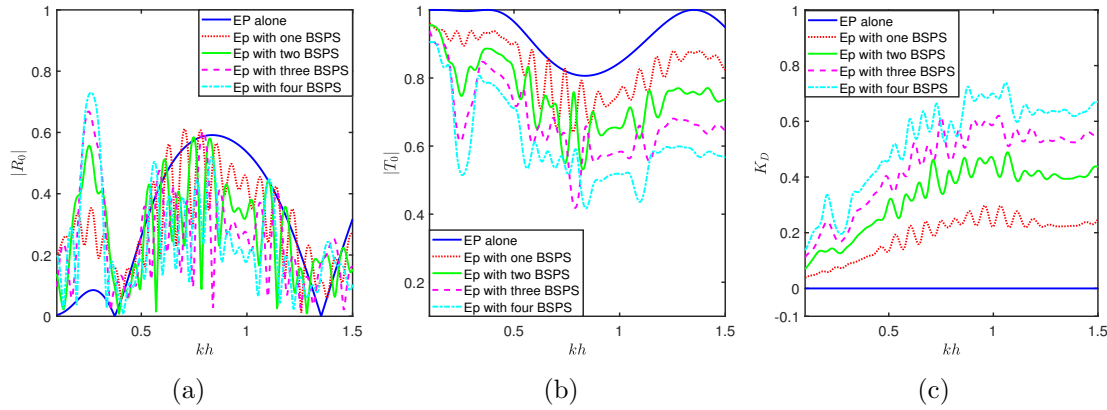
Figure 7.23: $|R_0|$, $|T_0|$ and K_D vs kh for different values of n (with $a_m/h = 0.5$, $c_m/h = 5$, $f_m = 1$, $\epsilon_m = 0.1$ $l_4/h = 5$ and $L/h = 20$).

Figures 7.23a, 7.23b and 7.23c shows the variation of wave reflection $|R_0|$, transmission $|T_0|$ and energy dissipation K_D against the relative wavelength kh for EP in the presence of multiple BSPS. The scattering coefficients are compared with the EP alone to verify the significance of BSPS in dissipating the incident waves. The minor peak in $|R_0|$, followed by a major peak with a larger bandwidth, is observed when EP is installed alone. After introducing the BSPS the pattern of $|R_0|$ is highly oscillatory due to the presence of free-gap regions. The primary peak is observed near $kh = 0.25$, and the magnitude of the peak is observed to be increasing after increasing the number of BSPS. The intense peak of wave reflection is generally treated as Bragg reflection, and the bandwidth is complimentary. In the present scenario, the Bragg reflection is observed with a minor change in the bandwidth when compared with the given range as discussed in Liu et al. [41]. Thereafter, the $|R_0|$ obtains a peak in oscillatory behavior and reduces to low values due to

the change in the wave damping. The $|T_0|$ is higher for EP alone, as the wave damping is zero, and the $|T_0|$ approaches to desirable value after introducing the multiple BSPS. It is repeatedly mentioned that the $|T_0|$ should be less than 0.5 for optimal protection of the side region, and this case may be satisfied after installing either three or four BSPS with EP. The zero K_D is observed when the EP is installed without BSPS, and the K_D approaches 20% after introducing the single BSPS, and the maximum wave dissipation $K_D = 0.7$ is obtained for four BSPS with EP. The level of protection against the incident waves is always site-specific. Thus the number of BSPS may be fixed based on the requirement in the reduction of wave height and the corresponding cost of construction.

7.5   Conclusion

This paper investigates the interaction between water waves and an EP structure amidst multiple BSPS configurations, aiming to reduce the structural response of EP. Utilizing eigenfunction expansion, velocity potential expressions are used to formulate the solution of the boundary value problem, subsequently solved numerically as an algebraic system. From this study it is found that the configuration featuring four BSPS achieves the highest wave damping, reaching almost 65%. Additionally, the superiority in wave damping capability is evident when comparing setups with four BSPS and EP to those with fewer BSPS installations. Notably, approximately 21%, 37%, and 53% wave damping are observed for configurations with one, two, and three BSPS with EP, respectively. The lowest values of shear force and strain are attained when utilizing four BSPS and EP, in contrast to configurations involving one, two, or three BSPS with EP. It is found that the Bragg reflection is identified when $kh = 0.25$, and the magnitude of R_0 enhances along with the corresponding bandwidth after increasing the number of BSPS. Afterward, the reflection coefficient experiences a peak in its oscillatory behavior and reduces to low values, attributed to changes in wave damping. Remarkably, in cases where n equals 1 or 2, no subharmonic peaks are found between the two harmonic peaks in wave reflection. Conversely, for other values of $n = 3, 4, 5$ and 6, the count of subharmonic peaks between two harmonic peaks amounts to $n - 2$. The zero minima of wave reflection is obtained due to the formation of standing waves. Overall, from the cost effective point of view, this study recommends three BSPS (wave damping capacity is almost 55%) of length $a_m/h = 0.5$, porosity $\epsilon_m = 0.5$, $f_m = 0.5$ and width $c_m/h = 10$ will be suitable to secure the EP and shore-side regions against the incident wave attack.

Chapter 8

Summary and Future Work

In this chapter, the first section provides an overall summary of the research conducted in this thesis. The subsequent section highlights the scope of future work.

8.1   Summary of the Present Work

The research conducted is presented across different chapters in this thesis, with the main conclusions drawn at the end of each chapter. The problems addressed in this thesis are solved using the eigenfunction expansion method and leveraging the orthogonality of eigenfunctions. However, a brief summary of the research work carried out in this thesis is as follows:

In Chapter 2, the study on gravity wave interaction with a vertical porous structure extending from the bottom to the free surface in the presence of an elastic plate demonstrates that the porous structure is highly effective in reducing the free-surface elevation on the lee side of the elastic plate. Notably, the plate deflection, shear force, and strain on the elastic plate decrease significantly with an increase in the frictional coefficient. Further, it is found that with an increase in the width of the porous structure, the wave reflection and transmission decrease as the porous structure dissipates a major part of the incident wave. In addition, a moderate porosity value of the porous structure is preferable for this problem.

In Chapter 3, the problem for mitigation of wave load on a sea wall by a vertical porous structure extending from the bottom to the free surface in the presence of an elastic plate is carried out. The study depicts that the gap between the structures plays a vital role in protecting the sea wall from wave load. It is also found that in the presence of a higher value of length and flexural rigidity of the elastic plate, the force acting on the wall is low. From the qualitative behavior of forces acting on the sea wall, the force on the wall shifted to the left due to the effect of the width and frictional factor of the porous structure. Furthermore, for a higher value of the width of PS (i.e., for $b/h=1.5$), energy dissipation by PS becomes nearly 100%, and the wave reflection becomes nearly zero when the gap between PS and EP $L_1/h = (1.4 + n \times 4.6), n = 0, 1, 2, \ldots$. It is also noticed that the free surface elevation between the elastic plate and sea wall, which aids in the creation of a calm zone, is significantly influenced by the structural characteristics of the porous structure and elastic plate.

In Chapter 4, wave scattering by truncated thick porous structures of two different configurations, (i) a bottom-standing porous structure and (ii) a surface-piercing porous

structure in the presence of an elastic plate is examined. The study reveals that since the porous structure dissipates a significant portion of wave energy, consequently, increasing the length, porosity, and frictional factor of the porous structure decreases the wave reflection and transmission. With an increase in the width of the porous structure, the reflection coefficient decreases in an oscillating pattern, and the reflection coefficient becomes constant for the higher value of structural width. The structural length, porosity and friction factor of the porous structure play an important role in reducing the plate deflection and the free surface elevation on the lee side of the elastic plate. It is found that the wave dissipation by the surface-piercing porous structure is more as compared to the bottom-standing porous structure case.

In Chapter 5, the problem involving mitigation of wave load on a sea wall by a truncated thick porous structure of two different configurations, (i) a bottom-standing porous structure and (ii) a surface-piercing porous structure in the presence of an elastic plate is investigated. The study depicts that when the distance between the porous structure and elastic plate is an odd multiple of the depth of water, the wave force experienced by the wall is minimum and this minimum value of the wave force corresponds to the minimum value of the reflection coefficient. Also, periodic harmonic oscillations are observed in the reflection coefficient, dissipation coefficient, and wave force experienced by the wall with respect to the variation of the gap length between the porous structure and elastic plate and also the gap length between the elastic plate and sea wall. There is a 60% reduction in force experienced by the wall and 50% enhancement in damping coefficient after installation of SPPS for wavenumber $k_0 h = 0.85$, porosity $\epsilon_p = 0.5$, frictional factor $f_p = 0.5$ when compared with the BSPS.

In Chapter 6, the interaction of oblique water waves with thick submerged porous structure near a sea wall over two steps bottom profile is examined. The study reveals that within the ranges of submergence depth between 0.1 to 0.3 and length 0.1 to 0.6 of the porous structure, the wave reflection and force experienced on the wall consistently register at less than 54% and 59%, respectively. Moreover, periodic harmonic oscillations are noted in the reflection coefficient, dissipation coefficient, and wave force experienced by the wall with respect to the variation of the gap length between the water region between SPS and the steps, as well as the width of step-1 and step-2. Further, it is found that force on the wall exhibits harmonic peaks at angles $\theta = 38°$ and $\theta = 61°$. Also, it is found that $\theta = 67°$ is the critical angle for the reflection coefficient and the dissipation coefficient.

In Chapter 7, the interaction between water waves and an elastic plate in the presence of multiple bottom-standing porous structures is investigated. The study reveals that the configuration featuring four bottom-standing porous structures achieves the highest wave damping, reaching almost 65%. Approximately 21%, 37%, and 53% wave damping are observed for configurations with one, two, and three BSPS with EP, respectively. It is found that the Bragg reflection is identified at wavenumber $kh = 0.25$, and the magnitude of the reflection coefficient enhances along with the corresponding bandwidth after increasing the number of bottom-standing porous structures. Remarkably, in cases

where n equals 1 or 2, no subharmonic peaks are found between the two harmonic peaks in wave reflection. Conversely, for other values of $n = 3, 4, 5$ and 6, the count of subharmonic peaks between two harmonic peaks amounts to $n - 2$.

The study presented in this thesis is expected to enhance the knowledge of the ocean engineering community for mitigating wave response on elastic plate/sea walls.

8.2 Scope of Future Work

This section highlights the future scope of the research conducted in this thesis. As an extension of our results, the following problems can be taken up.

- The time-domain analysis can be studied by using the Fourier transform technique to capture the hydrodynamic behavior of the problems assumed in the thesis.

- The problems involving water wave interaction with thick porous structures of arbitrary shapes over an arbitrary bottom topography can be considered. This problem may be solved by applying the Boundary element method coupled with the eigenfunction expansion method.

- The problems involving water wave interaction with submerged porous structure in the presence of arbitrary bottom topography can be examined for its approximate solution, where the arbitrary bottom topography can be approximated by steps so that the eigenfunction expansion method can be used in each step regions.

- The problems involving water wave interaction with thick porous structures of different configurations in the presence of elastic plate can be studied in a three-dimensional context.

References

[1] A. D. Craik. The origins of water wave theory. *Annu. Rev. Fluid Mech.*, 36:1—-28,, 2004.

[2] H. Lamb. *Hydrodynamics.* University Press, 1924.

[3] M. Rahman. *Water waves: relating modern theory to advanced engineering applications.* Oxford University Press, 1995.

[4] R. G. Dean and R. A. Dalrymple. *Water wave mechanics for engineers and scientists*, volume 2. world scientific publishing company, 1991.

[5] C. K. Sollitt and R. H. Cross. Wave transmission through permeable breakwaters. In *Proceedings of 13th International Conference on Coastal Engineering, New York*, pages 1827–1846, 1972.

[6] P. McIver. The dispersion relation and eigenfunction expansions for water waves in a porous structure. *Journal of engineering mathematics*, 34:319–334, 1998.

[7] S. Zhu. Water waves within a porous medium on an undulating bed. *Coastal Engineering*, 42(1):87–101, 2001.

[8] H. Behera and T. Sahoo. Gravity wave interaction with porous structures in two-layer fluid. *Journal of engineering mathematics*, 87:73–97, 2014.

[9] V. Venkateswarlu and D. Karmakar. Wave transformation due to barrier-rock porous structure placed on step-bottom. *Ships and Offshore Structures*, 15(8):895–909, 2020.

[10] O. S. Madsen. Wave transmission through porous structures. *Journal of the Waterways, Harbors and Coastal Engineering Division*, 100(3):169–188, 1974.

[11] R. A. Dalrymple, M. A. Losada, and P. A. Martin. Reflection and transmission from porous structures under oblique wave attack. *Journal of fluid mechanics*, 224: 625–644, 1991.

[12] W. Sulisz. Wave reflection and transmission at permeable breakwaters of arbitrary cross-section. *Coastal Engineering*, 9(4):371–386, 1985.

[13] J. F. Lee. A boundary element model for waves interaction with porous structures. *WIT Transactions on Modelling and Simulation*, 11, 1970.

[14] Y. Liu and H. J. Li. Wave reflection and transmission by porous breakwaters: A new analytical solution. *Coastal engineering*, 78:46–52, 2013.

[15] S. Das and S. N. Bora. Reflection of oblique ocean water waves by a vertical porous structure placed on a multi-step impermeable bottom. *Applied Ocean Research*, 47: 373–385, 2014.

[16] S. Das and S. N. Bora. Wave damping by a vertical porous structure placed near and away from a rigid vertical wall. *Geophysical & Astrophysical Fluid Dynamics*, 108(2):147–167, 2014.

[17] J. Dattatri, H. Raman, and N. J. Shankar. Performance characteristics of submerged breakwaters. In *Coastal Engineering*, pages 2153–2171. 1978.

[18] I. J. Losada, R. Silva, and M. A. Losada. 3-d non-breaking regular wave interaction with submerged breakwaters. *Coastal Engineering*, 28(1-4):229–248, 1996.

[19] S. Koley, H. Behera, and T. Sahoo. Oblique wave trapping by porous structures near a wall. *Journal of Engineering Mechanics*, 141(3):04014122, 2015.

[20] H. Behera, S. Koley, and T. Sahoo. Wave transmission by partial porous structures in two-layer fluid. *Engineering Analysis with Boundary Elements*, 58:58–78, 2015.

[21] S. Tabssum, R. B. Kaligatla, and T. Sahoo. Surface gravity wave interaction with a partial porous breakwater in the presence of bottom undulation. *Journal of Engineering Mechanics*, 146(9):04020088, 2020.

[22] R. B. Kaligatla, S. Tabssum, and T. Sahoo. Surface gravity wave interaction with a partial porous breakwater in a two-layer ocean having bottom undulations. *Waves in Random and Complex Media*, pages 1–32, 2021.

[23] K. R. Athul Krishna, K. Abdulla, and D. Karmakar. Dissipation of gravity waves due to submerged porous plate coupled with porous structures. *Journal of Offshore Mechanics and Arctic Engineering*, 145(1):011201, 2023.

[24] I. J. Losada, M. A. Losada, and A. Baquerizo. An analytical method to evaluate the efficiency of porous screens as wave dampers. *Applied Ocean Research*, 15(4): 207–215, 1993.

[25] T. W. Hsu, L. H. Tsai, and Y. T. Huang. Bragg scattering of water waves by multiply composite artificial bars. *Coastal Engineering Journal*, 45(02):235–253, 2003.

[26] S. W. Twu and C. C. Liu. Interaction of non-breaking regular waves with a periodic array of artificial porous bars. *Coastal Engineering*, 51(3):223–236, 2004.

[27] Y. Liu, Y. C. Li, and B. Teng. Interaction between obliquely incident waves and an infinite array of multi-chamber perforated caissons. *Journal of Engineering Mathematics*, 74:1–18, 2012.

[28] H. Behera and C. O. Ng. Interaction between oblique waves and multiple bottom-standing flexible porous barriers near a rigid wall. *Meccanica*, 53:871–885, 2018.

[29] H. W Liu, Y Liu, and P Lin. Bloch band gap of shallow-water waves over infinite arrays of parabolic bars and rectified cosinoidal bars and bragg resonance over finite arrays of bars. *Ocean Engineering*, 188:106235, 2019.

[30] F. C. Guo, H. W Liu, and J. J. Pan. Phase downshift or upshift of bragg resonance for water wave reflection by an array of cycloidal bars or trenches. *Wave Motion*, 106:102794, 2021.

[31] K. G. Vijay, T. Sahoo, and R. Datta. Wave-induced responses of a floating structure near a wall in the presence of permeable plates. *Coastal Engineering Journal*, 62(1): 35–52, 2020.

[32] C. T. Tran, J. Y. Chang, and C. C. Tsai. Step approximation for water wave scattering by multiple thin barriers over undulated bottoms. *Journal of Marine Science and Engineering*, 9(6):629, 2021.

[33] C. C. Tsai, H. Behera, and T. W. Hsu. Analysis of water wave interaction with multiple submerged semi-circular porous structures. *Archive of Applied Mechanics*, 93(7):2693–2709, 2023.

[34] M. B. M. Khan and H. Behera. Oblique wave scattering by double porous structures. In *Journal of Physics: Conference Series*, volume 1000, page 012168. IOP Publishing, 2018.

[35] Y. Cao, C. Jiang, and Y. Bai. Wave attenuation properties of double trapezoidal submerged breakwaters on flat-bed. *Transactions of Tianjin University*, 18(6): 401–410, 2012.

[36] S. W. Twu and D. T. Lin. Wave reflection by a number of thin porous plates fixed in a semi-infinitely long flume. In *Proceedings of 22nd International Conference on Coastal Engineering, Delft, The Netherlands*, pages 1046–1059. 1991.

[37] T. W. Hsu, H. K. Chang, and L. H. Tsai. Bragg reflection of waves by different shapes of artificial bars. *China Ocean Engineering*, (3):343–358, 2002.

[38] L. H. Tsai, Y. S. Kuo, Y. J. Lan, T. W. Hsu, and W. J. Chen. Investigation of multiply composite artificial bars for bragg scattering of water waves. *Coastal Engineering Journal*, 53(04):521–548, 2011.

[39] Y. Zhao, Y. Liu, H. Li, and A. Chang. Oblique wave motion over multiple submerged porous bars near a vertical wall. *Journal of Ocean University of China*, 16:568–574, 2017.

[40] A. C. Rambabu and J. S. Mani. Numerical prediction of performance of submerged breakwaters. *Ocean Engineering*, 32(10):1235–1246, 2005.

[41] Y. Liu, H. J. Li, and L. Zhu. Bragg reflection of water waves by multiple submerged semi-circular breakwaters. *Applied Ocean Research*, 56:67–78, 2016.

[42] V. Venkateswarlu and D. Karmakar. Significance of seabed characteristics on wave transformation in the presence of stratified porous block. *Coastal Engineering Journal*, 62(1):1–22, 2020.

[43] V. Venkateswarlu and D. Karmakar. Numerical investigation on the wave dissipating performance due to multiple porous structures. *ISH Journal of Hydraulic Engineering*, 27(sup1):202–219, 2021.

[44] J. Verne. *The Floating Island.* Sampson Low, Marston and Co, London, 1896.

[45] E. R. Armstrong. *Sea Station.* Patent No. 1, 1924.

[46] C. M. Wang, Z. Y. Tay, K. Takagi, and T. Utsunomiya. Literature review of methods for mitigating hydroelastic response of VLFS under wave action. *Appl. Mech. Rev.*, 63:1–18, 2010.

[47] M. Ohkusu and Y. Namba. Hydroelastic analysis of a large floating structure. *Journal of Fluids and Structures*, 19(4):543–555, 2004.

[48] T. Sahoo. *Mathematical techniques for wave interaction with flexible structures.* CRC Press, 2012.

[49] A. G. Greenhill. Wave motion in hydrodynamics. *American Journal of Mathematics*, 9:62–96, 1886.

[50] C. Fox and V. A. Squire. Reflection and transmission characteristics at the edge of shore fast sea ice. *Journal of Geophysical Research: Oceans*, 95(C7):11629–11639, 1990.

[51] M. H. Meylan. Wave response of an ice floe of arbitrary geometry. *Journal of Geophysical Research: Oceans*, 107(C1):5–1, 2002.

[52] A. D. Kerr. The critical velocities of a load moving on a floating ice plate that is subjected to in-plane forces. *Cold regions science and technology*, 6(3):267–274, 1983.

[53] C. Fox and V. A. Squire. Coupling between the ocean and an ice shelf. *Annals of Glaciology*, 15:101–108, 1991.

[54] M. Meylan and V. A. Squire. The response of ice floes to ocean waves. *Journal of Geophysical Research: Oceans*, 99(C1):891–900, 1994.

[55] S. R. Manam, J. Bhattacharjee, and T. Sahoo. Expansion formulae in wave structure interaction problems. *Proceedings of the Royal Society A: Mathematical, Physical and Engineering Sciences*, 462(2065):263–287, 2006.

[56] S. Mohapatra and S. N. Bora. Propagation of oblique waves over small bottom undulation in an ice-covered two-layer fluid. *Geophysical and Astrophysical Fluid Dynamics*, 103(5):347–374, 2009.

[57] P. Maiti, P. Rakshit, and S. Banerjea. Scattering of water waves by thin vertical plate submerged below ice-cover surface. *Applied Mathematics and Mechanics*, 32 (5):635–644, 2011.

[58] M. H. Meylan, L. G. Bennetts, J. E. M. Mosig, W. E. Rogers, M. J. Doble, and M. A. Peter. Dispersion relations, power laws, and energy loss for waves in the marginal ice zone. *Journal of Geophysical Research: Oceans*, 123(5):3322–3335, 2018.

[59] Y. A. Stepanyants and I. V. Sturova. Waves on a compressed floating ice plate caused by motion of a dipole in water. *Journal of Fluid Mechanics*, 907:A7, 2021.

[60] M. Kashiwagi. Research on hydroelastic responses of vlfs" recent progress and future work. In *ISOPE International Ocean and Polar Engineering Conference*, pages ISOPE–I. ISOPE, 1999.

[61] Y. Namba and M. Ohkusu. Hydroelastic behavior of floating artificial islands in waves. *International Journal of Offshore and Polar Engineering*, 9(01), 1999.

[62] E. Watanabe, T. Utsunomiya, and C. M. Wang. Hydroelastic analysis of pontoon-type vlfs: a literature survey. *Engineering structures*, 26(2):245–256, 2004.

[63] R. E. Taylor. Hydroelastic analysis of plates and some approximations. *Journal of engineering mathematics*, 58:267–278, 2007.

[64] D. V. Evans and R. Porter. Flexural waves on a pinned semi-infinite thin elastic plate. *Wave Motion*, 45(6):745–757, 2008.

[65] F. Xu and D. Q. Lu. Hydroelastic interaction between water waves and a thin elastic plate of arbitrary geometry. *Science China Physics, Mechanics and Astronomy*, 54: 59–66, 2011.

[66] S. Naskar, S. Kundu, and R. Gayen. An integral equation method for wave scattering by a pair of horizontal porous plates. *Topics in Integral and Integro-Differential Equations: Theory and Applications*, pages 229–255, 2021.

[67] H. Kagemoto, M. Fujino, and M. Murai. Theoretical and experimental predictions of the hydroelastic response of a very large floating structure in waves. *Applied Ocean Research*, 20(3):135–144, 1998.

[68] T. Sahoo, T. L. Yip, and A. T. Chwang. Scattering of surface waves by a semi-infinite floating elastic plate. *Physics of Fluids*, 13(11):3215–3222, 2001.

[69] K. Takagi. Hydroelastic response of a very large floating structure in waves—a simple representation by the parabolic approximation. *Applied ocean research*, 24 (3):175–183, 2002.

[70] A. J. Hermans. Interaction of free-surface waves with a floating dock. *Journal of engineering mathematics*, 45:39–53, 2003.

[71] T. P. Gerostathis, K. A. Belibassakis, and G. A. Athanassoulis. 3d hydroelastic analysis of very large floating bodies over variable bathymetry regions. *Journal of Ocean Engineering and Marine Energy*, 2:159–175, 2016.

[72] S. Koley. Water wave scattering by floating flexible porous plate over variable bathymetry regions. *Ocean Engineering*, 214:107686, 2020.

[73] T. Tsubogo. The motion of an elastic disk floating on shallow water in waves. In *ISOPE International Ocean and Polar Engineering Conference*, pages ISOPE–I. ISOPE, 2001.

[74] A. Korobkin, E. I. Pǎrǎu, and J. M. Vanden-Broeck. The mathematical challenges and modelling of hydroelasticity, 2011.

[75] A. I. Andrianov and A. J. Hermans. The influence of water depth on the hydroelastic response of a very large floating platform. *Marine Structures*, 16(5):355–371, 2003.

[76] K. Takagi, K. Shimada, and T. Ikebuchi. An anti-motion device for a very large floating structure. *Marine structures*, 13(4-5):421–436, 2000.

[77] H. Ohta, T. Torii, N. Hayashi, E. Watanabe, T. Utsunomiya, K. Sekita, and S. Sunahara. Effect of attachment of a horizontal/vertical plate on the wave response of a vlfs. In *Proceedings of the Third International Workshop on Very Large Floating Structures*, pages 265–274, 1999.

[78] E. Watanabe, T. Utsunomiya, M. Kuramoto, H. Ohta, T. Torii, and N. Hayashi. Wave response analysis of vlfs with an attached submerged plate. *International Journal of Offshore and Polar Engineering*, 13(03), 2003.

[79] Y. Cheng, G. j. Zhai, and J. Ou. Time-domain numerical and experimental analysis of hydroelastic response of a very large floating structure edged with a pair of submerged horizontal plates. *Marine Structures*, 39:198–224, 2014.

[80] Y. Cheng, C. Ji, G. Zhai, and G. Oleg. Dual inclined perforated anti-motion plates for mitigating hydroelastic response of a vlfs under wave action. *Ocean Engineering*, 121:572–591, 2016.

[81] S. Ohmatsu. Numerical calculation method for the hydroelastic response of a pontoon-type very large floating structure close to a breakwater. *Journal of marine science and technology*, 5:147–160, 2000.

[82] J. S. Yang. Hybrid active and passive control of a very large floating beam structure. *Nonlinear Dynamics*, 87:1835–1845, 2017.

[83] S. Singla, S. C. Martha, and T. Sahoo. Mitigation of structural responses of a very large floating structure in the presence of vertical porous barrier. *Ocean Engineering*, 165:505–527, 2018.

[84] J. Pu and D. Q. Lu. Mitigation of hydroelastic responses in a very large floating structure by a connected vertical porous flexible barrier. *Water*, 14(3):294, 2022.

[85] S. Singla, T. Sahoo, S. C. Martha, and H. Behera. Effect of a floating permeable plate on the hydroelastic response of a very large floating structure. *Journal of Engineering Mathematics*, 116:49–72, 2019.

[86] S. Singla, H. Behera, S. C. Martha, and T. Sahoo. Scattering of water waves by very large floating structure in the presence of a porous box. *Journal of Offshore Mechanics and Arctic Engineering*, 144(4):041904, 2022.

[87] H. H. Hsu and Y. C. Wu. The hydrodynamic coefficients for an oscillating rectangular structure on a free surface with sidewall. *Ocean Engineering*, 24(2):177–199, 1997.

[88] Y. H. Zheng, Y. M. Shen, Y. G. You, B. J. Wu, and D. S. Jie. On the radiation and diffraction of water waves by a rectangular structure with a sidewall. *Ocean Engineering*, 31(17-18):2087–2104, 2004.

[89] D. V. Evans and R. Porter. Hydrodynamic characteristics of an oscillating water column device. *Applied Ocean Research*, 17(3):155–164, 1995.

[90] J. Wu, Z. Wan, and Y. Fang. Wave reflection by a vertical wall with a horizontal submerged porous plate. *Ocean engineering*, 25(9):767–779, 1998.

[91] Y. Liu, Y. Li, and B. Teng. Wave interaction with a new type perforated breakwater. *Acta Mechanica Sinica*, 23(4):351–358, 2007.

[92] J. Schay, J. Bhattacharjee, and C. G. Soares. Numerical modelling of a heaving point absorber in front of a vertical wall. In *ISME 2013 32nd International Conference on Ocean, Offshore and Arctic Engineering, Nantes, France*, volume 55423, page V008T09A097. American Society of Mechanical Engineers, 2013.

[93] T. Sahoo, M. M. Lee, and A. T. Chwang. Trapping and generation of waves by vertical porous structures. *Journal of Engineering Mechanics*, 126(10):1074–1082, 2000.

[94] T. L. Yip, T. Sahoo, and A. T. Chwang. Trapping of surface waves by porous and flexible structures. *Wave Motion*, 35(1):41–54, 2002.

[95] S. Koley and T. Sahoo. Oblique wave scattering by horizontal floating flexible porous membrane. *Meccanica*, 52:125–138, 2017.

[96] J. Bhattacharjee and C. G. Soares. Oblique wave interaction with a floating structure near a wall with stepped bottom. *Ocean Engineering*, 38(13):1528–1544, 2011.

[97] H. Behera, R. B. Kaligatla, and T. Sahoo. Wave trapping by porous barrier in the presence of step type bottom. *Wave Motion*, 57:219–230, 2015.

[98] R. B. Kaligatla, M. Sharma, and T. Sahoo. Wave trapping by dual porous barriers near a wall in the presence of bottom undulation. *J. Mar. Sci. Appl*, 16(3):286–297, 2017.

[99] T. H. Havelock. Forced surface-waves on water. *Philosophical Magazine 8*, 8(51): 569–577, 1929.

[100] I. J. Losada, M. A. Losada, and A. J. Roldan. Propagation of oblique incident waves past rigid vertical thin barriers. *Applied Ocean Research*, 14(3):191–199, 1992.

[101] Xiping Yu. Diffraction of water waves by porous breakwaters. *Journal of waterway, port, coastal, and ocean engineering*, 121(6):275–282, 1995.

[102] M. M. Lee and A. T. Chwang. Scattering and radiation of water waves by permeable barriers. *Physics of Fluids*, 12(1):54–65, 2000.

[103] Masashi Kashiwagi, Igor Ten, and Makoto Yasunaga. Hydrodynamics of a body floating in a two-layer fluid of finite depth. part 2. diffraction problem and wave-induced motions. *Journal of marine science and technology*, 11:150–164, 2006.

[104] Y. H. Zheng, Y. M. Shen, and C. O. Ng. Effective boundary element method for the interaction of oblique waves with long prismatic structures in water of finite depth. *Ocean Engineering*, 35(5-6):494–502, 2008.

[105] Emiliano Renzi, A Abdolali, G Bellotti, and F Dias. Wave-power absorption from a finite array of oscillating wave surge converters. *Renewable Energy*, 63:55–68, 2014.

[106] A. Choudhary and S. C. Martha. Diffraction of surface water waves by an undulating bed topography in the presence of vertical barrier. *Ocean Engineering*, 122:32–43, 2016.

[107] Lizhu Hao, Ziying Pan, and Baoshan Wu. Three-dimensional green-function method to predict the water wave radiation of a submerged body with ice cover. *Applied Ocean Research*, 101:102297, 2020.

[108] S. Timoshenko, S. Woinowsky-Krieger, et al. *Theory of plates and shells*, volume 2. McGraw-hill New York, 1959.

[109] C. Fox and V. A. Squire. On the oblique reflexion and transmission of ocean waves at shore fast sea ice. *Philosophical Transactions of the Royal Society of London. Series A: Physical and Engineering Sciences*, 347(1682):185–218, 1994.

[110] G. Sahoo and S. C. Martha. Semi-analytical study of reduction of wave impact on an elastic plate in the presence of a vertical porous structure. *Acta Mechanica*, pages 1–16, 2024.

[111] S. Koley. *Integral equation and allied methods for wave interaction with porous and flexible structures.* PhD thesis, Indian Institute of Technology Kharagpur, 2016.

[112] J. Bhattacharjee and C. G. Soares. Flexural gravity wave over a floating ice sheet near a vertical wall. *Journal of Engineering Mathematics*, 75:29–48, 2012.

[113] M. K. Jain, S. R. K. Iyengar, and R. K. Jain. *Numerical Methods for Scientific and Engineering Computation*. New Age International, 2003.

[114] S. Koley and K. Panduranga. Energy balance relations for flow through thick porous structures. *International Journal of Computational Methods and Experimental Measurements*, 9(1):28–37, 2021.

[115] S. Koley, R. Mondal, and T. Sahoo. Fredholm integral equation technique for hydroelastic analysis of a floating flexible porous plate. *European Journal of Mechanics-B/Fluids*, 67:291–305, 2018.

[116] G. Sahoo, S. Singla, and S. C. Martha. Mitigation of wave impact on sea wall by a floating elastic plate and a porous structure. *Journal of Offshore Mechanics and Arctic Engineering*, 145(5):051202, 2023.

[117] M. Sharma, R. B. Kaligatla, and T. Sahoo. Wave interaction with a submerged floating tunnel in the presence of a bottom mounted submerged porous breakwater. *Applied Ocean Research*, 96:102069, 2020.

[118] G. Sahoo, S. Singla, and S. C. Martha. Scattering of oblique water waves by thick porous structure and thin elastic plate. *Ocean Engineering*, 248:110526, 2022.

[119] B.N. Mandal and A. Chakrabarti. Water wave scattering by barriers. *WIT Press*, 2000.

[120] G. Sahoo, S. Singla, and S. C. Martha. Interaction of surface water waves with partial porous structure and floating elastic plate in the presence of sea wall. *Ships and Offshore Structures*, pages 1–18, 2024.

[121] M. Kanoria, D. P. Dolai, and B. N. Mandal. Water-wave scattering by thick vertical barriers. *Journal of Engineering Mathematics*, 35:361–384, 1999.

[122] D. Karmakar and C. G. Soares. Oblique scattering of gravity waves by moored floating membrane with changes in bottom topography. *Ocean Engineering*, 54: 87–100, 2012.

[123] N.R.T. Biggs and D. Porter. Wave scattering by an array of periodic barriers. *IMA journal of applied mathematics*, 70(6):908–936, 2005.

[124] V. Venkateswarlu, K. M. Praveen, and D. Karmakar. Surface gravity wave scattering by multiple energy absorbing structures of variable horizontal porosity. *Coastal Engineering Journal*, 62(4):504–526, 2020.

[125] E. Dhanunjaya, E. S. Rayudu, and V. Venkateswarlu. Oblique wave trapping by periodic array of two-layer pile rock breakwaters placed on uneven seabed. *Coastal Engineering Journal*, pages 1–20, 2024.

[126] V. Venkateswarlu, K. M. Praveen, K. G. Vijay, K. Anil, and D. Karmakar. Oblique wave interaction with a two-layer pile-rock breakwater placed on elevated bottom. *Ships and Offshore Structures*, 17(4):852–865, 2022.